

# **NSLS-II Project**

## **PRELIMINARY DESIGN REPORT for the X-RAY POWDER DIFFRACTION (XPD) BEAMLINE AT NSLS-II**



*Intentionally blank.*

## Approvals and Reviewers

Compiled by	Signature	Date
Eric Dooryhee, XPD Group Leader, NSLS-II	_____	_____
<b>Reviewers</b>		
Simon Billinge, BAT Spokesperson, signing on behalf of the BAT	_____	_____
Andy Broadbent, Beamlines Manager	_____	_____
Nicholas Gmür, ESH Coordinator, NSLS-II	_____	_____
Sushil Sharma, Mechanical Engineering Group Leader, NSLS-II	_____	_____
<b>Approved by</b>		
Qun Shen, XFD Director, NSLS-II	_____	_____

## Document Updates

The Preliminary Design Report for the Powder Diffraction (XPD) Beamline at NSLS-II is a controlled document, revised under change control.

Version No.	Date	Authorized by	Changes made
0	07/19/2010	E. Dooryhee	Outline and template
1	08/25/2010	E. Dooryhee	First draft
2	09/08/2010	E. Dooryhee	Second draft
2	09/17/2010	K. Robinson	Start editing/formatting
3	09/22/2010	E. Dooryhee	Third draft
F	09/30/2010	E. Dooryhee	Final release
M	11/24/2010	E. Dooryhee	Modified public version (proprietary/confidential information removed)

## Authors

<b>Eric Dooryhee</b>	XPD Beamline Group Leader
<b>Sanjit Ghose</b>	Associate Scientist
<b>Margareta Rehak</b>	Mechanical Engineer
<b>Xianbo Shi</b>	Postdoctoral Scholar

*Intentionally blank.*

## Table of Contents

Document Overview.....	xiv
<b>1. Introduction.....</b>	<b>1</b>
1.1 Scientific objectives .....	1
1.2 Comparison with other instruments.....	3
1.3 Beamline Advisory Team .....	3
1.4 Acknowledgments .....	4
<b>2. Insertion Device .....</b>	<b>5</b>
<b>3. Front End.....</b>	<b>8</b>
3.1 General layout of the front end.....	8
3.2 Fixed aperture mask.....	9
3.3 Rationale for fixed mask aperturing.....	11
<b>4. Beamline Optical Design .....</b>	<b>12</b>
4.1 Introduction .....	13
4.2 Rationale for the deflection angle and the energy of the branchline .....	14
4.3 Description of the beamline operation modes.....	15
4.4 Beamline layouts .....	17
4.5 Ray tracings .....	17
<b>5. Description of the Beamline Components .....</b>	<b>18</b>
5.1 Major components .....	18
5.2 Enclosures .....	20
5.3 Beam transport.....	22
5.3.1 Beamline vacuum system .....	22
5.3.2 Radiation shielding of evacuated beampipes.....	22
5.3.3 Radiation safety components .....	23
5.3.4 Diagnostics system components .....	26
5.3.5 Beam doors .....	27
5.4 High heat load management.....	28
5.4.1 Introduction.....	28
5.4.2 Diamond and SiC filter systems .....	28
5.5 High energy monochromators.....	37
5.5.1 Sagittally focusing monochromator.....	37
5.5.2 Side-bounce monochromator .....	44
5.6 Monochromatic Beam Optics .....	46
5.6.1 Vertically focusing optics.....	46
5.6.2 High-resolution monochromator .....	55
5.6.3 Secondary focusing optics .....	56

<b>6.</b>	Beamline Performance.....	57
6.1	Beamline ray-tracing.....	57
6.1.1	The source contribution.....	57
6.1.2	The DLM contribution.....	57
6.1.3	The mirror contribution.....	58
6.1.4	Predictions of flux, resolution and beam size.....	59
6.2	Instrumental resolution function .....	61
6.3	Day One expected performance .....	63
<b>7.</b>	Endstation Instrumentation.....	65
7.1	Overview of endstation C.....	65
7.2	Diffraction in endstation C.....	65
7.2.1	General description.....	65
7.2.2	Specifications .....	67
7.3	High-energy x-ray detectors.....	68
7.3.1	Introduction.....	68
7.3.2	High energy detector efficiency challenge .....	68
7.3.3	Detector strategy .....	69
7.4	High-resolution analyzer stage.....	71
7.5	Sample environments.....	73
7.6	Endstations B and D.....	74
7.7	Beamline and motion controls.....	75
7.8	Beamline software .....	75
<b>8.</b>	Infrastructure for Beamline and User Support.....	77
8.1	Hutches.....	77
8.2	Environmental .....	78
8.3	Surveying requirements.....	78
8.4	Controls requirements .....	78
8.5	Utilities requirements .....	79
8.6	User space .....	81
8.7	Sample preparation and manipulation.....	81
8.8	Special beamline requirements.....	82
8.9	Preliminary safety analysis .....	83
8.9.1	Shielding.....	83
8.9.2	Personal Safety System.....	83
8.9.3	Equipment Protection System .....	84
<b>9.</b>	Future Upgrade Options.....	85
<b>10.</b>	Schedule.....	86
<b>11.</b>	Summary .....	88
<b>12.</b>	References .....	90
<b>13.</b>	Appendices .....	94

A	Brief Description of the Front End.....	95
A.1	Overview of the major components.....	95
A.2	Front end ray tracings.....	98
B	Reference Drawings.....	100
B.1	Front end layout .....	100
B.2	Beamline layout.....	101
B.3	Synchrotron ray trace .....	107
B.4	Bremsstrahlung ray trace.....	110
B.5	Control diagrams .....	112
B.6	Personnel safety system schematic layout.....	117
B.7	Vacuum system.....	118
C	Specifications for the Enclosures.....	119
D	Laue Monochromatization .....	120
D.1	Horizontally deflecting side bounce monochromator.....	120
D.2	Sagittally focusing double-crystal Laue monochromator .....	123
E	Design of the Double Laue Monochromator.....	125
E.1	Introduction .....	125
E.2	Measurement of the bending radii of the leaf bender.....	126
E.3	Numerical simulations.....	128
E.4	Analysis of the leaf bender.....	129
E.5	Analysis of the leaf bender with rib.....	129
E.6	Analysis of the roller bender with integrated cooling.....	130
E.7	Analysis of the roller bender with cooling through braids .....	131
F	Refractive Optics.....	134
G	Multilayered Mirrors.....	137
H	Detector Development.....	139
H.1	1D strip detectors .....	139
H.2	2D pixel detectors.....	139
H.3	Large-area image plates.....	140
H.4	High-resolution CCD cameras .....	140
H.5	High-speed flat panel detectors .....	140

## List of figures

Fig. 2-1: Comparison of the spectral brightness and spectral flux per unit of horizontal angle. ....	6
Fig. 2-2: Power density of the damping wiggler at 28 m from the source. ....	7
Fig. 2-3: Comparison of the horizontal (left) and vertical (right) angular profiles. ....	7
Fig. 3-1: Typical front end configuration at NSLS-II, as of 09/08/2010. ....	9
Fig. 3-2: Front end fixed aperture mask (FMK). ....	9
Fig. 3-3: Principle of the Glidcop wiggler absorber. ....	10
Fig. 3-4: Thermal calculations on the GlidCop mask. (Courtesy of V. Ravindranath).....	10
Fig. 3-5: Horizontal (left) and vertical (right) angular profiles of DW100 emission.....	11
Fig. 3-6: (left) Variation of the flux outputs; (right) Variation of the spectral power versus aperture. ....	11
Fig. 4-1: Schematic layout of the beamline (see also appendix B). ....	12
Fig. 4-2: Simplified scheme with hutch labeling. ....	13
Fig. 4-3: $2\theta$ angle versus the type of reflection (Si crystal) and the energy. ....	15
Fig. 4-4: Schematic side view of the optical layout of the beamline. ....	16
Fig. 5-1: XPD hutch Layout. ....	21
Fig. 5-2: Radiation safety components.....	23
Fig. 5-3: White beam stop. ....	25
Fig. 5-4: Monochromatic Photon Shutter. ....	26
Fig. 5-5: View of the diffractometer and beam door at the Australian Source Powder Diffraction beamline. ....	27
Fig. 5-6: Absorbed heat for different materials vs. thickness, first pass only.....	29
Fig. 5-7: Percent of Transmitted flux for different materials. ....	29
Fig. 5-8: Sequence of diamond and SiC: thickness needed to let 0.8 kW through, and percentage transmitted flux.30	
Fig. 5-9: Schematic of diamond and SiC filters. The power spectrum after filtering is shown at right.....	31
Fig. 5-10: Final power spectrum distribution. Sequential filtering causes beam hardening.....	31
Fig. 5-11: Diamond Windows, JEEP beamline. Courtesy M. Drakopoulos. ....	31
Fig. 5-12: von Mises stresses and temperature distribution. ....	32
Fig. 5-13: SiC Filters, JEEP beamline, courtesy M. Drakopoulos. ....	33
Fig. 5-14: Transmitted power versus total SiC thickness.....	34
Fig. 5-15: DLM design concept for a sagittally bent Double Laue geometry (6) (7). ....	38
Fig. 5-16: X-ray beam trace in the DLM.....	39
Fig. 5-17: Shadow ray tracing calculations for the flux per energy bandwidth.....	40
Fig. 5-18: Roller bender schematic showing bending concept. ....	41
Fig. 5-19: (left) DLM at the JEEP beamline of DLS. (right) DLM at ID11 of ESRF. ....	43
Fig. 5-20: Schematics (top view) of three possible geometries for the side bounce mono of the XPD beamline. ....	44
Fig. 5-21: The efficiency of a SL mirror for different coating materials. ....	49
Fig. 5-22: Calculated reflectivity with respect to grazing angle. ....	51
Fig. 5-23: Calculated reflectivity with respect to the grazing angle for the PDF branchline 3-stripes ML mirror.....	51
Fig. 6-1: Comparison of the horizontal (a and c) and vertical (b and d) angle and position profiles at 50 keV.....	57
Fig. 6-2: The rocking curves of the sagittally bent Laue crystals at different thicknesses and bending radii. ....	58
Fig. 6-3: The multi-layer treatment of the sagittally bent crystal. ....	58
Fig. 6-4: The relative output flux (a), the energy bandwidth (b) and the flux per energy bandwidth.....	60
Fig. 6-5: The simulated vertical profiles (left) in the high-flux mode and the energy profile (right). ....	61
Fig. 6-6: The FWHM of the IRF at different energies with varying $\Delta_m$ (left) and $k$ (right) as a function of Q.....	62
Fig. 6-7: The FWHM in the high-flux mode (solid lines) and the high-resolution mode (dotted lines). ....	63
Fig. 7-1: Conceptual design of the NSLS-II high-energy high-resolution powder diffraction beamline.....	65
Fig. 7-2: Transmission efficiency of 250 $\mu$ m Si and Ge as a function of x-ray energy. ....	69
Fig. 7-3: (left) MA system at I11 Diamond, courtesy of C.C. Tang. (right) MA system at 11-BM APS.....	72
Fig. 7-4: The Laue crystal array from (38). ....	72
Fig. 7-5: The concept of modular towers supporting different parts of the experimental set-up is illustrated. ....	74
Fig. 8-1: View of a completed hutch at DESY. ....	77
Fig. 8-2: Location of the safety shutters and hutches.....	84
Fig. 13-1: One design being considered for the XBPMs is shown above. ....	96

Fig. 13-2: Principle of the photon shutter.....	97
Fig. 13-3: Photographs of the safety shutter.....	98
Fig. 13-4: Front-end layout plan of the front end of XPD. (L. Doom). ....	100
Fig. 13-5: Beamline layout plan view. ....	101
Fig. 13-6: Elevation layout of the XPD beamline, NSLS-II.....	102
Fig. 13-7: Beamline plan: shielding enclosure layout.....	102
Fig. 13-8: Beamline overall perspective view. ....	103
Fig. 13-9: Conceptual layout for the powder diffraction beamline FOE.....	104
Fig. 13-10: Conceptual layout for the powder diffraction beamline: FOE and all three endstations.....	105
Fig. 13-11: Conceptual layout for the powder diffraction beamline endstations.....	106
Fig. 13-12: Horizontal synchrotron radiation optical aperture ray tracings. ....	108
Fig. 13-13: Vertical synchrotron radiation optical aperture ray tracings. ....	109
Fig. 13-14: Horizontal bremsstrahlung ray tracings. ....	110
Fig. 13-15: Vertical bremsstrahlung ray tracings. ....	111
Fig. 13-16: Beamline Schematic. See legend on next page.....	112
Fig. 13-17: FE Schematic. ....	113
Fig. 13-18: Symbol legend for process and instrumentation diagrams. ....	113
Fig. 13-19: Control block diagram, part 1 of 3.....	114
Fig. 13-20: Control block diagram, part 2 of 3.....	115
Fig. 13-21: Control block diagram, part 3 of 3.....	116
Fig. 13-22: Personnel safety system schematic. ....	117
Fig. 13-23: The focusing geometries of the bent Laue/Bragg crystals (41). ....	120
Fig. 13-24: The bending radius as a function of the asymmetry angle ..... 121	121
Fig. 13-25: (a) $R_s$ as a function of $\chi$ , (b) the Poisson's ratio $\nu_a$ . .... 123	123
Fig. 13-26: (left) Roller bender design DLM at X17B1 NSLS. (center) Roller bender schematic. .... 126	126
Fig. 13-27: (right) Leaf bender design DLM without cooling at X7B NSLS..... 126	126
Fig. 13-28: The crystal geometry showing crystal planes. (right). .... 127	127
Fig. 13-29: The inverse of the meridional bending radius $1/R_m$ vs. the inverse of the sagittal bending radius $1/R_s$ . 127	127
Fig. 13-30: Si (100) crystal orientation used in the ANSYS calculation. .... 128	128
Fig. 13-31: Leaf bender (quarter model). .... 129	129
Fig. 13-32: ANSYS results showing the bending of the leaf bender with rib (quarter symmetric model). .... 129	129
Fig. 13-33: ANSYS model showing the bending of the roller bender. .... 131	131
Fig. 13-34: Roller bender design with indirect LN cooling through Cu braids. .... 132	132
Fig. 13-35: FEA analysis of the Roller bender design. .... 132	132
Fig. 13-36: FEA results: Calculated $R'_m$ at variable energies for the roller bender ..... 133	133
Fig. 13-37: Effective aperture as a function of photon energy ..... 134	134
Fig. 13-38: Photo of commercially available CRL <sup>28</sup> ..... 136	136
Fig. 13-39: Linear Al lens: opening = $1 \times 3.5 \text{ mm}^2$ and $R = 200 \text{ }\mu\text{m}$ . (Lengeler, Snigirev) ..... 136	136
Fig. 13-40: Mythen detector at the PD beamline at the Australian Source. .... 139	139
Fig. 13-41: View of the XPAD detector at the BM02 beamline at the ESRF. .... 140	140
Fig. 13-42: Perkin-Elmer flat panel detector. .... 141	141
Fig. 13-43: Flat panel detector at 11-ID, courtesy of P. Chupas..... 141	141

**List of tables**

Table 1-1: High-energy, high-power powder diffraction beamlines at other facilities.....	3
Table 2-1: NSLS-II damping wiggler parameters.....	5
Table 2-2: RMS electron beam values at the center of the high- $\beta$ straight section (9.3 m). ....	5
Table 2-3: Brightness and flux of the damping wiggler source at NSLS-II.....	7
Table 3-1: Components of the XPD front end.....	8
Table 3-2: Characteristic numbers of the design and FEA results.....	10
Table 4-1: Hutch labeling convention and main purposes. ....	14
Table 4-2: Parallel operation of the hutches.....	16
Table 4-3: Vertical beam positions in experimental hutches C and D.....	16
Table 5-1: Components of the Powder Diffraction Beamline.....	18
Table 5-2: Characteristics of the enclosures.....	20
Table 5-3: Radiation shielding of evacuated beampipes.....	22
Table 5-4: Beamline components critical for safety.....	24
Table 5-5: Requirements for the monochromatic photon shutter.....	26
Table 5-6: Material properties.....	33
Table 5-7: Filter performance.....	34
Table 5-8: Consequences of failure of one diamond window.....	35
Table 5-9: Filter specifications.....	35
Table 5-10: Preliminary specifications for the XPD white beam slits.....	36
Table 5-11: Comparison among monochromators for high energy wiggler x-ray beam.....	37
Table 5-12: Optimized performance parameters for the XPD DLM.....	40
Table 5-13: Crystal dimension and specification.....	41
Table 5-14: Preliminary specifications for the motion controls of the XPD DLM.....	42
Table 5-15: Preliminary specifications for the vessel.....	43
Table 5-16: Summary of the FEA results for design under consideration.....	44
Table 5-17: Comparison of single crystal monochromators for the PDF branch.....	45
Table 5-18: SBM design parameters.....	45
Table 5-19: Preliminary SBM crystal design parameters.....	46
Table 5-20: Preliminary specifications for the motion controls of the SBM.....	46
Table 5-21: Comparison of different focusing optics available for hard x-ray focusing.....	47
Table 5-22: Comparison of useful flux at the sample in the focusing mode of the vertical optics.....	48
Table 5-23: Ray tracing results for XPD beamline after the SL mirror (in both modes).....	49
Table 5-24: Characteristics of SL mirror at two different operation modes.....	52
Table 5-25: Preliminary specifications for the SL mirror.....	53
Table 5-26: Preliminary specifications for the bender.....	54
Table 5-27: Preliminary specifications for the vessel.....	54
Table 5-28: Preliminary specifications for the ML mirror.....	55
Table 6-1: SHADOW ray tracing results for the XPD beamline.....	59
Table 6-2: Vertical beam sizes at different mirror slope errors in the high-flux mode.....	60
Table 6-3: Energy resolutions at different mirror slope errors in the high-resolution mode.....	61
Table 6-4: Values of the profile FWHMs of the optics.....	62
Table 6-5: The basic configuration shows which components are required to start beamline operation.....	64
Table 7-1: Preliminary specifications for the diffractometer of endstation C.....	67
Table 7-2: Potential PD detector concerns.....	68
Table 7-3: Impact of point detectors on the science and operation of XPD.....	69
Table 7-4: Impact of linear position sensitive detectors on the science and operation of XPD.....	70
Table 7-5: Impact of area detectors on the science and operation of XPD.....	71
Table 7-6: A list of detectors and their requirements in terms of data storage and data rate.....	76
Table 8-1: Utility provisions.....	79
Table 8-2: Cooling water requirements for XPD.....	80
Table 8-3: Flow requirements for the various XPD optical components.....	80
Table 8-4: Potential catalysis applications and chemicals involved.....	81

Table 8-5: XPD Beamline Electron Beam Stability Requirements .....82

Table 8-6: Attenuation lengths of shielding materials (Pb, W) vs. energy.....83

Table 13-1: Comparison of the three cases for the PDF branchline with: .....122

Table 13-2: Expected performance of the SBM with:  $p = 35.7$  m,  $q = 11.7$  m, crystal thickness  $T_0 = 3$  mm. ....122

Table 13-3: Design characteristics of DLMs at other beamlines .....125

Table 13-4:  $R_m$  for different crystal dimensions at various bending radii  $R_s$ . .....127

Table 13-5: Evaluation of different cooling schemes. ....131

Table 13-6: FEA results: Variable  $R'_m$  for variable energies for the roller bender.....133

Table 13-7: Calculated Be CRL parameters at 74.8 keV with:  $d = 10$   $\mu$ m,  $F = 5.5$  m.....135

Table 13-8: Calculated Be CRL parameters at 50 keV with:  $d = 10$   $\mu$ m,  $F = 10.5$  m.....135

Table 13-9: Optimized parabolic CRL parameters for the XPD beamline. ....135

Table 13-10: Calculated multi-layered mirror characteristics with different materials. ....137

Table 13-11: Calculated Pt / B<sub>4</sub>C multi-layered mirror (2nm bilayers) characteristics . ....137

Table 13-12: Calculated multi-layered mirror characteristics with different numbers of bilayers. ....138

Table 13-13: CCD and pixel detectors.....142

Table 13-14: Image plate and flat panel CMOS detectors. ....143

Table 13-15: 1D pixel detectors.....144

*Intentionally blank.*

## Acronyms

APS	Advanced Photon Source	LN	Liquid Nitrogen
Be	Beryllium	LSFR	Low Spatial Frequency Roughness
BM	Bending Magnet	LTP	Long Trace Profiler
BMPS	Bending Magnet Photon Shutter	MA	Multi Analyzer
BPM	Beam Position Monitor	ML	Multilayer (mirror)
BRC	Bremsstrahlung collimator	MLL	Multilayer Lens
BRS	Bremsstrahlung stop	MLM	Multilayer Monochromator
CDR	Conceptual Design Report	MSFR	Mid Spatial Frequency Roughness
CMOS	Complementary Metal Oxide Semicond.	NMR	Nuclear Magnetic Resonance
CO	Lead Collimator	PAD	Pixel Array Detector
CRL	Compound Refractive Lens	PD	Powder Diffraction
CTG	Cartridge	PDF	Pair Distribution Function
DCM	Double Crystal Monochromator	PDR	Preliminary Design Report
DFF	Diffractometer	PLC	Programmable Logical Controller
DLM	Double Laue Crystal Monochromator	PPS	Personal Protection System
ES	Endstation	PSD	Position Sensitive Detector
ESRF	European Synchrotron Radiation Facility	PSH	Photon Shutter
EXAFS	Extended X-ray Absorption Fine Structure	RWC	Ratchet Wall Collimator
FE	Front End	SAXS	Small Angle X-ray Scattering
FEA	Finite Element Analysis	SBM	Side Bounce Monochromator
FGV	Fast Gate Valve	SCM	Screen in Mono Beam
FLT	Filter	SCW	Screen in White Beam
FMK	Fixed Aperture Mask	SGV	Slow Gate Valve
FOE	First Optics Enclosure	SL	Single-Layer (mirror)
FWHM	Full Width at Half Maximum	SLM	Monochromatic SLIT
FZP	Fresnel Zone Plates	SLW	White beam slit water cooled
GTV	Gate Valve	SSH	Safety Shutter
HCH	Hutch (Radiation Enclosure)	STP	Beam Stop
HOPG	Highly Oriented Pyrolytic Graphite	TSP	Titanium Sublimation Pump
HRM	High-resolution Monochromator	UPS	Uninterruptible Power Supply
HSFR	High Spatial Frequency Roughness	VFM	Vertically Focusing Mirror
ICB	Ion Chamber	WBS	White Beam Slits
ID	Insertion Device	WIN	Diamond Window
IPP	Stand alone pump	XBPM	Photon Beam Position Monitor
IP	Image Plate	XPD	Powder Diffraction Beamline
IRF	Instrumental Resolution Function	XYSLT	X/Y Slit
IVU	In-Vacuum Undulator		

## DOCUMENT OVERVIEW

The current report covers the *preliminary design phase activities* for the NSLS-II XPD Project Beamline:

- Design specifications for the enclosures and optical systems
- Design specifications for radiation safety systems
- Final design of beam transport systems
- Preliminary design of endstation instrumentation
- Synchrotron and bremsstrahlung tracings of the beamline
- PSS, utility and vacuum layouts
- Beamline control and instrumentation (PI&D) diagrams

It follows the guidelines given in the NSLS-II “Experimental Facilities Beamline Final Design Plan,” June 6, 2009.

# 1. INTRODUCTION

## 1.1 Scientific objectives

The primary purpose of the beamline is the quantitative characterization of the atomic structure of complex materials; not just carefully prepared ideal systems, but materials as they are actually used. Detailed knowledge of atomic structure is a prerequisite for understanding material properties, and essential in any rational materials design and synthesis effort. Development of meaningful structure/property correlations requires simultaneous measurement of structure and properties. Next-generation technologies will place increasing demands on materials, requiring enhanced functionality and performance under a wide range of environments. The ability to design functional materials at the atomic level, taking advantage of new synthetic approaches and computational modeling, unavoidably requires dedicated characterization tools with an increasing level of sophistication and hardware/software integration.

The scientific grand challenge is to obtain robust and quantitative (micro) structural information about materials that are complex, nanostructured and often heterogeneous. Along with studying structure in the ground state in ambient conditions, it is increasingly important to study structure in systems that are evolving in time (for example, after excitation or while undergoing chemical reaction), and in materials that are in a metastable state. These situations are becoming the norm rather than the exception in frontier science and technology, but there is a dearth of robust tools for studying structure in such systems. An important scientific goal is the study of materials under extreme conditions of temperature, pressure, magnetic/electric/stress field, chemical environment, etc. **Real materials in Real Time and in Real Conditions** is identified by the DOE Basic Energy Sciences office as one of today's Grand Challenges<sup>1</sup>. Such studies present special challenges to the experimentalist, not only in generating the extreme conditions, but also in getting the x-ray probe into and out of the apparatus.

The proposed X-ray Powder Diffraction (XPD) beamline will provide unique capabilities for addressing these problems, and is designed with Total Structure Studies in mind. High-throughput, good-resolution powder diffraction (with well-defined peak shapes and low background) will be carried out using hard x-rays, with a beam size (tens to hundreds of microns) adjustable to match the graininess and heterogeneity scales. The need for high resolution applies either in reciprocal space or in direct space but more rarely in both; this is one of the objectives for XPD. High-Q and Pair Distribution Function studies (also with small beams) will permit determination of both long- and short-range structures.

XPD will cover the new trends in x-rays Materials Science and PD Science: higher energy, faster acquisition rates, *in situ*, extreme environments, combined methods. The beamline will pay special attention to sample environments, allowing for time-resolved and *in situ* measurements. Recent examples of high-energy x-ray research also include measurements of stress/strain in materials, powder diffraction of compounds containing heavy elements, diffuse scattering of defects in complex oxides, high/small-angle scattering from thermal-barrier coatings, imaging, and tomography (1) (2). The beamline must address future scientific challenges in (for example) hydrogen storage, CO<sub>2</sub> sequestration,

<sup>1</sup> <http://www.er.doe.gov/bes/reports/list.html>

### The advantages of hard x-rays are:

- The ability to penetrate thick samples and environmental chambers (less problems with windows).
- To provide access to a larger portion of reciprocal space, and to access reciprocal diffraction vectors  $Q$  as large as  $60 \text{ \AA}^{-1}$ .
- The scattering geometry is simplified because of the large (flat) Ewald sphere and allows for rapid transmission diffraction (forward diffraction, no scan).
- Most importantly, absorption and extinction corrections are minimal and hard x-rays yield more accurate diffracted intensities. This is critical for charge density mapping.
- The polarization factor is close to unity (small Bragg angles).
- The radiation dose is also lower, opening the method to a wide range of otherwise radiation-sensitive materials, e.g., bio materials.
- The diffraction scattering signal can be recorded in the tomographic mode.

advanced structural ceramics, catalysis, and materials processing—all *in situ/in operando* experiments difficult at other national user facilities (more details in the Materials Diffraction Suites White Paper (March 2008)<sup>2</sup> and in the CDR<sup>3</sup>).

The major XPD beamline scientific program areas are summarized below:

- Complexity and the nanostructure problem
- Extreme environments
- Time resolved studies
- Total structure studies

The source for the beamline is a full length 7 m long damping wiggler designed to obtain the highest possible flux in the desired energy range of 30-80 keV, with optimization at ~50 keV and ~80 keV. The XPD beamline will build upon active programs at the NSLS (and elsewhere), concentrating on higher energies (30-80 keV), while in conventional x-ray diffraction, any energy greater than 20 keV is considered exotically high. The beamline also has of novel optical design, making use of techniques and instrumentation pioneered at the NSLS (e.g., Laue monochromators and Ge strip array detectors).

The major technical challenges of XPD are identified and addressed in the present document:

- Optimize flux at high energies, while the critical energy of the source is  $E_c = 11.1$  keV
- High heat load emanates from the 61 kW radiating source
- The large natural divergence of the source ( $1.1 \times 0.15$  mrad<sup>2</sup>) must be captured while working with small reflection angles (reflective optics) and small acceptance (refractive optics)
- Use of Laue diffractive optics
- Manipulation of sample environments (gas, high  $T$ - $P$ ...), including potentially hazardous conditions
- Minimize set-up time overhead (several endstations, several diffraction techniques) in a multi-purpose beamline
- Enhance high-energy x-ray detection efficiency
- On-line data acquisition and analysis

---

<sup>2</sup> [http://www.nsls.bnl.gov/newsroom/events/workshops/2008/lscp/white\\_papers/mse-diffraction.pdf](http://www.nsls.bnl.gov/newsroom/events/workshops/2008/lscp/white_papers/mse-diffraction.pdf)

<sup>3</sup> [http://www.bnl.gov/nsls2/docs/PDF/cdr/6\\_XPD\\_23Mar2010.pdf](http://www.bnl.gov/nsls2/docs/PDF/cdr/6_XPD_23Mar2010.pdf)

## 1.2 Comparison with other instruments

**Table 1-1:** High-energy, high-power powder diffraction beamlines at other facilities.

Beamline	Source	Beam divergence	Energy Range (keV)	Resolution Powder Diffraction	Materials Science	Imaging	Extreme conditions
ESRF ID11	undulator	low	29 - 140	medium	yes	no	yes
ESRF ID15	undulator & wiggler	low	30 - 400	medium	yes	scanning	yes
ESRF ID31	undulator	low	5 - 31	high	yes	no	no
APS 11D	undulator	low	50 - 130	high	yes	no	no
APS 11ID	undulator	low	60, 90, 115	low	yes	no	yes
Diamond I12	wiggler	high	50 - 150	medium	yes	Full field	no
Diamond I15	wiggler	high	20 - 70	low	yes	scanning	yes
Soleil Psyché	wiggler	high	30 - 70	low	yes	scanning	yes
Australian Source IMBL	wiggler	high	30 - 100	medium	no	Full field	no
SPRING-8 BL08W	wiggler	high	100 - 300	medium	yes	scanning	no
SPRING-8 BL10XU	undulator	low	14 - 58	high	no	scanning	yes
PETRA P02	undulator	low	30 - 60	high	yes	scanning	yes
PETRA P07	undulator	low	50 - 300	low	yes	scanning	no
XPD	wiggler	high	30 - 80	medium	yes	Scanning	yes

## 1.3 Beamline Advisory Team

The XPD Beamline Advisory Team (BAT), formed in March 2008, is a group of expert scientists with common interest and experience in the XPD scientific program and in the beamline optics and endstations needed to carry out this forefront program. The members are as follows:

Simon Billinge (spokesperson)	Columbia University and BNL
Peter Chupas	Argonne National Laboratory
Lars Ehm	Stony Brook University
Jon Hanson	Brookhaven National Laboratory
James Kaduk	Poly Crystallography Inc.
John Parise	Stony Brook University
Peter Stephens	Stony Brook University

Sign-up agreement between NSLS-II Project Director Steve Dierker and the Beamline Advisory Team, 11/24/2008.



## 1.4 Acknowledgments

All BNL staff members below are acknowledged for help, support, and discussion and for providing relevant material (calculations, figures, drawings, etc.). ACCEL (now Bruker) is also thanked for the preliminary case study and design for the XPD project beamline.

Berman, Lonny	Experimental Systems Division (ESD), NSLS
Broadbent, Andrew	XFD, NSLS-II
Carlucci-Dayton, Mary	XFD, NSLS-II
Chabot, Daron	NSLS-II
Chubar, Oleg	XFD, NSLS-II
Conley Raymond	XFD, NSLS-II
DeSantis Andrew	NSLS-II
Doom Lewis	Accelerator System Division (ASD), NSLS-II
Evans –Lutterodt, Kenneth	NSLS
Ferreira, Marcelo	NSLS-II
Haas, Edwin	NSLS & NSLS-II
Hussain, Aftab	NSLS-II
Job, Panakkal	NSLS-II
Johanson, Michael	NSLS-II
Kaznatcheev, Konstantine	XFD, NSLS-II
Keister, Jeffrey	NSLS & NSLS-II
Northrup, Paul	NSLS
Ravindranath, Viswanath	NSLS-II
Robinson, Kathleen	NSLS-II
Siddons, Peter	ESD, NSLS
Shen, Qun	XFD, NSLS-II
Zhong, Zhong	ESD, NSLS & NSLS-II
Zigrosser, Doug	NSLS-II

## 2. INSERTION DEVICE

The powder diffraction beamline will provide hard x-rays over a large energy range (30-80 keV). The continuity of the power spectrum of a wiggler source is therefore ideal. In addition, the requirements of the XPD beamline for high throughput data acquisition and for access to large  $Q$  values necessitate the high total flux of a wiggler source. The powder diffraction beamline will be located at the damping wiggler source DW100, in a high- $\beta$  straight-section of the NSLS-II ring<sup>4</sup>. The NSLS-II damping wiggler extends the range of x-ray energies well beyond 50 keV, thus matching the scientific case described in section 1. This source requires a dedicated strategy for handling the exceptional power output (section 5.4), as well as proper shielding and thick enclosure walls (section 8.9). The power output of 61 kW is unprecedented for a permanent magnet wiggler<sup>5</sup>. The power density is about half that of the 14 mm period superconducting undulator at its highest  $K$  at NSLS-II. Power reduction (filtering) and high heat load optics warrant careful investigation (sections 5.4 and 5.5).

The basic parameters for the damping wiggler source DW100 used in this design are shown below.

**Table 2-1:** NSLS-II damping wiggler parameters.

	DW100
Type	PMW
Photon energy range (keV)	<0.01–100
Type of straight section	High- $\beta$
Number of periods	68
Period length (mm)	100
Total device length (m)	7.0
Canted	No
Minimum magnetic gap (mm)	15
Peak field linear mode B (T)	1.85
$K_{\text{eff}}$	16.5
Critical energy (keV)	11.1
Maximum total power (kW)	61
Horizontal power density (kW/mrad)	14.4
On-axis power density kW/mrad <sup>2</sup>	56
W/mm <sup>2</sup> at a distance of 28 m from source	72
Fan angle* (mrad H)	6.47 / 6.76
Fan angle* (mrad V)	0.87 / 1.46

\*The fan angles of the radiation are at 28 m from the source, and account for the effect of the source length. The two values are for the points where the power density falls to values that are 1% and 0.1% of the central value. Designs of the XBPM and fixed mask entrance take into account these fringe power loads.

**Table 2-2:** RMS electron beam values at the center of the high- $\beta$  straight section (9.3 m).

Horizontal electron beam size, $\sigma_x$	137 $\mu\text{m}$
Vertical electron beam size, $\sigma_z$	4.9 $\mu\text{m}$
Horizontal electron beam divergence, $\sigma'_x$	6.6 $\mu\text{rad}$
Vertical electron beam divergence, $\sigma'_z$	1.6 $\mu\text{rad}$

<sup>4</sup> <http://www.bnl.gov/nsls2/docs/PDF/SourceProperties.pdf>

<sup>5</sup> The APS sector 11 wiggler produces 8 kW for  $K=14$ , SPring-8 BL08W wiggler produces 14 kW for  $K=10$



**Table 2-3:** Brightness and flux of the damping wiggler source at NSLS-II. DW100 is the current design option of the damping wiggler, it supersedes the previous version DW90 presented in the CDR.

Energy (keV)	Brightness ph/sec/0.1%BW/mrad <sup>2</sup> /mm <sup>2</sup>		Flux ph/sec/0.1%BW/mrad	
	DW100	DW90	DW100	DW90
30	$1.4 \times 10^{18}$	$1.6 \times 10^{18}$	$8.4 \times 10^{14}$	$9.8 \times 10^{14}$
40	$7.2 \times 10^{17}$	$8.6 \times 10^{17}$	$3.8 \times 10^{14}$	$4.5 \times 10^{14}$
50	$3.6 \times 10^{17}$	$4.3 \times 10^{17}$	$1.7 \times 10^{14}$	$2.0 \times 10^{14}$
60	$1.7 \times 10^{17}$	$2.1 \times 10^{17}$	$7.4 \times 10^{13}$	$8.8 \times 10^{13}$
70	$8.1 \times 10^{16}$	$1.0 \times 10^{17}$	$3.2 \times 10^{13}$	$3.9 \times 10^{13}$
80	$3.7 \times 10^{16}$	$4.7 \times 10^{16}$	$1.4 \times 10^{13}$	$1.7 \times 10^{13}$
100	$7.6 \times 10^{15}$	$9.7 \times 10^{15}$	$2.5 \times 10^{12}$	$3.1 \times 10^{12}$

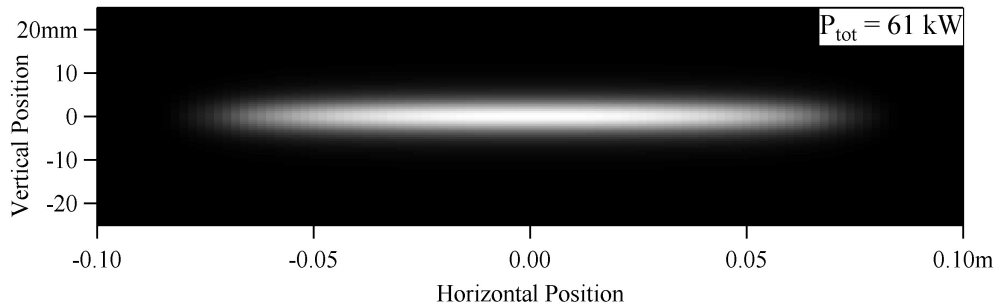


**Fig. 2-2:** Power density of the damping wiggler at 28 m from the source.

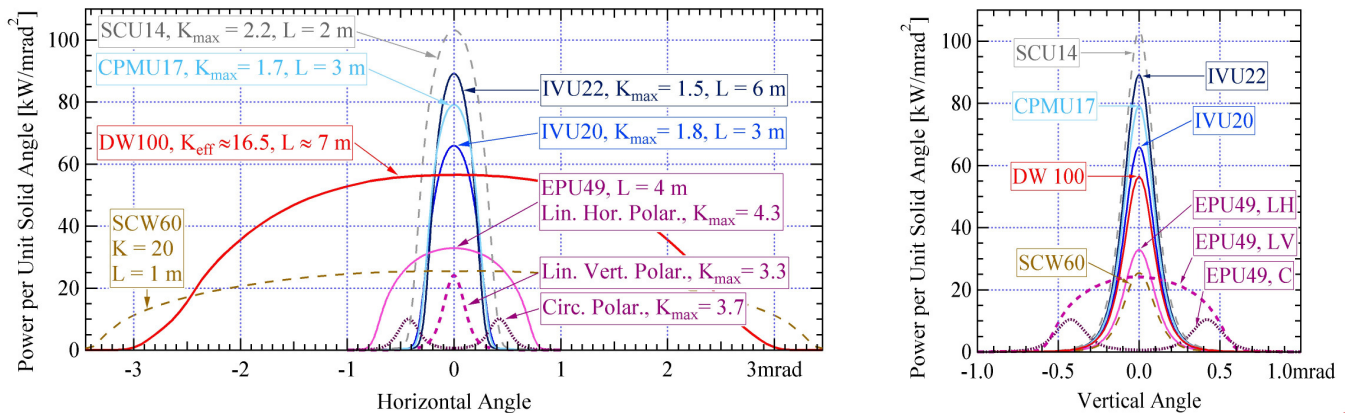


**Fig. 2-3:** Comparison of the horizontal (left) and vertical (right) angular profiles. (O. Tchoubar, NSLS-II)

### 3. FRONT END

#### 3.1 General layout of the front end

**Table 3-1:** Components of the XPD front end.

	XPD		XPD
Photon shutter (BMPS)	Y	X/Y Slits	Y
Slow Gate Valve (SGV)	Y	X-Slit opening (mrads)	1.3 to 0
Beam Position Monitor 1 (XBPM1)	Y	Y-Slit opening (mrads)	0.20 to 0
Compound Refractive Lens with protective mask	N	Slit blades closing speed	Not critical
Beam Position Monitor 2 (XBPM2)	Y	Position stability ( $\mu\text{m}$ )	2
Vert position stability ( $\mu\text{m}$ )	2	Position stability *	L
Horiz position stability ( $\mu\text{m}$ )	2	Aperture stability ( $\mu\text{m}$ )	5
V/H position stability *	L	Aperture stability *	L
Vert position resolution ( $\mu\text{m}$ )	2	Position resolution ( $\mu\text{m}$ )	2
Horiz position resolution ( $\mu\text{m}$ )	2	Position resolution *	H
V/H position resolution *	H	Tungsten thickness (mm)	5
Fixed Aperture Mask (FMK)	Y	Photon Shutter (SSH)	Y
Type	Single	Fast Gate Valve (FGV)	Y
Vertical aperture (mrad)	0.15	Bremsstrahlung Collimator BC2	Y
Horizontal aperture (mrad)	1.1	Safety Shutter (x2)	Y
Approximate numbers of closing/opening of the safety shutter during the lifetime of the beamline (25 yrs).	~5,000	Cycles per year required	5,000
No. of XBPM (beam position monitors)	1	Ratchet Wall Collimator	Y
Bremsstrahlung Collimator BC1	Y	Gate valve outside Ratchet Wall.	Y

*Continued next column...*

The XPD front end is designed by the front end group within the Accelerator System Division of NSLS-II. The effort is led by L. Doom. A layout of the standard NSLS-II front-end is shown in Fig. 3-1 and in appendix A.

More details in the Requirements, Specifications and list of Interfaces (RSI)<sup>7</sup> for the front end of the XPD.

<sup>7</sup><http://groups.nsls2.bnl.gov/ExperimentalFacilities/DocumentReferenceLibrary/RSIDocuments/1.04.06%20Front%20Ends%20for%20Project%20Beamlines/Front-ends%20RSI%20AJB%2019%20Aug%202010.doc>

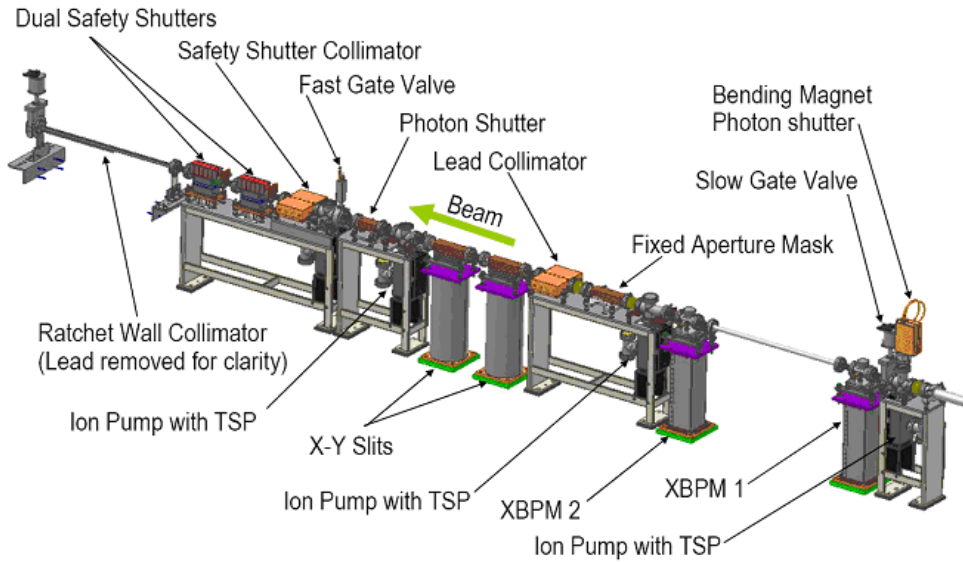


**Fig. 3-1:** Typical front end configuration at NSLS-II, as of 09/08/2010.

The basic configuration of the damping wiggler front end is similar to that of the In-Vacuum Undulator (IVU) front ends but must be designed to sustain the higher heat load and increased beam size. An absorber capable of trimming the sides of the damping wiggler beam will be mounted at the outlet of the bending magnet vacuum chamber immediately upstream of the front end. This absorber must trim the beam from  $\pm 2.6$  mrad down to below  $\pm 1.7$  mrad, in order to allow it to pass the sextupole and quadrupole magnets at the upstream end of the girder assembly in section 4 of the storage ring. A maximum drift pipe size of 1.75" OD is allowable in this area.

**The components together with the synchrotron and bremsstrahlung tracings are shown in appendix B.**

### 3.2 Fixed aperture mask

The fixed aperture mask (FMK, Fig. 3-2) provides radiation fans to the FOE as defined in Table 3-1. No tolerance is added to the mask for mis-positioning or mis-steering; however, a total manufacturing tolerance of  $\pm 0.2$ mm for the aperture (at the downstream end of the mask) is included in the downstream fan definition.

The FE FMK is at 20.652 m from the source; its aperture is  $22.72 \times 3.10$  mm<sup>2</sup>. It is made of two masks in order to simplify manufacturing of the assembly. When trimming the beam from 3.4 mrad down to the specified 1.1 mrad, the mask absorbs 55 kW of power. 60 cm of length at a 1.6 degree angle in the vertical direction and 3.9 degree angle in the horizontal direction is required to keep the water-cooled Glidcop surface below 315°C. The preliminary design is shown in Fig. 3-3.

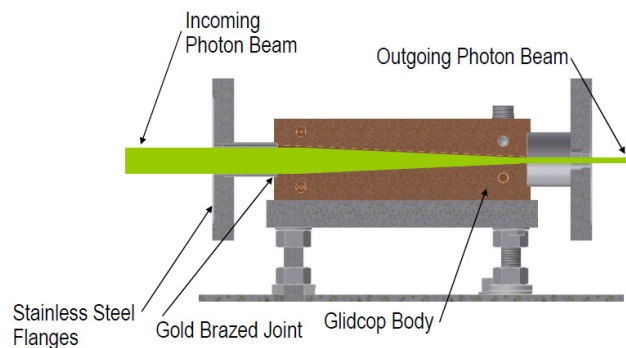
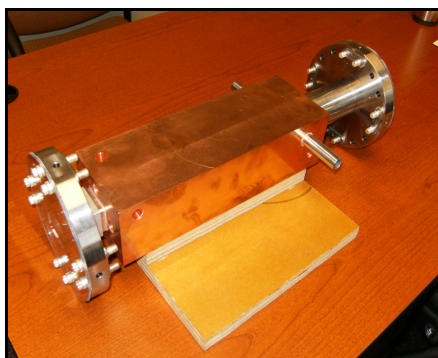


**Fig. 3-2:** Front end fixed aperture mask (FMK).

The absorber is cantilevered from the upstream flange to allow thermal expansion during bakeout. A formed bellow is mounted between the masks to allow for alignment and thermal movement during bakeout.

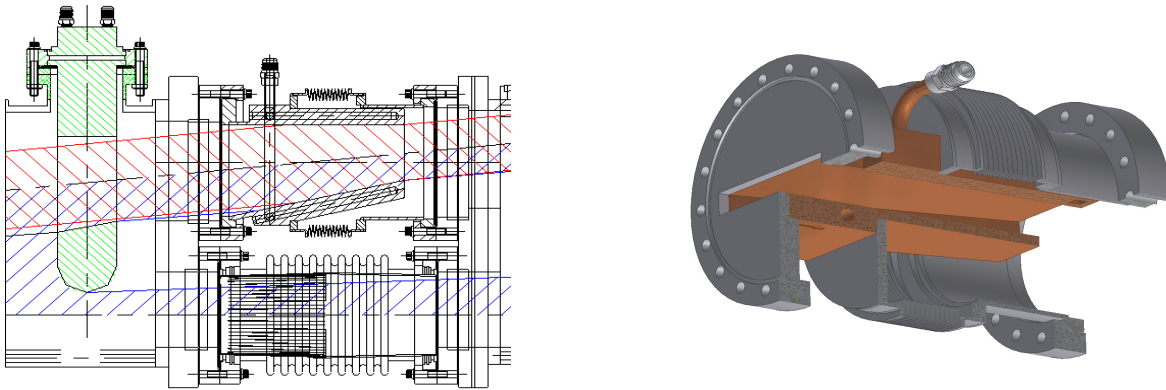


**Fig. 3-3:** Principle of the Glidcop wiggler absorber.

The FEA calculations are shown in Table 3-2 and Fig. 3-4. It is assumed that the full beam is intercepted by the mask (no aperture). This is a worst case scenario which accounts for any mis-steering of the beam.

**Table 3-2:** Characteristic numbers of the design and FEA results.

Location	17 m
Absorbed Power	65 kW
Beam incidence angle	
Vertical	~1.6°
Horizontal	~3.9°
Peak Power Density	~200 W/mm <sup>2</sup>
Component Length	~60 cm
Peak Temperature	~315 °C

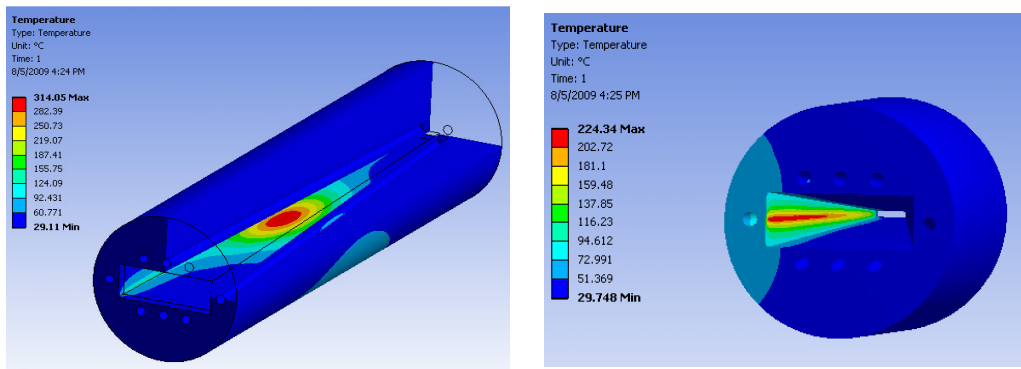


**Fig. 3-4:** Thermal calculations on the GlidCop mask. (Courtesy of V. Ravindranath)

### 3.3 Rationale for fixed mask aperturing

Fig. 3-5 shows the angular profile of the DW100 emission at different energies and Fig. 3-6 shows the variation of the flux outputs at 50 keV and 80 keV as a function of the vertical opening, together with the total power output. It reflects the dependence of the vertical distributions on the x-ray energy. A 0.15 mrad vertical aperture reduces the total power by 48% while it still lets 89% of the 50 keV photons through<sup>8</sup>. At 80 keV, the useful flux is 96% of the flux without vertical aperturing<sup>9</sup>. Therefore a vertical aperture > 0.15 mrad increases the total power more than it increases the useful flux at these high energies. **The nominal mask aperture in the FE is set at 1.1 mrad × 0.15 mrad, with the option to reduce the vertical aperture using the white beam slits and a second mask in the FOE (section 5.3.3.2).** The horizontal aperture can be reduced in order to keep the beam footprint on the crystal to a reasonable size.

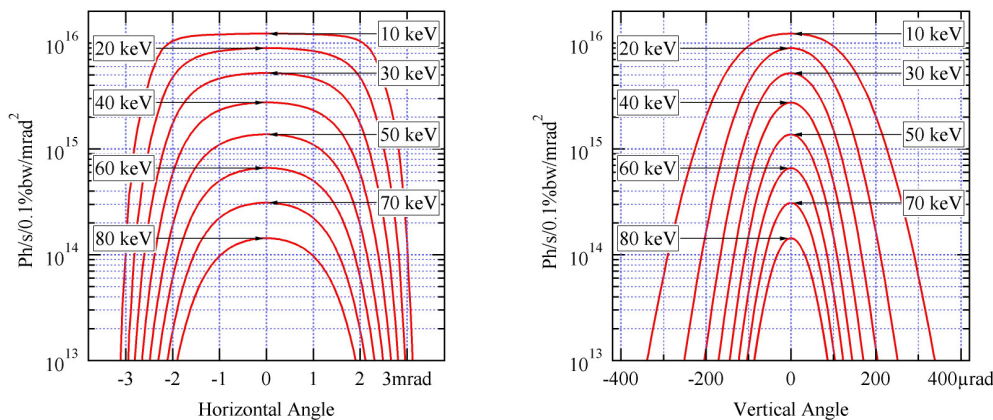


**Fig. 3-5:** Horizontal (left) and vertical (right) angular profiles of DW100 emission at different photon energies (logarithmic scales).

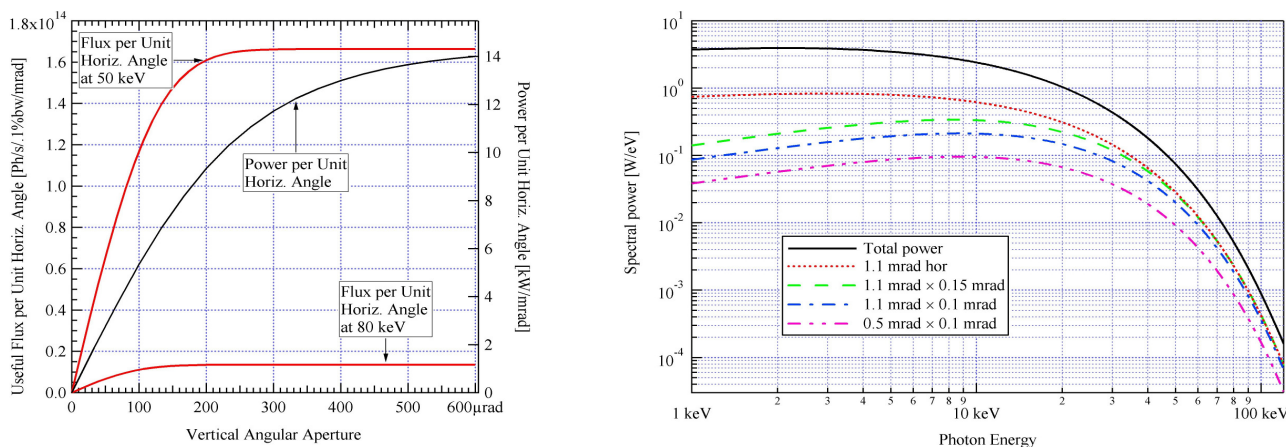


**Fig. 3-6:** (left) Variation of the flux outputs at 50 keV and 80 keV, and of the total power output as a function of the vertical opening; (right) Variation of the spectral power versus aperture. The total power is: 61.2 kW (full); 15.9 kW (1.1 mrad horizontal); 8.3 kW (1.1 × 0.15 mrad<sup>2</sup>); 5.8 kW (1.1 × 0.1 mrad<sup>2</sup>); 2.6 kW (0.5 × 0.1 mrad<sup>2</sup>).

<sup>8</sup> The FWHM of the flux vertical distribution at 50 keV is 0.11 mrad

<sup>9</sup> The FWHM of the flux vertical distribution at 80 keV is 0.09 mrad

#### 4. BEAMLINE OPTICAL DESIGN

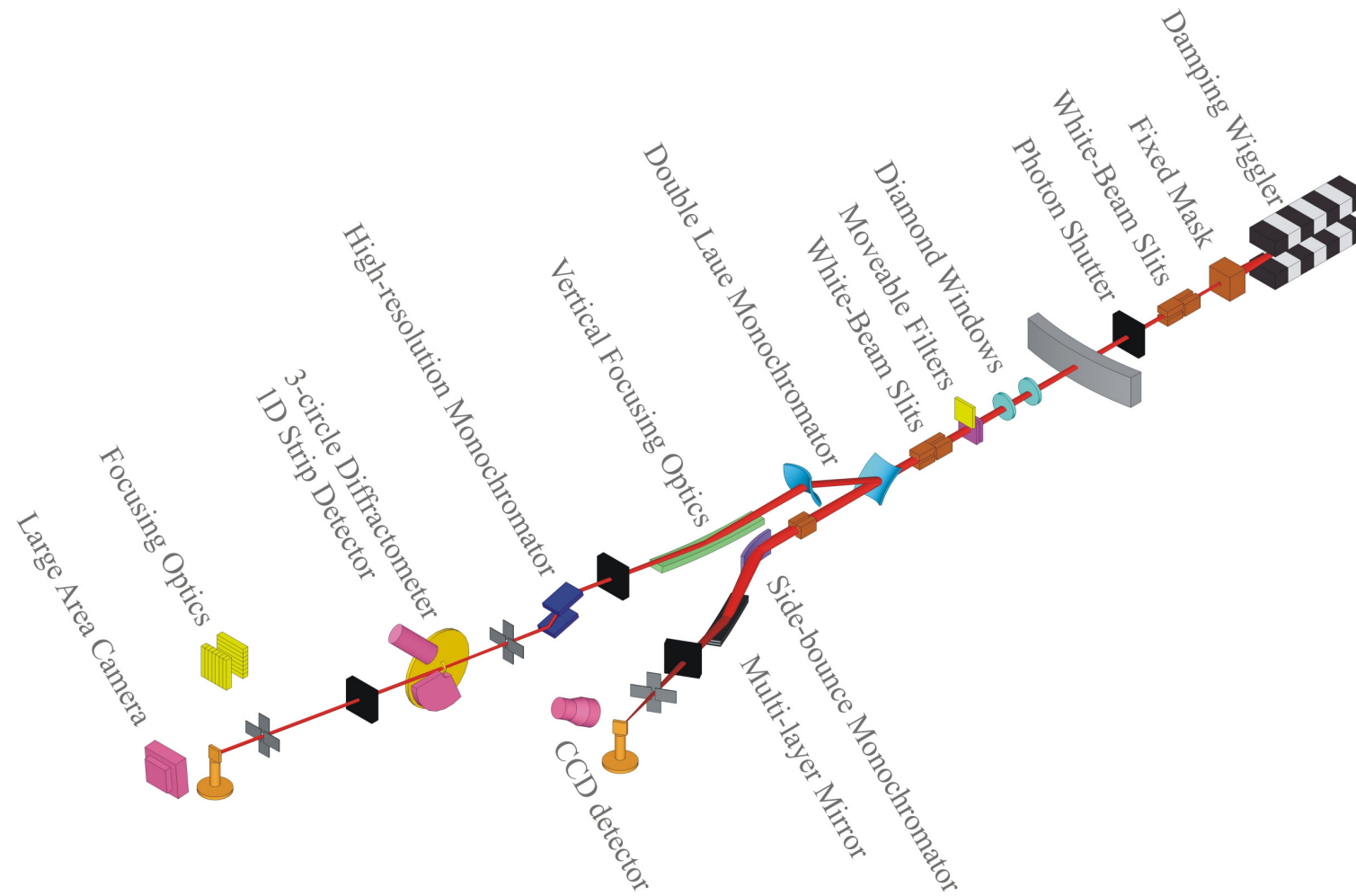


Fig. 4-1: Schematic layout of the beamline (see also appendix B).

## 4.1 Introduction

The intended parameters of XPD are:

- Energy range = 30–80 keV
- Energy resolution (high:  $\Delta E/E \sim 2 \times 10^{-4}$ ; medium:  $\Delta E/E \sim 1 \times 10^{-3}$ )
- Intensity  $>10^{13}$  photons/sec/0.1%BW
- Flexibility of focal lengths and sizes: 2 mm – 500  $\mu\text{m}$ , down to 10  $\mu\text{m}$  (horizontal)
- Beam stability (intensity and position)
- Low background and high filtering of forward, parasitic scattering and of low energy photons
- Use proven technology whenever possible
- Ease of use
- Independent operation (shuttering) for the different hutches

By using a modular design for the endstations, special environments can be designed and inserted at different locations into the beamline with compatible interfaces. Standardization of equipment, safety protection, and software across all stations is important for ease of operation. Thus the floor plan of the beamline is designed to easily move equipment and samples, in particular between hutch C ("standard" powder diffraction) and hutch B (PDF).

Close attention is paid to the considerable divergence of the wiggler source, its high power output, and the low reflection angles in the x-ray high energy range: all three features further constrain the optics and overall performance.

The layout of the beamline consists in two branches and three in-line endstations (see reference drawings in appendix B). The angular deviation between the two beam axes is  $5.8^\circ$ , given by the setting of the side-bounce monochromator (section 4.2). The conceptual layout for the NSLS-II powder diffraction beamline is shown in Fig. 4-1 and in appendix B. The optical components are listed in Table 5-1 in section 5.1 (distances from the source are shown).

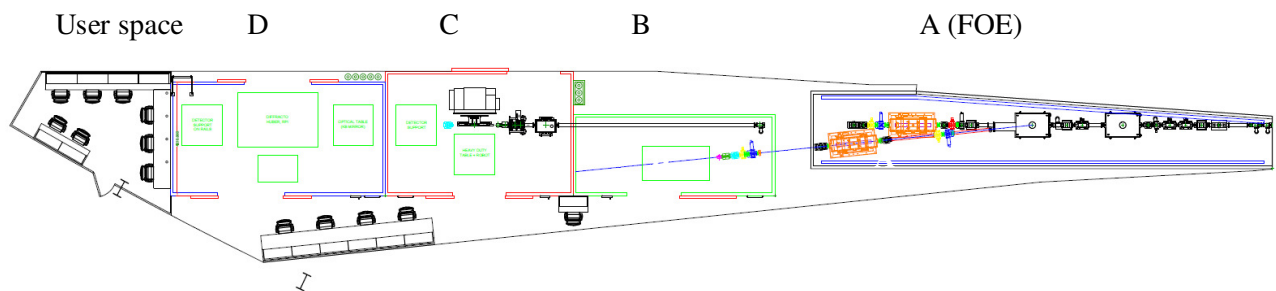


**Fig. 4-2:** Simplified scheme with hutch labeling.

A summary is given in Table 4-1; the logic for access to hutches is given in Table 4-2.

**Table 4-1:** Hutch labeling convention and main purposes.

Hutch A	First Optical Enclosure (FOE). Contains the optics (monochromators and mirrors) of both branchlines.
Hutch B	Operates at fixed high energies, and is specialized and optimized for total scattering measurements (PDF) over a large Q range. Diffraction work in the tomographic mode is an option.  Most equipment for this station will be transferred from NSLS and/or purchased with funds and grants from other sources.
Hutch C	Hosts the diffractometer described in section 7.2 for high energy powder diffraction. The PDF measurements can also be performed there until hutch B becomes operational. A range of sample environments will be provided, and the emphasis will be on maximizing the throughput of the station; a robot sample changer is included.  The fit-out of hutch C is in the baseline budget, but not that of hutches B and D.
Hutch D	Accommodates large equipment, custom sample environments (large pressure cells, non routine reaction chambers, combined spectrometry, gas handling, stress apparatus, etc). Suited for experiments requiring long set-up time. With equipment in place, hutch D accepts the beam with minimum overhead time. A SAXS camera is available in this hutch when taking data in hutch C (3). There is also provision to install secondary focusing optics to produce a smaller focal spot size (section 5.6.3).  Most equipment for this station will be transferred from NSLS and/or purchased with funds and grants from other sources.

The major components of the FOE are:

- the secondary Fixed Aperture Mask — section 5.3.3.2
- the high-heat-load filter assembly combined with white beam slits — section 5.4.2
- the single-bounce monochromator (SBM), deflecting the beam sideways towards endstation B — section 5.5.2
- the double Laue crystal monochromator (DLM) serving hutches C and D — section 5.5.1
- the focusing optics (one per branchline) — section 5.6.1

## 4.2 Rationale for the deflection angle and the energy of the branchline

The angle between both branches is driven by the  $2\theta$  angle of the side-bounce monochromator (SBM) and by the steric impediments. Using the SBM in the Bragg geometry favors a small angle for higher reflectivity. However, the SBM in the Laue geometry offers several sets of lattice planes in the diffraction condition. At any one particular Bragg angle, several energies can be selected (Fig. 4-3). Too low an angle restricts the operation of the beamline to the Si(111) reflection. Too high an angle is incompatible with the experimental floor space constraints. An optimum angle deflection is  $5.8^\circ 2\theta$  (section 4.2).

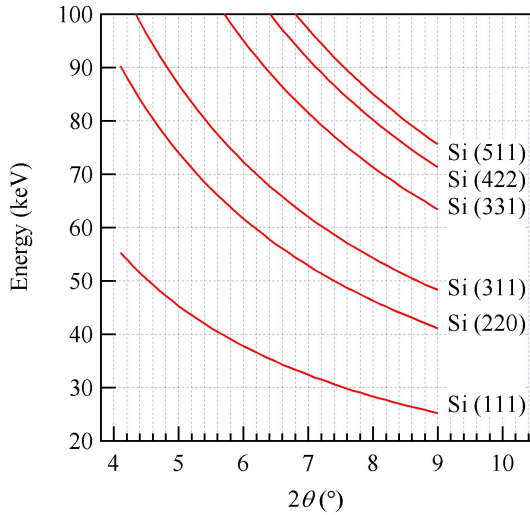


**Fig. 4-3:**  $2\theta$  angle versus the type of reflection (Si crystal) and the energy. At  $5.8^\circ$   $2\theta$ , the endstation can be operated at (311) 74.8 keV (Si 311), 63.8 keV (Si 220) and 39.1 keV (Si 111).

### 4.3 Description of the beamline operation modes

- **High flux mode:** the beam is horizontally focused by the Double Laue Crystal monochromator (DLM) and vertically by the mirror (VFM) (Fig. 4-4a). The modest 0.1% energy bandwidth is acceptable for many high-energy experiments e.g., *in situ*, time-resolved, materials science, stress and strain, PDF.
- **High spatial resolution mode:** an additional refractive or reflective optical system placed closed to the sample in hutch D is foreseen to produce a focal beam size of the order of 10  $\mu\text{m}$  (mature scope).
- **High  $2\theta$  resolution mode:** the beam is collimated in the vertical diffraction plane, and impinges an optional channel-cut monochromator (HRM) which is placed in hutch C (Fig. 4-4b). Both the induced lower vertical divergence and the higher monochromaticity ( $\Delta E/E \approx 10^{-4}$ ) improve the resolution performance (section 6.2) for such experiments as structure solving, lattice parameter measurement and line shape analysis.
- **High Q mode:** hutch B operates at high energies and specializes in high Q diffraction.

Fig. 4-4 shows the two different settings of the mirror and HRM. A collimator mask is placed behind the VFM to prevent any unwanted missteering of the beam caused by misalignment of the mirror. Provision is made to operate the beam when the mirror is out of the beam path.

High resolution at high energy is difficult to achieve with the white-beam Laue optics, given the high energy bandpass and the small angular instabilities,  $\delta\theta$ , arising from thermal load, cooling and bending. This results in large energy changes  $\delta E = E \cot\theta \delta\theta$  where  $\theta$  is small and  $E$  is large. Shastri at the APS (11) (12) show that narrower energy bandwidth is best attained by using a second optics after the DLM. This method keeps the white-beam optics unchanged and does not compromise its performance. The high-resolution optics (collimating VFM and HRM) operates in the absence of thermal load. The HRM can easily be bypassed and the beamline quickly returned to the high-flux modest-resolution configuration. Similar configurations are implemented at APS and ESRF. Although these beamlines use undulator beams, a similar strategy can be implemented at NSLS-II, for enhanced flexibility in flux/resolution and keeping the setup configuration relatively flexible and automated.

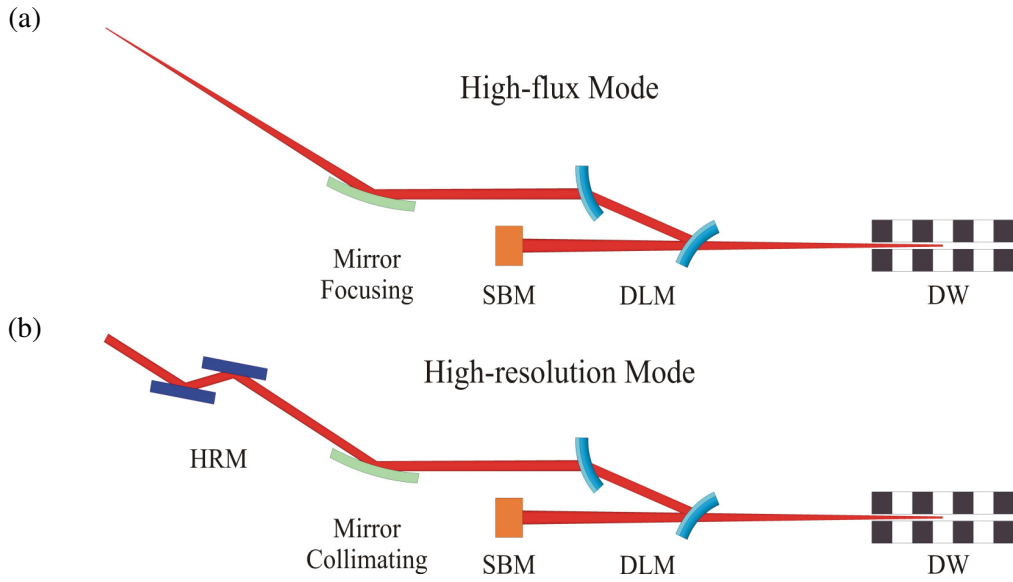


**Fig. 4-4:** Schematic side view of the optical layout of the beamline.

**Table 4-2:** Parallel operation of the hutches.

Hutch C	Hutch D	Comment	Hutch B
Beam On	Beam Off	Measurements in hutch C. Access to D is allowed.	Station B works in parallel with C and/or D, as well as independently.
Beam Off	Beam On	Measurements in D. C is accessible only if a shielded pipe is installed along the entire beam path in hutch C.	
Beam On	Beam On	Sample is mounted on diffractometer in hutch C. Wide angle diffraction and small angle scattering are measured simultaneously.	

**Table 4-3:** Vertical beam positions in experimental hutches C and D.

VFM 40.1 m	HRM 51.8 m	Operation mode	Effect	Deflection (mrad)	Hutch C beam height (mm)	Hutch D beam height (mm)
Out	Out	Occasional	None	N/A	1450.0	1450.0
In	Out	High flux	Focused beam	2 min	1478.6	1493.2
				4 max	1507.2	1536.4
In	In	High resolution	Collimated beam Smaller energy bandwidth	2 min	1453.6	1468.2
				4 max	1482.2	1511.4

VFM = Vertically Focusing Mirror  
 HRM = High-resolution Monochromator

## 4.4 Beamline layouts

See appendix B for a selection of reference drawings.

## 4.5 Ray tracings

The beamline ray tracings use the same guidelines as the front-end tracings (appendix A.2) and start with the following input given by the front end: maximum fan angle at the ratchet wall, bremsstrahlung and synchrotron source locations, front end collimator maximum apertures. Given the possibility of further changes in the front end design at the time of this PDR, ray traces in the beamline are performed in the most conservative mode. One conservative assumption is **to perform the ray traces without a second fixed mask in the beamline**, another assumption is to determine the outboard horizontal bremsstrahlung source point from the front end layout only instead of the front end and beamline layout as a whole. The consequence of a conservative assumption is that the collimator aperture might be larger than necessary, not a problem in itself but a smaller aperture is always desirable. As with the front end, the outcome of the synchrotron ray trace is the minimum aperture for device components, and a maximum aperture for the collimator. The purpose of the bremsstrahlung traces is to define the outer dimensions of the collimator and white beam bremsstrahlung tungsten stop.

**The synchrotron and bremsstrahlung tracings for FE and beamline are shown in appendix B.** From a safety stand point, the tracings show that the second mask is not required. The tracings with the second mask are also available but not shown here (section 5.3.3.2). **The layout of the beamline was thus not altered on the basis of the ray tracings.**

## 5. DESCRIPTION OF THE BEAMLINE COMPONENTS

### 5.1 Major components

**Table 5-1:** Components of the Powder Diffraction Beamline

	Component	Description	Section	Dist. to source (m)
FOE A	GTV1	Gate Valve	Appendix A.1	26.8
	Pressure sensor FE			
	IPP1	Ion pump	5.3.1, B.7	27
	WIN1	Diamond window	5.4.2.1	27.2
	Pressure sensor WIN			
	IPP2	Ion pump		27.4
	WIN2	Diamond window		27.6
	GTV2	Gate valve		
	FLT	Pre-filter assembly	5.4.2.2	28.2
	IPP3/FLT	Ion pump		
	FMK	Fixed mask	5.3.3.2	29.3
	BRC1	Bremsstrahlung collimator	5.3.3.1	29.3
	GTV3	Gate valve		29.6
	SLW1	White beam X,Y slits	0	29.9/30.5
	IPP4	Ion pump		31
	BPM1	Beam position monitor	5.3.4	31
	SCW1	Fluorescent screen	5.3.4	31.3
	GTV4	Gate valve		31.6
	DLM	Double Laue monochromator	5.5.1	32.3
	IPP5/DLM	Ion pump		
	GTV5	Gate valve		32.8
	SLW2	White beam X,Y slits		33.8
	BRC2	Bremsstrahlung collimator		34.4
	IPP6	Ion pump		34.7
	GTV6	Gate valve		35
	SBM	Side bounce monochromator	5.5.2	35.6
	IPP7/SBM	Ion pump		
	SCW2	White beam screen		36.6
	STW	White beam stop	5.3.3.3	36.6
	GTV7	Gate valve		37.7
	BRS1	Bremsstrahlung stop	5.3.3.4	37.9
	SLM1	Monochromatic beam slits		38.3
IPP8	Ion pump		38.6	
BPM2	Beam position monitor		38.6	
SCM1	Monochromatic beam screen		38.9	
VFM1	Vertical focusing mirror	5.6.1	40.1	
IPP9/VFM1	Ion pump			
CMK	Collimating mask	4.3		

*Continued...*

Components of the Powder Diffraction Beamline (*concluded*)

<b>FOE A</b> <i>(continued)</i>	GTV8	Gate valve		41.1	
	SLM2	Monochromatic beam slits		41.3	
	BPM3	Beam position monitor		41.6	
	SCM2	Monochromatic beam screen		41.9	
	PSH1	Photon shutter	Appendix A.1	42.3	
	IPP10	Ion pump		42.3	
<b>Hutch C</b>	GTV9	Gate valve		45.6	
	IPP11	Ion pump		45.8	
	HRM	High-resolution monochromator	5.6.2	51.8	
	IPP12/HRM	Ion pump			
	SLM3	Monochromatic beam screen		52.7	
	BPM4	Beam position monitor		52.9	
	WIN3	Exit window		53.1	
	CTG1	Cartridge		53.3	
	ICB1	Ion chamber	5.3.4	53.5	
	Optical bench				
	DFF	Diffractometer	7.2	54.4	
	SCM3	Monochromatic beam screen		55.5	
	Analyzer Arm		7.4		
	Detector support		7.3.3, H		
	heavy duty table				
	robot				
	sample stage				
	sample table				
	STM	Monochromatic beam stop			
<b>Hutch D</b>	optical table				
<b>PDF Branch</b>	<i>GTV10</i>	Gate valve		37.3	
	<i>SLM4</i>	Monochromatic beam slit		38.8	
	<i>IPP13</i>	Ion pump		39.2	
	<i>BPM5</i>	Beam position monitor		39.2	
	<i>SCM4</i>	Monochromatic beam screen		41.1	
	<i>GTV11</i>	Gate Valve		41.3	
	<i>VFM2</i>	Vertical focusing mirror		42.2	
	<i>IPP14/VFM2</i>	Ion pump			
	<i>GTV12</i>	Gate valve		43.3	
	<i>PSH2</i>	Photon shutter		43.5	
	<i>IPP15</i>	Ion pump		43.5	
	<b>Hutch B</b>	<i>GTV13</i>	Gate valve		45.8
		<i>SLM5</i>	Monochromatic beam slit		46.1
<i>IPP16</i>		Ion pump		46.5	
<i>BPM6</i>		Beam position monitor		46.8	
<i>SCM5</i>		Monochromatic beam screen		47.1	
<i>WIN4</i>		Exit window		47.3	
<i>ICB2</i>		Ion chamber		47.4	

Items in italics are not in the base project scope. A detailed description of key components follows this table.

## 5.2 Enclosures

Four radiation-shielded enclosures house the various x-ray optical systems as well as endstation instruments. The First Optical Enclosure is lead-shielded for white beam and bremsstrahlung scatter. These are standard components similar to those in other synchrotron facilities, and therefore substantial expertise and experience exist in commercial industry worldwide. We are providing the preliminary design specifications; the final designs will be produced by suppliers, following NSLS-II specifications. At this stage, wall and ceiling material and thickness, all sizes and heights, and the location of each enclosure are finalized; all labyrinths positions and hutch door sizes and locations are specified. See section 8 and appendix C for details.

**Table 5-2:** Characteristics of the enclosures.

	Dimensions (m)	Doors	Fans	Labyrinths	Roof access	Bridge	Comments
<b>A</b>	17.1 × 2.87	2	2	5	Yes	Yes	
<b>Egress</b>	1.2 × 40	N/A	N/A	N/A	N/A	N/A	
<b>B</b>	5.5 × 4.21	2	1	1	Yes	Yes	
<b>C</b>	7 × 4.21	1	1	2	Yes	N/A	
<b>D</b>	8 × 4.21	2	1	2	N/A	N/A	Emergency ladder with safety gate
<b>User space</b>	8 × 6	1	N/A	N/A	N/A	N/A	N/A

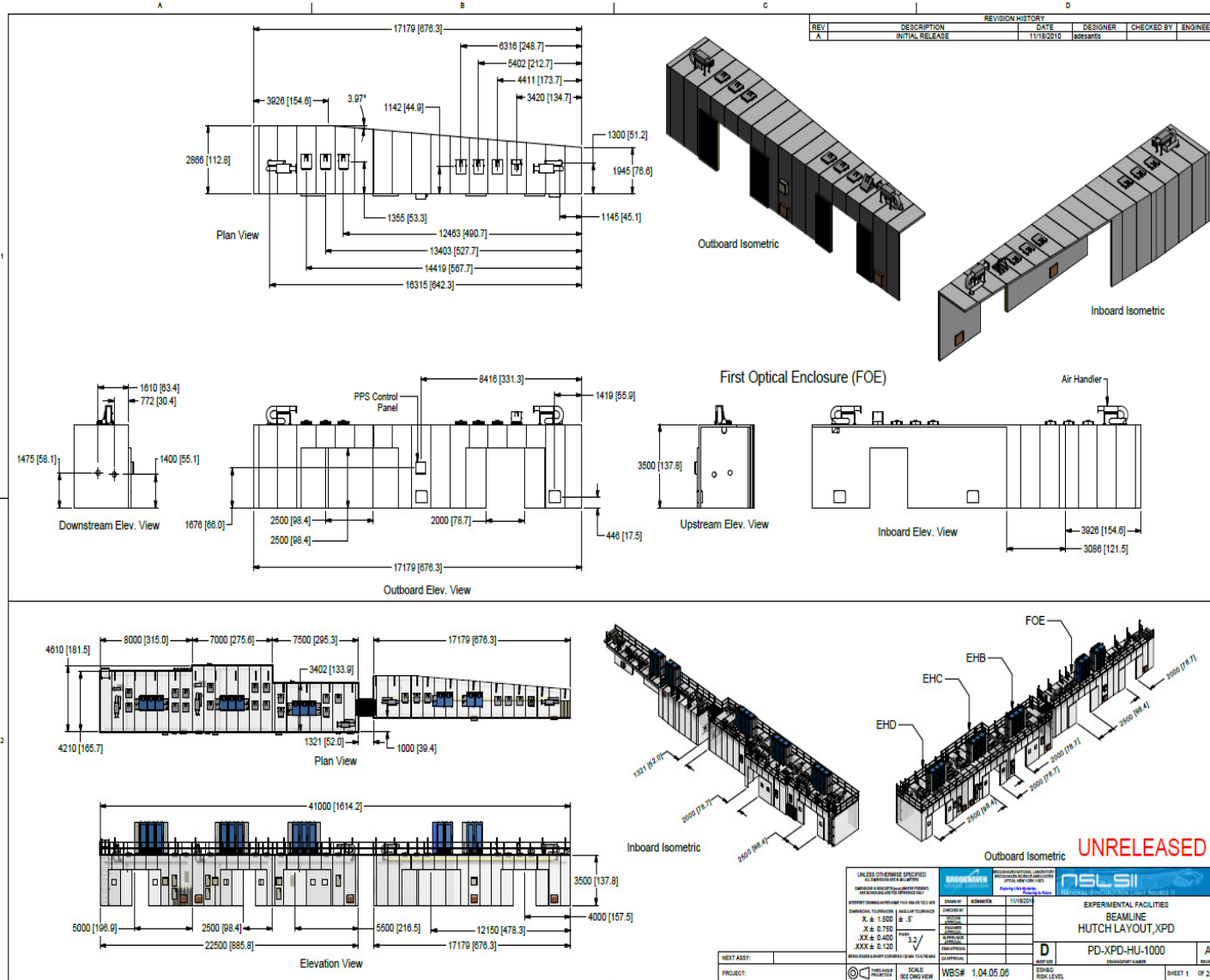


Fig. 5-1: XPD hut Layout.

## 5.3 Beam transport

The beamline schematic is shown in appendix B.

Beam transport refers to radiation-shielded evacuated beampipes connecting the radiation enclosures. This includes the complete vacuum system (with gate valves, spool pieces, pump-out ports, bellows, etc.), apertures, flags, monitors (such as  $I_0$ ) and also includes embedded safety and diagnostics system components such as beam shutters and bremsstrahlung collimators, as well as x-ray beam position monitors and windows. Most dimensions are final and all components are identified and incorporated in the design at this stage.

### 5.3.1 Beamline vacuum system

See appendix B.7.

### 5.3.2 Radiation shielding of evacuated beampipes

**Table 5-3:** Radiation shielding of evacuated beampipes.

	Branch 1	Branch 2	Diameter* (mm)	Shield thickness (mm)	Length (m)
Hutch A (FOE)	none	none	101.6/304.8	7	17.18
Between A and B	permanent	none	101.6	7	1
Hutch B	permanent	N/A	101.6	7	5.5
Hutch C	moveable	N/A	101.6	7	7
Hutch D	none	N/A	101.6	7	8

\*The pipe diameter accommodates both the white beam and the monochromatic beam in the FOE. The deviation of the mirror-deflected beam as described in Table 4-3 is also taken into account.

### 5.3.3 Radiation safety components

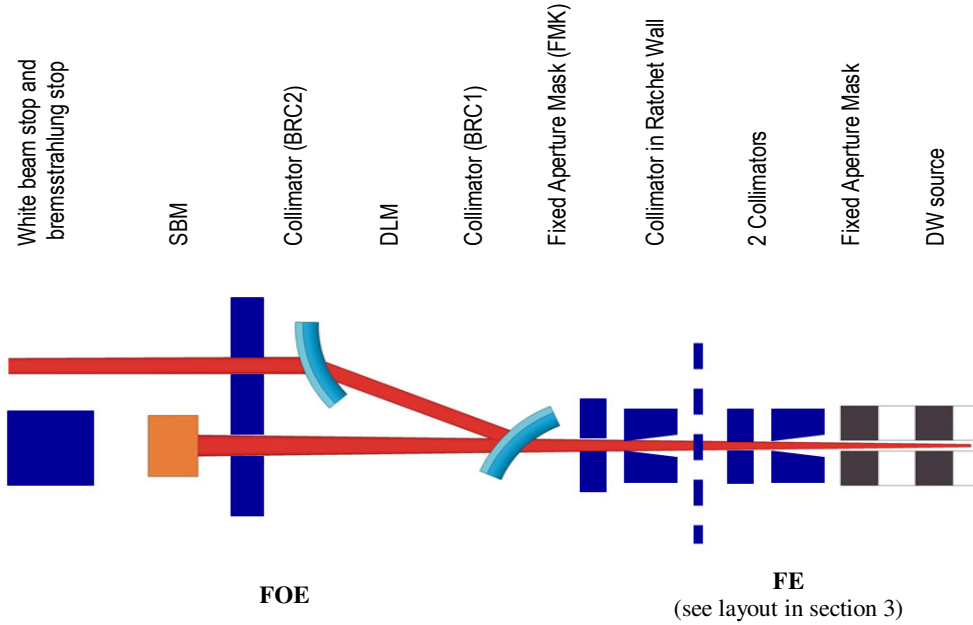


**Fig. 5-2:** Radiation safety components

The radiation shielding is an essential aspect in the selection of the optical design and the layout of beamline components. Full functionality required by the scientific program is provided at reduced cost and with easy maintenance by integrating the beamline shielding with the optical design. Part of the methodologies used to determine the shielding requirements are described in ANL/APS/TB-21<sup>10</sup>.

<sup>10</sup> <http://aps.anl.gov/Science/Publications/techbulletins/tb21.pdf>

**Table 5-4:** Beamline components critical for safety.

	Item	Heat load	Consequence of overheating / failure	Interlock * required for overheating or burn-through.
<b>FOE Components</b>	Fixed Aperture Mask	Exposed to white beam, must be cooled to prevent overheating.	Aperture will fail and result in larger beam downstream, exposed components may fail – no radiological consequences	Loss of return water flow is monitored by EPS and will shutdown ring RF and magnet power supplies.
	White Beam Stop	Exposed to white beam, must be cooled to prevent overheating.	Stop will fail and result in white beam incident on bremsstrahlung stop, which will also fail. White beam may enter Endstation when occupancy is possible with potential for severe radiological consequences.	Water flow is monitored by EPS and will shutdown ring RF and magnet power supplies.
	Bremsstrahlung Stop	Shielded from white beam by the white beam stop.	Stop will fail in case of white beam stop failure-see white beam stop failure.	Bremsstrahlung stop will be fitted with burn-through monitor (BTM) which senses heat load on stop front surface, and will shutdown ring RF and magnet power supplies on alarm through PPS.
	Photon (monochromatic beam) Shutter (PSH)  Two PSH provided for redundancy	Beam at this point is monochromatic and has low power; burn-through will not occur. *	No radiological impact.	None
<b>Endstation</b>	Photon Stop	No significant power load.	No radiological impact.	None

\* This column contains interlock requirements for overheating conditions. Redundant safety limit switches, as a part of the PPS, will also be required on all safety critical components that can move – e.g., shutters.

### 5.3.3.1 Bremsstrahlung collimators

The bremsstrahlung collimators define a line of sight to the source and allow a cone of beam to pass through. This device consists of a circular vacuum chamber with conflat flanges surrounded by lead blocks to absorb scattered x-rays and bremsstrahlung. The ray tracing procedure determines the collimators' dimensions. The thickness of lead is 300 mm. The last collimator in the FOE (BRC2) limits the bremsstrahlung scattering, which might be leaking through the aperture of the white beam stop (section 5.3.3.3): it helps clean the monochromatic beam.

### 5.3.3.2 Fixed aperture mask

The second mask (FMK) in the FOE restricts the beam to a vertical opening which matches the acceptance of the optics (e.g., a 1.3 m-long mirror at 1.6 mrad tilt angle only intercepts 0.05 mrad of the vertical fan). This mask limits the power incident on the filters and white beam optics and protects the collimator. The vertical opening of FMK in the FOE is not determined yet: it will be adjusted to admit a vertical synchrotron fan of the order of 0.1 mrad.

### 5.3.3.3 White beam stop

The beam stop is designed for the worst-case failure scenario. This would occur if all diamond windows and SiC filters were to fail, upon which the double Laue monochromator would also fail. In this case, the stop would see the full impact of the 8.3 kW. A block of GLICOP  $450 \times 50 \times 100 \text{ mm}^3$  tilted at 5 degrees in the horizontal direction is designed to absorb the more conservative value of 9.3 kW. It is assumed that the heat is uniformly distributed on the tilted beam footprint. The maximum temperature is about 100 °C and the stress is 130 MPa. These numbers are well below the acceptable values of 300 °C and 200 MPa.

An aperture is needed to let the monochromatic beam pass through but is not shown in **Error! Reference source not found.**, as it is not affecting the thermal analysis.

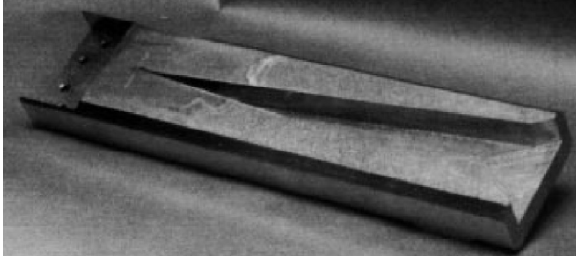
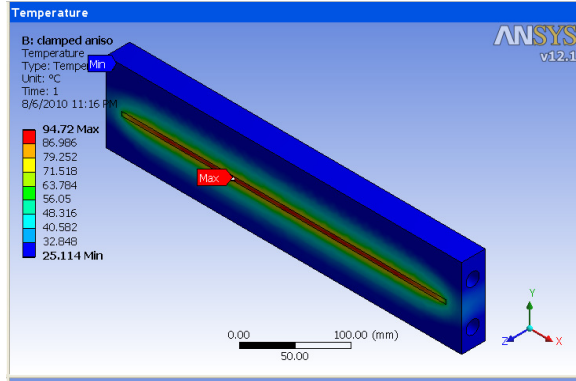


**Fig. 5-3:** White beam stop.

a) View of the beam stop at the A-line operating a 32kW 25-pole permanent magnet wiggler at CHESS<sup>11</sup>.



b) White beam stop. Maximum temperature is 100°C.

#### 5.3.3.4 Bremsstrahlung stop

This component is ideally positioned as close as possible to the white beam stop and designed according to safety guidelines. In this instance, it is made of tungsten with a thickness of 200 mm. The bremsstrahlung stop must completely block the possible line of sight of the radiation, including the bremsstrahlung shower, from upstream as seen from downstream. In all cases a small offset aperture will allow the desired synchrotron radiation to pass through the stop. Transverse dimensions of the tungsten bremsstrahlung stop are determined from the primary bremsstrahlung ray tracing. The extremal rays in the case of primary bremsstrahlung ray tracing should not be closer than 24 mm from any lateral edge of the tungsten stop. If an aperture is interposed, then the sum of distances – from the extremal ray to the edge of the aperture and from the opposite edge to the edge of the tungsten stop – should be larger than 24 mm. It is suggested that these distances should be kept larger than about 26 mm. This allows to adjust the beam opening at the precise location in the beam while following the rules stated above, even with a surveying uncertainty as large as 2 mm. The minimal distance between extremal rays and the edge of an aperture should be kept larger than 10 mm for a “moderate” aperture size (i.e., 10-15 mm). A final validation of any particular bremsstrahlung stop design is ultimately provided by a numerical estimate, using what is known as shower theory, of the radiation dose passing through the X-ray aperture.

#### 5.3.3.5 Monochromatic photon shutter

Two monochromatic photon beam shutter designs are being pursued; they will be used for the majority of beamlines at NSLS-II (**Error! Reference source not found.**). One design will be used for most of the damping wiggler beamlines, and another similar design will be used for most other insertion device and bending magnet beamlines (see the radiological analysis<sup>12</sup>). Both photon shutter designs contain two separate moveable shutter blocks inside of a custom-designed stainless steel UHV vacuum vessel. The overall length of the photon shutters (between flange faces) is currently set at 245 mm (not final). These blocks shall be moved independently by two separate pneumatic actuators. The entire shutter assembly shall be mounted on a steel stand. Redundant limit switches shall be used to indicate when the shutters have reached their fully closed and fully open positions. The

<sup>11</sup> <http://www.chess.cornell.edu/pubs/1993/NL93.pdf>

<sup>12</sup> <http://groups.nsls2.bnl.gov/eshqa/Lists/Radiological%20Analysis/DispForm.aspx?ID=44&Source=http%3A%2F%2Fgroup.s%2Ensls%2Ebnl%2Egov%2Feshqa%2FLists%2FRadiological%2520Analysis%2FSummary%2Easp&RootFolder=%2Feshqa%2FLists%2FRadiological%20Analysis>

design of the shutters shall be fail safe, that is, if pneumatic actuation pressure is lost, the shutters will fail in the closed position.

The shutters shall be designed for a life of 400,000 cycles. A mechanical counter will be used to keep track of the number of cycles that each bellows actuates. The photon shutter bellows assembly shall be made so that it can be replaced quickly without cutting welds.

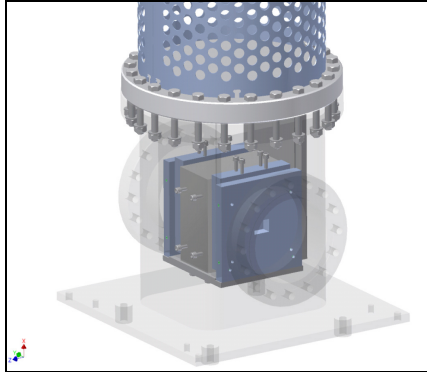


Fig. 5-4: Monochromatic Photon Shutter.

Table 5-5: Requirements for the monochromatic photon shutter

<b>Photon Beam Specifications</b>	
Beam size 3" into FOE (horiz/vert, mm)	37.4 / 6.9
Beam divergence full angle (horiz/vert, mradians)	1.40 / 0.26*
Distance between 1st DLM crystal and source (m)	31.84
<b>Photon Shutter Specifications</b>	
Distance from source to shutter face (m)	42.3
Distance between source & FOE upstream wall (m)	26.7

\* See synchrotron ray tracings in appendix B.

### 5.3.4 Diagnostics system components

Beam monitoring elements are extremely important for beamline alignment. In this section, three such systems are described.

- a) Water-cooled White Beam CVD fluorescence screen. The device consists of a retractable water-cooled CVD diamond foil, acting as x-ray screen, mounted to a pneumatic drive; the fluorescent effect is based on the residual doping with nitrogen atoms. The diamond screen is transparent, i.e., beam detecting further downstream is possible. The assembly is mounted to a DN100 CF cross with one view port permitting a side view of the screen. The pneumatic drive is equipped with limit switches. The vacuum feed-through is made of edge-welded bellows. The water lines are brazed to the screen support to avoid vacuum-to-water joints. The foil is clamped to the cooled support. The projection of the beam onto the 45° inclined foil will be monitored with a CCD camera. This system is capable of staying in the beam after the filter-attenuator assembly. To increase the lifetime of the foil and prevent overexposure of the camera, this screen should only be used at reduced power levels, i.e., in combination with filters. This screen has been installed at the high power wiggler beamline at the Australian Synchrotron Project.
- b) The fluorescence screen monitors typically are mounted on a pneumatic drive via a vacuum feed-through on a Conflat flange. The water-cooled monitor is inserted in the beam by a stepper motor. The flange is also

equipped with a view port for the camera that provides side view of the screen. Examples can be seen in **Error! Reference source not found.**, for a water-cooled device and an un-cooled device.

- c) The x-ray beam monitor is a visualization system for x-rays based on commercially available optics and a YAG screen. Such a system provides a field of view large enough to study the beam size, beam profile and the beam position stability of a focused beam in the endstation (at atmosphere).

### 5.3.5 Beam doors

The beam door is interlocked and allows safe operation of endstation C and personnel access to hutch D (**Error! Reference source not found.**). The door latch should be inside the hutch to avoid possible accidental tripping of ring if opened from outside.



**Fig. 5-5:** View of the diffractometer and beam door at the Australian Source Powder Diffraction beamline.

## 5.4 High heat load management

### 5.4.1 Introduction

Most of the thermal power of the wiggler source lies inherently within the low-energy spectrum (50% occurs below the critical energy of 11.1 keV). Reduction of heat load needs to be carefully considered, addressing earlier requests from advisory/review committees for reduced technical risk. A lower power will always improve the performance of white beam optical components such as the Laue monochromators. For the XPD beamline, calculations of the absorbed power indicate that a **Be window in the direct white wiggler beam would simply fail**.

Several options have been considered, e.g.:

- 1) The 8.3 kW output of the wiggler (after FE mask) is filtered through a pre-assembly of graphite filters: due to its high thermal conductivity and mechanical stability, carbon is typically used as protective filter material in front of the Be window. Considering that the maximum acceptable temperature for Be is 100°C, the pre-filter is designed for reducing the incident power on the window by a factor of ~10. The upfront pyrolytic graphite filters need to be as thin as 5 µm, and each absorbs ~450 W; the resulting peak temperature in the 5 µm graphite foil is ~1160°C. As a first approximation, assuming the power absorption is kept constant in each foil, 20 foils are needed to reduce the incident power on the Be window from 10 kW down to 1 kW. The power is predominantly thermally radiated away by each graphite layer, from both of its surfaces, as the graphite gets very hot. These filters have been successfully placed in the NSLS beamlines, but there is concern that a vacuum break would expose them to air and thus make them susceptible to burning. The Be material has been eliminated due to its toxicity when pulverized.
- 2) The engineering cost and effort in the design of the pre-filtering stage can be saved if the beamline operates windowless using differential pumping. The windowless option relying on differential pumping has also been eliminated in favor of the more robust solution of using CVD diamond windows in conjunction with an assembly of moveable SiC filters
- 3) A rotating Si disk spreads the heat over the Si wheel. This is successfully implemented at the ESRF (ID15 beamline) but this solution is not retained, due to concerns over the motor reliability in the radiation environment.
- 4) A set of two diamond windows (whose thermal properties are superior to those of Be) are followed by a set of moveable SiC filters. The diamond windows serve both as heat filters and vacuum barrier while providing added reliability because each is capable of carrying the full load. The SiC filters are moveable and modulate the heat passing through.

### 5.4.2 Diamond and SiC filter systems

The heat load in this beamline is attenuated with a set of fixed filters and one set of adjustable filters. The second filter assembly consists of a controllable attenuator design and carries SiC. This unit allows tailoring the power load on the optical elements to the appropriate level for the operational mode of the beamline. The water-cooled mounts are motorized and attached to pneumatic drives.

Heat load management requirements are as follows:

- The damping wiggler DW100 generates 8.3 kW after aperturing.
- The filters must have a dynamic range to allow as low as 0.3 kW incident on white beam optics (DLM).

- Minimal loss of transmitted beam flux above 30 keV.
- Must work at 100, 300 or 500 mA ring current.

The solution method consists of the following:

- Use the code SRW (4) to determine absorbed heat by each filter and flux transmission rate
- Use fixed diamond filters acting as windows and heat shields
- Use redundancy for safety (i.e., two identical diamond windows)
- Use a set of moveable SiC filters for dynamic range
- Optimize material choice and select material sequence and thickness from SRW
- Analyze with ANSYS thermal dissipation and stress
- Iterate to keep temperature and stresses at safe levels.

A systematic investigation of material, sequence and thickness is performed in conjunction with finite element analysis to ensure that temperatures and stress remain at acceptable values.

Choice of material: The two figures below indicated that diamond and SiC are good choices. Metals have excellent heat absorption properties but very low x-ray transmission rates. In addition metal and Si have low melting temperature when compared to diamond and SiC.

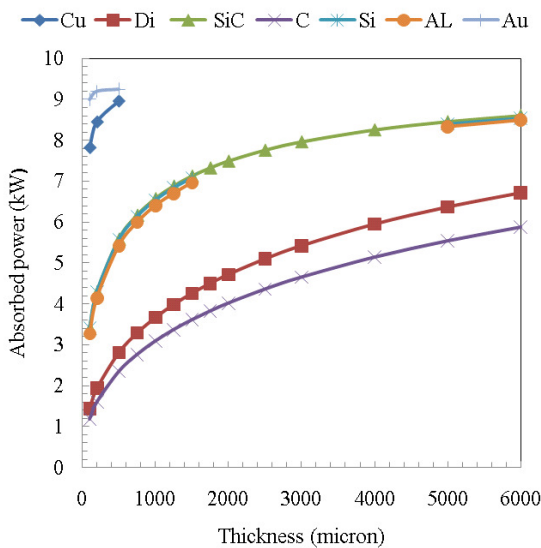


**Fig. 5-6:** Absorbed heat for different materials vs. thickness, first pass only.

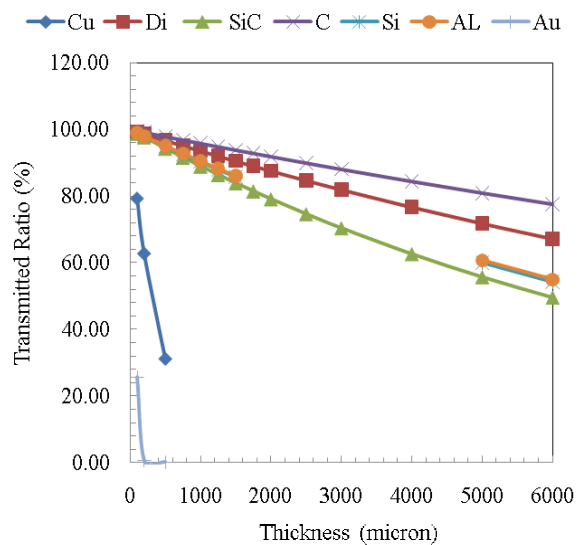


**Fig. 5-7:** Percent of Transmitted flux for different materials.

Choice of thickness: Diamond can conduct heat more readily than SiC, thus it is decided that 3 mm will act as a heat shield. For this application one finds that 3 mm of diamond absorbs 4.8 kW and 8 mm of SiC absorbs 3.1 kW. The SiC is further subdivided in a binary sequence in five filters to modulate the amount of transmitted power on the monochromator. The thinnest SiC filter is the one with the highest temperature and drives the total thickness. The diamond filter which could consist of a single 3 mm-thick window will be made for safety reasons of two 1.5 mm thick windows.

Choice of sequence: A parametric study has confirmed that the sequence placing diamond upstream of SiC is the most advantageous consideration (heat removal, transmitted flux, cost). **Error! Reference source not found.** (a) through (d) show thicknesses of diamond and SiC needed to allow an arbitrary 0.8 kW of power to pass through. If diamond is placed upstream as shown in (a) and (c), the diamond foil should be as thin as possible. The optimum case is when a very thin foil of diamond is followed by ~5.5 mm of SiC, therefore 50% of the flux is transmitted through. If SiC is placed upstream as shown in (b) and (d), an exorbitant 18 mm of diamond is needed and a very thin foil of SiC is used: the transmission is about 30%. Thus placing diamond upstream is highly cost effective and maximizes transmitted flux.

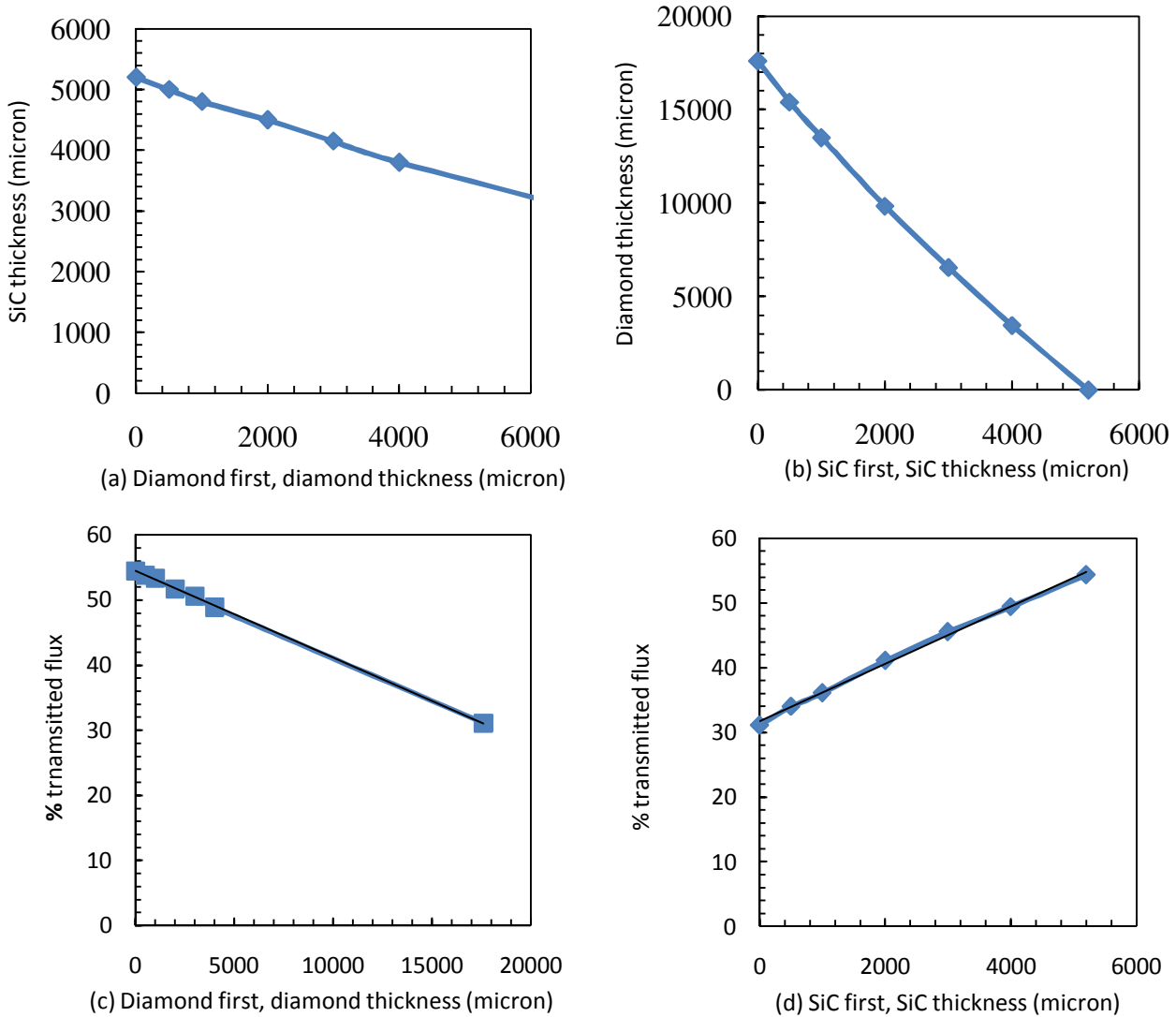


**Fig. 5-8:** Sequence of diamond and Sic: thickness needed to let 0.8 kW through, and percentage transmitted flux.

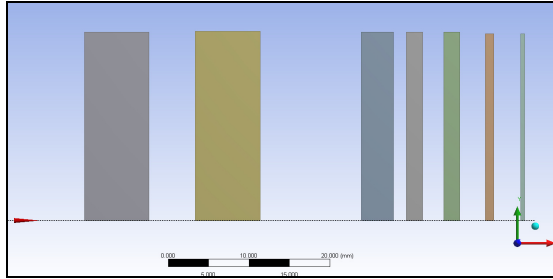


**Fig. 5-9:** Schematic of diamond and SiC filters. The power spectrum after filtering is shown at right.

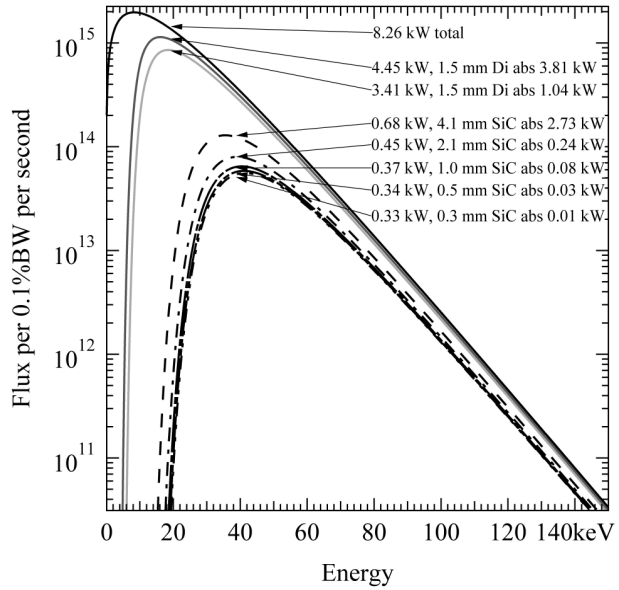


**Fig. 5-10:** Final power spectrum distribution. Sequential filtering causes beam hardening.

5.4.2.1 *Diamond vacuum isolation windows*

The filtering scheme proposed for this beamline closely follows the solution adopted at the JEEP beamline at the Diamond light source, UK.

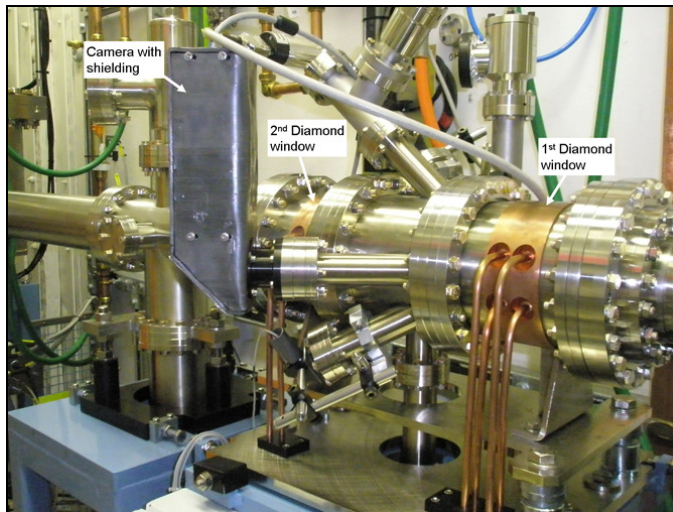


**Fig. 5-11:** Diamond Windows, JEEP beamline. Courtesy M. Drakopoulos.

The window must be able to withstand a one atmosphere pressure differential. The finite element analysis demonstrates that the 1.5 mm diamond window can sustain the impact of a 5 atm pressure wave that could be generated during a vacuum loss event. The model below is one-quarter representation of a 1.5 mm thick circular diamond window in perfect thermal contact with molybdenum, with water cooling channels. Finite element analysis of the diamond windows and of the filters relies on the perfect thermal contact that would be achieved through diffusion bonding, for instance. Maximum stress is 345 MPa (< 4500 MPa) and temperature is 267 °C (< 700 °C), well below limit values.

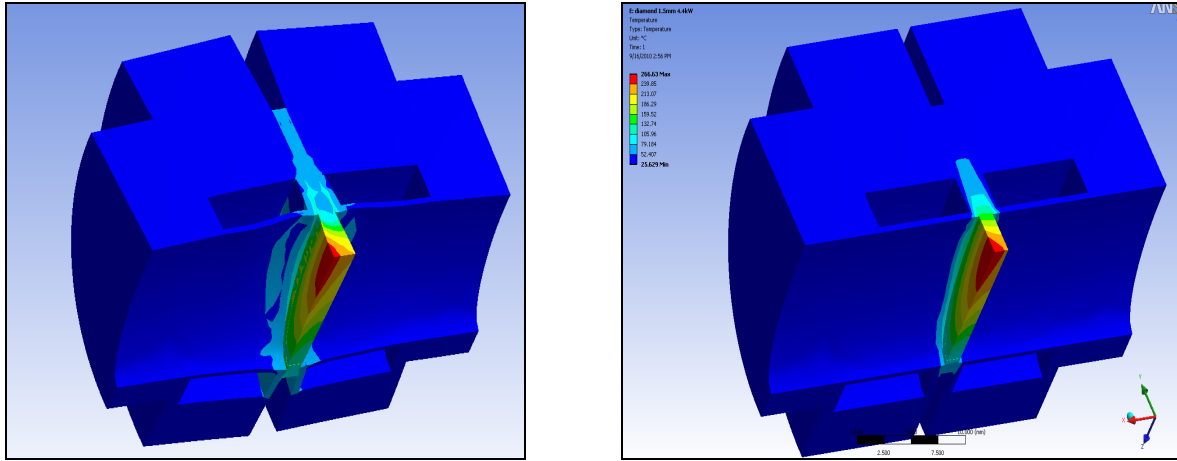


**Fig. 5-12:** von Mises stresses and temperature distribution.

The windows are CVD diamond and fluorescence can be used for diagnostic purposes. They are individually instrumented with temperature and pressure sensors and cameras, the return flow is also monitored.

#### 5.4.2.2 SiC moveable filters

CVD SiC shows excellent thermo-mechanical properties (5) with thermal conductivity almost as high as that of Cu. The figure-of-merit  $\kappa/\alpha$ , the ratio of the thermal conductivity to the heat expansion coefficient, is much higher than for Cu due to a much smaller thermal expansion coefficient and more than two times higher than for Si (at room temperature) mostly due to the two times higher thermal conductivity.



**Fig. 5-13:** SiC Filters, JEEP beamline, courtesy M. Drakopoulos.

**Table 5-6:** Material properties.

	$T_{max}$ (°C)	$T_{oper}$ (°C)	$K$ (W/m·K)	Tensile Ultimate (MPa)	CTE ( $10^6$ )
Diamond	700		2000	750	1
SiC	2400	1400	120	550	4
HOPG (aniso.)	500 air/2500 vac	2500	160/8	200	20/<0
Molybdenum	2617		138	324	5
Cu	1083		385	210	16
Au	1064		301	120	14.4
Al 6061	580		180	124	24
Si	1412		124	124	2.5
Vitreous C	3000		4.6	210	3.5

Table 5-7, column 3 shows the power absorbed by each SiC filter directly exposed to the beam (the diamond windows are fixed). Column 7 shows the cumulative power absorbed by the SiC filters when they are in place, and column 8 (Flux) is the corresponding percentage of transmitted flux at 50 keV. The ratio  $t/P$  where  $t$  is the thickness and  $P$  the absorbed power represents the ability of the filter to dissipate power. A thinner filter will absorb less heat but have a relatively smaller conduction path. The smallest ratio occurs for the thinnest filter, which experiences the highest temperature, while the thickest filter has the highest stress.

**Table 5-7:** Filter performance.

Operation		Individual*				Cumulative*	Flux
mode	$t$ ( $\mu\text{m}$ )	$P_{\text{abs}}$ (kW)	$t/p$	$T_{\text{max}}$ ( $^{\circ}\text{C}$ )	Stress (MPa)	$P_{\text{abs}}$ (kW)	(% trans)
Diamond	1500	3.8	394	266	345	3.8	90.7
Diamond	1500	1.0	1446			1.0	82.1
SiC	4129	2.7	1512	682	256	2.7	50.6
SiC	2065	2.2	925	716	241	0.24	39.6
SiC	1032	1.7	616	873	224	0.08	35.2
SiC	516	1.2	445	1155	188	0.03	33.3
SiC	258	0.7	361	1370	144	0.01	32.1

\*Individual means that only one SiC filter at a time is in place. Cumulative means that all the preceding filters are in place. In all cases, the diamond windows are in the beam.

There are  $2^5-1$  possible combinations of SiC whose total thickness is shown on the abscissa on Fig. 5-13 for three different currents. At 500 mA, the transmitted power is 3.40 kW when all the SiC filters are up and 0.32 kW when they are all down. With a set of two fixed diamond windows, all sequences of SiC filters are safe. Filter combinations that allow 0.3 kW to pass through are shown for the three different currents. A “1” indicates that the filter is down, and “0” that the filter is up. As with diamond windows, the filters are instrumented with cameras, temperature sensors and water flow meters. As a safety feature, if one diamond window fails, all sequences of moveable filters are still safe, albeit without safety margin.

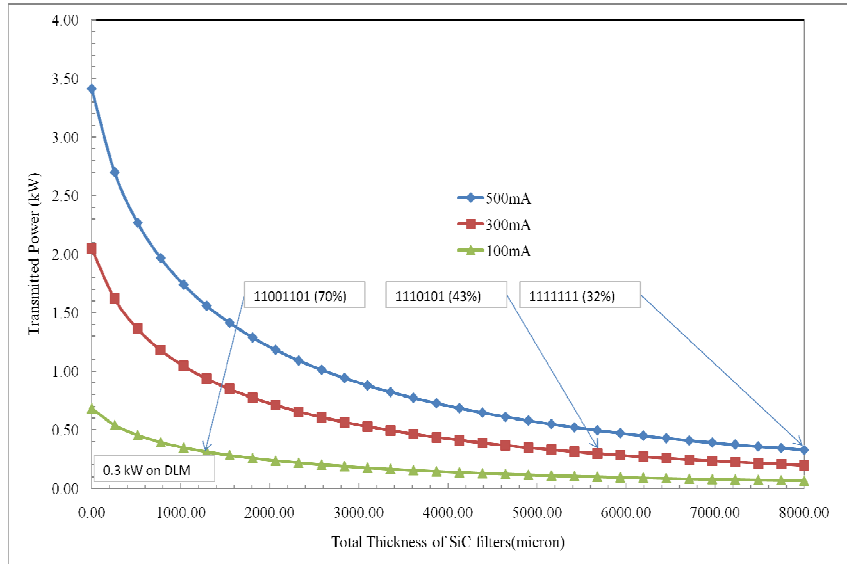


**Fig. 5-14:** Transmitted power versus total SiC thickness.

**Table 5-8:** Consequences of failure of one diamond window.

Filters	$t$ ( $\mu\text{m}$ )	$P_{\text{abs}}$ (kW)	$t/\rho$	$T_{\text{max}}$ ( $^{\circ}\text{C}$ )
Diamond	1500	3.8	394	266
Diamond	failure			
SiC	4129	3.7	1121	920
SiC	2065	3.1	665	997
SiC	1032	2.4	423	1271
SiC	516	1.8	293	1758
SiC	258	1.2	221	2242

**Table 5-9:** Filter specifications.

Axis #	1	2	3	4	5	6
Location	upstream					downstream
Elements supported	SiC filter	SiC filter	SiC filter	SiC filter	SiC filter	diode screen
A	(1)	(1)	(1)	(1)	(1)	screen
B	(1)	(1)	(1)	(1)	(1)	(1)
C	(1)	(1)	(1)	(1)	(1)	(1)
D	(1)	(1)	(1)	(1)	(1)	(1)
Movements	Pneumatic or stepper4 positions in, 1 position off					
Vertical translation z						
motor type						
range						
resolution	TBD					
accuracy	TBD					
Rotation Tz	Stepper					
type	-5 + 30°					
range	$\pm 0.1^{\circ}$					
resolution	TBD					
accuracy	TBD					
Cooling	Water					
Temperature control (interlock)	Yes					
Viewports	Yes	Yes	Yes	Yes	yes	
Mount and bonding	TBD					
Thermal radiation shields	TBD					
Vacuum	yes					
Vessel flange-to-flange dimension	700 mm					
Beam transverse dimensions	31 X 4.2					
Beam height (mm)	1400					

(1) This position can hold a variety of other filter materials: Al, Cu, graphite... or different apertures.

5.4.2.3 *White beam slits*

**Table 5-10:** Preliminary specifications for the XPD white beam slits.

	SLW1	SLW2
Operation in UHV	yes	yes
Distance from the source (m)	29.5 (H) and 30.5 (V)	33.8 (H only)
Horizontal	range TBD – aperture $\geq 1.1$ mrad	range TBD – aperture $\geq 1.1$ mrad
Vertical	range TBD – aperture $\geq 0.15$ mrad	none
Opening/closing speed	TBD	TBD
Operation cycles	5000/year	5000/year
Material	Glidcop/OFHC copper	Glidcop/OFHC copper
Water cooling	yes	yes
Incident power	kW total, w/mm <sup>2</sup> peak	kW total, w/mm <sup>2</sup> peak
Length	TBD	TBD
Wedge angle	TBD	TBD
Blade surface polishing quality	TBD	TBD
Counter wedge	Yes (to avoid over-heating of the upper edge of the slits in case of beam mis-steering)	
Thermal FEA	required	required
Tungsten edges with camera (beam flag)	yes	yes
Limit switches	yes	yes

Note: See list of components in Table 5-1.

SLW1 and SLW2 are of similar design to those in the front end.

SLW1 are used to adjust the Ho and Ve divergences of the beam and the total incident power on the white-beam optics. SLW1 works in conjunction with the FOE fixed aperture mask, and acts as anti-scatter slits behind the filters.

SLW2 operates in the horizontal direction only, and has a direct effect on the resolution performance of the PDF branchline.

## 5.5 High energy monochromators

### 5.5.1 Sagittally focusing monochromator

#### 5.5.1.1 Introduction

Three different types of monochromators are most widely used at synchrotron radiation sources:

- Double Crystal Bragg Monochromator (DCM)
- Multi-Layer Monochromator (MLM)
- Double Laue Monochromator (DLM)

Each type has its advantages and drawbacks for use at a wiggler beamline with high energy, high brightness, high divergence, high heat load, and large size beam. For a powder diffraction beamline, the major requirements are: energy tunability, maximized total flux, medium energy resolution, adequate size of the beam, and stability of the beam. Table 5-11 compares different types of monochromators and shows that the Double-Laue geometry best matches the XPD case. Table 1-1 (in section 1.2) shows that XPD is a rather unique facility when compared to other wiggler beamlines designed for high energy powder diffraction at third generation synchrotron radiation sources.

**Table 5-11:** Comparison among monochromators for high energy wiggler x-ray beam.

	DCM	Asymmetric-Bragg Crystal	MLM	DLM
Energy Tunable	Yes	No	Small Range	Yes
Energy Resolution ( $\Delta E/E$ )	$10^{-5}$ – $10^{-4}$	$10^{-5}$ – $10^{-4}$	$10^{-3}$ – $10^{-2}$	$10^{-4}$ – $10^{-3}$
Focusing (large beam)	No	Yes	Yes	Yes
Incident beam acceptance	Low	Low	Low-high	High
Thermal Load Sensitivity	High	Medium	Low	Medium
Vibration Sensitivity	High	High	Medium	Medium

Sagittal focusing using Laue crystals was pioneered at NSLS (6) (7) (8) (9). The concept (Fig. 5-15, appendix D) is increasingly used at high energy x-ray beamlines (10). The focusing capability is similar to that of the sagittal focusing by a Bragg crystal, except for a factor related to the asymmetry angle. This monochromator concept is very attractive at high energies for its flux, energy resolution, tunability and in-line-geometry properties. The good performance is attributed to some compensation effect whereby the second crystal significantly undoes the substantial brilliance degradation of the first crystal. In relaxing the bending radius of the first crystal, one finds an optimal setting where a much closer compensation occurs (11) (12).

Characteristics of monochromators based on Laue-Laue geometries are described in Table 13-3 (appendix E). The XPD monochromator will be the first of its kind and its specifications (see below) meet the scientific scope of the XPD beamline.

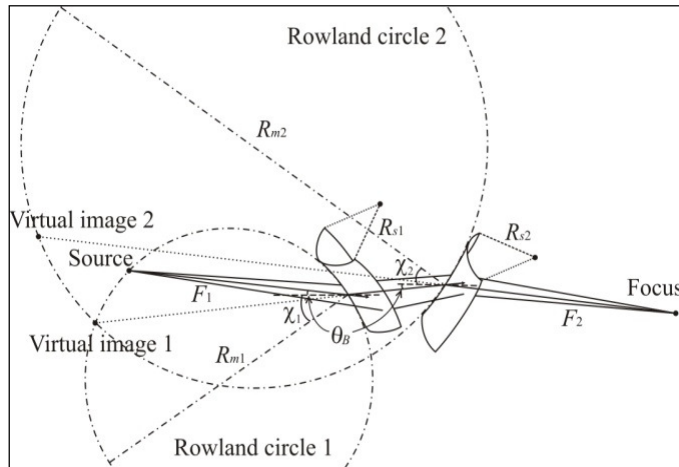


**Fig. 5-15:** DLM design concept for a sagittally bent Double Laue geometry (6) (7).

### 5.5.1.2 Design concept

The XPD beamline intends to use a sagittally bent Double Laue Monochromator (DLM) for providing a focused and adjustable monochromatic beam with optimized flux at the sample. The aim is to focus the 35 mm-wide beam to a size of 0.5 mm with a flux of  $\sim 10^{13}$  ph/s and an energy resolution  $\Delta E/E \sim 10^{-3}$  at the sample.

The position of the DLM is optimized taking three major considerations into account:

1. **Consideration 1:** To be as close as possible to the source in order to capture the maximum horizontal flux by accepting the whole 1.1 mrad beam fan.
2. **Consideration 2:** As the first (white-beam) optical element, this leaves enough room for the next optical focusing element and for the PDF branchline beam optics. The configuration where the SBM (side bounce monochromator) is first and DLM is next has been abandoned for four reasons:
  - a. Branch 1 (endstations C and D) requires the full beam flux either for optimum throughput in the high flux mode or for compensation of the flux loss in the high-resolution mode. If the SBM was a single Laue crystal placed upstream, the incident flux would decrease by 10% due to absorption; the beam flux is reduced by more than 50% if SBM is a 0.5 mm thick Bragg crystal.
  - b. Assuming that the SBM is placed upstream (before the DLM), the side-deflected monochromatic beam goes past the DLM with severe space constraints, further constraining the design and the alignment of the DLM.
  - c. Placing the DLM first and the SBM second makes it possible to align all hutches. The floor footprint of the beamline and the access to the hutches can be better rationalized in this configuration. In the reverse configuration, hutch B must be located on the side of the other endstations.
  - d. The support and bender of the SBM are not designed to let the direct beam through.
3. **Consideration 3:** To optimize the focal length of the DLM. The focal length and the demagnification factor require a sagittal bending radius  $R_s$  of the order of 1 m. A smaller focal length would require an even smaller bending radius ( $< 1$  m) and hence would prohibitively increase mechanical stress on the crystal.

The double Laue crystal monochromator is the first white-beam optical component of the XPD beamline and is used to select the energy of x-rays produced by the damping wiggler (DW). The monochromator must provide focused (horizontal) monochromatic beam at a fixed height with respect to the incident white beam, regardless of the selected x-ray energy. The relatively large vertical offset gives enough clearance downstream for bremsstrahlung shielding (see tracing in appendix B.4) and for providing another monochromator (SBM) with the direct beam. The holder for the first crystal is at a fixed location, and should let the direct white beam pass through. The second crystal can move along the beam axis and is able to catch the diffracted beam from the first crystal at a

constant height (Fig. 5-16). The distance  $D$  between the two crystals along the beam direction varies as the energy changes. The bender is such that there must be a dynamic control of the sagittal bending radius  $R_s$  (between 2 m and  $\leq 1$  m) with energy and there is a less frequent control of the meridional bending radius  $R_m$  (between 25 m and 50 m) over discrete energy intervals (see appendix D for details). The mechanical and thermal stabilities of the monochromator are critical for the experiments carried out at the XPD beamline. The DLM characteristics and performance parameters are as follows:

- Adjustable x-ray energy 30-70 keV
- Fixed exit beam with fixed offset of 50 mm
- Incident Beam size: 35 mm (H)  $\times$  4.8 mm (V) at normal incidence
- Dynamic bending of both crystals to keep the image spot size and position similar at all energies
- Energy resolution  $\sim 10^{-3} \Delta E/E$
- Source to first crystal distance ( $F_1$ ): 31840 mm
- First crystal to sample distance ( $F_2$ ): 22560 mm
- Horizontally focused beam size at the sample: 0.5 mm

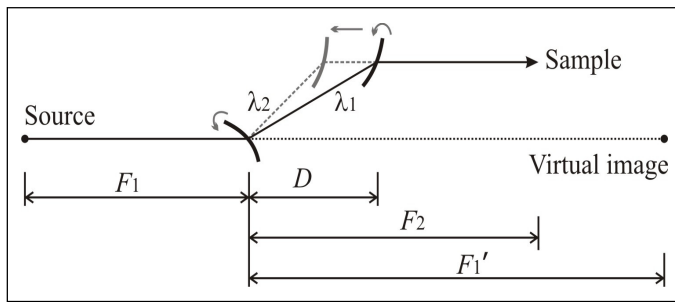


Fig. 5-16: X-ray beam trace in the DLM.

### 5.5.1.3 Design challenges

The design of the DLM for XPD poses important challenges:

- Required uniform sagittal bending radius  $R_s$
- Matching meridional radius  $R_m$  to the Rowland condition at different energies over the whole beam footprint while reducing the thermal effect.
- Choice of crystal dimension (based on Bragg planes, asymmetric cut, sagittal & meridional bending radii).
- Dynamical operation of the crystals in vacuum.
- Bender Design: The crystal support should allow unconstrained thermal expansion to limit deformation. The thermal contribution to deformation then comes uniquely from the non linear dependence of thermal conductivity and coefficient of thermal expansion on temperature. At the same time, the support should control  $R_s$  and  $R_m$  independently from each other. Cooling must also be provided through the support system for conduction cooling schemes.

### 5.5.1.4 Design optimization

We have been examining the optical and x-ray responses of the crystal under different bending conditions as a function of the crystal aspect ratio and we have been measuring the rocking curve as a function of the crystal distortion using two crystal benders based on Zhong’s leaf bender design (6). The details of the optical mapping and results are discussed in appendix E. The outcome of these test measurements is guiding us in controlling  $R_s$ ,  $R_m$  as a function of the crystal aspect ratio, asymmetry angle and thickness. Furthermore, the rocking curve gives

information about the crystal deformation and is used in section 6.1 to calculate the flux enhancement through the crystal. Detailed FEA analyses have been carried out (as described in appendix E) for the leaf and roller bender designs with different cooling arrangements.

From the above test measurements and modeling, the leaf bender design with a rigidly clamped crystal is found to pose several major issues:

- non-uniform stress distribution which affects the bending radius distribution over the beam footprint while dynamically changing the bending radius
- difficulty to achieve a  $R_m$  range (25 – 50 m) over the beam footprint for different energies, sufficiently close to the Rowland conditions at the required energy resolution and flux (Fig. 5-17).
- handling the heat load while minimizing vibrations.

This leads us to a bender design which uses four rollers (two fixed, two adjustable). The design allows  $R_s$  to vary (around 1 m) while keeping  $R_m$  within the acceptable 25 – 50 m range (Fig. 5-17), and handles the thermal load and vibration effects (appendix E for details). Based on our measurements, calculations, and FEA analyses, **a preliminary design of the XPD DLM is produced**. The optimized performance parameters of the DLM are listed in Table 5-12.

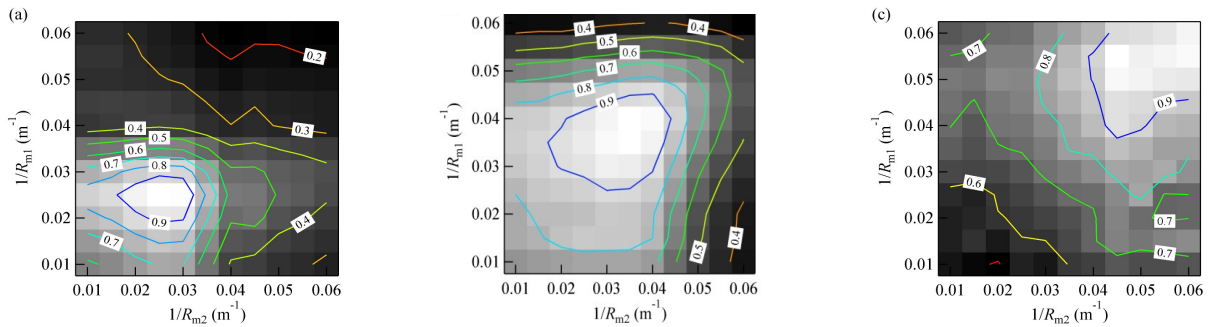


**Fig. 5-17:** Shadow ray tracing calculations for the flux per energy bandwidth as a function of the meridional bending radius of the two Laue crystals in the high-flux mode for 30, 50 & 70 keV. The numbers are normalized. See section 6.1 for details.

**Table 5-12:** Optimized performance parameters for the XPD DLM

Energy (keV)	30	40	50	60	70
Bragg angle $\theta_B$ ( $^\circ$ )	3.78	2.83	2.27	1.89	1.62
Sagittal radius $R_s$ (m)	1.99	1.49	1.19	0.99	0.84
Meridional radius $R_m$ (m)	31.8	27.7	25.4	24.2	23.6
Ho gap between crystals $D$ (m)	0.38	0.50	0.63	0.76	0.88
Energy resolution FWHM $\Delta E/E$ at the sample	$0.4 \times 10^{-3}$	$0.6 \times 10^{-3}$	$0.9 \times 10^{-3}$	$1.3 \times 10^{-3}$	$2.2 \times 10^{-3}$
Horizontal size of focused beam at sample (mm)	0.5	0.5	0.5	0.5	0.5
Flux at the sample ( $10^{12}$ ph/s) with a 1 m Pt-coated mirror	3.3	7.6	7.8	4.6	2.1

### 5.5.1.5 Crystal dimensions and orientation

The present evaluation of the crystal dimension follows Zhong's DLM performance at NSLS, calculations (FEA analyses and shadow ray tracings) and also experimental measurements (section 6.1 and appendix E). The crystal plane and orientation (8) (9) are selected taking into account the geometry of the DLM design, the diffraction

efficiency (scattering intensity) and the rocking curve width upon bending. The optimized crystal dimension is mainly based on three factors, the asymmetry angle, the sagittal bending radius  $R_s$  and the meridional bending radius  $R_m$  (appendix D for more details).

**Table 5-13:** Crystal dimension and specification.

Crystal Planes	(111) reflection of (100) oriented Si crystal. Surface normal (100) in Z, (0-11) in X and (011) in Y
asymmetry angle	35.26°
Bragg Angles (30-70 keV)	3.78° - 1.62°
Crystal dimension	Length(X) = 70-100 mm, Width(Y) = 40-60 mm, thickness = 0.5 mm – 0.65 mm

5.5.1.6 *Specification of motion controls*

The monochromator consists of two crystal stages (1 & 2). Each crystal has independent motions for pitch (Bragg angle), roll, yaw, bending force (on two outer bars, Fig. 5-18) and one side twist (twist could come from vertical misalignment of the set of rollers c and d on which the crystal rests). The angular resolution of crystal rotation is required to be better than 0.5  $\mu$ rad and its repeatability better than 1  $\mu$ rad. There are two combined motions such as changing the X & Y motions of both stages simultaneously.

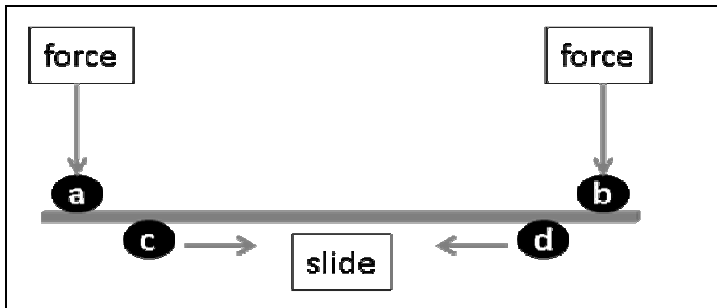


**Fig. 5-18:** Roller bender schematic showing bending concept.

The coordinate system and the axes are defined here:

- +Z horizontal along the beam direction, away from the source point;
- +X horizontal, perpendicular to Z, away from the storage ring centre;
- +Y is vertical, upwards;
- Pitch is rotation about X, describing the Bragg/Laue ‘diffraction angle’, positive is anticlockwise;
- Roll is rotation about Z, positive is anticlockwise;
- Yaw is rotation about Y, positive is anticlockwise;
- 1 & 2 refer to monochromator crystal stage 1 & monochromator crystal stage 2;
- a & b refer to force on both the rollers, both in negative Y direction.;
- c & d refer to slide of both rollers, positive and negative X direction, respectively;
- Twist is the rotation about X direction of one side of the crystal relative to the other fixed side.

**Table 5-14:** Preliminary specifications for the motion controls of the XPD DLM.

Axis	Prototype	Stepper	Stage Type	Max	Min	Resolution	Units	Encoder & Limits	Notes
Pitch <sub>1</sub>	Y	1	Tilt cradle	+2	-2	0.00003	degree	Y & Y	Bragg angle
Roll <sub>1</sub>	Y	1	Tilt cradle	+2	-2	0.001	degree	N & Y	Horizontal Tilt
Yaw <sub>1</sub>	Y	1	Tilt cradle	+2	-2	0.001	degree	N & Y	Tilt
Bend <sub>1a</sub>	Y	1	Translation	+10	-10	0.01	mm	Y & Y	Vertical Push Y
Bend <sub>1b</sub>	Y	1	Translation	+10	-10	0.01	mm	Y & Y	Vertical Push Y
Twist <sub>1</sub>	Y	1	Translation	+2	-2	0.001	mm	N & Y	Vertical Push Y on one side
Pitch <sub>2</sub>	N	1	Tilt cradle	+2	-2	0.00005	degree	Y & Y	Fine Bragg angle
Roll <sub>2</sub>	N	1	Tilt cradle	+2	-2	0.001	degree	N & Y	Horizontal Tilt
Yaw <sub>2</sub>	N	1	Tilt cradle	+2	-2	0.001	degree	N & Y	Tilt
Bend <sub>2a</sub>	N	1	Translation	+10	-10	0.01	mm	Y & Y	Vertical Push Y
Bend <sub>2b</sub>	N	1	Translation	+10	-10	0.01	mm	Y & Y	Vertical Push Y
Twist <sub>2</sub>	N	1	Tilt cradle	+2	-2	0.001	mm	N & Y	Vertical Push Y on one side
Z <sub>1</sub>	N	1	Translation	950	350	0.005	mm	Y & Y	Stage separation
Y <sub>1-2</sub>	N	2	Translation	+20	-20	0.1	mm	Y & Y	Vertical Translation
X <sub>1-2</sub>	N	2	Translation	+20	-20	0.1	mm	Y & Y	Horizontal Translation

#### 5.5.1.7 DLM prototyping

A prototype monochromator will be built and tested in order to fine tune the specifications for the potential manufacturer. The prototype, as delivered by the vendor, will be mounted on a sample stage with motor-controlled X/Y/Z translations. The prototype crystal assembly has pitch (in the plane of diffraction), yaw and roll (perpendicular to the plane of diffraction) angular adjustments under motor control. The performance of the prototype will be tested using both white beam and monochromatic beam at NSLS beamlines. Further tests will be carried out with larger and high heat load beams at other wiggler beamlines at one of the 3<sup>rd</sup> generation synchrotron sources (Diamond Light Source, Australian Light Source or Canadian Light Source).

#### 5.5.1.8 Monochromatic beam diagnostics

Tuning and optimizing the energy (angle change), focusing, energy resolution (bending) and the alignment (crystal translations and angles) of the high energy monochromatic beam both after the first stage and the second stage of the DLM are delicate. A few diagnostic methods have been reviewed for the XPD DLM. For the prototype DLM, the energy spread of the monochromatic beam is tested against the bending radius using a pencil beam and an analyzer crystal. The final DLM will then have simple diagnostics for the monochromatic beam: during an energy scan around a particular energy, the brightness and footprint shape are adjusted on a screen with finely tuned Bragg angle and bending.

Two removable diagnostics are present in the DLM vacuum chamber, one after the first crystal stage and another one after the second stage. Each diagnostic component has an aperture selector (for pencil and large beam), a foil selector (for discrete energies 30/40/50/60/70 keV), fluorescent screens and photodiode. A photodiode and energy foil arrangement for the ESRF ID11 DLM beamline and a screen diagnostics for the DLM of the JEEP beamline of DLS are shown as examples in Fig. 5-19.

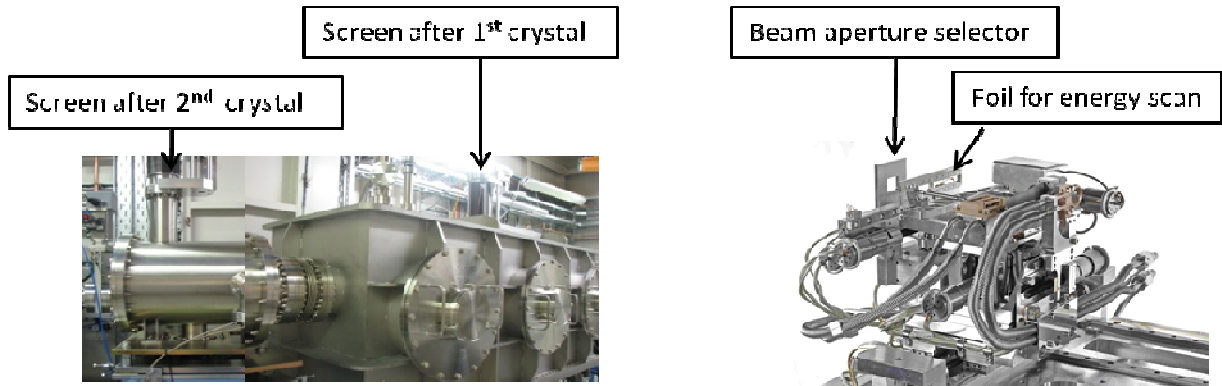


Fig. 5-19: (left) DLM at the JEEP beamline of DLS. (right) DLM at ID11 of ESRF.

5.5.1.9 Vacuum requirements and shielding

The DLM is operated in vacuum with in-vacuum cooling. The vacuum is required for ease of operation in conjunction with other beamline components and transport compatibility. It also eliminates ozone production with white beam and keeps the crystals, motors and other components safe and free of contamination. The high energy white beam when diffracted through the silicon crystal produces massive Compton scattering radiation. The Compton scattering radiation heats up the vessel and other components. A proper anti-Compton shielding is placed into the DLM vessel. A beam mask in combination with Compton shielding is placed inside the chamber before the first stage crystal. A couple of viewports fitted with vacuum glass or sapphire are used for survey and alignment purposes. An inner shutter prevents the radiation blackening of the windows.

Table 5-15: Preliminary specifications for the vessel.

Operation vacuum	Yes, 10 <sup>-9</sup> Torr or better		
Beam diagnostics	Fiducials – requirements, Fluorescence Screen & Camera feed through		
Total size (mm)	<b>Length</b>	<b>Height</b>	<b>Width</b>
	1400	600 + 300 (diagnostic Tube)	600

5.5.1.10 Cooling and vibration analysis of the crystal bender

As previously noted, the monochromator cooling minimizes the thermal bump which in turn affects the crystal's double curvatures. The whole design of the DLM bender requires reliable, reproducible and robust mechanical and cooling schemes in order to bend the crystal to the desired radii while removing the incident heat, eliminating vibrations, and providing thermal and mechanical stability.

Table 13-3 (appendix E) gives a summary of the results of different designs and cooling schemes. Several different designs have been studied using finite element analysis (appendix E). Among the options, a water-cooled crystal clamped at the edges and a crystal immersed in an In/Ga bath (APS BESSRC CAT (13)) have been eliminated due to insufficient cooling. A cryo-cooled Laue-Laue monochromator operates at APS 1-ID (10) and proves to satisfy the meridional bending geometry requirements. The retained design (appendix E) uses a roller bender mechanical design similar to that of X17B1 NSLS. The heat is dissipated by conduction through Cu braids cooled by liquid nitrogen in order to minimize cooling induced vibrations. Table 5-16 summarizes the results of FEA analysis for that crystal bender design under consideration. Most requirements are satisfactorily met: bending radii, heat load and vibration isolation. This design is now being considered for prototyping.

**Table 5-16:** Summary of the FEA results for design under consideration.

Design Type	Adjustable radii Roller bender
Crystal dimension and geometry	84 (L-X) × 38 (W-Y) × 0.5 (T) mm <sup>3</sup> at 35° asymmetry angle
Heat load	Incident power = 500 W, absorbed power density = 0.51 kW/mm <sup>3</sup> over volume = 35 × 8.7 × 0.5 mm <sup>3</sup>
Cooling Scheme and temperatures	Conduction cooling through Cu braids LN cooled, crystal Max temp = -34°C
Mechanical Bending Scheme	Apply force on fixed set of rollers and displace supporting set of rollers for dynamical curvature adjustment
Vibration Isolation	Cu braids transmit very low vibration from the LN cooling channels

**5.5.2 Side-bounce monochromator**

The target photon energies for the side-bounce monochromator are 74.8 keV, 63.8 keV and 39.1 keV for the fixed 2θ angle of 5.8 degrees given by the beamline geometry (section 4.2 for details).

The most commonly used single crystal monochromator setups are the focusing Bragg, the focusing Laue and the Rowland Laue geometries (Fig. 5-20). A detailed comparison of these three cases is presented in appendix D and summarized here in Table 5-17.

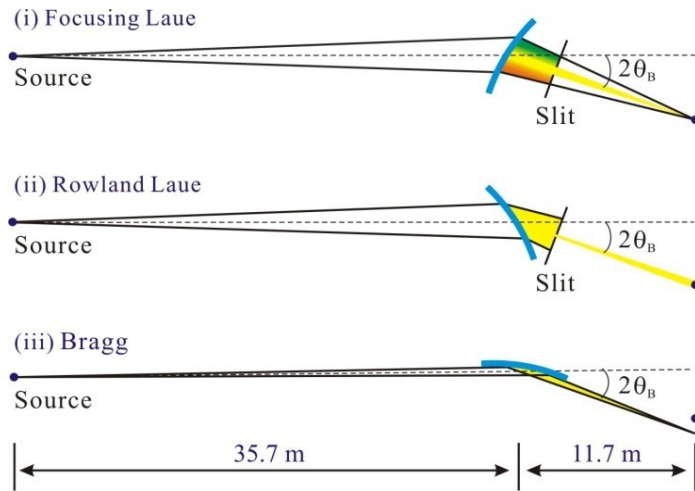


**Fig. 5-20:** Schematics (top view) of three possible geometries for the side bounce mono of the XPD beamline.

**Table 5-17:** Comparison of single crystal monochromators for the PDF branch.

Case	Focusing Laue	Rowland Laue	Bragg
Horizontal Focusing	Polychromatic focusing	Defocusing	Monochromatic focusing
Bending radius	Comparable to focal distances	Comparable to focal distances	Very large
Rocking curve width	Large	Large	Small (absorption limited)
Rowland geometry	No	Yes	Yes
Energy resolution ( $\Delta E/E$ )	$10^{-3} - 10^{-2}$ (slit determined)	$\sim 10^{-3}$	$10^{-4} - 10^{-3}$
Total Flux	Large	Large	Small
Horizontal beam size	Small	Large (slit determined)	Small
Output beam divergence	Large	Small	Large
Crystal length	Small	Small	Large

The Bragg geometry is a very attractive solution. However, this crystal is placed at a Bragg angle of  $2.9^\circ$  and needs to be long enough ( $> 780$  mm) to intercept the horizontal fan. Its response relies heavily on the alignment at the grazing incidence and on the response to bending with a radius  $> 470$  m. There is a large uncertainty as to whether the Bragg crystal will be stable and reliable under the high thermal load. The divergence of the output beam is also detrimental to the diffraction resolution. The Laue crystal monochromators are more forgiving when considering alignment and thermal stresses, and thus are most suited for the XPD branchline.

The SBM accepts the straight-through white beam after the first crystal of the DLM and horizontally deflects the selected energies at a fixed angle of  $5.8^\circ$ . The SBM design parameters are shown in Table 5-18.

**Table 5-18:** SBM design parameters.

Source to SBM distance	35.7 m
SBM to sample distance	11.7 m
Incident beam size(H × V)	$39.3 \times 5.4$ mm <sup>2</sup>
Side bounce angle ( $2\theta$ )	$5.8^\circ$
Working Energies	74.8, 63.8, 39.1 keV

There exist numerous side bounce monochromators around the world working at fixed energies. The 11ID-C (14) beamline at APS operates at a fixed angle of  $1.9^\circ$ , where the Si (111), (220) and (311) Laue crystals provide 60, 98 and 114 keV respectively. The 11ID-B beamline uses Si (311), (400) and (511) crystals to provide 58, 70 and 91 keV respectively with a fixed  $\theta = 3.75^\circ$ . The thermal load is managed by the combination of water cooling and Ga-In-Sn eutectic bath. NSLS X17A side station (currently under design) is due to operate at 74.8 keV and will be using the (311) reflection of a Si 511 crystal ( $\Delta E/E \approx 10^{-3}$  and angle deflection  $\approx 7.4^\circ$ ). The 3 mm × 3 mm beam is expected to be focused to  $< 0.5 \times 0.5$  mm<sup>2</sup>, using both the sagittal and the meridional bendings of the crystal mounted on a specially-designed two-axis bender. A silicon crystal on a cryo-cooled Glidcop bender (incident power is 40 W) is being implemented at ESRF-ID24 (energy-dispersive EXAFS) with a 30:1 demagnification at 7 keV. PETRA III (beamline P07) is also considering the horizontally deflecting Laue geometry for energies  $> 60$  keV (15): the diffraction efficiency and bandwidth are controlled by a silicon crystal with either a Ge composition-gradient or a thermal gradient.

The proposed design of the monochromator assembly requires stability and reliability. The side-bounce crystal and mechanism reside in a (UHV) vacuum vessel. There is the possibility of implementing more than one crystal, leaving the choice of different pre-aligned crystals for different energies. For each crystal, one can optimize the energy bandwidth and the focusing properties by adjusting the thickness,  $T_0$ , the asymmetry angle,  $\chi$ , and the bending radius,  $\rho$ . The mechanical design should also accommodate the fact that the SBM is located 50 mm below

the monochromatic beam of the DLM. Using three different crystals requires three benders with cooling attachments that can be exchanged using the horizontal translation arm or rotation stage. Instead, a special cut Laue crystal is proposed for all three energies (optimized at 74.8 keV). The crystal design parameters are listed in Table 5-19 and the motion control specifications are shown in Table 5-20.

**Table 5-19:** Preliminary SBM crystal design parameters.

Energy	74.8 keV	63.8 keV	39.1 keV
Crystal dimension	Length = 100-150 mm, width = 10-20 mm, thickness = 3-5 mm		
Crystal reflection	Si 311	Si 220	Si 111
Asymmetry angle	39.1°	25.7°	9.6°
Beam footprint (H × V)	48.7 × 5.4 mm <sup>2</sup>	44.8 × 5.4 mm <sup>2</sup>	39.3 × 5.4 mm <sup>2</sup>
$\rho$ (focusing mode)	48.9 m	36.9 m	36.0 m
$\rho$ (Rowland mode)	44.2 m	40.6 m	35.9 m

**Table 5-20:** Preliminary specifications for the motion controls of the SBM.

Movement	Range	Resolution	Repeatability
<i>Whole optic assembly:</i>			
Transversal (Y)	150 mm	≤ 0.1 mm	≤ 50 μm
<i>Crystal units:</i>			
Roll rotation	-10 – 10°	≤ 10 μrad	≤ 20 μrad
Bragg rotation (coarse)	Full turn	≤ 10 μrad	≤ 20 μrad
Bragg rotation (fine)	± 50 μrad	≈ 0.01 μrad	≈ 0.3 μrad (uni-directional)

Appendix D shows preliminary calculations for both the focusing Laue and the Rowland Laue setups. The focusing Laue case can provide a total flux of  $3 \times 10^{12}$  ph/s with a resolution  $\Delta E/E \approx 0.01$  in a focused 1 mm horizontal beam. The Rowland Laue case provides a similar total flux with a  $10^{-3}$  resolution in an unfocused 10 mm beam. A horizontal slit before/after the SBM is needed to regulate the energy resolution in the focusing Laue case and the beam size in the Rowland Laue case. As a result, the total flux will change proportionally. In the present design, the slit defining resolution or size is placed before the SBM given the space constraints: this also helps reduce the thermal load on the SBM.

## 5.6 Monochromatic Beam Optics

### 5.6.1 Vertically focusing optics

#### 5.6.1.1 Introduction

There are two modes of operation for the XPD beamline (section 6.1): i) the high-resolution mode and ii) the high-throughput mode. In i), the monochromatic beam is vertically collimated and reaches the HRM; in ii), the monochromatic beam is vertically focused and directed to the sample. The function of the vertical beam optics is to re-condition the vertical monochromatic beam coming out of the DLM for optimum energy resolution, beam size and/or flux. The major challenges with this optics are to handle these two operation modes for high energies ranging from 30-70 keV and for a large beam size 23(H) × 6(V) mm<sup>2</sup> (focused horizontally by the DLM).

The vertical focusing optics of XPD offers many options, for instance;

- diffractive optics as used in Fresnel Zone Plates (FZP) and Multilayer Laue Lenses (MLL)
- refractive optics as used in Compound Refractive Lenses (CRL) and Kinoform Lenses

- reflective optics as used in single layer (SL) mirrors and multilayer (ML) mirrors.

Table 5-21 gives comparative information on different focusing optics.

**Table 5-21:** Comparison of different focusing optics available for hard x-ray focusing.

Optics	Geometry	Pros	Cons	Comments
FZP & MLL	diffractive	<ul style="list-style-type: none"> <li>- very small focused beam size</li> <li>- uniform beam shape.</li> </ul>	<ul style="list-style-type: none"> <li>- performance limited by aspect ratio</li> <li>- small focal distance</li> <li>- small aperture</li> <li>- sensitive to beam stability</li> <li>- fixed focused beam size</li> <li>- not optimized for energy &gt; 15 keV</li> </ul>	<ul style="list-style-type: none"> <li>- manufacturing limitation for high energy x-rays both for FZP &amp; MLL</li> </ul>
CRL, Kinoform lenses.	Refractive	<ul style="list-style-type: none"> <li>- adjustable focused spot size</li> <li>- insensitive to beam stability</li> <li>- many choices of elements suitable for different ranges of energies</li> </ul>	<ul style="list-style-type: none"> <li>- small aperture</li> <li>- beam shape and figure depend on lens manufacturing quality and material.</li> </ul>	<ul style="list-style-type: none"> <li>- aperture too small for a large wiggler beam</li> <li>- large number of lenses required for very high energy x-rays and thus focusing adjustment is more complex.</li> </ul>
SL & ML mirrors	reflective	<ul style="list-style-type: none"> <li>- adjustable focused beam size</li> <li>- large energy band acceptance</li> <li>- harmonic rejection capability</li> <li>- routine use for micron size beam</li> <li>- easy coating and Si technology</li> <li>- large size better for heat load management.</li> </ul>	<ul style="list-style-type: none"> <li>- smaller angle of reflection restricts focusing and beam acceptance</li> <li>- slope error and roughness over a larger footprint are the major issues</li> <li>- Pre-bending or dynamical bending affects the focusing indirectly through slope error</li> <li>- ML mirrors are not energy tunable for a wide range of energies.</li> </ul>	<p>Due to recent developments of large Si mirrors, achieving slope error down to 0.3 Å and roughness to 1 Å and fine coating grades make the ML and SL mirrors very attractive for high energy and large beam size x-ray sources.</p>

From the above table it is apparent that the best suitable optics for XPD requirements and for energy tunability are either the CRL or the SL mirror. However, for the fixed energy PDF line, a ML mirror would be a better choice. For using the ML mirror on the energy tunable branchline, the  $d$  spacing is varied in such a way that rays with different energies are reflected from different depth zones of the total stack. It is possible to get a 3.5% energy bandpass ( $\pm 0.7$  keV) with a reasonably good reflectivity (43%) at 40 keV. At higher energies, the reflectivity for the same bandpass becomes even lower. Therefore for a beamline with continuously tunable energy, the ML mirror is not the appropriate focusing optics when compared to the SL mirror.

Refractive lenses are an attractive solution for XPD due to their relatively simple mechanics, compactness and low cost. CRL are relatively simple to align, very stable, immune to vibrations and relatively forgiving of orientation errors. It is recommended to use guard slits in front of the sample to eliminate incident beam tails arising from imperfections in the CRL (blurred focus, etc) and to minimize small-angle scattering halos. However, a significant drawback is the aperture-limited gain in flux for long-focal-length (low demagnification) focusing. It is shown in appendix F that for energies above 30 keV, the effective vertical aperture is always less than 1 mm. Considering the focal length, energy range and beam size at the sample and taking the effective aperture into consideration, the calculated vertical transmission and horizontal acceptance for 30 keV and 70 keV are much less than 20% (appendix F). The reduction in overall useful flux assumes as a first approximation that the overall angular acceptance is ultimately defined by the effective aperture of the optics (CRL or mirror) at 40 m and not by the mask in the FE. Table 5-22 shows a comparison of the flux for a 1.2 m effective length Pt-coated mirror and an optimized CRL for both 30 keV and 70 keV x-rays. The SL mirror is the best choice as the vertical focusing optics for XPD beamline.

**Table 5-22:** Comparison of useful flux at the sample in the focusing mode of the vertical optics

	CRL (30 keV) 3.5(H) × 1.2(V) mm <sup>2*</sup>	CRL (70 keV) 3.5(H) × 0.6(V) mm <sup>2*</sup>	Pt-mirror (30 keV) 23(H) × 2.4(V) mm <sup>2*</sup>	Pt-mirror (70 keV) 23(H) × 1.3(V) mm <sup>2*</sup>
Flux (10 <sup>12</sup> ph/s)	0.24	0.10	3.9	2.5

\*The CRL parameters are from

Table 13-9. The mirror is 1.2 m effective length and Pt-coated (incident angle for 30 keV is 2.0 mrad and for 70 keV is 1.1 mrad).

Therefore, CRL-based optics is not retained in the baseline of the present layout due to their low throughput in a wiggler beam (see calculations on the performance of CRL in appendix F). However, refractive optics can easily be implemented in the present layout of XPD at a later stage. CRL with more complex patterns remain an attractive solution for future optical options for XPD:

- a. Parabolic (16)
- b. Triangular/Parabolic saw tooth (12)
- c. Kinoform profile (17) (18)
- d. Prism, Clessindra (19)

The next sections a) and b) discuss the applicability of respectively the SL mirror and the ML mirror for the XPD branchlines.

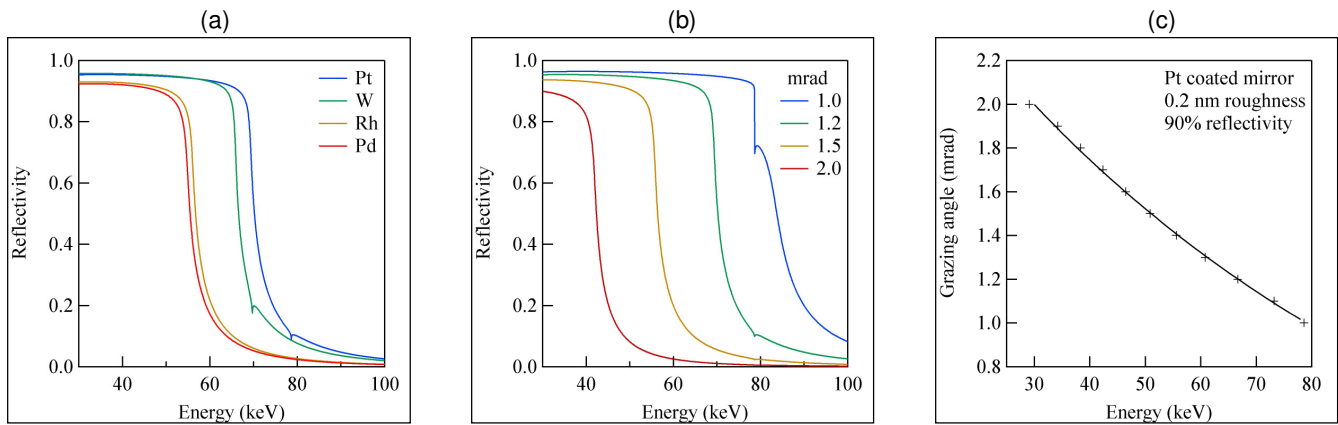
#### a) Single-layer (SL) Mirrors

Table 5-22 shows that a **SL mirror is the right choice as a focusing optics for the XPD beamline**. The other important aspect is that the SL mirror is achromatic, which is one of the requirements for the XPD beamline. As stated before, the high-resolution mode requires a collimated beam directed to the HRM and the high throughput mode requires a focused beam at the sample. The major manufacturing parameters for the SL mirror are:

- the choice of coating materials for optimized reflectivity for high energies ranging from 30 keV to 70 keV
- the length of the SL mirror to capture the maximum part of the vertical fan (beam size at the SL mirror location is 23(H) × 6(V) mm<sup>2</sup>).

The energy bandwidth and the length of the mirror, both depend on the coating materials which determine the total reflection angle. Fig. 5-21a shows the reflectivity of different coating materials with respect to energy at a median incident angle of 1.2 mrad. This figure clearly shows that Pt coating gives the maximum reflectivity for the required energy range of 30 – 70 keV.

Fig. 5-21c shows that the XPD beamline energy range can be covered with 90% reflectivity using a Pt-coated mirror within an incident angle range of 1-2 mrad.



**Fig. 5-21:** The efficiency of a SL mirror for different coating materials and the maximized parameters for a Pt-coated mirror. (a) reflectivity with respect to energy for Pt, W, Rh, and Pd-coated mirror with 0.2 nm roughness and 1.2 mrad incident angle, (b) reflectivity with respect to energy for Pt-coated mirror for different incident angles and with 0.2 nm roughness, and (c) grazing angle variation with energy for a Pt-coated mirror with 0.2 nm roughness and 90% reflectivity.

A Pt-coated mirror of size greater than 1 m is readily available. The challenges for the fabrication of mirrors with lengths greater than 1m long are to maintain the rms roughness low (<0.2 nm) and to keep a high figuring (slope error <1 μrad) over a large active length. The reflectivity decreases with increasing roughness and the focus spot size increases with increasing slope error. In high-resolution mode, the slope error enlarges the energy bandwidth. **For an ideal output of flux and resolution, a slope error less than 1.2 μrad is required** (see Table 6-2 and Table 6-3). Detailed analyses of these parameters on the mirror efficiency are discussed in section 6.1.

The other important aspect of a focusing or collimating mirror is the bending shape and radius. For a spherical shaped Pt-coated mirror with source-to-mirror distance  $F_1 = 40.1$  m, and mirror-to-sample distance  $F_2 = 14.3$  m, the required bending radius is  $R = 1.8 \times 10^4$  m for a 1.2 mrad grazing angle. To avoid spherical aberration, an elliptical or parabolic mirror should be considered.

**Table 5-23:** Ray tracing results for XPD beamline after the SL mirror (in both modes).

$E$ (keV)	70	60	50	40	30
Mirror Grazing angle (mrad)	1.14	1.32	1.52	1.75	2
Mirror reflectivity	90%	90%	90%	90%	90%
Mirror slope error (μrad)	1.27	1.27	1.27	1.27	1.27
<b>High-Flux Mode</b>					
$\Delta E/E$ (FWHM)	$2.2 \times 10^{-3}$	$1.3 \times 10^{-3}$	$0.9 \times 10^{-3}$	$0.6 \times 10^{-3}$	$0.4 \times 10^{-3}$
beam size (FWHM) (mm <sup>2</sup> )	$0.75 \times 0.054$	$0.75 \times 0.053$	$0.75 \times 0.056$	$0.70 \times 0.070$	$0.63 \times 0.095$
Flux at sample (ph/s)	$2.1 \times 10^{12}$	$4.6 \times 10^{12}$	$7.8 \times 10^{12}$	$7.6 \times 10^{12}$	$3.3 \times 10^{12}$
Intensity at sample (ph/s/mm <sup>2</sup> )	$5.3 \times 10^{13}$	$1.1 \times 10^{14}$	$1.9 \times 10^{14}$	$1.6 \times 10^{14}$	$5.5 \times 10^{13}$
<b>High-Resolution Mode</b>					
$\Delta E/E$ (FWHM)	$1.6 \times 10^{-4}$	$1.2 \times 10^{-4}$	$1.3 \times 10^{-4}$	$1.4 \times 10^{-4}$	$1.7 \times 10^{-4}$
beam size (FWHM) (mm <sup>2</sup> )	$0.51 \times 1.2$	$0.60 \times 1.3$	$0.53 \times 1.4$	$0.45 \times 1.5$	$0.57 \times 1.6$
Flux at sample (ph/s)	$1.5 \times 10^{11}$	$4.4 \times 10^{11}$	$1.2 \times 10^{12}$	$1.7 \times 10^{12}$	$1.3 \times 10^{12}$
Intensity at sample (ph/s/mm <sup>2</sup> )	$2.5 \times 10^{11}$	$5.7 \times 10^{11}$	$1.6 \times 10^{12}$	$2.5 \times 10^{12}$	$1.4 \times 10^{12}$

Table 5-23 provides the ray tracing results (section 6.1) from combined DLM and SL mirror in both the high-flux and the high-resolution modes.

The state of the art is a mirror of 1300 mm effective length with 0.1 nm roughness and 0.3  $\mu$ rad slope error (as being fabricated for SPring8). Considering the current manufacturing capabilities in providing a mirror of such a large effective length, and the required surface figuring to preserve the resolution and reflectivity while bending the mirror, the optimum mirror specifications (Table 5-25) for the XPD beamline can be summarized as:

- Pt-coated mirror of effective length 1300 mm
- rms roughness  $\leq 0.2$  nm
- slope error over the active length  $\leq 1.2$   $\mu$ rad
- required bending radius  $\sim 1 - 7 \times 10^4$  m.

The detailed specifications for the bender are listed in Table 5-26.

### b) Multilayer (ML) mirrors

The major advantage of a ML mirror over a SL mirror is the large angle of incidence: it can either intercept a larger part of the incident vertical fan or it can be made considerably shorter and easier to handle. Currently, ML mirrors up to 1m in length can be produced (20) (21) (22) (23).

The major disadvantage is that a ML mirror works over a relatively narrow energy band, whereas a SL mirror works over a continuous energy range. Therefore, for the XPD variable energy (30–70 keV) branchline, a SL mirror is a better choice. Today, multilayered mirrors with an energy resolution between 0.2% and 40% can be manufactured (24). Such an energy bandwidth is about two orders of magnitude larger than that of perfect crystals. This yields a significant gain in flux when the ML mirror is placed in a broad energy band-pass incident beam. For the PDF beamline with fixed energies, a ML mirror is the best choice. The PDF beamline will run at three fixed energies: 39.1 keV, 63.8 keV, and 74.8keV (section 4.2).

The ML mirror design is such that the energies should not be close to the absorption edge of the coating materials to avoid fluorescence background. The  $d$ -spacings of the ML mirrors are such that the ML mirror is kept at a fixed angle to reflect all three energies. Therefore the ML mirror focusing bender can be designed for a fixed radius and a fixed incidence angle. The beam footprint is thus kept constant for all three energies. A major requirement for the ML mirror is the presence of three different stripes for the three different energies.

For a particular x-ray energy, flux depends on the acceptance aperture (large grazing angle) and reflectivity of the ML mirror. The above two parameters mainly depend on the material combination, period length, and gamma (period ratio) of the bilayers of the ML mirrors. We have been looking into several ML mirror options: typical material combinations are W/Si, Ru/C, Mo/Si, Pt/B<sub>4</sub>C, Pd/B<sub>4</sub>C but also Ni/C, Cr/Sc, W/B<sub>4</sub>C, La/B<sub>4</sub>C, Ni/ B<sub>4</sub>C and numerous others (25). See discussion in b) of section 5.6.1.

Table 13-10 in appendix G shows the ML mirror characteristics for different materials combinations for different energies, period lengths, and for gamma = 0.5, number of bilayers = 500, and interface roughness = 0.25 nm.

See discussion in b) of section 5.6.1.

**Table 13-10 suggests that Ni/B<sub>4</sub>C with optimized bilayer period and gamma gives the maximum reflectivity, similar energy resolution, and comparable divergence for all the chosen energies. For the sake of fabrication quality and simplicity, it is necessary to keep the number of bilayers low (~200), with optimized period length and gamma value and, most importantly, the interface roughness needs to be below 0.3 nm.**

Table 13-11 in appendix G shows the reflectivity dependence of a ML mirror on gamma for a particular ML mirror at a particular energy reflection. Table 13-12 shows the reflectivity dependence of different ML materials on the number of bilayers for a particular energy and a given period length.

For operation at a fixed incidence angle and off the absorption edge of the materials, the ML mirror design is optimized (choice of materials, thickness of the bilayers) for best reflectivity. Fig. 5-22 shows the reflectivity from three materials and optimized  $d$ -spacings for energies 74.8 keV, 63.8 keV, and 39.1 keV.

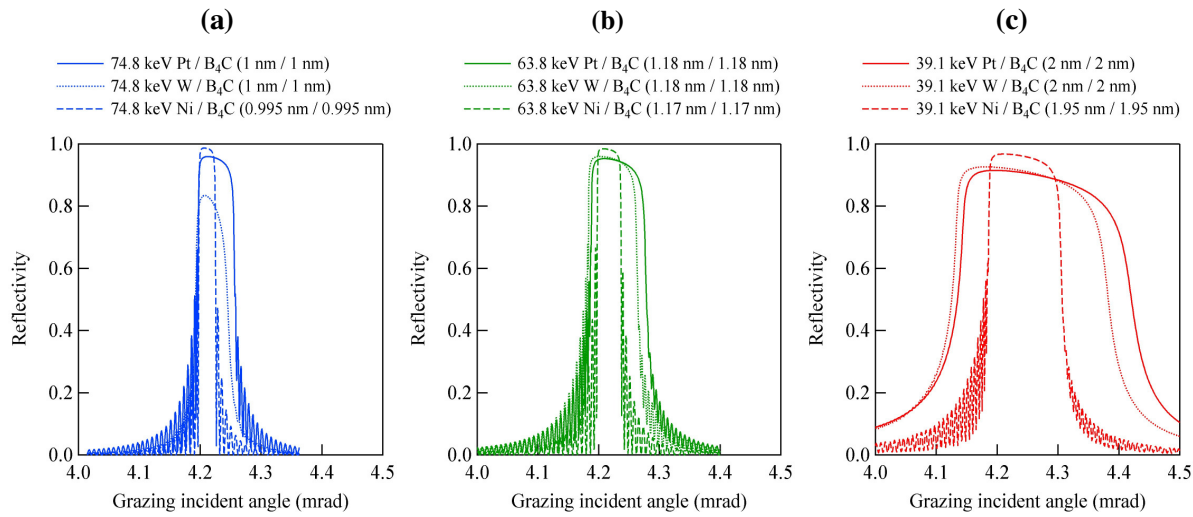


**Fig. 5-22:** Calculated reflectivity with respect to grazing angle. The number of bilayers ( $N = 200$ ) and the substrate roughness (0.2 nm) are kept the same for all three cases.

Although the maximum reflectivity is obtained with Ni/B<sub>4</sub>C, we have to consider the large energy range of reflections, the suppression of fluorescence background, the wide grazing angular range, and the high reflectivity (~95%). This led us to choose:

- Pt/B<sub>4</sub>C as the appropriate ML stripe for the 74.8 keV energy
- W/B<sub>4</sub>C as the appropriate ML stripe for the 63.8 keV energy
- Ni/B<sub>4</sub>C as the appropriate ML stripe for the 39.1 keV energy.

Fig. 5-23 shows the optimized calculated performance of the PDF branchline ML mirror.

The divergence of the incident beam could be matched with the period ratios along the beam footprint by making the ML mirror laterally graded. For an incident angle of 4.25 mrad over a 1m ML mirror, the maximum incident beam divergence for the PDF beamline is 0.1 mrad. This is very small and the lateral grading needed for the ML mirror would be minimal. Therefore, all our simulations assume a uniform grading of the ML mirror.

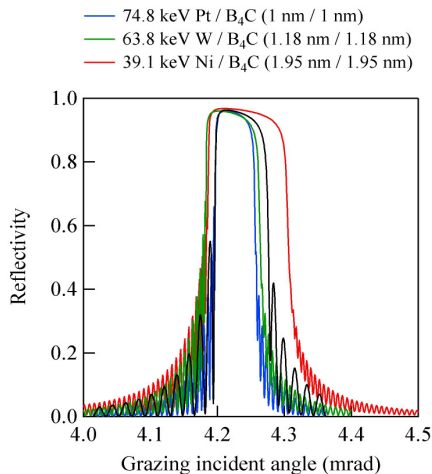


**Fig. 5-23:** Calculated reflectivity with respect to the grazing angle for the PDF branchline 3-stripes ML mirror at energies 74.8 keV, 63.8 keV, and 39.1 keV. The number of bilayers is ( $N = 200$ ) for each stripe and the substrate roughness is 0.2 nm.

Thus we propose that **the PDF beamline vertically focusing ML mirror be manufactured with three different stripes of different materials and  $d$ -spacings.** This allows the ML mirror to operate at three different energies at a

fixed incidence angle ( $\sim 4.25$  mrad) and with a fixed bending radius. The details of the specification of the ML mirror are given in section 5.6.1.4 and Table 5-28.

#### 5.6.1.2 Rationale for the position of the vertical focusing optics

XPD is designed to run independently:

- the horizontally focusing DLM serving endstations C and D with high flux or high-resolution x-rays beams at energies varying between 30 and 70 keV
- the SBM serving endstation B with high flux and moderate resolution at fixed energies of 74.8, 63.8, and 39.1 keV.

The vertically focusing mirror (VFM) is usually placed before the monochromator(s) as the first white beam, high heat load optical element. In the present case, independent operation of both branchlines is important and it would be disadvantageous to serve simultaneously both monochromators with the VFM placed upstream. The requirements of the SBM and the DLM regarding the incident energy range and vertical divergence are not the same. Moreover, the DLM is designed to accept the natural vertical divergence of the incident beam over the entire fan; there is no gain for the VFM to truncate or modify this incident fan. The high-resolution mode is obtained by combining the VFM with the HRM. The source-to-VFM distance, whether the VFM is placed before or after the monochromator, does not significantly affect the vertical acceptance angle. The focal lengths of the mirror and of the monochromator are a major input in our modeling; the current setting yields better results in terms of focusing capability and beam size at the sample. Furthermore, placing the VFM in the white beam would increase the engineering complexity of the beamline in terms of high heat load management.

#### 5.6.1.3 Mirror serving endstation C

This mirror is a long ( $> 1$  m) Pt-coated mirror designed to work in the 30-70 keV range with high reflectivity and matching the vertical divergence of the DLM, and only accepting the central part of the 6 mm high beam. The SL mirror deflects the beam upward or downward to the sample or the HRM. This mirror is dynamically bent to focus the beam at the sample for different energies and has a reverse bender to compensate the gravity sag. The characteristics of the SL mirror are described in Table 5-24 for the two modes of operation. The mirror is thus positioned at 40.1 m from the source and 14.3 m from the sample. The specification details of the mirror are described in Table 5-25. The preliminary specifications are in the “cost effective” range.

**Table 5-24:** Characteristics of SL mirror at two different operation modes.

Operation mode	Collimating (30 keV)	Collimating (70 keV)	Focusing (30 keV)	Focusing (70 keV)
Ideal mirror figure	Parabolic	Parabolic	Elliptical	Elliptical
Grazing angle (mrad)	2.00	1.14	2.00	1.14
Bending radius*, R (m)	$4.01 \times 10^4$	$7.04 \times 10^4$	$1.05 \times 10^4$	$1.85 \times 10^4$
Energy Resolution ( $\Delta E/E$ )	$0.17 \times 10^{-3}$	$0.16 \times 10^{-3}$	$0.4 \times 10^{-3}$	$2.2 \times 10^{-3}$

The bending radius in Table 5-24 is obtained from  $1/F_1 + 1/F_2 = 2/(R \sin\theta)$  for a spherical mirror. Table 5-24 shows that the mirror can be bent to a cylindrical shape with a mechanical system to focus the x-ray beam down to 50 microns.

**Table 5-25:** Preliminary specifications for the SL mirror.

Mirror body (substrate material)	Silicon		
Coating Material	Pt: density > 95% of bulk material, thickness > 500 Å		
Working Energy (keV)	30 - 70		
Beam size (mm)			
Transverse	44 (full horizontal beam) or 23 (focused horizontal beam)		
vertical	6 (full width of vertical beam)		
Fit surface (convex)	Cylindrical, bent to focus		
Mirror orientation	Facing up – vertical deflection (downward is an option depending on bender design – IRF done for the upward configuration in section 6.2)		
Distance to source (m)	40.1		
Focus distance (m)	14.3		
Useful (active optical) size (mm)	Length	Width	Thickness
	1300	Active width + polishing edge “roll-off”	To be decided from Gravitational Sag and Effective Length of Mirror ( $\geq 90$ mm)
longitudinal radius (m)	$> 1 \times 10^4$		
transverse radius (m)	$> 1 \times 10^6$ (relaxed natural curve)		
Major axis	TBD		
Minor axis	TBD		
Mirror angle (mrad)	1.0 – 2.0		
Maximum slope errors			
Longitudinal	1.2 $\mu$ rad rms over 500mm longitudinal (section 6.1)		
Transverse	< 10 $\mu$ rad rms		
Height error (PTV)	N/A		
Surface micro-roughness	0.2 nm (Measured over a (10 $\mu$ m $\times$ 10 $\mu$ m ) area with a $\times 10$ or $\times 20$ magnification)		
Max. absorbed heat in operation	negligible		
Max. generated stress	Depends on bending radius and thickness, should be very low for 5 km min		

The mirror bender is designed to be a self-contained system mechanically decoupled from the external mounting system. The design should be such that there is no additional slope error in addition to the intrinsic flat surface slope error. **The design should consist of a two-way bender to compensate for the gravity sag.** The bender specifications are given in Table 5-26. The mirror vessel is designed to maintain the whole system in vacuum. The vessel specifications are given in Table 5-27.

**Table 5-26:** Preliminary specifications for the bender.

Shape	cylindrical			
Radius of curvature (m)	$>5 \times 10^3$ ( with reverse bending capability)			
Relative radius repeatability	0.5%			
Mirror angle (mrad)	1.0 to 2.0			
Cooling	none			
Gravity	weight compensation for gravity ( depends on the design, in the merit of the bounce-up/down geometry)			
Gauges and sensors for shape control and correction	yes			
Movements	<b>Range</b>	<b>Step</b>	<b>Precision</b>	<b>Repeatability</b>
Translation Tx (mm)	N/A	N/A	N/A	N/A
Translation Ty (mm)	N/A	N/A	N/A	N/A
Translation Tz (mm)	+/- 20	0.002	relative	0.004
Roll (mrad)	Manual & lockable	N/A	N/A	N/A
Pitch angle (mrad)				
Min	-5.0	0.001	relative	0.004
Max	+10.0			
Limit Switch & Hard Stop	Yes, limit switch resolution = 1 $\mu\text{m}$ with encoders			

Note : X along beam direction, Y along transversal and Z along vertical

**Table 5-27:** Preliminary specifications for the vessel.

Operation vacuum	better than $1 \times 10^{-9}$ Torr		
Optical (laser) alignment	Not required (mirror, mirror mechanics, and the vessel adjustments are independent)		
Viewport	One viewport at the outboard side		
Total size (mm) (flange to flange)	<b>Length</b>	<b>Height</b>	<b>Width</b>
	TBD	TBD	TBD

**5.6.1.4 Multi-stripes multilayer mirror serving endstation B**

Endstation B is served with the ML mirror positioned at 42.2 m from the source and 5.8 m from the sample. This is a long (~1 m) lateral graded ML three-stripes mirror designed to work at three fixed energies (74.8, 63.8, 39.1 keV) at a single incidence angle with high reflectivity. It matches the divergence of the monochromatic beam from the SBM. The ML mirror deflects the beam upward to the sample and is dynamically bent to focus the beam at the sample for different energies. The specifications of the ML mirror are described in Table 5-28. The specifications are in the “cost effective” range.

**Table 5-28:** Preliminary specifications for the ML mirror.

Mirror body (substrate material)	Silicon		
	Stripe 1	Stripe 2	Stripe 3
Optical coating materials	Ni / B <sub>4</sub> C	W / B <sub>4</sub> C	Pt / B <sub>4</sub> C
Working energy (keV)	39.1	63.8	74.8
lateral design	graded	graded	graded
depth design	uniform	uniform	uniform
d-spacing (nm)	3.9	2.36	2.0
Number of bilayers	200	200	200
Angle of incidence (mrad)	4.14	4.22	4.23
Active Length (mm)	1000	1000	1000
Energy Bandpass (%)	0.8	2.0	1.6
Calculated peak reflectivity(%)	96.8	96.0	96.0
Gap between stripes	TBD		
Stripe active width (mm)	TBD		
Active length (mm)	1000		
Fit surface (convex)	Spherical bending, compensation for gravity		
Mirror orientation	Facing up – vertical deflection		
Distance to source (m)	42.2		
Focus distance (m)	5.8		
Beam size (mm)	Depending on slits and SBM focusing		
Transverse			
vertical	6.3		
longitudinal radius (m)	$> 2.5 \times 10^3$		
transverse radius (m)	$> 1 \times 10^6$		
<b>Maximum slope errors</b>			
Meridional	1.5 $\mu$ rad rms over 500mm longitudinal		
sagittal	10 $\mu$ rad rms transverse		
Height error			
<b>Surface micro-roughness</b>			
Mid-spatial	0.3 nm		
High-spatial			
Max. absorbed heat in operation	negligible		
Max. Generated stress	Depends on the dimension of the substrate		

### 5.6.2 High-resolution monochromator

The approach of beamline APS 1-ID is followed for achieving higher energy resolution (11). The high resolution requires a low-energy band-pass, typically  $2 \times 10^{-4}$ . This cannot be achieved with a monochromator in the Laue geometry exposed to a large heat load. The current proposal is to accommodate a channel-cut monochromator in hutch C, which can be translated in and out of the beam. The large-bandwidth double-Laue monochromator (in the FOE hutch A) is combined with the high-resolution monochromator (in hutch C). Owing to the small (a few microradians) vertical angular acceptance of the high-resolution DCM system, the beam divergence needs to be reduced by tuning the collimating optics (VFM) between the two monochromators.

### 5.6.3 Secondary focusing optics

The horizontal radiation fan is 1.1 mrad wide. Focusing the x-rays is thus crucial to collect the large fan in order to increase the available flux at the sample. The DOE review committee in June 2009 strongly recommended to “*include secondary optics into the design of the XPD beamline to provide 1-2micrometer focus.*” The DOE committee underlines: “*Adding such optics should not have a significant impact on the beamline design while greatly broadening the user base for experiments that can be performed at the beamline. One example is the use of high-pressure cells.*” We are therefore considering the ability to tune the beam size, in particular to resolve some particular inhomogeneities or for diffraction mapping. This goal should be achievable by combining the sagittally bent double-Laue monochromator with secondary focusing optics in hutch D. The expectation is to deliver a 10  $\mu\text{m}$  focused beam for the mature scope of the XPD project; this would be exceptional at these energies, and particularly suited for heterogeneous compounds. Modeling and x-ray tracing have not been attempted yet to test the focusing capability of such a set-up.

## 6. BEAMLINE PERFORMANCE

### 6.1 Beamline ray-tracing

The beamline ray-tracing was performed for the high-flux mode as well as for the high  $2\theta$  resolution mode using the SHADOW code (26) with the visual user interface (VUI 1.08) in the XOP2.3 package (27). Section 4.3 presents the different operation modes. Calculations include three terms: (1) the source, (2) the DLM and (3) the focusing mirror.

#### 6.1.1 The source contribution

The damping wiggler source profiles are simulated and agree with the SRW results (Fig. 6-1). After the Front End fixed aperture mask (appendix A), the horizontal beam position profile is almost flat while the vertical position profile remains Gaussian with truncated tails. The beam size at the first Laue crystal (31.84 m) from the source is  $35 \times 4.8 \text{ mm}^2$ .

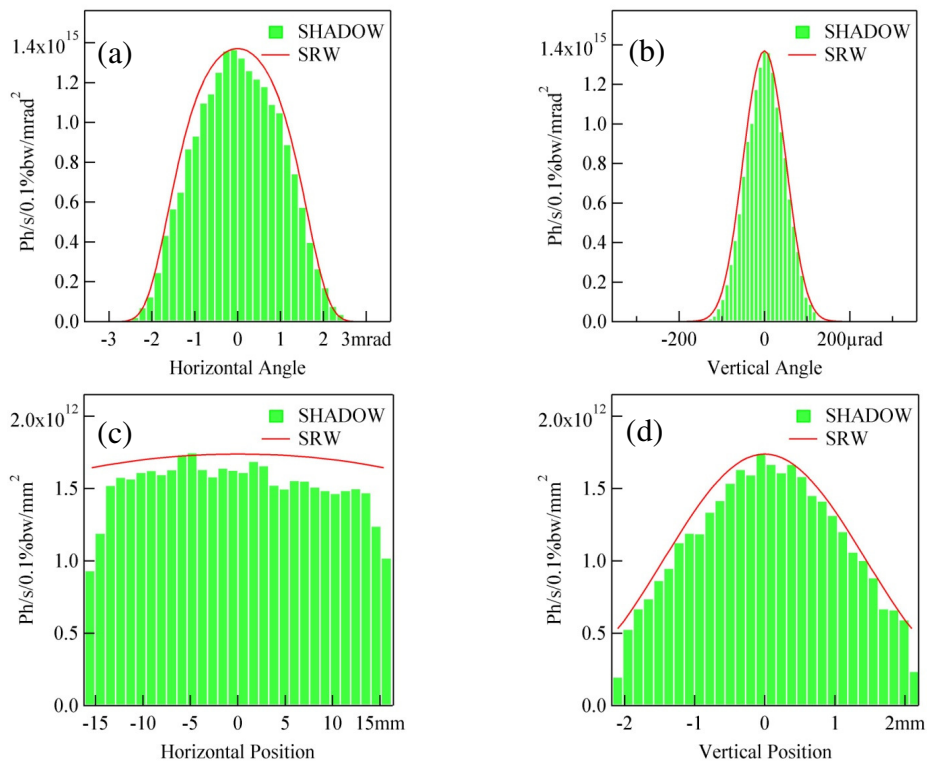


**Fig. 6-1:** Comparison of the horizontal (a and c) and vertical (b and d) angle and position profiles at 50 keV before (a and b) and after (c and d) the front end fixed aperture mask as calculated with SHADOW and SRW. The position profiles are calculated at 28 m from the source.

#### 6.1.2 The DLM contribution

The DLM crystals are 0.5mm-thick Si(100) crystals. The asymmetry angle of the (111) reflection is  $35.3^\circ$  and the sagittal bending axis is in the [011] direction. The meridional bending radii ( $R_m$ ) are extrapolated from the measured  $R_s$ - $R_m$  curve of a 3-in.  $\times$  2-in. crystal on a test bender made at the NSLS (appendix E for details).

The sagittally bent Laue crystal suffers severe lattice distortion and therefore provides a large energy bandwidth. The total deviation ( $\Delta\theta_D$ ) from the Bragg condition resulting from the lattice distortion contains two terms: (1) the change of the lattice orientation through the crystal thickness, and (2) the angle change due to the lattice spacing

variation. The total deviation is directly proportional to the crystal thickness ( $T_0$ ) and inversely proportional to the sagittal bending radius ( $R_s$ ) (appendix D for details). Fig. 6-2 presents the rocking curves calculated using the multi-lamellar approximation (28).

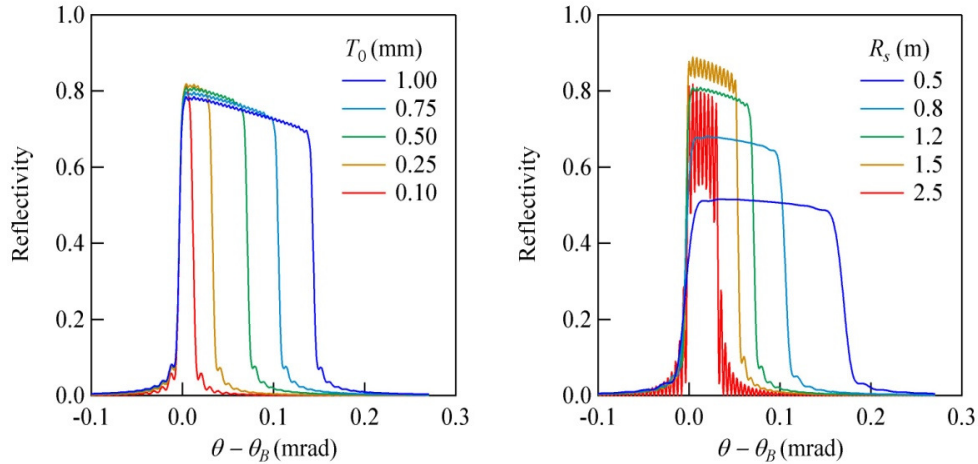


**Fig. 6-2:** The rocking curves of the sagittally bent Laue crystals at different thicknesses and bending radii.

To include these effects, the DLM was ray traced using SHADOW by dividing the bent Laue crystal into  $n$  thin layers. The Bragg plane in each layer is tilted by an angle relative to the Bragg planes in its neighbor layers, that is, the asymmetry angle varies from one layer to the next (Fig. 6-3). The reflectivity and transmission of each layer can be calculated from the dynamical theory, and the overall reflectivity of a crystal consisting of  $n$  layers is then

$$R = \sum_{i=1}^n \left( R_i \prod_{j=1}^{i-1} T_j e^{-\mu S_j} \right),$$

where  $R_i$  is the reflectivity of the  $i$ th layer,  $T_j$  is the transmission of the  $j$ th layer before the  $i$ th layer,  $\mu$  is the linear absorption coefficient, and  $S_j$  is the path length of the reflected beam. In this work, the reflectivity and transmission of each layer is simulated using SHADOW. The thickness of the layer is chosen so that the tilt angle ( $\Delta\theta_D/n$ ) between two sequential layers equals the Darwin width of the perfect crystal.

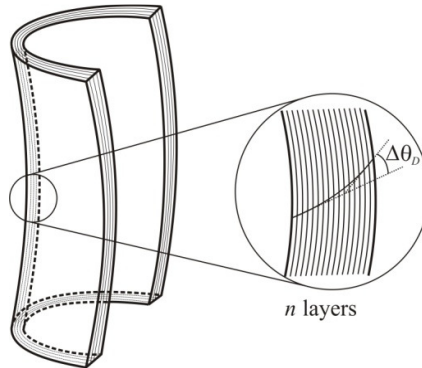


**Fig. 6-3:** The multi-layer treatment of the sagittally bent crystal.

### 6.1.3 The mirror contribution

The mirror slope error was incorporated using measured mirror profiles provided by a manufacturer. The modeling uses three mirror surfaces (as measured) whose rms slope errors are 1.27, 2.88, and 5.11  $\mu$ rad, respectively. The

grazing incident angles at different energies were optimized using XOP2.3 to ensure 90% reflectivity while assuming 0.2 nm roughness. The ray tracing does not reveal any significant difference between cylindrical bending and elliptical (or parabolic) bending due to the modest magnification factor  $F_2/F_1 \approx 0.7$ .

#### 6.1.4 Predictions of flux, resolution and beam size

Table 6-1 lists the SHADOW ray-tracing results for the XPD beamline in both the high-flux mode and the high-resolution mode. The total fluxes at the sample were calculated using

$$I = I_0 N_r \Delta E_i / N_i / E / 0.1\%$$

where  $I_0$  is the total incident flux (ph/s/0.1%BW) after the aperture,  $N_i$  is the number of the incoming rays,  $N_r$  is the number of the reflected rays recorded by SHADOW,  $\Delta E_i$  is the input photon energy bandwidth over which the ray tracing was performed, and  $E$  is the central photon energy. The output energy bandwidth is  $\Delta E$ .

**Table 6-1:** SHADOW ray tracing results for the XPD beamline.

$E$ (keV)	70	60	50	40	30
$\theta_B$ (°)	1.62	1.89	2.27	2.83	3.78
$F_1$ (m) (source to the first crystal)	31.84	31.84	31.84	31.84	31.84
$F_2$ (m) (first crystal to the sample)	22.56	22.56	22.56	22.56	22.56
$D$ (m) (between the two crystals)	0.88	0.76	0.63	0.50	0.38
$R_{s1}, R_{s2}$ (m)	0.84	0.99	1.19	1.49	1.99
$R_{m1}, R_{m2}$ (m)	23.6	24.2	25.4	27.7	31.8
Flux after aperture <sup>1</sup> (ph/s/0.1%BW)	$3.2 \times 10^{13}$	$7.2 \times 10^{13}$	$1.6 \times 10^{14}$	$3.4 \times 10^{14}$	$7.0 \times 10^{14}$
Transmission (filtering <sup>2</sup> )	50%	45%	37%	23%	7%
Mirror Grazing angle, $\theta_g$ (mrad)	1.14	1.32	1.52	1.75	2
Mirror reflectivity	90%	90%	90%	90%	90%
Mirror slope error ( $\mu$ rad)	1.27	1.27	1.27	1.27	1.27
<b>High-flux mode</b>					
Mirror radius (m)	18493	15971	13870	12047	10541
$\Delta E/E$ (FWHM)	$2.2 \times 10^{-3}$	$1.3 \times 10^{-3}$	$0.9 \times 10^{-3}$	$0.6 \times 10^{-3}$	$0.4 \times 10^{-3}$
beam size (FWHM) (mm <sup>2</sup> )	$0.75 \times 0.054$	$0.75 \times 0.053$	$0.75 \times 0.056$	$0.70 \times 0.070$	$0.63 \times 0.095$
Flux at sample (ph/s)	$2.1 \times 10^{12}$	$4.6 \times 10^{12}$	$7.8 \times 10^{12}$	$7.6 \times 10^{12}$	$3.3 \times 10^{12}$
Intensity at sample (ph/s/mm <sup>2</sup> )	$5.3 \times 10^{13}$	$1.1 \times 10^{14}$	$1.9 \times 10^{14}$	$1.6 \times 10^{14}$	$5.5 \times 10^{13}$
<b>High-resolution mode</b>					
Mirror radius (m)	70351	60758	52763	45828	40100
$\Delta E/E$ (FWHM)	$1.6 \times 10^{-4}$	$1.2 \times 10^{-4}$	$1.3 \times 10^{-4}$	$1.4 \times 10^{-4}$	$1.7 \times 10^{-4}$
beam size (FWHM) (mm <sup>2</sup> )	$0.51 \times 1.2$	$0.60 \times 1.3$	$0.53 \times 1.4$	$0.45 \times 1.5$	$0.57 \times 1.6$
Flux at sample (ph/s)	$1.5 \times 10^{11}$	$4.4 \times 10^{11}$	$1.2 \times 10^{12}$	$1.7 \times 10^{12}$	$1.3 \times 10^{12}$
Intensity at sample (ph/s/mm <sup>2</sup> )	$2.5 \times 10^{11}$	$5.7 \times 10^{11}$	$1.6 \times 10^{12}$	$2.5 \times 10^{12}$	$1.4 \times 10^{12}$

<sup>1</sup> The fixed mask apertures the beam down to 1.1 mrad  $\times$  0.15 mrad.

<sup>2</sup> The filter setup is based on section 5.4.

The sagittal bending radii ( $R_{s1}$  and  $R_{s2}$ ) of the two crystals are determined by the source to DLM distance ( $F_1$ ), the DLM to sample distance ( $F_2$ ) and the asymmetry angle. Ideally, the anticlastic bending radii ( $R_{m1}$  and  $R_{m2}$ ) of both crystals are the same for the same crystal shape and size. However, they also depend on the bending mechanism, the bender manufacturing error, and most importantly, the heat load. Since the first crystal sees the white beam and

operates under extreme cooling (liquid  $N_2$ ), the resulting  $R_{m1}$  might vary from that of the second crystal. This second crystal receives much less power under the monochromatic beam.

Fig. 6-4 shows the relative output flux and resolution at 50 keV with different  $R_{m1}$  and  $R_{m2}$  combinations keeping  $R_{s1}$  and  $R_{s2}$  constant. Note that the rocking curve width of the sagittally bent crystal is predominantly dependent on  $R_s$ , while affected by  $R_m$  through the ratio  $R_s/R_m$  (appendix D for details). If  $R_m$  is larger or smaller than the natural value (intrinsic  $R_m \sim 19$  m for  $R_s = 1.2$  m with the Poisson's ratio,  $\nu = 0.064$  for a free standing crystal), it actually indicates that the crystal is under additional stress (e.g., from the bender and the heat load), and therefore the crystal exhibits a larger lattice distortion, and hence a higher flux due to a wider rocking curve. More importantly, Fig. 6-4a suggests that the matching of the two crystals (along the diagonal in Fig. 6-4a) is essential to ensure high flux.

On the other hand, the high resolution requires that at least one crystal has the desired meridional bending radius (25 m as shown in Fig. 6-4b, as an example). Note that this optimized  $R_m$  does not exactly match the Rowland condition (i.e., 40 m in the example case). This will be discussed in section 6.2. As a result, the optimized flux per energy bandwidth is then achieved when both conditions are considered ( $R_{m1} = R_{m2} = 29$  m). This optimized condition will provide the highest flux in the high-resolution mode, in which the HRM confines the energy bandwidth. Fig. 6-4c also indicates that the tolerance on  $R_m$  is quite large.

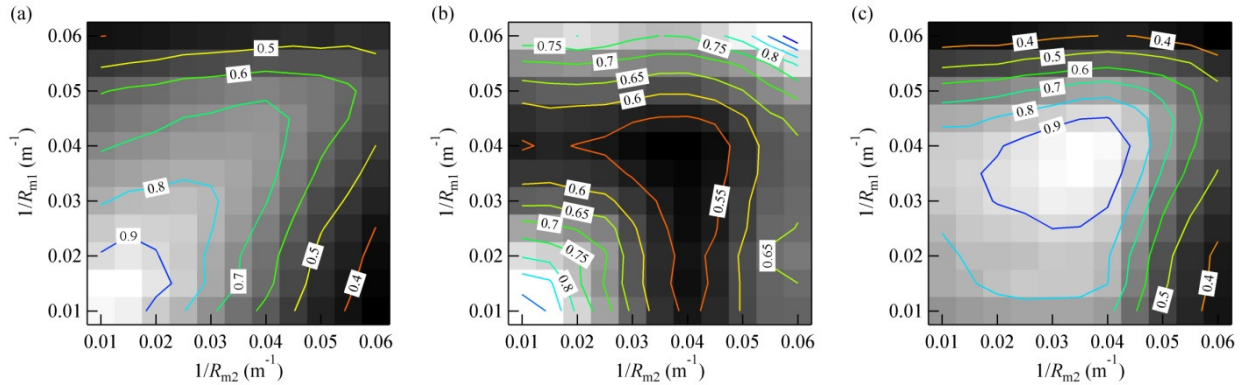


**Fig. 6-4:** The relative output flux (a), the energy bandwidth (b) and the flux per energy bandwidth as a function of the meridional bending radii of the two Laue crystals in the high-flux mode. The numbers are normalized.

The slope error of the Pt-coated mirror affects the beamline performances by: (1) increasing the beam size in the high-flux mode (Table 6-2), and (2) enlarging the energy bandwidth in the high-resolution mode (Table 6-3). To achieve the ideal output, a slope error less than  $1.2 \mu\text{rad}$  is required (Fig. 6-5 for the comparison).

**Table 6-2:** Vertical beam sizes at different mirror slope errors in the high-flux mode.

Slope error ( $\mu\text{rad}$ )	Vertical beam size FWHM (rms) $\mu\text{m}$		
	70 keV	50 keV	30 keV
0	43 (53)	46 (39)	89 (141)
1.27	54 (56)	56 (42)	96 (143)
2.88	206 (87)	211 (77)	225 (157)
5.11	321 (131)	314 (79)	290 (184)

**Table 6-3:** Energy resolutions at different mirror slope errors in the high-resolution mode.

Slope error ( $\mu\text{rad}$ )	$\Delta E/E$ (FWHM) ( $10^{-4}$ )		
	70 keV	50 keV	30 keV
0	1.2	1.3	1.6
1.27	1.6	1.3	1.7
2.88	5.1	3.3	2.8
5.11	7.7	4.4	2.1

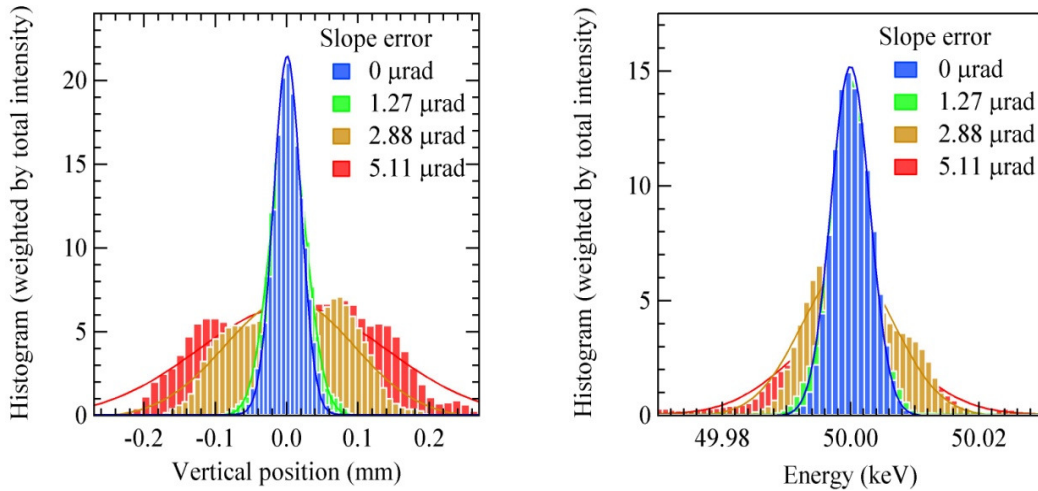


**Fig. 6-5:** The simulated vertical profiles (left) in the high-flux mode and the energy profile (right) in the high-resolution mode with different mirror slope errors.

## 6.2 Instrumental resolution function

The peak shape function of the XPD data depends on the instrumental resolution function (IRF) and the sample microstructure (grain size and strain). Therefore, the accurate description of the IRF is extremely important for characterizing the XPD beamline. Sabine (29) generalized the analytical solutions of the instrumental diffraction line broadening of the  $N$ -crystal spectrometer by assuming the Gaussian angular distribution of the incident beam and Gaussian shape profiles for each optical element. More recently, Gozzo et al. (30) extended Sabine’s theory to include the collimating and focusing mirrors. Here, we further extend this analytical method to study the IRF width of the XPD beamline within the different operation modes.

The diffraction profile of the XPD beamline high flux setup is a convolution of the incident beam profile, the Laue crystal monochromator rocking curve, the slit function, the residual divergence after the focusing mirror, and the profile of the analyzer crystal on the detector arm, with  $\alpha_m, \Delta_m, \tau_s, \tau_f, \Delta_a$  as the FWHM respectively in the vertical diffraction plane. Table 6-4 lists the values of the profile FWHMs of the optics for the XPD beamline in the high-flux operation mode.

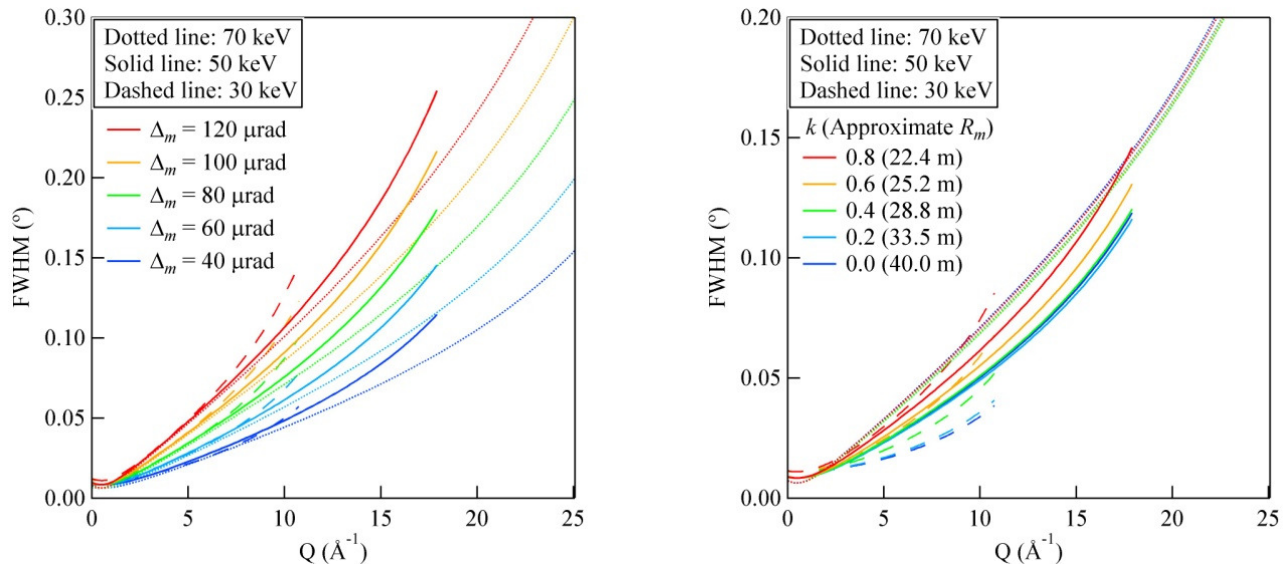
**Table 6-4:** Values of the profile FWHMs of the optics.

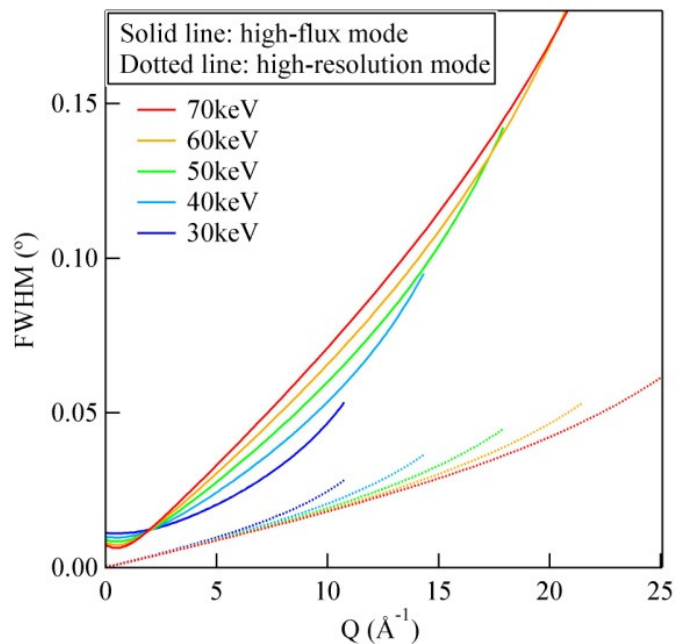
	70 keV	60 keV	50 keV	40 keV	30 keV
$\Delta_m$ ( $\mu\text{rad}$ )	80	69	58	47	36
$\tau_s$ ( $\mu\text{rad}$ )	40	46	53	61	70
$\tau_f$ ( $\mu\text{rad}$ )	112	129	149	171	196
$\Delta_a, \Delta_c$ ( $\mu\text{rad}$ )	3.9	4.6	5.5	6.9	9.3

Fig. 6-6 shows the FWHM of the IRF at different  $\Delta_m$  and  $k$ . For the sagittally bent Laue crystal,  $\Delta_m$  is normally tens of micro-radians and therefore dominates the resolution. As shown in appendix D,  $\Delta_m$  is a function of the bending radii ( $R_s, R_m$ ) and the crystal thickness  $T_0$ .  $R_s$  is determined by the monochromator position and the chosen asymmetry angle (appendix D) to achieve the horizontal focusing. The crystal thickness should be optimized to balance the resolution and the total flux. The meridional radius  $R_m$  affects the peak shape function in two respects: (1) the deviation from the Rowland condition and (2) the change of the rocking curve width,  $\Delta_m$ , through the changing of the  $R_s, R_m$  ratio. The results in Fig. 6-6 (right) are consistent with the ray-tracing results (Fig. 6-4): the optimized resolution is achieved when the two above effects are balanced. We also see that the IRF is more sensitive to  $R_m$  and  $k$  at lower energies.

To achieve the highest possible resolution, a pseudo channel-cut double-crystal monochromator (HRM) is placed after the mirror. The mirror is then used to collimate the monochromatic beam emanating from the DLM, so that the divergence  $\tau_f$  of the mirror-reflected beam matches the angular acceptance of the HRM.

Fig. 6-7 compares the resolution of the two operation modes ( $\tau_f$  is taken to be 15  $\mu\text{rad}$  for the high-resolution mode).


**Fig. 6-6:** The FWHM of the IRF at different energies with varying  $\Delta_m$  (left) and  $k$  (right) as a function of  $Q$ .



**Fig. 6-7:** The FWHM of the IRF at different energies in the high-flux mode (solid lines) and the high-resolution mode (dotted lines).

### 6.3 Day One expected performance

#### Scientific Capabilities on Day One:

- First branch and endstation C operational
- x-ray energy = 30-70 keV
- High flux at sample  $> 10^{12}$  ph/s in variable 0.5-2 mm focus
- Powder diffraction resolution:  $\Delta d/d \sim 10^{-3}$  with upgrade to  $2 \times 10^{-4}$
- Time resolved capability in the sub-second range
- Basic suite of sample environments (4-1500 K, high P)
- Flat plate and capillary geometries
- Initial PDF capabilities, with upgrade to dedicated PDF endstation B

**Table 6-5:** The basic configuration shows which components are required to start beamline operation, and which components can tolerate some delay.

Component	Section #	Day One (baseline scope)	
		Basic configuration	Optimum configuration
Safety Components	5.3.3	R	R
Beam Transport	5.3	R, <i>incl.</i> transport to hutch B (down to the exit window)	R
Diamond windows Filters	5.4.2	R	R
DLM	5.5.1	R	R
VFM	5.6.1	NR	R
Diffractionmeter	7.2	R	R
Scanning OD detectors	7.3	R	R: fitted with analyzer crystals (MA)
Strip detector	7.3.3	NR	R
2D pixel/CCD	7.3.3	R	R
2D flat panel detector	7.3.3	NR	R

R = required

NR = not required, where "*not required*" means that the beamline is ready for operation and the beam can reach the sample. This is the minimum required configuration, although the performance is affected by the missing components.

## 7. ENDSTATION INSTRUMENTATION

### 7.1 Overview of endstation C

Endstation C (Table 5-2) is 4.2 m wide  $\times$  7.0 m long and very similar to modern, highly productive stations at the ESRF, SLS, APS, ASP, etc. and will cater to a wide range of users interested in higher energies ( $> 30$  keV). The core instrument consists of a highly accurate triple-axis diffractometer (Fig. 7-1): The “inner” stage will be for sample rotation, with a capacity  $\geq 35$  kg at a distance of  $\sim 250$  mm from the interface plate; this allows the rotation of heavy samples with environmental cells where applicable. The interface plate is fitted with “spherolinders” (heavy-duty kinematic-type mountings with cylindrical rather than spherical attachments); these allow sample environments to be swapped over easily and with minimal alignment. A close/open Euler cradle and a x-y-z stage can be fitted on that circle, with appropriate sample positioning (metrology, alignment) and beam position monitoring. Opposite the diffractometer, a translating table can support larger loads such as large cryostats and furnaces and high-pressure cells. In addition, a robot for fast and automated sample changing is recommended for high-throughput measurements for combinatorial investigation and screening purposes.

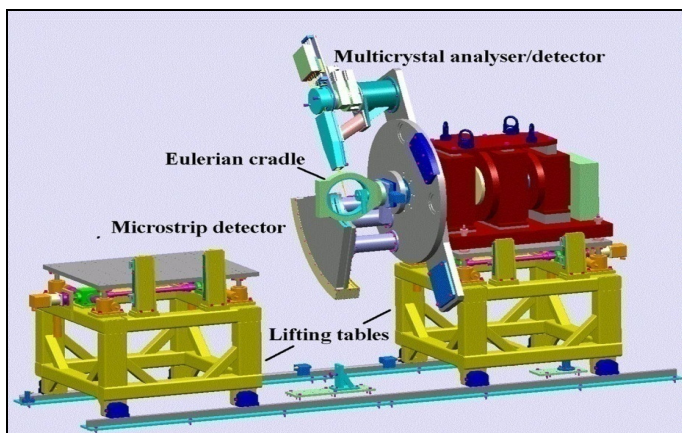


**Fig. 7-1:** Conceptual design of the NSLS-II high-energy high-resolution powder diffraction beamline. For clarity, sample environments (such as cryostats, furnaces and diamond-anvil cells) and a robotic sample changer for high-throughput applications are not included in the figure.

The second axis holds a fast read-out position-sensitive strip detector for *in situ* time-resolved studies and remains essentially fixed. The implementation of a fast position-sensitive strip-array detector allows the real-time, microsecond timescale study of phase transitions, transformations, and catalytic reactions as a function of temperature, chemical gradients, and pressure. The third axis is essentially used to hold a multi-crystal array analyzer system that can be rotated in the vertical diffraction plane, and is meant for high-resolution, high-energy studies. This arrangement proves to work satisfactorily and to cover a wide range of users’ needs on several PD endstations. In the mature scope, it can be envisaged to mount a second angle-scanning stage for scanning over the high-angle range with a medium resolution (larger angle step size and longer count time are required over the far-Q range). In this unique arrangement, both angle-scanning stages could operate simultaneously, recording complementary parts of the diffraction diagram. They run in a continuous scanning mode, replacing the usual step-by-step “move and count” mode for better efficiency (minimal overhead).

The DOE review committee of June 2009 recommended that novel detection schemes such as Ge Strip detectors and Laue Crystal Analyzers should continue to be explored. These issues are addressed in the following sections.

### 7.2 Diffractometer in endstation C

#### 7.2.1 General description

This state-of-the-art instrument is a triple-axis diffractometer with appropriate flexibility for high-resolution measurements, as well as for measurements in two dimensions of the reciprocal space or for measurements with high momentum transfers. It is designed to meet the challenging mechanical and optical specifications for producing high-quality powder diffraction data with high throughput and different detection schemes.

This diffractometer utilizes the vertical scattering plane to take full advantage of the smaller vertical divergence of the wiggler beam and to allow focusing of the broad wiggler x-ray horizontal fan without disturbing the resolution. The unit consists of three goniometer circles (tables A, B, and C) with a common horizontal axis. Each rotary table is fitted with an independent mount which takes the sample holders and detectors at varying distances to the central axis of rotation. Each axis is fitted with an angle encoder to measure the angular positions of the detectors and sample.

The rear tables B and C are connected via drive shafts which pass through the axis of the front table A. Tables B and C support the detector assemblies with proper balancing counter-weights. Table A is designed for flexible sample mounting using a range of different fixings. The sample stage must deliver sub-micron precision, and the vertical rotation must be able to function through  $>250^\circ$  without degradation of performance. The sample mount can be any of these below and more:

- a fast spinning capillary head
- a high precision translation-rotation stage
- an Eulerian cradle
- a support which attaches onto the sample cell, e.g., cryostat, furnace,...

The axis alignment should show minimal radial error and torsion. The angle accuracies and the rigidity of the tables and mounts are critical factors in the overall specification. The unit is supported by a common supporting base plate resting on the facility floor with three translations and two tilts. The complete unit is aligned with the tables (at any angle) being parallel to the beam axis. Limit switches and encoders are also required. The diffractometer must be fairly compact and the co-axial rotation of each table, in particular, must respect very stringent (sub micron) eccentricity and wobble requirements at the sample position. Moreover, the instrument is designed to carry heavy sample equipment and detectors, while maintaining high resolution and low radiation background.

The transport, on-site assembly and positioning at the XPD beamline need to be described by the vendor (including lift points). We are asking for a complete, assembled, and tested system.

## 7.2.2 Specifications

**Table 7-1:** Preliminary specifications for the diffractometer of endstation C

	Table A (sample)	Table B (detector 1)*	Table C (detector 2)#	Comments
Axis height Z (mm)				
Min		1400		see Table 4.3
Max		1550		
Beam to wall distance (mm)		1500		distance to back wall in Y direction
Motor type		Stepper/Servo		depending on speed
Concentricity (mm)		0.01		
Max. rotary table wobble (arc sec)		< 3"		
Rotation range		-50° to +200°		
Angle				
Resolution		0.2"		
Accuracy		1"		
Repeatability		±1"		
Control and motor drives		TBD		see NSLS-II specs
Encoder		yes		resolution < 0.2"
Angular Speed (°/sec)				
Min		0.1		
Max		5 (TBD)		
Gear system		yes		speed vs. resolution
Limit switch (end of run)		yes		adjustable
Zero switch (home)		yes		adjustable
Weight capacity (load) in kg	50	200	200	
Counterweight	yes	yes	yes	
Detector to axis distance (mm)	N/A	>800	>1200	radial direction
Plate to beam distance (mm)	250	TBD	TBD	distance from surface of mounting plate to diffraction plane (load offset) in Y direction.
Environmental conditions	ambient			
Floor anchoring				TBD
Supporting base plate	Range – Accuracy – repeatability in mm:			
Translation Tx (mm)	± 30			resolution = 1µm
Translation Ty (mm)	± 30			no encoder
Translation Tz (mm)	> ± 90			stepper motors
Tilt X (°)	± 1			see axis height above
Tilt Z (°)	± 1			compensate for misalignment

\* Detector 1 is likely to be a 1D PSD such as the Mythen detector: sample-to-detector distance = 760 mm.

# Detector 2 is likely to be a 2D CCD camera or a N-fold crystal-analyzer/scintillator detector.

X = along the beam; Y = perpendicular to the beam axis. Z = vertical.

## 7.3 High-energy x-ray detectors

### 7.3.1 Introduction

The two major areas of concern for applications of detectors in PD are shown in Table 7-2.

**Table 7-2:** Potential PD detector concerns.

Concern	Possible mitigation
Most diffracted photons are lost or wasted	1a. <u>Large field of view</u> (solid angle of detection): from 0-1D (now) towards 1-2D (now and future). 1b. <u>Speed</u> : fast (Hz) to ultrafast time slicing (kHz). The responsiveness of the detectors often depends on the readout schemes. An expected improvement is the multiple frame accumulation during the same data acquisition cycle (e.g., using more registers per individual pixel). 1c. <u>Detection efficiency</u> , particularly at high energy (it also helps reduce radiation damage to the sample). 1d. Handling of low and high count rates requires a <u>high dynamic range</u> and an adjustable gain (counting individual photon up to $\sim 10^{10}$ photons/s). 1e. (single photon) Sensitivity (above the noise).
Information diffracted from the sample is not fully exploited	2a. <u>Energy resolution/discrimination</u> makes it possible to separate out the inelastic and the Bragg signals. The association of spectroscopy with diffraction (anomalous, DAFS, white beam diffraction) is an asset. 2b. Improved <u>spatial (angular) resolution</u> 2c. Higher <u>uniformity and minimal spread function</u> for accurate measurements of intensities and positions: peak indexing, peak fitting for structure solution, refinement, peak profile analysis 2d. <u>Low noise</u> 2e. Photon counting with a Poisson statistics for physical interpretation of the data

1D and 2D area detectors (1a in Table 7-2) are increasingly used in PD. They can considerably improve the detection of very weak signals, and help improve the detection limit to identify intermediate steps in the synthesis or processing of a material. In materials science and solid state studies, as opposed to crystallographic and microstructural studies, time resolution (1b) takes precedence over angular resolution (2c), requiring high efficiency photon counting (1c). Fast acquisition rate is also required for applications such as diffraction imaging (31) or diffraction tomography (32). Energy discrimination (2a) is also useful in those high-energy measurements where the inelastic (Compton) background could be screened out electronically (e.g., the energy resolution of CdZnTe is 1.9 keV at 60 keV), and the signal-to-background ratio improved. Better statistics can thus be achieved in the high-Q range. Evidently, the trade-off has often been between diffraction image quality and speed, since high-resolution, high-contrast systems usually require longer read-out times.

The next section, 7.3.2, reflects our current views and thinking on the detector needs for XPD. Section 7.3.3 reviews the current options, notwithstanding that the performance of the detectors is likely to change in three years' time.

### 7.3.2 High energy detector efficiency challenge

The detection ( $\sim$ absorption) efficiency at 100 keV of Si 0.5 mm, Ge 0.5 mm and Ge 1 mm is 2%, 14% and 25%, respectively (Fig. 7-2). This drastically limits the efficiency of Si-based detector technology for high-energy x-rays, thus impacting a large part of material science experiments and hard X-ray imaging. An increased thickness of silicon is impaired by the parallax error, a degraded lateral spatial resolution and a high depletion voltage. The higher mobility of carriers combined with the low effective mass in Ge, when compared to Si, have generated a lot of interest in Ge-based devices. The challenge is to have a robust barrier oxide, since native Ge oxide is hygroscopic. Cooling is also an issue. Current technology used for making germanium-based solid-state sensors is not yet amenable to making monolithic planar segmented devices such as microstrip detectors. If materials engineering is successful in the coming years, **a 10-fold increase in detector efficiency at 60 keV could be**

**expected!** Other alternatives for semiconductor sensors currently under investigation include: GaAs, CdTe or CdZnTe, n/p Ge, ZrO<sub>2</sub> and HfO<sub>2</sub> on Ge. High-Z scintillating screens from YAG:Ce to LAG:Eu are also being explored.

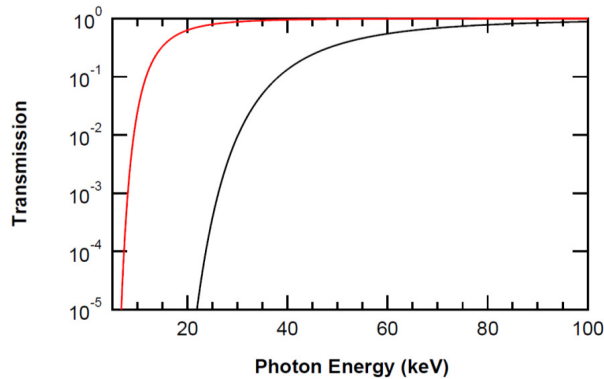


**Fig. 7-2:** Transmission efficiency of 250µm Si and Ge as a function of x-ray energy.

### 7.3.3 Detector strategy

#### 7.3.3.1 Point detectors

**Table 7-3:** Impact of point detectors on the science and operation of XPD.

Detector option	Detector config.	Operation	Application	Performance	Base scope	Mature scope
1 point detector	-YAG:Ce or YAP:Ce -resolution slits	step-by-step scan (stop-and-count mode)	- crystallography - microstructure	- low efficiency - high resolution - no E discrimination	no	no
N parallel point detectors	-LAG:Eu scintillators - resolution slits	fly scan	- strain -lattice defects	-high count/sec=1.5 MHz	yes	
	Si or Ge MA			-low background	TBD	TBD

The point detector with a high-resolution slit or an analyzer crystal suffers from the first drawback described in the introduction in Table 7-2: “most photons are lost or wasted.” This has been mitigated in several PD stations with the multi-analyzer (MA) geometry, as described in section 7.4. The MA configuration works well for several instruments below 35 keV. Given the source and optics characteristics of XPD, we believe we cannot compete with the resolving capability of the existing machines, except for those cases where structure solving requires intensities at a higher accuracy which can be better achieved using the high-energy, transmission diffraction mode. In addition, XPD can operate in the high-resolution MA mode only at the cost of an additional high-resolution monochromator in the beamline. Section 6.2 shows the net advantage of the VFM-HRM-MA configuration for high resolution operation.

However, thanks to its angle and energy selectivity, the analyzer crystal may still be needed, as it remains superior to a 1D PSD or a slit/counter assembly in presence of:

- inelastic scattering (fluorescence, Compton) (energy error)
- large sample size, sample displacement or sample transparency (angle error)
- parasitic signal not originating from the sample (angle and/or energy error)
- high background (at the detriment of the quality of the PDF pattern over the high-Q region)

We are also looking into an alternative solution which consists of **collecting the diffracted beams over the entire horizontal fan**, by placing appropriate horizontal separators.

### 7.3.3.2 1D detectors

XPD requirements:

- high diffraction angle coverage ( $\geq 50^\circ$ , customized with the number of modules)
- intrinsic high angle resolution  $\leq 0.01^\circ 2\theta$ , low spread function
- high dynamic range ( $>10^5$ ), high count rate
- high acquisition rate ( $<0.1$ s over  $40^\circ$ ), short readout time
- low noise
- shutterless operation
- adjustable threshold to suppress fluorescence
- compact, no cooling, radiation resistant

**Table 7-4:** Impact of linear position sensitive detectors on the science and operation of XPD.

Detector option	Operation	Application	Performance	Base scope	Mature scope
Si sensor	Fixed on diffractometer circle	-structure	-fair resolution -fast	Yes (R&D or commercial)	
high-Z sensor, e.g., Ge		-kinetics	-higher efficiency	no	Yes (R&D)

With the advent of photon-counting silicon microstrip detector arrays (33), it becomes possible to achieve a resolution approaching that of an analyzer crystal set-up when used in Guinier geometry. A  $50\mu\text{m}$  strip at a radius of 760 mm corresponds to a  $0.004^\circ 2\theta$  (Mythen) resolution for a small sample in transmission (34). The quality of the data (in terms of FWHM, peak profile, S/N) progressively approaches that of “traditional” high-resolution point detectors with the additional advantage of large angle detection and fast acquisition.

**The design of an energy resolving wide-angle photon counting Ge strip detector** (~11 individual modules tiled to provide the necessary angular  $100^\circ$  coverage, 250  $\mu\text{radian}$  resolution on 0.5 m radius, cryogenic cooling) with good efficiency at around 75 keV, would have a very substantial impact on the beamline performance.

### 7.3.3.3 2D detectors

XPD requirements:

- high solid angle of detection (customized with the number of modules)
- low spread function
- high dynamic range, high count rate
- high acquisition rate, short readout time
- low noise
- shutterless operation
- adjustable threshold to suppress fluorescence
- radiation resistant

**Table 7-5:** Impact of area detectors on the science and operation of XPD.

Detector option	Detector config.	Operation	Application	performance	Base scope	Mature scope
IP				-low read-out	no	no
CCD/scintillator	- dynamic* - noise	Fixed on diffractometer circle or optical table	- Materials Science - 2D diffraction - imaging - texture	-compact -fast -well proven	yes	no
CMOS	- pixel size - solid angle - frame rate			-high frame rate -noise -large active area	yes	
PAD				-E discrimination -photon counting -small active area	no	yes

At high energy, a fixed 2D detector can capture a significant part of the diffraction signal and the detector plane is rather close to the Ewald sphere. The angular resolution is easily controlled in the conventional capillary sample transmission Debye geometry, given the sample size, the sample-to-detector distance, and the beam divergence. Averaging over a large solid angle diminishes the coarse grain and preferred orientation effects and provides high statistical accuracy. The sample might not necessarily be spinning since the scattering volume probed along the azimuthal direction is equivalent to that probed with a point detector. This is an important advantage for in situ work using stationary sample environments.

The effect of axial divergence (diffraction line asymmetry at low angles) is removed. The much smaller active area of a CCD or a pixel detector can readily be compensated, if needed, by scanning the detector with the 2θ arm of the diffractometer. Corrections such as inclined beam incidence and polarization variation for the whole detector plane can be taken into account. The proof of principle was recently shown at HASYLAB with a MAR CCD (2048 x 2048 pixels) detector (35). As shown in this work, data of sufficient quality for Rietveld refinement can probably be obtained.

Placing the detector behind a set of horizontal slits and using the Frame Transfer Mode also bridges the gap between the 1D and 2D detection schemes. For these reasons, **XPD places its priority on the 2D detectors**. A high-resolution pixel detector and a fast-frame camera adequately cover the needs of XPD in the baseline scope. More elaborate detector strategies can easily be implemented in the mature scope. See more in appendix H.

### 7.4 High-resolution analyzer stage

The most advanced powder diffraction machines now provide instrumental peak widths (FWHM) as low as <5 milli-degrees in the 10-30 keV energy range, thus allowing accurate peak profile measurements and minimizing the peak overlap effect. The former is essential for the study of strain, microstructure and lattice defects. The latter is required for peak indexing and peak intensity extraction (using the Le Bail approach) in structure solution.

The high-resolution operation is achieved using a bank of *N* analyzer crystals on the diffracted beam paths. All existing designs rely on the concept developed at the ESRF by J-L. Hodeau et al. (36) and use Bragg crystals. Scintillator-based crystal analyzer detectors deliver resolution below 0.005° 2θ and are the state of the art in high-resolution powder diffraction. The Multi-Analyzer (MA) array enhances the quality of the diffraction data, through suppression of the fluorescence and Compton components (including diffuse scattering). MA systems already are implemented at many PD beamlines:

- SLS (MS) *N*=5 where *N* is the number of channels.

- ESRF (ID31)  $N=9$  (36)
- APS (11BM)  $N=12$
- ALBA  $N=13$
- SOLEIL (CRISTAL)  $N=21$
- DIAMOND (I11)  $N=45$  (5 banks of 9) (37)

but all operate below 40 keV. P02 at PETRA III will be using a 10-channels MA system at 60 keV.

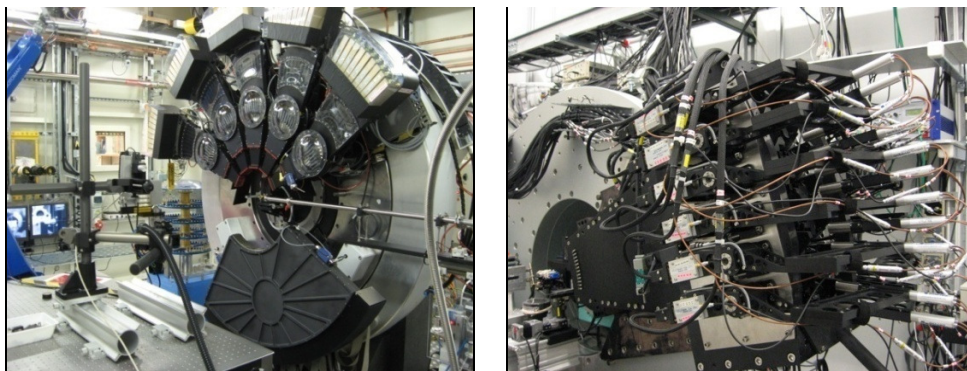


**Fig. 7-3:** (left) MA system at I11 Diamond, courtesy of C.C. Tang. (right) MA system at 11-BM APS, courtesy of B. Toby and M. Suchomel.

High-energy diffraction imposes very shallow Bragg angles (extended footprint of the impinging beam on the analyzer crystals) and higher shielding and collimating for reducing the cross-talk and noise level. Given the limitations of the existing MA concept at energies  $> 40$  keV, several options/designs are being looked at for XPD:

- a) Using smaller  $d$  reflections: Si(220) or Ge(111)

X-ray tracing is planned, with the view of keeping the design compact and lightweight.

- b) Using Laue crystals:

Low Bragg angles at short working wavelengths make it less suitable to use an array of parallel post-sample crystals in the reflection geometry. Moreover, any energy change may cause important drift of the sample-diffracted beam impact point over the surface of each analyzer crystal, making the alignment extremely difficult. The analyzer stage might work better in the transmission geometry using Laue crystals. To the best of our knowledge, such a design does not exist yet. A solution is proposed by Siddons et al. (38) as a relatively simple 16-element crystal analyzer based on a single monolithic piece of Si (Fig. 7-4), elastically bent in a pseudo-Rowland circle geometry and combined with a compact 16-channel pulse-counting detector. This detector could be a custom multi-element germanium or CdZnTe detector, made in-house by the NSLS Detector Development Group. The main difficulty we are now anticipating is the separation of the multi-beams transmitted and diffracted through the analyzer.

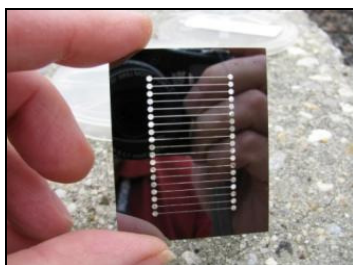


**Fig. 7-4:** The Laue crystal array from (38).

The rectangular slats in the center of the crystal are the diffracting elements. The wide side plates are the elastically deforming part. The crystal is clamped at top and bottom, and a bending moment applied to curve the object into a segmented cylinder. The strain induced by the bending is isolated from the diffracting elements by the small cross section of the connecting fillets.

We think it more appropriate to investigate alternative options rather than to duplicate the Bragg MA system which excels at lower energies with a parallel incident x-ray beam.

## 7.5 Sample environments

Considerable efforts will be expended to ensure that a wide range of sample environments are made available to the user community. The access and facilities are designed to allow very flexible setups with reasonably easy changeover of experiments. A variety of sample environments (not shown) are included in the budget, consisting of cryostats, furnaces, laser heating and diamond-anvil cells for high-pressure research. The importance of sample environments is emphasized. Transferability of sample environments between beamlines will greatly enhance the experimental capabilities. Part of this effort could be led by a centralized sample environment group, which standardizes mounts and controls and develops new sample environments. A typical suite of ancillary equipment on modern powder diffraction instruments includes:

- capillary furnace ( $T = 300 - 1700\text{K}$ )
- flat plate furnace, ( $T=300 - 2000\text{K}$ )
- Humidity chamber ( $-5^{\circ}\text{C}$  up to  $75^{\circ}\text{C}$  dew-point,  $T= 25 - 90^{\circ}\text{C}$ )
- Hot air blower ( $T = \text{RT}-1300\text{K}$ )
- He Cryostat ( $T = 11 - 300\text{K}$ )
- cryostat ( $T= 4 -300\text{K}$ )
- Cryosystem 700+ cryostream ( $T = 80 - 500\text{K}$ )

This suite of sample cells will progressively be extended to multiple extreme environments, such as high fields and/or pressures, extreme temperatures, facilities for reactive samples and user-custom devices.

- mechanical stress: in situ multi-axial stress apparatus, shock waves
- in situ very high temperatures (mirror furnace or laser heating:  $2500\text{ K}$ ) with controlled atmosphere (inert/corrosive/oxidizing – static or flowing)
- gas cycling to 10-100 bar (e.g., in Pt capillary)
- low temperatures
- high pressures (1 Mbar)
- applied E/B field
- light excitation
- electrochemical cells

Extreme conditions (300 bar,  $300^{\circ}\text{C}$ , pH 3, brine) and the use of toxic/reactive/flammable/explosive gases (hydrocarbons,  $\text{H}_2$ ,  $\text{CO}$ ,  $\text{O}_2$ ,  $\text{NO}_x$ ,  $\text{H}_2\text{S}$ ,  $\text{SO}_2$ ,  $\text{CH}_4$ , ...) are part of the scope of XPD: the hazards and risks were reviewed and discussed at the latest safety review.

A class IV IR laser will be used for high-pressure laser heating of samples contained in diamond anvil cells (power  $\approx 100\text{W/pulse}$ ; interlocked with the hutch door). See BNL Standard Operating Procedure<sup>13</sup>.

To support modularity, rapid interchange of sample environments, and future upgrades, instrument interfaces and software will be carefully designed and specified. The scattering from sample environments often compromises the data quality in experiments at non ambient conditions. Tight collimation and/or small focus are necessary to minimize or totally exclude parasitic scattering from the sample environment.

---

<sup>13</sup> [https://sbms.bnl.gov/sbmsearch/subjarea/113/113\\_SA.cfm?parentID=113](https://sbms.bnl.gov/sbmsearch/subjarea/113/113_SA.cfm?parentID=113)

## 7.6 Endstations B and D

Hutch D (Table 5-2) is intended for special sample environments and long setups. It covers as much as the existing floor allows, i.e.,  $4.2 \times 8 \text{ m}^2$ , and is accessed through two doors on opposite sides (see section 5.2 on enclosures). The access and facilities are designed to allow very flexible setups with reasonable ease for experiments changeovers.

For easy configuration changes, we are considering the use of “towers” guided on optical rails: sample tower, detector tower, optics tower. The optics tower holds filters, slits, shutter, laser, collimator,.... The user specific setup can be accommodated on the top of a heavy-duty (200 kg) Huber table (rotations, translations X and Y, coarse and fine Z), supported on a granite base plate and motorized on rails. This concept is implemented at different beamlines, e.g., at the APS (39) as shown in Fig. 7-5 or at DORIS (40).

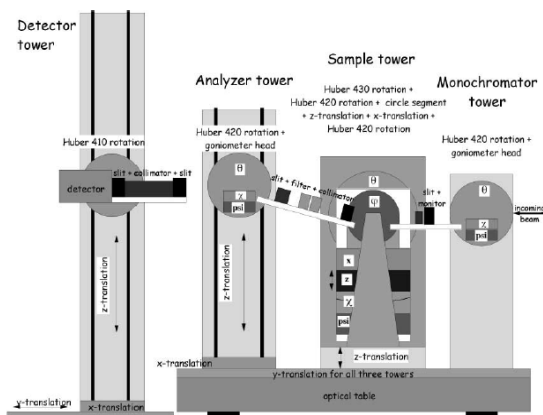
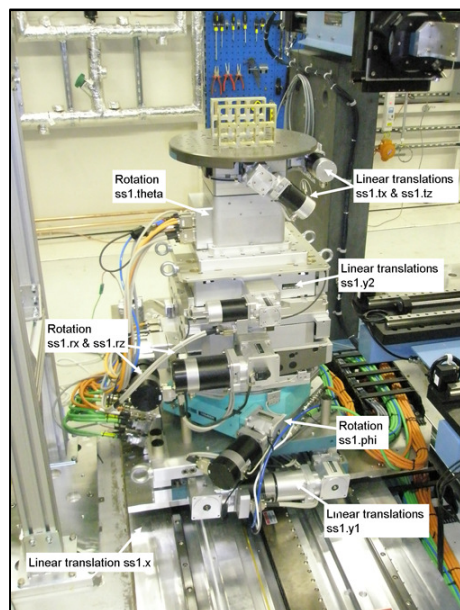


**Fig. 7-5:** The concept of modular towers supporting different parts of the experimental set-up is illustrated.

- a) from (39). The monochromator can be replaced by the secondary focusing optics. The analyzer tower is not required in hutch D.



- b) Sample tower at beamline I12, Diamond Light Source.  
Courtesy: M. Drakopoulos.

Hutch D could be partially populated by existing NSLS equipment and will be able to accommodate a variety of users’ designed chambers and cells using heavy-duty supports and a crane. We anticipate such a facility would also be in high demand at NSLS-II. In the mature scope, a graded bendable multilayer system or a 2D focusing CRL may be used to focus the beam to  $\sim 10$  microns for studying small samples (e.g., for high-pressure diamond-anvil cell research). This focusing optics is located relatively close to the sample position to minimize beam motion.

Local and nanostructure studies are often referred to by the method's name, pair distribution function analysis (PDF), or total scattering, which refers to the fact that all the scattering (Bragg and diffuse) is utilized. Hard x-rays are well suited to PDF studies of nanostructures in particular (e.g., see workshop “Nanoscale Diffraction of Materials” at the NSLS Users Meeting 2010<sup>14</sup>). Current approaches for studying nanostructure utilize the PDF method combined with full profile fitting structural modeling. Efforts are underway to incorporate information from complementary methods (anomalous diffraction, EXAFS, x-ray and neutron data, NMR, IR, quantum chemistry, etc.) in a rational way when the problem is under-constrained. A recent breakthrough was the first demonstration of ab initio structure solution of a nanoparticle from PDF data. However, a substantial effort is required to develop these tools to bring them to the level of confidence enjoyed by crystallographic methods. Beyond the present baseline proposal, we are considering combining the structural Q-dependent measurement with a space-resolved probe. Recently, it was shown how diffraction and the tomographic method could be combined for 3D phase imaging (32). The PDF work can be accommodated in hutch B; its instrumentation is not in the scope of the present project.

Station B (Table 5-2) is  $4.2 \times 5.5 \text{ m}^2$ . The concept for this station is based on APS beamline 11-ID-B and NSLS beamline X17A, which feature a single horizontal bounce design. A thin bent silicon crystal in the Laue geometry will kick the beam sideways and simultaneously provide horizontal focusing (section 5.5.2). This comes at the expense of bandwidth, although this will not be an issue, as 0.1% energy bandwidth is sufficient for PDF studies. The usable energies are: 39.1, 63.8, and 74.8 keV.

## 7.7 Beamline and motion controls

See appendix B.5 for more detail.

## 7.8 Beamline software

The practicalities of standardization of user interface software, data formats, visualization, analysis, backup and retention policy were recently discussed during a workshop at NSLS-II<sup>15</sup>.

User functionalities	proposal submission, peer review, experiment management, user training, safety,...
Experiment data management	<i>incl.</i> automatic sample tracking
Automation	<ul style="list-style-type: none"> <li>- beamline general automation and I/O control (ID, FE, vacuum, motors, PSS, beam monitoring,...)</li> <li>- optics alignment &amp; diagnostics</li> <li>- sample handling (<i>incl.</i> robotic sample changer), centering (using video input and/or diffraction)</li> <li>- video survey of the experiment and entire hutch</li> <li>- detector control and interface software, detector operations e.g., continuous scan, on-the-fly read</li> <li>- user macros, automated metadata capture (“log book”), remote beamline access and control (on-site, off-site, collaborative work)</li> </ul>
Data acquisition	<ul style="list-style-type: none"> <li>- data transfer link</li> <li>- data writing management (speed, allocation, format...)</li> <li>- data archiving/retrieval and metadata</li> <li>- parametric data (vs. external parameters <math>l_0</math>, <math>p</math>, <math>T</math>, time, ...)</li> </ul>
Data/image-processing	<ul style="list-style-type: none"> <li>- create &amp; process ROIs</li> <li>- integration on 2D images, binning, statistics, correct bad pixels or flat field,...</li> <li>- real-time processing of data (not running over the EPICS channels)</li> <li>- smart file saving, e.g., every 1,000 images, reject images on various criteria (temperature, <math>l_0</math>)</li> <li>- representations of dynamical processes as 2D or 3D movies</li> </ul>
On-line data analysis	<ul style="list-style-type: none"> <li>- on-line quick data assessment for rapid evaluation</li> <li>- feedback loop allowing experiments to evolve guided by preliminary results</li> <li>- data screening</li> </ul>

<sup>14</sup> <http://www.nsls.bnl.gov/users/meeting/workshops/workshop.aspx?id=10>

<sup>15</sup> [http://www.bnl.gov/nsls2/workshops/041910\\_DAC\\_UserInterface.asp](http://www.bnl.gov/nsls2/workshops/041910_DAC_UserInterface.asp)

	- online conversion of data type to common formats (tiff, jpeg, bin, edf, cbf ...) - versatile graphical output (on-line, remote) with click-on and batch modes
Off-line data reduction and analysis	- all common and user-custom PD software - modeling

The scientific case of XPD emphasizes the need for time-resolved/fast studies, and 1 kHz acquisition rate is anticipated to become routine work in the future. High bandwidth data transfer/storage is thus required at the beamline (Table 7-6).

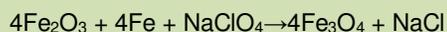
**Table 7-6:** A list of detectors and their requirements in terms of data storage and data rate.

Detector / station	Data production	Data rate
CMOS flat panel detector	50MB image size, 10 Hz.	500 MB/sec
Strip detector (high throughput)	13 x 80mm modules with 125 micron strips (8320 elements) running at 1kHz	6 MB/sec
Crystal analyzer detectors	Very low data rate	
2D CCD	30MB image size, 1 Hz	30 MB/sec
Pixel Array detector	kx1k, 65MB/ASIC/s	400 TB/day continuously
High resolution, high speed camera	1360 x 1024 at 30fps	40MB/s
Tomographic imaging	4000 x 2000 x 6000 projections	>100Gb (with 16 GPU based calculations boards)

The user community often comments that data handling and analysis are a recurrent bottleneck for producing science. More and more, users expect to find user-friendly “expert” software that ensures they leave the facility with pre-processed data. Advanced data analysis and modeling software integrated into the beamlines will mean that the users focus on science during their beamtime and are not in the dark while collecting gigabytes of unprocessed raw data. For the sake of beamline efficiency and reliability, this is desirable and achievable, provided significant software development accompanies the implementation of the endstation instruments. Therefore this particular issue will be addressed at the post-PDR stage of the project, and should be an integrated part of the beamline design. Both the ease of running the beamline with a variety of ancillary equipment, and the user-friendliness of the software, allow a most efficient use of the limited beamtime and are the way towards high scientific productivity.

**Kinetic study test case:**

Study of the change of iron oxidation using the FReLoN2k camera:



- 8,192 diffraction patterns using 64 x 2048 ROI and 64 x 2 rebin
- collection rate = 50 Hz, i.e., 19 ms integration time and 1 ms for data processing and transfer (67).

## 8. INFRASTRUCTURE FOR BEAMLINE AND USER SUPPORT

The NSLS-II support and safety systems include utilities (compressed air, chilled water, liquid nitrogen, gaseous nitrogen, etc), personnel safety systems (PPS), and equipment protection systems (EPS). The design responsibilities of these support systems are within the baseline scope of the Conventional Facilities and Accelerator Systems, with the final procurements processed by the Experimental Facilities.

### 8.1 Hutches

The first optical enclosure is densely populated and extends 16 m past the ratchet wall. An egress passage separates it from the experimental hutches. By keeping the egress width at the required value, there is room to accommodate the mirrors in the FOE. The first hutch downstream of the FOE (hutch B) will be mostly used for the PDF experiments and is not part of the present baseline. Proceeding downstream, the next two hutches (C and D) are populated by the diffractometers, optical tables, detector supports, and heavy-duty tables as described in Table 4-1 (see also Table 5-2).

The NSLS-II Beamline Design Guide contains guidelines and policies related to mechanical/electrical engineering, beamline shielding, NSLS-II beamline vacuum policy, control systems, utility and support information, personnel safety, and equipment and vacuum protection. All equipment and procedures must comply with BNL safety requirements.

The hutch footprint occupies much of the floor space: there is room left at the end of the beamline for a control room that doubles as a basic sample preparation area. This leaves a very small amount of residual space that can be used for desks, tools, etc. The electronic racks are therefore located on the roofs of the hutches and are easily accessible through a fixed staircase designed to NY state code, which is more stringent than OSHA. In addition, permanent stairs connecting the beamline to the ratchet wall are located in the adjacent beamline. If these prove adequate for roof access, then the set of stairs specific to the beamline might be removed. An emergency ladder is installed at the end of hutch D to provide egress from the roof. A bridge connects the FOE to hutch B. Hutches B, C, and D are contiguous. The hutch roof is equipped with a safety hand rail and kick plates in accordance with safety standards. Access to the roof comes from stairs leading down from the storage ring mezzanine.

There are two entry outboard doors into the FOE to ensure easy access and allow for unobstructed movement of equipment into and out of the hutch. Each of the hutches has a (motorized) sliding door. Both doors are of the double sliding type, 2.4 m wide by 2.4 m high, with floor grooves and mounting plates for a magnetic lock and dual position switches.



**Fig. 8-1:** View of a completed hutch at DESY. Note the air handler, heavy duty crane rails, utilities, window to control room, beampipe and surveying door, wiring labyrinth.

## 8.2 Environmental

Temperature in the hall is typically controlled within  $\pm 1^\circ\text{C}$ , and can become  $\pm 0.1^\circ\text{C}$  in hutches with a little care ( $\pm 0.3^\circ\text{C}$  is relatively easy providing electronics is not inside the hutch). There are air intakes located at the two ends of the FOE and one for each hutch. An “air sock” device will be used on the inside of the hutch to create a uniformly distributed airflow into the hutch. It is located at the ceiling and runs the length of the hutch. Air exits the hutch through two air outlet labyrinths located at the base of the outboard sidewall at the upstream and downstream corners of the hutch.

## 8.3 Surveying requirements

The NSLS-II facility, including the storage ring tunnel and experimental floor, is fitted with a network of survey monuments referenced to a pair of monuments in the center of the ring. This network will be regularly surveyed with a laser tracker to create a robust and accurate network of arbitrarily positioned monuments. Monuments can be added as required, including inside hutches and on the storage ring wall etc. Positioning a laser tracker on a tripod such that it can view more than three monuments allows it to calculate its position, and the position of any new monuments.

All beamline components will be surveyed and aligned in place by the facility. To facilitate ease of alignment, all components will be fiducialized to external reference points on their table during assembly. Precision machined holes in components are surveyed prior to installation, relative to the component aperture, crystal or mirror etc. Fitting a reflector into the precision hole allows the laser tracker to survey the absolute reflector position so that the aperture or optic position can be accurately calculated. This system of surveying is extremely accurate; globally (within the NSLS-II complex), components may be positioned to within 100 microns, and where components are close to one another (within a few meters and without sighting restrictions), the accuracy improves to  $\sim 30$  microns.

## 8.4 Controls requirements

Control requirements have been graphically represented in appendix B.5.

## 8.5 Utilities requirements

**Table 8-1:** Utility provisions.

<b>Electrical</b>	<p>Includes all electrical outlets in the enclosures and along the beamline, plus wiring to light fixtures, electrical outlets, fans, hoists, etc inside the enclosures. Also includes electrical power outlets in the user and control areas.</p> <p>Each beamline has 2 × 30 kVA transformers for “sensitive” and “non-sensitive” power.</p> <p>Expected total electrical load &lt; 30 kVA - at 50% transformer loading the hum noise will be negligible.</p> <p>Aim to dissipate 60% of electrical power into the chilled water system – helps maintain high temperature stability in experimental hall.</p> <p>Small distributed UPS system to be included in beamline racks as required.</p>
<b>Water</b>	<p>High quality de-ionized Low conductivity Water (LCW) for cooling of accelerator components, front ends and beamline optics.</p> <ul style="list-style-type: none"> <li>▫ 12 GPM average, 15 GPM peak allowed per beamline.</li> <li>▫ Pressure is 100 psi nominal, 150 psi max.</li> <li>▫ 85°F ± 0.2°F (29.5 ± 0.1°C).</li> <li>▫ Piping comes through ratchet wall from SR tunnel into FOE.</li> </ul> <p>Chilled water for cooling of electronics racks and some endstation equipment (e.g., furnaces, pumps, etc).</p> <ul style="list-style-type: none"> <li>▫ 3 GPM average, 6 GPM peak allowed per beamline.</li> <li>▫ Pressure is 100 - 120 psi nominal, 150 psi max.</li> <li>▫ 53 °F inlet temperature (20 °F temperature rise assumed at full rated flow and power removal).</li> <li>▫ Piping comes from roof of RF tunnel along top of beamline.</li> </ul>
<b>Other Standard Utility Provisions</b>	<p>Liquid nitrogen</p> <ul style="list-style-type: none"> <li>▫ 40 Gal/hr average allowed per beamline (dominant usage from DCMs on DW beamlines).</li> <li>▫ Pressure is 30-45 psi nominal.</li> <li>▫ Piping around facility above the SR tunnel, with drops at each ID beamline.</li> </ul> <p>Gaseous nitrogen</p> <ul style="list-style-type: none"> <li>▫ 20 cfm maximum allowed per beamline (main usage; purge gas and IR spectrometers etc).</li> <li>▫ Pressure is 30 psi nominal, 125 psi max.</li> <li>▫ Piping runs adjacent to LN system.</li> </ul> <p>Compressed air</p> <ul style="list-style-type: none"> <li>▫ 10 cfm maximum (intermittent) allowed per beamline (main usage; valves, air skates etc).</li> <li>▫ Pressure is 75 psi nominal, 125 psi max.</li> <li>▫ Piping runs from SR tunnel through ratchet wall into FOE.</li> </ul> <p>Any local gas distribution from gas cylinders into hutches, etc., including toxic gas</p> <p>Exhaust</p> <ul style="list-style-type: none"> <li>▫ Exhaust system above walkway allows HEPA filtered extraction to be linked in at any beamline position.</li> <li>▫ Gas exhausts from enclosures to common exhaust manifold in building</li> </ul> <p>Communications, including fiber optic cable reticulation and CAT6 LAN with switches and racks (including outlets in the control or user area)</p> <p>Cabling and piping support structures, including for EPS and PPS</p>
<b>Non Standard Utility Provisions</b>	<p>Fire department equipment</p> <p>Temperature sensors (inside enclosures)</p> <p>Gas and oxygen-depletion sensors</p> <p>Nanoparticle handling: HEPA filtering</p> <p>Ouside gas cabinet(s)</p>

**Table 8-2:** Cooling water requirements for XPD

Approximate temperature	20°C to 30°C
Temperature stability	± 1°C
Maximum pressure	6 bar
Pressure stability	± 0.1 bar
Quality	de-ionized but not ultra-pure

**Table 8-3:** Flow requirements for the various XPD optical components.

Component	# of Circuits	Max. Consumption
Fixed window	3	4 l/min
Filter Assembly	4	8 l/min
Cooling of side-bounce monochromator	1	Cryocooler
Cooling of double Laue monochromator	1	Local Chiller
White Beam Stop	1	4 l/min

The monochromatic photon beam shutter, all gate valves, and the pneumatically driven attenuator filter units must be connected to a dry, filtered, compressed air supply having a pressure of between 70 and 100 psi.

For utilities and services there will be labyrinths located on the FOE and hutch roofs. Utilities will approach the hutch from the storage ring mezzanine (tunnel roof) and drop down to the hutch roof. The liquid nitrogen cryocooler will also be located on the storage ring mezzanine; due to the thickness of the concrete tunnel roof, no problems are foreseen with vibration being transmitted to sensitive optical elements. Low conductivity water and compressed air will enter the hutch directly from the storage ring tunnel through penetrations in the side ratchet wall without passing through hutch labyrinths.

Because the scope of the beamline is to study materials under operational conditions, we can anticipate that most (if not all) of the 241 substances in CAA 112R, the EPA list of Regulated Toxic, Explosive, or Flammable Substances, will be used at some time—in small quantities. Many of them are involved in catalytic processes and/or semiconductor manufacturing, two key areas of beamline science. A ventilated cabinet for hazardous gas bottles is required, and the gases will be routed to the three hutches.

Many catalytic studies will involve multiple reagents. It is feasible that mixture of gas, gaseous hydrocarbon, and liquid hydrocarbon be fed into a reactor. Systems to control the flows of such materials (including mass flow controllers interfaced to data collection software), as well as to monitor the composition of the products (on-line GS/MS, also interfaced to the data collection software) will be required. Because each experiment will have different requirements, modularity of the endstation equipment will be critical, but standard infrastructure should prevail as much as possible for productivity reasons.

**Table 8-4:** Potential catalysis applications and chemicals involved.

Reaction	Potential "interesting" compounds involved
Amoxidation	NH <sub>3</sub> , air, propylene/propane, acrylonitrile, acrolein (avoid flammability limits)
Partial oxidation	Butane, air (flammability limits)
Xylene isomerization	Hydrogen, xylenes, toluene, ethylbenzene, benzene, ethane/ethylene
Hydrotreating	H <sub>2</sub> S, NH <sub>3</sub> , H <sub>2</sub> (P < 5000 psig)
Offgas treating	CO <sub>x</sub> , NO <sub>x</sub> , SO <sub>x</sub> , HCl, HBr
Oxychlorination	Cl <sub>2</sub> , HCl, vinyl chloride monomer
Olefin Polymerization	Metal alkyls, metal chlorides, HCl, BF <sub>3</sub>
Alkylation	H <sub>2</sub> SO <sub>4</sub> , H <sub>3</sub> PO <sub>4</sub>
Many reactions	H <sub>2</sub> O (steam)
Hydrogenation	H <sub>2</sub> , aromatic acids, acetic acid

## 8.6 User space

The user space is shown in Fig. 13.7 of appendix B. Procurement and installation of the work area includes: hardware, desks, chairs, shelving, cabinets, partitioning walls, user computers, printer, etc. It excludes computers associated with control of the beamline and endstation. Since the hutches and FOE occupy most of the floor space, there is only room at the end of the beamline for a secluded space suitable for routine sample preparation and a modest work area.

## 8.7 Sample preparation and manipulation

The powder or polycrystalline sample is accommodated in a variety of flat plate, capillary, and custom-design supports, and mounted on the diffractometer omega circle (described in section 7.2). A robot operates in hutch C for high throughput measurements. The proximity of the Center for Nanomaterials and trends in current frontier science suggest that many experiments involving nanomaterials<sup>16</sup> will be performed at the beamline. A HEPA filtration system needs to be an integral part of the endstations.

A **laboratory close to the beamline** should allow routine manipulation of powders and nanopowders. Its equipment includes:

- Workbenches
- Sinks
- Refrigerator
- Chemical storage
- High-precision balance
- Powder press
- Heating plate

<sup>16</sup> For nanoparticle hazards, see <https://sbms.bnl.gov/sbmsearch/IP/2006-001/2006-001.cfm> and attachment #5 in <http://www.nsls.bnl.gov/newsroom/publications/manuals/prm/LS-ESH-PRM-1.3.5a.html>

- Hood
- Ultra sonic bath
- Glove box
- Microscope

## 8.8 Special beamline requirements

### Requirements on the Conventional Facilities Division

- Vibration stability: TBD
- Temperature stability:  $\pm 1$  K
- Utilities
- Exhaust from multi-use enclosures: TBD
- Nanoparticle handling: HEPA filtering
- Special gas environments and user-custom environmental cells should be accommodated
- Sufficient floor strength to accommodate large and heavy pieces of equipment
- Prep lab for fast/easy sample preparation in close proximity to beamline

### Requirements provided to the Accelerator Systems Division

**Table 8-5:** XPD Beamline Electron Beam Stability Requirements<sup>17</sup>

Parameter		Unit	Value
Vertical Position	<i>Centroid</i>	$\mu\text{m}$	10
	<i>Width</i>	-	No special requirement.
Vertical Angle	<i>Centroid</i>	$\mu\text{rad}$	8
	<i>Width</i>	-	No special requirement.
Horizontal Position	<i>Centroid</i>	$\mu\text{m}$	10
	<i>Width</i>	-	No special requirement.
Horizontal Angle	<i>Centroid</i>	-	Not applicable
	<i>Width</i>	-	No special requirement.
Time Range			No special requirement.

<sup>17</sup> For reference, see NSLS-II Stability Workshop April 18-20, 2007 and Report of the NSLS-II Stability Task Force, September 26, 2007: [http://www.bnl.gov/nsls2/workshops/Stability\\_Wshop\\_4-18-07.asp](http://www.bnl.gov/nsls2/workshops/Stability_Wshop_4-18-07.asp)

## 8.9 Preliminary safety analysis

### 8.9.1 Shielding

The Shielding Policy for NSLS-II requires that the hutches be shielded to reduce radiation levels in contact with the exterior of the hutch to less than 0.05 mRem/h for normal operating conditions and as low as reasonably achievable. A radiation area monitor mounted on the exterior of the First Optics Enclosure is required to protect against elevated radiation levels created by unusual electron losses in the accelerator ring. Access to all hutches is strictly controlled with the PPS and the PLC. Assuming an occupancy of 2,000 hours per year, this will reduce annual exposure to 1000 mrem or less, in accordance with 10 CFR 835.1001.

Wall thickness, materials and dimensions are calculated and specified in LT-ESHDES-08-003-rev001 “Guidelines for NSLS-II Beamlines and Front End Radiation Shielding Design,” by P.K. Job and W.R. Casey May 15, 2008<sup>18</sup>. All radiation protection policies and guidelines at NSLS-II must comply with these regulations along with the BNL Radiation Control Manual and other pertinent documents in the BNL Standards Based Management System.

#### Shielding Recommendations for NSLS-II Monochromatic Experimental Stations

FOE A	<ul style="list-style-type: none"> <li>▪ side wall 18 mm lead</li> <li>▪ downstream wall 50 mm lead</li> <li>▪ roof 10 mm lead</li> </ul>
Hutches B,C,D	<ul style="list-style-type: none"> <li>▪ all walls 4 mm lead</li> <li>▪ roof 3 mm lead</li> </ul>
Pipe shielding	<ul style="list-style-type: none"> <li>▪ 7 mm lead</li> </ul>

**Table 8-6:** Attenuation lengths of shielding materials (Pb, W) vs. energy. The absorption K-edge energy is 88 keV for Pb and 69.5 keV for W.

	energy (keV)	69.5	60	50	40	30
Pb	attenuation length (cm)	0.026275654	0.017684	0.011022391	0.006163	0.002937
W	attenuation length (cm)	0.020422326	0.01403	0.008743081	0.00487	0.002355

### 8.9.2 Personal Safety System

The PSS includes switches, touch panel, door switches, shutter control, interlock keys, PLC and programming, indicator lights, audible warning devices, etc. See PPS diagram in appendix B.6. Access to hutch B is always possible when PSH 2 is closed (Fig. 8-2 and Table 4-2). The operation of hutch B is fully independent from the operation of hutches C and D.

<sup>18</sup><http://groups.nsls2.bnl.gov/eshqa/Shared%20Documents/Signed%20Documents/shielding%20guidelines%20for%20beamlines.pdf>

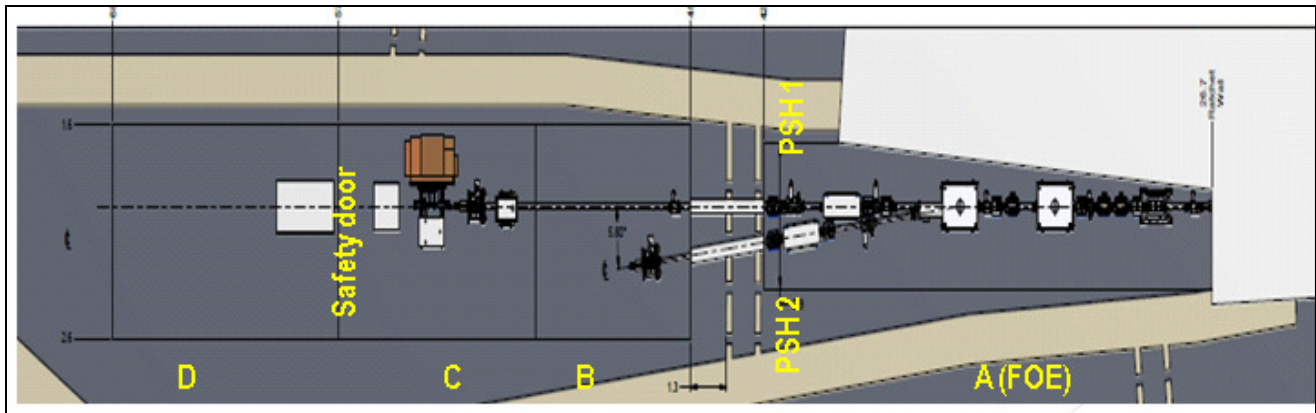


**Fig. 8-2:** Location of the safety shutters and hutches. The Front End Safety Shutter serves hutch A. PSH 1 serves hutches C and D. PSH 2 serves hutch B. Safety Door serves D (see Table 4-2 for hatch operation).

### 8.9.3 Equipment Protection System

This system will protect equipment from damage due to excessive beam heating, vacuum faults, etc. This system is not meant to protect personnel. It includes interfaces to other systems for equipment status (e.g., filter position, water flow, vacuum gauges, etc.). The EPS includes shutter and valve control, PLC and programming, indicator panel, etc. and excludes sensors (pressure, temperature, etc.). The wiring to such sensors is included, however (see PI&D diagram of appendix B). The EPS will consist of standardized PLC hardware distributed along the beamline as required and may be monitored remotely by EPICS.

## 9. FUTURE UPGRADE OPTIONS

Item	Description
PDF branchline optics (serving station B)	This includes the SBM, the ML mirror and the diagnostics. Beam transport is partially in place in the baseline design. Priority 2A of the project beamline scope enhancement plan.
Fit-out of station B	Mature scope
Fit-out of station D	Mature scope
He-flow cryostat	Ultra-low temperature. Priority 2A of the project beamline scope enhancement plan.
Use a super-conducting wiggler source (e.g., SCW60 (Fig. 2-1))	Provides a larger critical energy and therefore provides a higher flux at energies above 40 keV. The current optical layout is compatible with this option.
Secondary focusing optics in hutch D	The capability of delivering small beams (below 10 $\mu$ m) is considered as part of the mature scope of the project. This priority is lower than that of the build-out of station B. The current layout keeps the option of a primary focus and slits at the first hutch C and then refocusing optics to produce a 10 $\mu$ m focus in hutch D; <b>this would be unique at these energies.</b> Priority 2A of the project beamline scope enhancement plan.
Extend detector capability	The upgrade to a Ge-strip detector is a priority 2B of the project beamline scope enhancement plan (appendix H.1). MAR353 (section appendix H.5) Second detection stage (mature scope) – see section 7.1
Extend sample environments beyond the basic set of standard cells	Including pressure cells.
Control cabin	Provides better (noise free) private user space; serves as airlock for T stability. Low priority in the project enhancement plan.

The NSLS-II project rescoping priorities are listed here:

Priority	Description	decision date	activity start date	activity end date
2A	<b>Beamline Scope Enhancements</b>			
	Secondary focusing	Jun-12	Oct-12	Feb-14
	Station B optics and transport	Mar-12	Jun-12	Feb-14
	He cryostat	Mar-13	Jun-13	Feb-14
2B	<b>Beamline Detectors</b>			
	Ge strip detector	Jun-12	Oct-12	Feb-14
	Mar555 TFT	Jun-13	Oct-13	Feb-14
21	Control cabin	Mar-13	May-13	Feb-14

## 10. SCHEDULE

---

### 2010

September 30	Preliminary Design Report
October 19-20	PDR Technical Review
November 15-17	DOE review
November	Technical Design – Approval of Long Lead Term Procurement Send Request For Proposal for Hutches

---

### 2011

April	Start Long Lead Time Procurements (monochromator, mirror, diffractometer,...) Start fabrication of Hutches
September	Start Fabrication of first Long Lead Time Components
December	Complete Final Design Report - Start Installation

---

### 2012

June	Start Sub-System Testing Start Other Procurements
------	--

---

### 2013

February	End Fabrication of FOE procurement package
September	Delivery of DLM
August	Start Integrated Testing
October	End Procurements – Complete Installations
November	Complete sub-system testing

---

### 2014

January	Complete Integrated Testing – Beamline available for Commissioning
<b>February</b>	<b>Beam-ready</b> (instead of June 2015 in earlier plans)

---

### 2015

<b>June</b>	<b>CD-4, Approve Start of Operations</b>
-------------	--

In most cases, beamline commissioning can proceed prior to the final installation of the endstation instruments. Several x-ray experiments are planned in the mid-term to support the design and construction of critical or non-standard components of XPD:

DLM	crystal testing and prototyping (section 5.5.1)
ML mirror	mirror coating, surface mapping and x-ray testing (section 5.6.1.4)
IRF modeling	combine a (SL and ML) mirror test piece with the DLM of X7B NSLS and study the instrumental contribution to the diffraction data (section 6.2)
MA	crystal testing and prototyping (section 7.4)
Diamond/SiC window testing	behavior under high heat load (section 5.4.2)

## 11. SUMMARY

The proposed powder diffraction (XPD) beamline at NSLS-II will be a tunable facility with the ability to collect data at high energies (30 keV-70 keV), offering exceptional capabilities such as fast (milli-second) readout rates and high angular resolution on the same instrument. The key scientific goals are to structurally characterize materials at the frontier of complexity, whether the frontier is nanostructure, heterogeneity or *in situ* environments.

This report presents the preliminary design of the XPD project beamline with the vision to accomplish the above-mentioned goals. The current design and optical layout shown here are supported by extensive modeling: we propose a stable and robust configuration tailored to the characteristics of the damping wiggler source. Special attention is devoted to the unique development of the double-bend double-crystal high heat load monochromator, for optimum performance and maximized flux in the 30 keV- 80 keV energy range. The current design aims at maximizing the technical capabilities of XPD in areas such as *in situ* and time resolved measurements. It also proposes the options to collect diffraction data at high energies with high resolution either in reciprocal space (minimal  $2\theta$  broadening) or in direct space (access to large values of  $Q$ ). The design of XPD offers as much flexibility as possible for the simultaneous or combined use of three hutches with dedicated and specialized equipment. As a result, XPD will be capable of carrying out powder diffraction and PDF/total scattering measurements on the same sample with a high-throughput, moderate resolution mode and a high-resolution, moderate throughput mode. XPD is thus designed to offer the unique capability to carry out sample-limited  $Q$ -space-resolution diffraction measurements, simultaneously with sample-limited real-space-resolution PDF measurements.

The preliminary design of XPD meets the scientific objectives as they were laid out in the Letter Of Interest of March 2008:

- Complex materials structure characterization
- Nanostructured materials characterization
- Heterogeneous materials characterization
- Time-resolved materials characterization
- In situ materials characterization
- In-operando materials characterization (materials are in real functioning devices). In practice, this combines all of the above points in a single experiment.

High-energy beams are ideal to penetrate into special sample environments and into the bulk of heterogeneous samples. High-energy x-rays will be able to propagate through environmental cells, and are suitable for powder diffraction measurements in difficult environments, e.g., stainless steel reaction tubes and high temperature capillaries. They also allow for the investigation of materials made up of high-Z components, and enable high- $Q$  accessibility, which is crucial for atomic pair distribution function (PDF) analysis and high-pressure cell research.

High-resolution mode with manageable line shapes are required for complex materials, typically forming in special environments such as reaction cells. Such materials are complex in the crystallographic sense but are not nanostructured. The study of condensed matter at extreme conditions is developing into a very rich field of research. Structure models are derived from high-resolution diffraction, which is essential for systematic searches for new classes of materials and for rationalizing their desirable properties.

High resolution is not needed for PDF work and in general for nanostructured materials where the diffraction peak width is dominated by the nanostructuring rather than by the instrument resolution.

High flux of high-energy photons makes time-resolved measurements possible, and also facilitates diffraction from samples where the phase of interest is dilute. XPD will be an outstanding research facility for studying the structure and kinetics of materials under real conditions.

In addition to normal sized beams for powder diffraction work (0.5-0.7 mm), small beams and accurate sample positioning capability are envisaged for studying heterogeneous samples with good spatial resolution. Small beams imply a poor powder average, so an extension to total crystallography-type methods for data analysis is identified as being an important capability.

Because of the nature of complex materials research, the scientific impact depends equally on beamline characteristics and on the availability of appropriate software and special environments, as well as on the success with which researchers can combine data from complementary approaches (such as conventional powder diffraction and PDF).

Recognizing both the commonality in some parts of the XPD beamline (for which designs and standard components are readily available) and the complexities in some other parts (e.g., Laue optics, high-energy x-ray detectors, extreme conditions) that strive for the state of the art, we believe the current design is sufficiently mature to start procurements of long lead-time components.

Detailed costing of the beamline suggests that not all the desired capabilities can be delivered within the baseline, so some capabilities must be delayed to a mature scope for the project. The current design allows staging the construction of the beamline so that critical capabilities are present on Day One, but an upgrade path is presented here for realization of the more complete mature scope.

Another important part of the preliminary design phase is the assessment of the risks and/or critical issues. They are identified and addressed in the present report, and mitigation solutions are discussed:

- radiation safety
- high energy x-ray detection
- high power, high heat load
- large beam divergence in horizontal and vertical directions, large fan, large beam size
- restricted acceptance of refractive and diffractive optics
- data acquisition

In conclusion, the preliminary design of the XPD beamline is shown to adequately meet the technical performance requirements for carrying out the scientific mission of the beamline. A key capability of XPD is to carry out powder diffraction and PDF/total scattering measurements from heterogeneous samples. A list of priorities of initial science capabilities and Day One deliverables is drawn up, along with the budget (29)ary and scope constraints. An upgrade path to the mature scope is defined. The risks are well identified and a mitigation plan is considered.

## 12. REFERENCES

1. **U. Rütt, J.R. Schneider, M.A. Beno, G.S. Knapp, P.A. Montano.** 1998, Proc. SPIE, Vol. 3348, p. 132.
2. **K.D. Liss, A. Royer, T. Tschentscher, P. Suortti, A.P. Williams.** 1998, J. Synchrotron Rad. , Vol. 5, p. 82.
3. **J.E. Daniels, D. Pontoni, R.P. Hoo, V. Honkimaki.** 2010, J. Synchrotron Rad., Vol. 17, pp. 473-478.
4. **O. Chubar, P. Elleaume, J. Chavanne.** 1998, J. of Synchrotron Radiation, Vol. 5, pp. 481-484.
5. **J.S. Goela, M. A. Pickering, L.E. Burns.** 1996, Proc. SPIE 2855, pp. 2-13.
6. **Z. Zhong, C. Kao, D.P. Siddons, H. Zhong, J.B. Hastings.** 2001, J. Appl. Cryst., Vol. 34, pp. 646-653.
7. **Z. Zhong, C. Kao, D.P. Siddons, H. Zhong, J.B. Hastings.** 2001, J. Appl. Cryst., Vol. 34, pp. 504-509.
8. **Z. Zhong, C. Kao, D.P. Siddons, H. Zhong, J.B. Hastings.** 2002, Acta Cryst, Vol. A 58, pp. 487-493.
9. **Z. Zhong, C. Kao, D.P. Siddons, H. Zhong, J.B. Hastings.** 2003, Acta. Cryst, Vol. A 59, pp. 1-6.
10. **S. D. Shastri, K. Fezzaa, A. Mashayekhi, W.-K. Lee, P. B. Fernandez, P. L. Lee.** 2002, J. Synchrotron Rad., Vol. 9, p. 317.
11. **S.D. Shastri.** 2004, J. Synchrotron Rad., Vol. 11, pp. 150–156.
12. **S. D. Shastri, J. Almer, C. Ribbing , B. Cederstrom.** 2007, J. Synchrotron Rad., Vol. 14, pp. 204–211.
13. **U. Rütt, J. Heuer, H. Schulte-Schrepping. Work based on R. Smither, K. Abu Saleem, M. Beno, C. Kurtz, A. Khounsary, N. Abrosimov.** 2005, Rev. of Sci. Instrum., Vol. 76, p. 123107.
14. **M.A. Beno, U. Rütt, C. Kurtz, G. Jennings.** 2004, Synchrotron Radiation Instrumentation, Vol. 705, pp. 675-678.
15. **N. Schell, A. King, F. Beckmann, H. Ulrich Ruhnu, R. Kirchhof, R. Kiehn, M. Müller, A. Schreyer.** 2009, Proc. of SRI Melbourne.
16. **C.G. Schroer, M. Kuhlmann, B. Lengeler, T.F. Günzler, O. Kurapova, B. Benner, C. Rau, A.S. Simionovici, A.A. Snigirev, I. Snigireva.** 2002, Proc. SPIE, Vol. 4783, pp. 10–18.
17. **A. Stein, K. Evans-Lutterodt, N. Bozovic, A. Taylor.** 2008, J. Vac. Sci. Technol., Vol. B 26, p. 122.
18. **A. F. Isakovic, A. Stein, J. B. Warren, S. Narayanan, M. Sprung, A. R. Sandyd, K. Evans-Lutterodt.** 2009, J. Synchrotron Rad., Vol. 16, pp. 8–13.
19. **W. Jark, F. Perennes, M.J. Matteucci.** 2006, J. Synchrotron Rad, Vol. 13, pp. 239–252.
20. **C. Morawe, C. Borel, J-C. Peffen.** 2007, Proc. SPIE, Vol. 6705.
21. **C. Morawe, J-C. Peffen.** 2009, Proc. SPIE, Vol. 7448.
22. **M. Störmer, C. Horstmann, D. Häussler, E. Spiecker, F. Siewert, F. Scholze, F. Hertlein, W. Jäger & R. Bormann.** 2008, Proc. SPIE, Vol. 7077.
23. **C.Morawe.** 2007, AIP Conf. Proc., Vol. 879, pp. 764-769.
24. **R. Conley, C. Liu, C.M. Kewish, A.T. Macrander, Ch. Morawe.** 2007, SPIE Proceedings, Vol. 6705, p. 670505.
25. **A. Rack, et al.** 2010, J. Synchrotron Rad., Vol. 17, pp. 496-510.
26. **C. Welnak, G.J. Chen, F. Cerrina.** 1994, Nucl. Instr. Methods A, pp. 344-347.
27. **M. Sanchez del Rio, R.J. Dejus.** SPIE Proc. : s.n., 2004, Vol. 5536, pp. 171-174.
28. **H.W.Zachariasen.** 1945, Theory of X-ray Diffraction in Crystals, Wiley, New York.
29. **M.T. Sabine.** 1987, J. Appl. Cryst, Vol. 20, pp. 23-27.
30. **F. Gozzo, L. De Caro, C. Giannini, A. Guagliardi, B. Schmitt, A.Prodi.** 2006, J. Appl. Cryst., Vol. 39, pp. 347-357.
31. **E. Dooryhee, M. Anne, I. Bardiès, J.-L. Hodeau, P. Martinetto, S. Rondot, J. Salomon, G.B.M. Vaughan, P. Walter.** 2005, Appl. Phys. A , Vol. 81, p. 663.
32. **P. Bleuet, E. Welcomme, E. Dooryhee, J. Susini, J-L. Hodeau, P. Walter.** 2008, Nature materials , Vol. 7, p. 468.
33. **F. Fauth, C. Bronnimann, H. Auderset, G. Maehlum, P. Pattison & B. Patterson.** 2000, Nucl. Instrum.Methods Phys. Res. A, Vol. 439, pp. 138–146.

34. **A. Bergamaschi, A. Cervellino, R. Dinapoli, F. Gozzo, B. Henrich, I. Johnson, P. Kraft, A. Mozzanica, B. Schmitt, X. Shi.** 2010, *J. Synchrotron Rad.* 17, pp. 653–668.
35. **S.Sulyanov.** 2010, European Powder Diffraction Conference.
36. **J.L. Hodeau, P. Bordet, M. Anne, A. Prat, A. N. Fitch, E. Dooryhée, G. Vaughan, A. Freund.** 1998, SPIE Conference on Crystal and Multilayer Optics SPIE 3448, p. 353.
37. **N. Tartoni, S. P. Thompson, C. C. Tang, B. L. Willis, G. E. Derbyshire, A. G. Wright, S. C. Jaye, J. M. Homer, J. D. Pizzey and A. M. T. Bell.** 2008, *J. Synchrotron Rad.* , Vol. 15, pp. 43–49.
38. **D. P. Siddons, Z.Yin, L. Furenlid, P. Pietraski, Zheng Li, R. Harlow. A. Freund.** 1998, SPIE Conference on Crystal and Multilayer Optics, Vol. 3448, p. 120.
39. **U. Rutt, M.A. Beno, J. Strempler, G. Jennings, C. Kurtz, P.A. Montano.** 2001, *Nuclear Instruments and Methods in Physics Research A* , Vols. 467–468, pp. 1026–1029.
40. **R. Bouchard, D. Hupfeld, T. Lippmann, J. Neufeind, H.-B. Neumann, H.F. Poulsen, U. Rütt, T. Schmidt, J.R. Schneider, J. Süßenbach, M. von Zimmermann.** 1998, *J. Synchrotron Rad.* , Vol. 5, p. 90.
41. **P. Suortti, U. Lienert, C. Schulze.** 1997, *AIP Conf. Proc.*, Vol. 389, pp. 175–192.
42. **P. Suortti, S. Fiedler, A. Bravin, T. Brochard, M. Mattenet, M. Renier, P. Spanne, W. Thomlinson, A. M. Charvet, H. Elleaume, C. Schulze-Briese, A. C. Thompson.** 2000, *J. Synchrotron Rad.*, Vol. 7, p. 340.
43. **C. Schulze, U. Lienert, M. Hanfland, M. Lorenzen, F. Zontone.** 1998, *J. Synchrotron Rad.* 5 , p. 77.
44. **M. Sanchez del Rio, C. Ferrero, V. Mocella.** 1997, *SPIE Proc.*, Vol. 3151, pp. 312–323.
45. **U. Lienert, et al.** 1998, *J. Synchrotron Rad.* , Vol. 5, p. 226.
46. **M. Krisch, A. Freund, G. Marot, L. Zhang.** 1991, *Nucl. Instrum. and Methods in Phys. Res. A*, Vol. 305, pp. 208–213.
47. **O.Proux, et al.** 2006, *J. Synchrotron Rad.* , Vol. 13, pp. 59–68.
48. **V. Kohn, I. Snigireva, A. Snigirev.** 2003, *Opt. Comm.* , Vol. 216, p. 237.
49. **A. Snigirev, V. Kohn, I. Snigireva, A. Souvorov, B. Lengeler.** 1998, *Appl. Opt.* 37, p. 653.
50. **M. Simon, E. Reznikova, V. Nazmov, A. Last, W Jark.** 2008, *Proc. of SPIE*, Vol. 7077.
51. **P. Pangaud, S. Basolo, N. Boudet et al.** 2007, *Nucl.Instrum. and Methods in Phys. Res. A*, Vol. 571, pp. 321–324.
52. **S. Basolo, et al.** 2007, *J. Synchrotron Rad.* , Vol. 14, pp. 151–157.
53. **S. Basolo, JF. Berar, et al.** 2008, *Nucl. Instrum. Methods Phys. Res. A*, Vol. 589, pp. 268–274.
54. **C. Fröjdh, H. Graafsma, H.E. Nilsson, C. Ponchut.** 2006, *Nucl. Instrum. Meth. Phys. Res. A*, Vol. 563, pp. 128–132.
55. **M. Clajus, V.B. Cajipe, S. Hayakawa, T.O. Turner, P.D. Willson.** 2006, *IEEE Nucl. Sci. Symp. Conf. Rec.*, Vol. 6, pp. 3602–3606.
56. **A. Zwerger, A. Fauler, M. Fiederle, K. Jakobs.** 2007, *Nucl. Instrum. Methods Phys. Res.* , Vol. A576, pp. 23–26.
57. **B. Henrich, A. Bergamaschi, C. Broennimann, R. Dinapoli, E.F. Eikenberry, et al.** 2009, *Nucl. Instrum. Methods Phys. Res.*, Vol. A607, pp. 247–249.
58. **B. Schmitt, Ch. Bronnimann, E.F. Eikenberry, F. Gozzo, C. Hormann, R. Horisberger, B. Patterson.** 2003, *Nuclear Instruments and Methods in Physics Research A* , Vol. 501, pp. 267–272.
59. **C. Ponchut, J. Clement, J. M. Rigal, E. Papillon, J. Vallerger, D. Lamarra, B. Mikulec.** 2007, *Nucl. Instrum. Methods Phys. Res. A*, Vol. 576, pp. 109–112.
60. **V.A. Wright, A. Blue, M. Horn, I. Johnston, E. Koskiahde, L. Lea, J. Melone, S. Nenonen, V. O’Shea, M. Rahman, P. Roy, K. Smith.** 2004, *Nuclear Instruments and Methods in Physics Research A* , Vol. 531, p. 56.
61. **S. Basolo, J-F. Bélar, N. Boudet, P. Breugnon, B. Caillot, J-C. Clemens, P. Delpierre, B. Dinkespiler, et al.** 2007, . *J. Synchrotron Rad.* , Vol. 14, pp. 151–157.
62. **J-F. Berar, L. Blanquart, N. Boudet, P. Breugnon, B. Caillot, J-C. Clemens, P. Delpierre, I. Koudobine, C. Mouget, R. Potheau, I. Valin.** 2002, *J. Appl. Cryst.* 35, pp. 471–476.
63. **P. Pangaud, et al.** 2008, *Nuclear Instruments and Methods in Physics Research A* 591, pp. 159–162.
64. **K. Medjoubi, T. Bucaille, S. Hustache, J-F. Bélar, N. Boudet, J-C. Clemens, P. Delpierre, B. Dinkespiler.** 2010, *J. Synchrotron Rad.* , Vol. 17, pp. 486–495.

65. **P. Sarin, R. P. Haggerty, W. Yoon, M. Knapp, A. Berghaeuser, P. Zschack, E. Karapetrova, N. Yang, W. M. Kriven.** 2009, *J. Synchrotron Rad.* , Vol. 16, pp. 273–282.
66. **P. Kraft, A. Bergamaschi, Ch. Broennimann, R. Dinapoli, E. F. Eikenberry, B. Henrich, I. Johnson, A. Mozzanica, C. M. Schlepütz, P. R. Willmott, B. Schmitt.** 2009, *J. Synchrotron Rad.* , Vol. 16, pp. 368–375.
67. **J-C. Labiche, O. Mathon, S. Pascarelli, M. A. Newton, G. G. Ferre, C. Curfs, G. Vaughan , A. Homs, D. F. Carreiras.** 2007, *Rev of Sci. Instrum.* , Vol. 78, p. 091301.
68. **J. Chupas, Karena W. Chapman, Peter L. Lee.** 2007, *J. Appl. Crystallogr.* 40, pp. 463-470.
69. **J. E. Daniels, M. Drakopoulos.** 2009, *J. Synchrotron Rad.* 16, pp. 1-6.
70. **J. Headspith, J. Groves, P. N. Luke, M. Kogimtzis, G. Salvini, S. L. Thomas, R. C. Farrow, J. Evans, T. Rayment, J. S. Lee, W. D. Goward, M. Amman, O. Mathon, S. Diaz-Moreno.** 2007. *IEEE Nuclear Science Symposium Conference Record N55 2.*

*Intentionally blank.*

## 13. APPENDICES

## A BRIEF DESCRIPTION OF THE FRONT END

### A.1 Overview of the major components

#### *Photon shutter*

The bending magnet photon shutter (BMPS) is part of the storage ring vacuum system and is designed to protect the slow gate valve (SGV) from BM radiation before the upstream straight is fitted with an insertion device and a complete front end. The BMPS will also be used to protect the SGV if the completed front end needs to be isolated from the machine. If it is required to close the SGV during machine operation, the insertion device power will first be reduced followed by closing the BMPS and then the SGV.

#### *Slow gate valve*

The SGV is part of the storage ring vacuum system and is included to isolate the machine and FE, but will not withstand white beam from IDs or BM radiation. The SGV is controlled and monitored by storage ring vacuum PLC using a voting scheme with inputs from vacuum sensors at both sides of the valves and position of BMPS.

#### *Beam position monitors*

The XBPMs (Fig. 13-1) are designed to work with the damping wiggler.

Material	Water-cooled mountings and Tungsten blades
Power protection	A pre-mask may be included if design considerations dictate
Motorized	Yes to allow centering of the device around the beam.

The XBPMs shall be mounted on X/Y stages with the following specifications:

Position stability	Low stability: $\Delta x, \Delta y = 2 \mu\text{m}$ or better over any 8-hour period
Speed	No requirement
Position resolution	x and y = $0.1 \mu\text{m}$ (expected value; $\ll 1$ micron guaranteed).

The X/Y stage for the XBPM and the X/Y slits are expected to be the same design, including the stand, where possible.

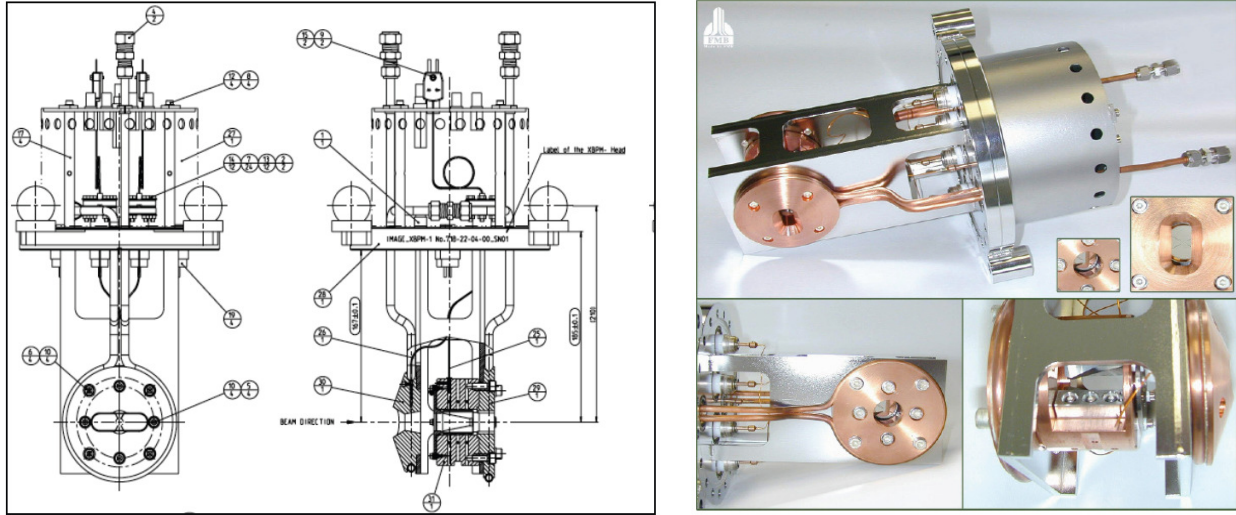


Fig. 13-1: One design being considered for the XBPMs is shown above.

Beam Position Monitor 2 (XBPM2) and its X/Y stages shall be identical to XBPM1; however, the blades shall be relocated to avoid masking effects.

**Bremsstrahlung collimator**

The bremsstrahlung collimators restrict the bremsstrahlung radiation fan exiting the shield wall. Bremsstrahlung collimators 1 and 2 and the ratchet wall collimator should be made as tight as possible to the beam as is reasonable without undue mechanical tolerances or alignment difficulty, using a combination of in-vacuum tungsten and out-of-vacuum lead designs. The ratchet wall lead collimator length does not change but the horizontal aperture increases from 20 mm to 36 mm.

**X/Y slits**

A pair of white-beam X/Y slits is located immediately downstream of the first lead collimator to further reduce power loads and reduce the angular acceptance, if required. These slits will increase in length and aperture in order to accept the damping wiggler beam. In addition to the increased size of the Glidcop slit bodies, the stages supporting the slit assemblies require larger horizontal strokes.

The X/Y slits shall be of the SPring-8 dual “L” type design, connected with bellows to allow full adjustment of all four “blades” via two X/Y stages. The specifications are as follows:

Material	Water-cooled Glidcop with Tungsten blocks
Power protection	A pre-mask may be included if design considerations dictate
maximum opening angle	Sufficient to allow full FMK fan to continue to the FOE without clipping.
Motorized	Yes to allow selection of any part of the FMK fan. The same X/Y stage shall be used for the XBPMs.
Aperture stability	Low stability: $\Delta x, \Delta y = 4 \mu\text{m}$ or better over any 8-hour period

The aperture stability specification is governed by differential movement between the two X/Y slit units; the specification will be met with high stability X/Y stages. For the high stability stages some form of additional coupling between stands may be required to constrain any differential movement.

**Photon shutter**

The photon shutter is required to stop full white beam, for IDs this is expected to be water cooled Glidcop at a grazing incidence angle. The Photon shutter length will be increased from 20 cm for an Undulator Beamline to 30 cm and the horizontal aperture will increase from 20 mm to a minimum of 39 mm. The same actuator and position sensors will be used as on the Undulator front ends to reduce spare part requirements.

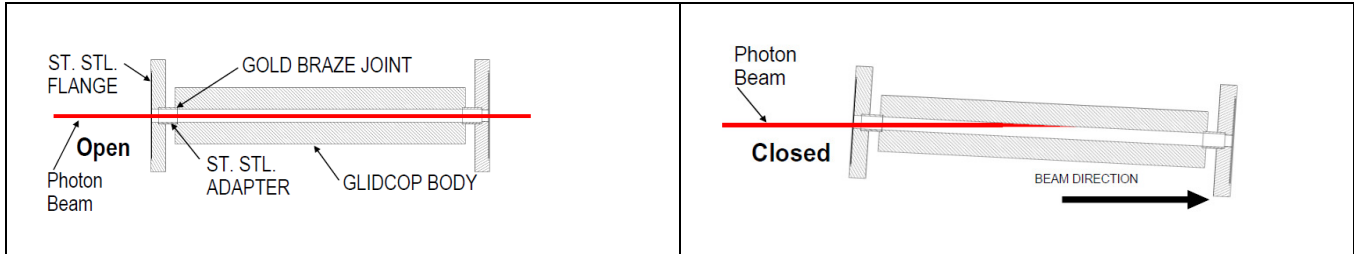
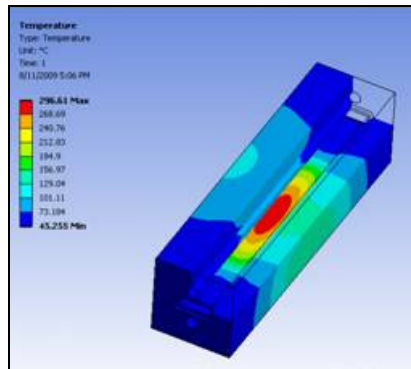


**Fig. 13-2:** Principle of the photon shutter.

Location	20 m
Absorbed Power	~10 kW
Beam incidence angle	~2°
Peak Power Density	~160.5 W/mm <sup>2</sup>
Component Length	~25 cm
Peak Temp	~296 °C

Thermal calculations on the photon shutter.  
(Courtesy of V. Ravindranath)



**Fast gate valve**

The fast gate valve (FGV) is to shut within a few milliseconds once triggered by FGV sensors located in the FE and beamline, whenever there is a sudden increase of pressure of a few decades. The stored beam has to be dumped prior to FGV closing, and the cause then investigated and mitigated.

**Safety shutter**

The safety shutter is actually a pair of shutters, required for redundancy, air actuated with independent redundant and diverse position sensing. An external lead design is being used as shown below.

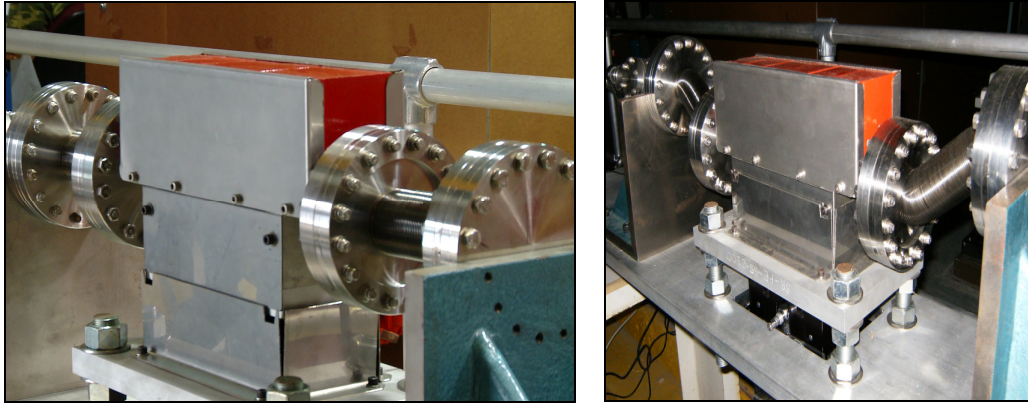


**Fig. 13-3:** Photographs of the safety shutter.

The safety shutter aperture will be increased from 21 mm to 38 mm. In addition to the primary aperture the edge welded bellows will be increased in size to 1.5" ID. Prior to final design of the damping wiggler safety shutter, cycle tests will be completed to confirm the fatigue life of the larger bellows.

### *Gate valve downstream of ratchet wall*

This slow gate valve, pneumatically actuated, with position sensing switches will be monitored and controlled by the SR vacuum PLC using vacuum sensors in the FE and beamlines. This gate valve cannot be removed after commissioning and must be protected from any exposure to beam.

## **A.2 Front end ray tracings**

Preliminary front end x-ray tracings have been developed for the damping wiggler beamline to confirm the apertures and locations of the various front end components. The FE ray tracings are shown in appendix B. There are two sets of traces: synchrotron and bremsstrahlung. These are performed in the vertical and horizontal planes. In general, the first step consists of tracing the synchrotron radiation of the front end whose purpose is to:

- define mask size
- obtain the maximum fan from tolerances on the beam position and manufacturing
- obtain the minimum aperture of components (slits, BPM)
- obtain the maximum lead collimator aperture (including manufacturing and positional tolerance)
- verify that the synchrotron rays impinge only on the optical devices intended for that purpose.

This defines the inner dimension of devices such as slits, collimators, apertures in stops and is followed by bremsstrahlung tracing, whose purpose is to:

- define the outer collimator dimensions
- define outer stop dimensions

Tracings are predicated on assumptions concerning tolerances and sources of the synchrotron and bremsstrahlung:

- XPD required (downstream) aperture of the FE FMK =  $1.1 \times 0.15 \text{ mrad}^2$
- Therefore, at 20.65 m, the FE Fixed Mask aperture is  $22.7 \times 3.1 \text{ mm}^2$  (nominal fixed mask aperture without manufacturing tolerance added)
- $\pm 0.2 \text{ mm}$  manufacturing tolerance
- $\pm 0.5 \text{ mm}$  linear deviation of the beam defining the source points (inboard and outboard – floor and roof)

- $\pm 0.25$  mrad beam mis-steering (used to define the upstream aperture of the mask)

The assumptions are:

- Bremsstrahlung horizontal inboard source point: source is set at 4 m downstream of the centreline of the straight
- Bremsstrahlung horizontal outboard source point: source is set at 38 mm by the vacuum vessel
- Bremsstrahlung vertical source points given by vacuum vessel
- Stopped bremsstrahlung rays must be at least 36 (+2) mm from the extreme outer edge (lead). 24 (+2) mm for tungsten (total length in case of inserted aperture).
- Stopped bremsstrahlung rays must be at least 12.5 mm from the inner edge of inserted aperture.
- Shutters, collimators and stops at least 300 mm lead or 200 mm of tungsten thick in the beam direction

Ray tracing relies on input specific to the XPD beamline, assumptions and tolerances and radiation protection guidelines. All these are documented in references given in appendix B.4. The maximum fan, bremsstrahlung horizontal inboard source point, and ratchet wall collimator serve as input to the beamline ray tracings.



## B.2 Beamline layout

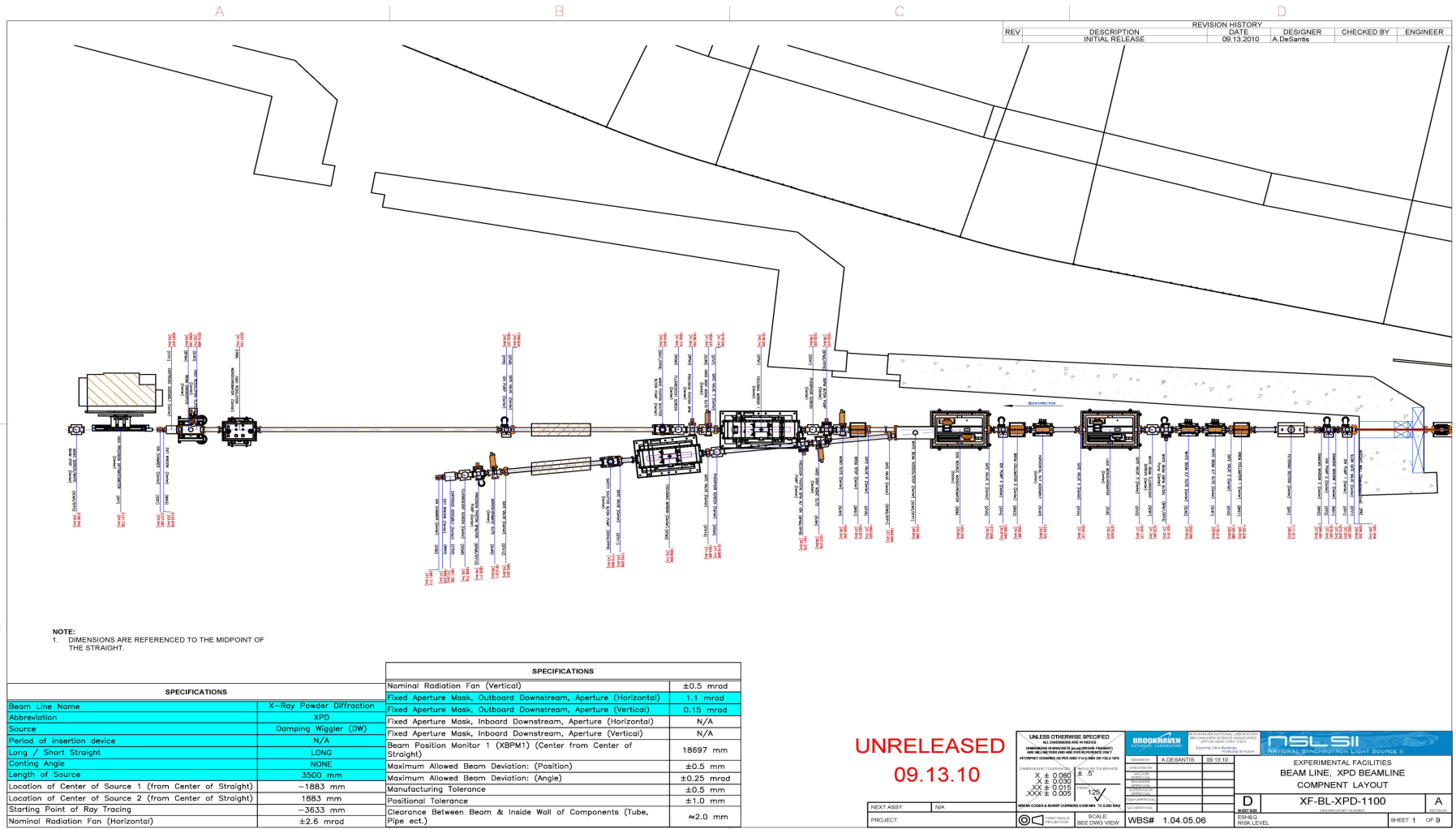


Fig. 13-5: Beamline layout plan view.

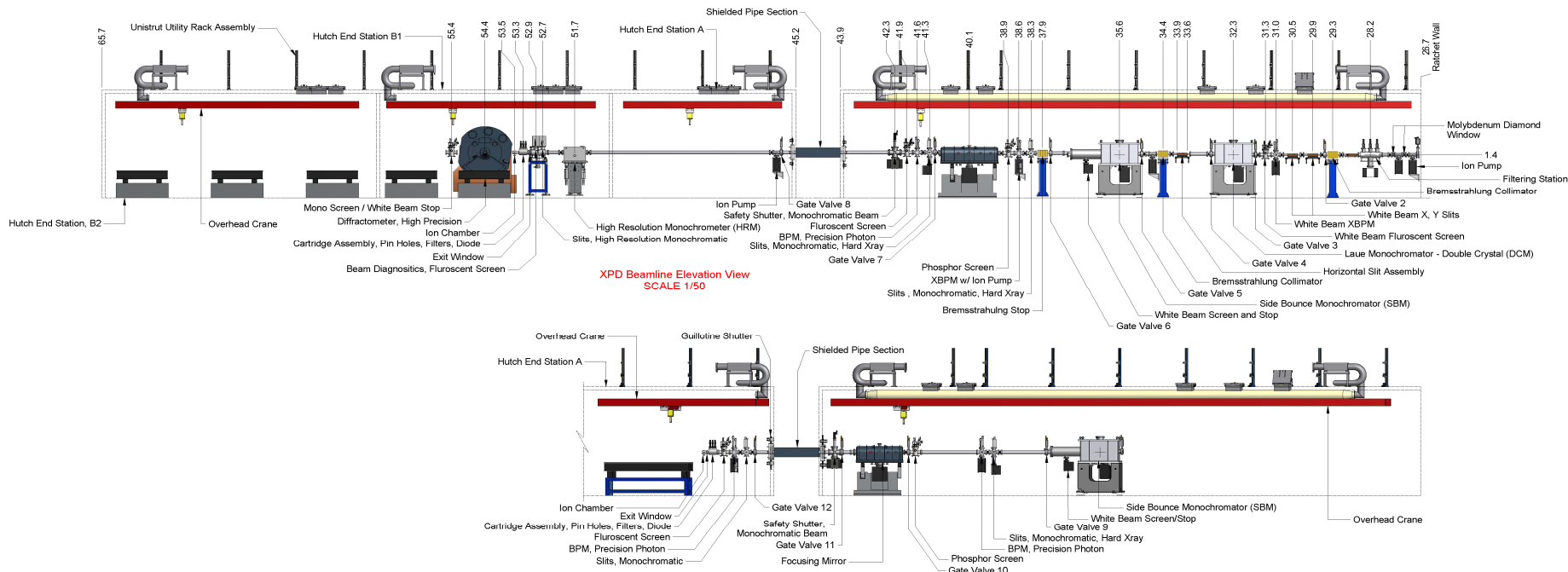


Fig. 13-6: Elevation layout of the XPD beamline, NSLS-II.

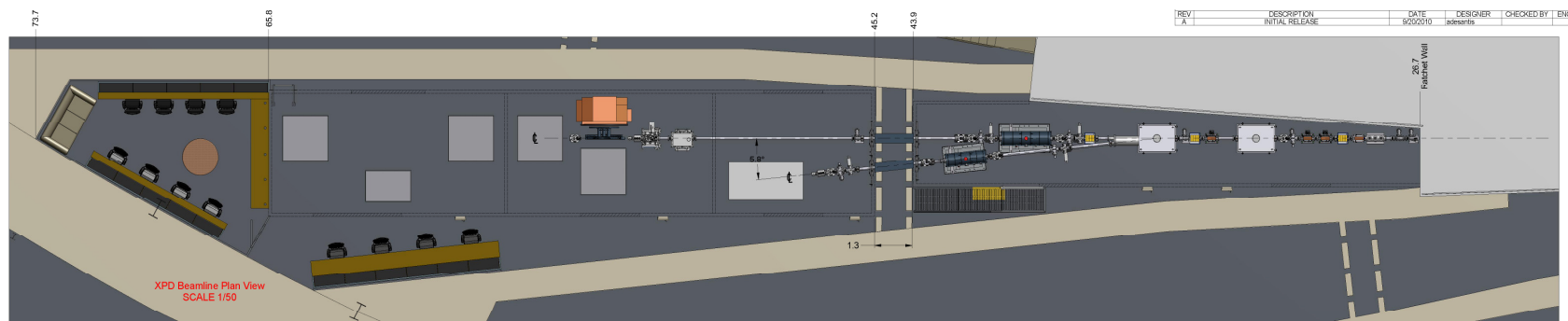
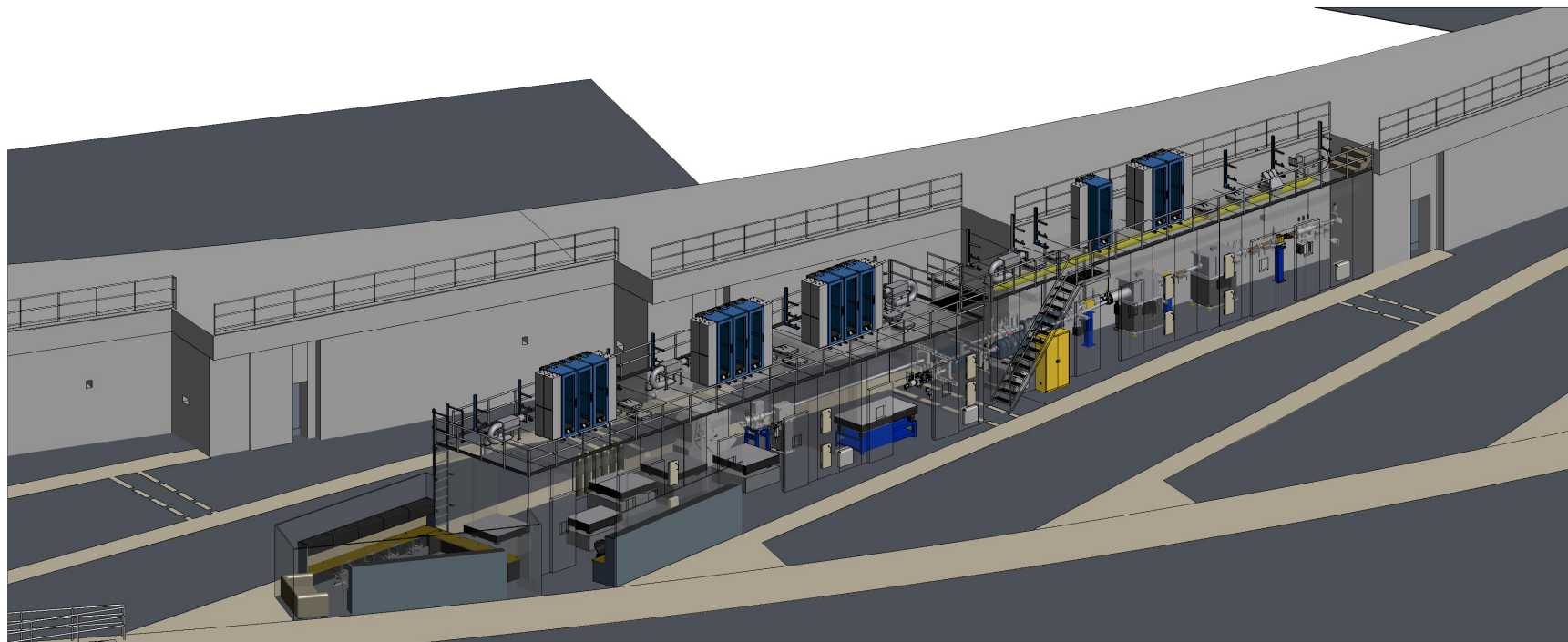
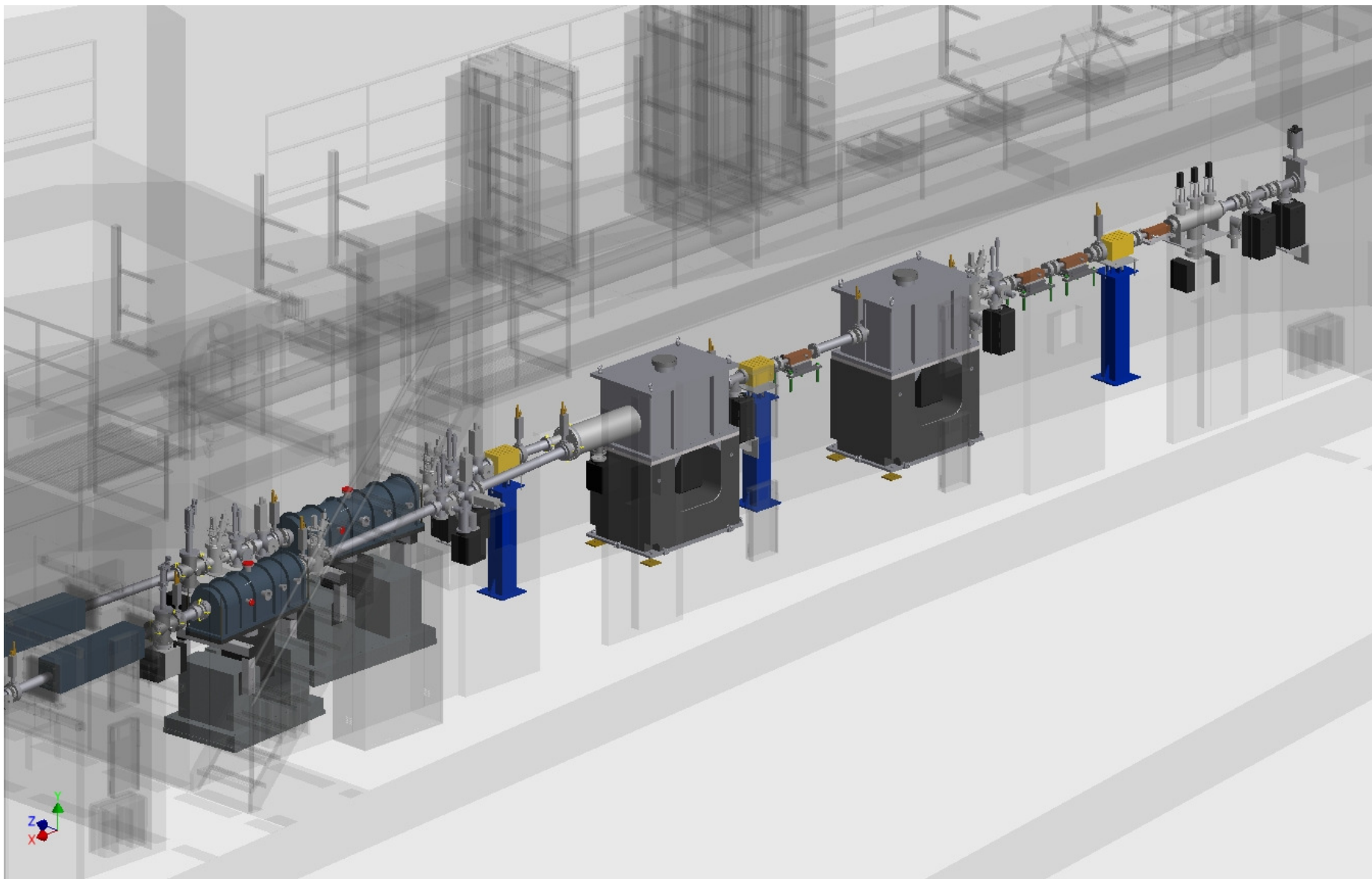


Fig. 13-7: Beamline plan: shielding enclosure layout.



**Fig. 13-8:** Beamline overall perspective view.



**Fig. 13-9:** Conceptual layout for the powder diffraction beamline FOE.

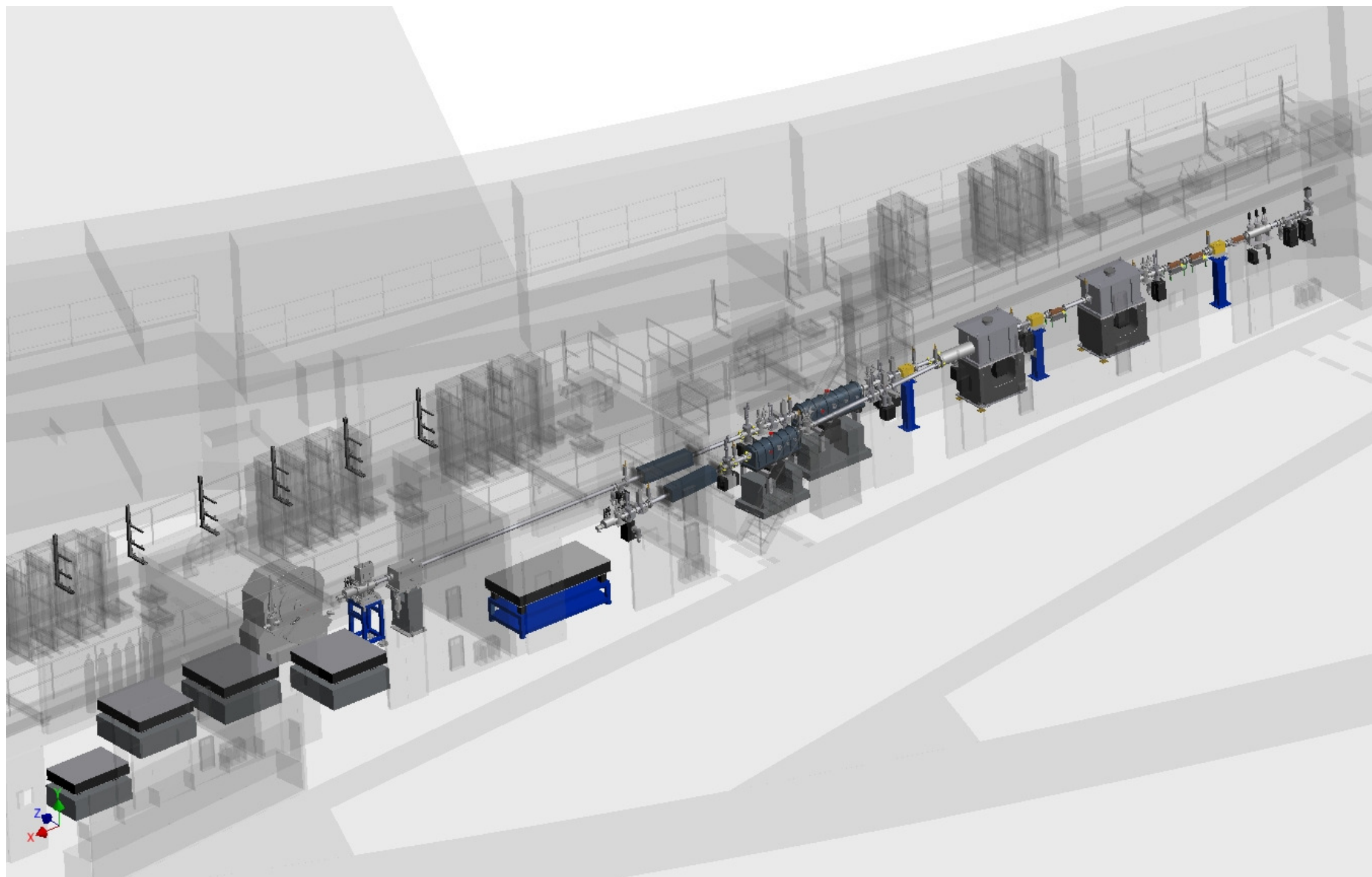


**Fig. 13-10:** Conceptual layout for the powder diffraction beamline: FOE and all three endstations.

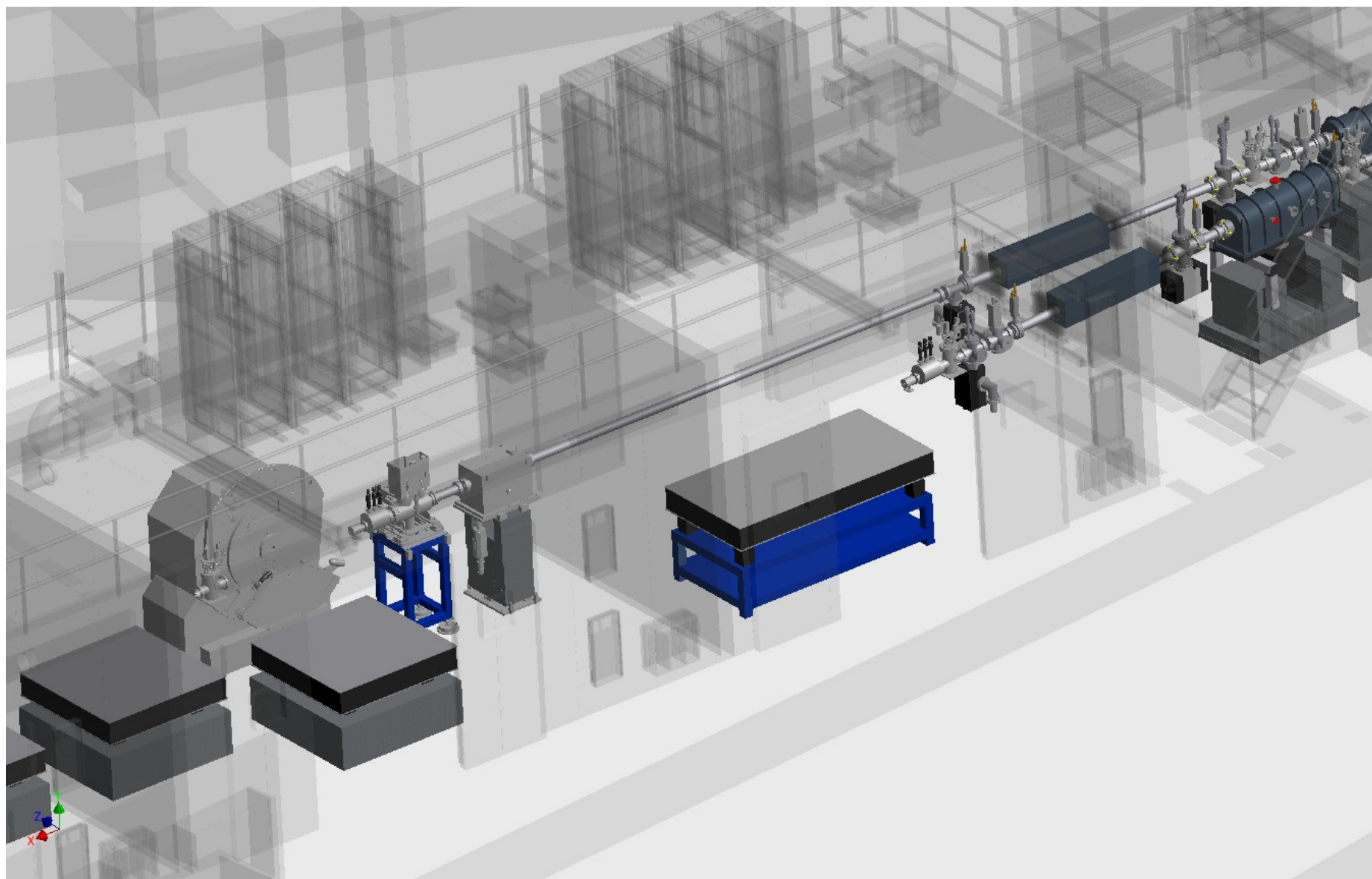


Fig. 13-11: Conceptual layout for the powder diffraction beamline endstations.

## B.3 Synchrotron ray trace

List of supporting documents:

- Front end ray tracing tutorial, NSLS-II – 04/09/10<sup>19, 20</sup>
- XPD ray tracings guidelines<sup>21</sup>
- Spreadsheet with input parameters to ray tracing<sup>22</sup>
- Reference for numbers used in Spreadsheet<sup>23</sup>
- Mask analysis. Needed for angle of incidence on mask<sup>24, 25</sup>
- Ray tracing guidelines ALS<sup>26</sup>

---

<sup>19</sup> <http://groups.nsls2.bnl.gov/acceleratorsystems/mech/frontends/Front%20End%20Requirements/Front%20Ends%20Ray%20Tracing%20Procedure%204-9-2010.ppt>

<sup>20</sup> <http://groups.nsls2.bnl.gov/acceleratorsystems/mech/frontends/Front%20End%20Requirements/Front%20Ends%20Configurations%20NSLS-II,%20specifications%20and%20ray%20tracings.ppt>

<sup>21</sup> <http://groups.nsls2.bnl.gov/acceleratorsystems/mech/frontends/XPDDWBeamline/Forms/AllItems.aspx>

<sup>22</sup> <http://groups.nsls2.bnl.gov/acceleratorsystems/mech/frontends/Front%20End%20Requirements/Front%20end%20specifications.xls>

<sup>23</sup> <http://groups.nsls2.bnl.gov/ExperimentalFacilities/DocumentReferenceLibrary/RSIDocuments/Forms/AllItems.aspx?RootFolder=/ExperimentalFacilities/DocumentReferenceLibrary/RSIDocuments/1.04.06%20Front%20Ends%20for%20Project%20Beamlines&FolderCTID={BC324BE7-6001-402C-9304-D25DD622E1CC}>

<sup>24</sup> <http://groups.nsls2.bnl.gov/acceleratorsystems/mech/frontends/HXNBeamline/Forms/AllItems.aspx>

<sup>25</sup> [http://groups.nsls2.bnl.gov/technotes/TechNotes/20\\_Bremsstrahlung\\_Ray\\_Tracing\\_%20Guidelines\\_NSLS\\_II\\_beamlines\\_Front-ends.pdf](http://groups.nsls2.bnl.gov/technotes/TechNotes/20_Bremsstrahlung_Ray_Tracing_%20Guidelines_NSLS_II_beamlines_Front-ends.pdf)

<sup>26</sup> [http://www.als.lbl.gov/als/bdguide/BDG.print\\_version.pdf](http://www.als.lbl.gov/als/bdguide/BDG.print_version.pdf)

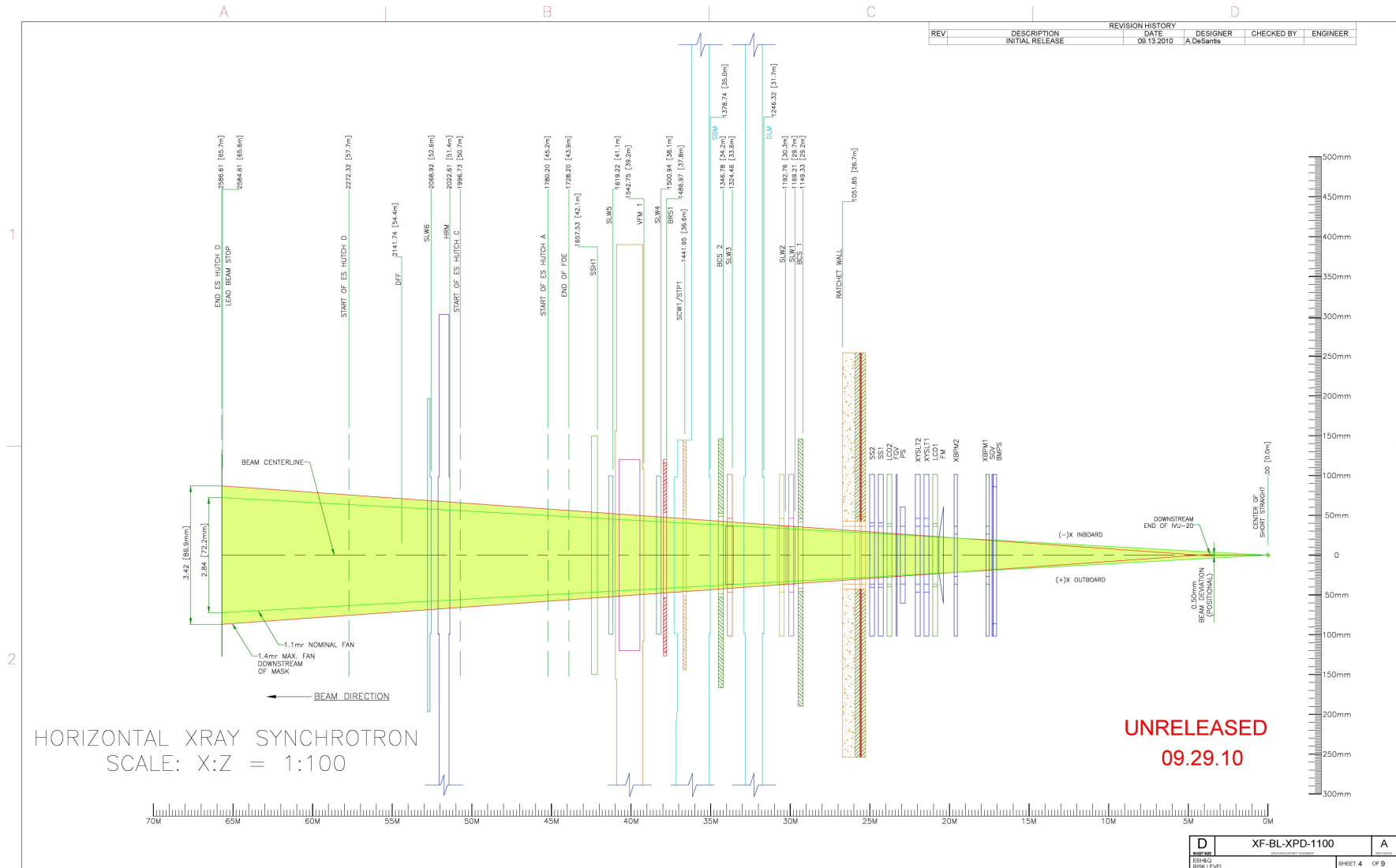


Fig. 13-12: Horizontal synchrotron radiation optical aperture ray tracings.

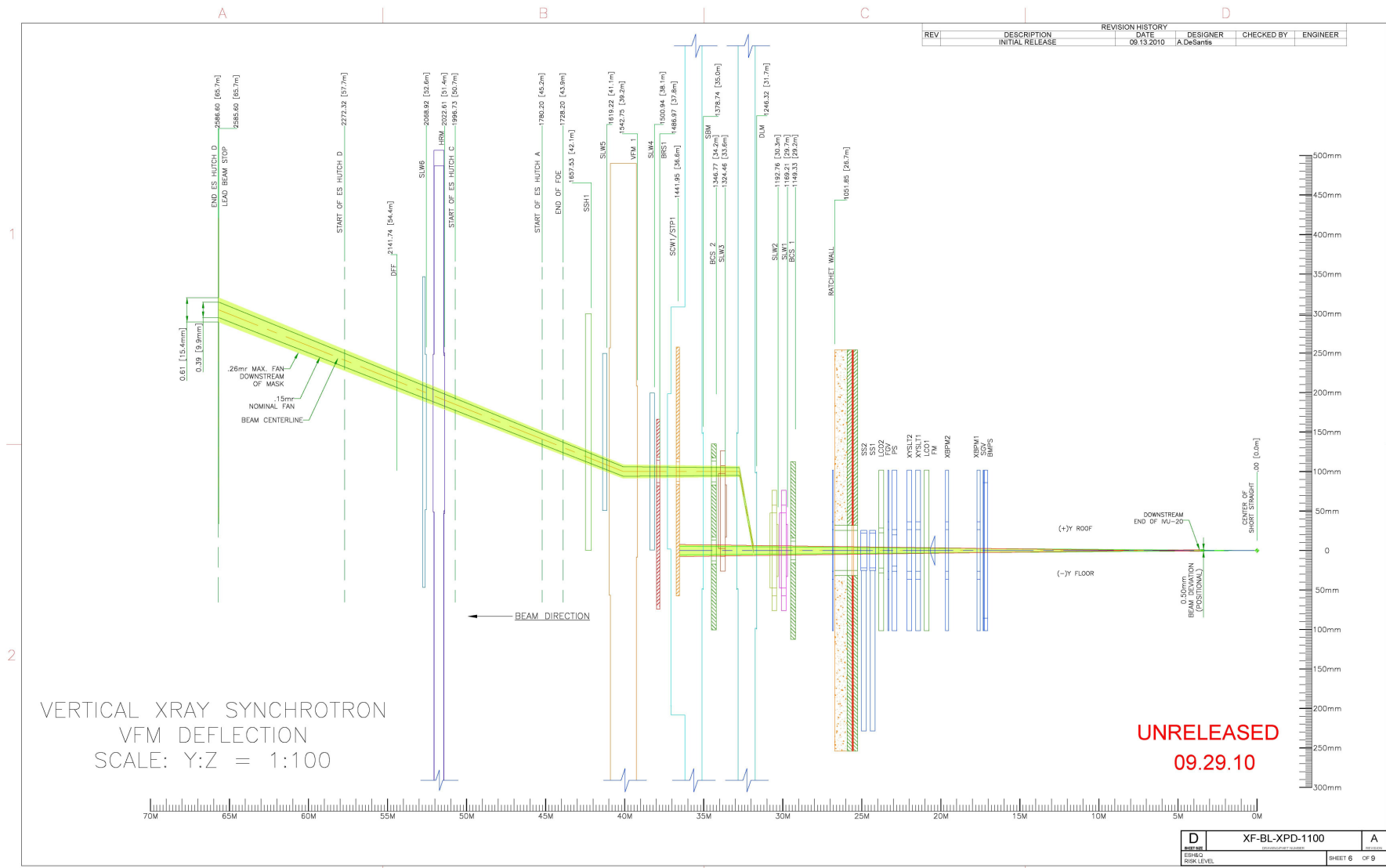


Fig. 13-13: Vertical synchrotron radiation optical aperture ray tracings.

### B.4 Bremsstrahlung ray trace

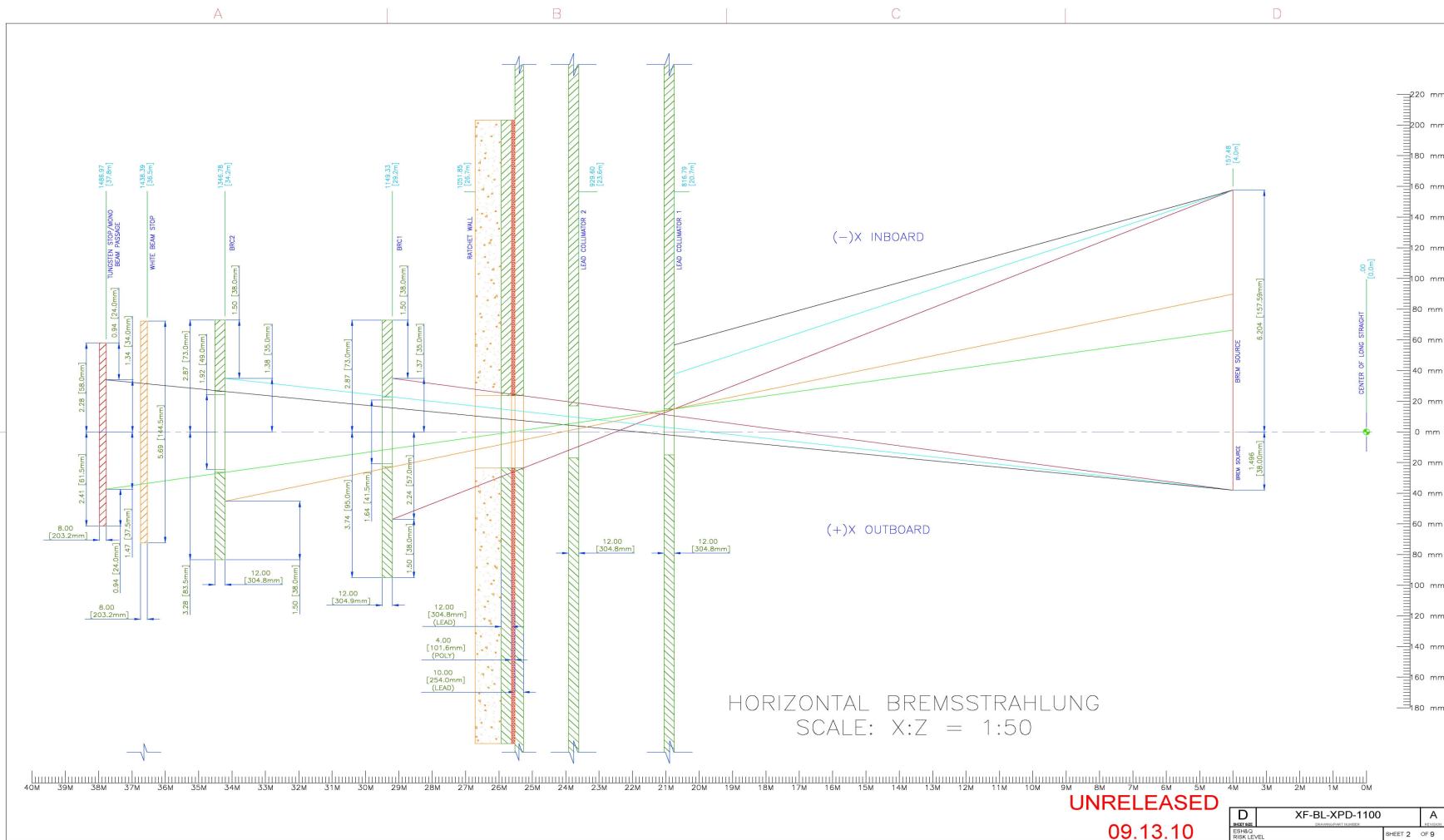
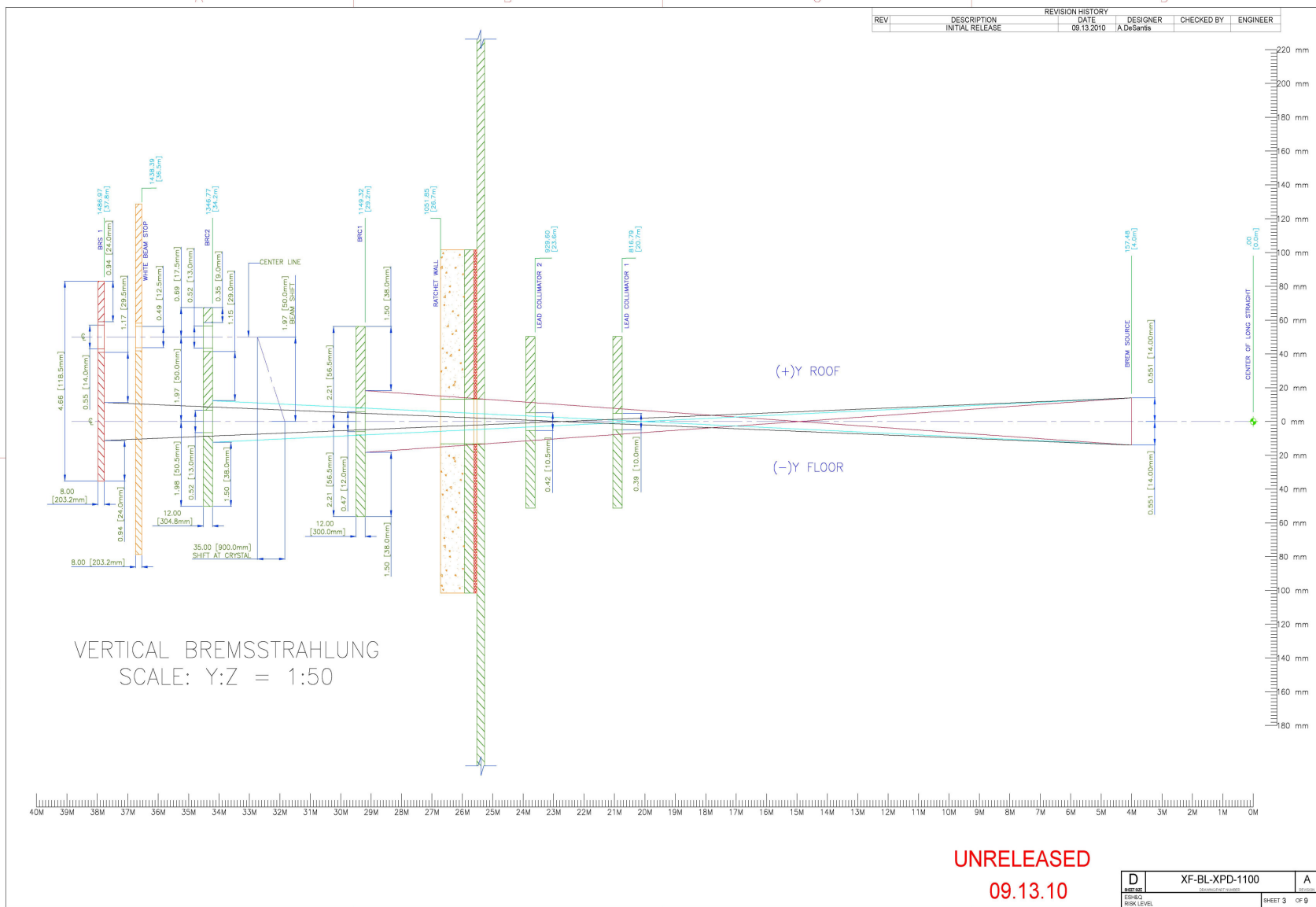


Fig. 13-14: Horizontal bremsstrahlung ray tracings.



UNRELEASED  
09.13.10

**Fig. 13-15:** Vertical bremsstrahlung ray tracings.

## B.5 Control diagrams

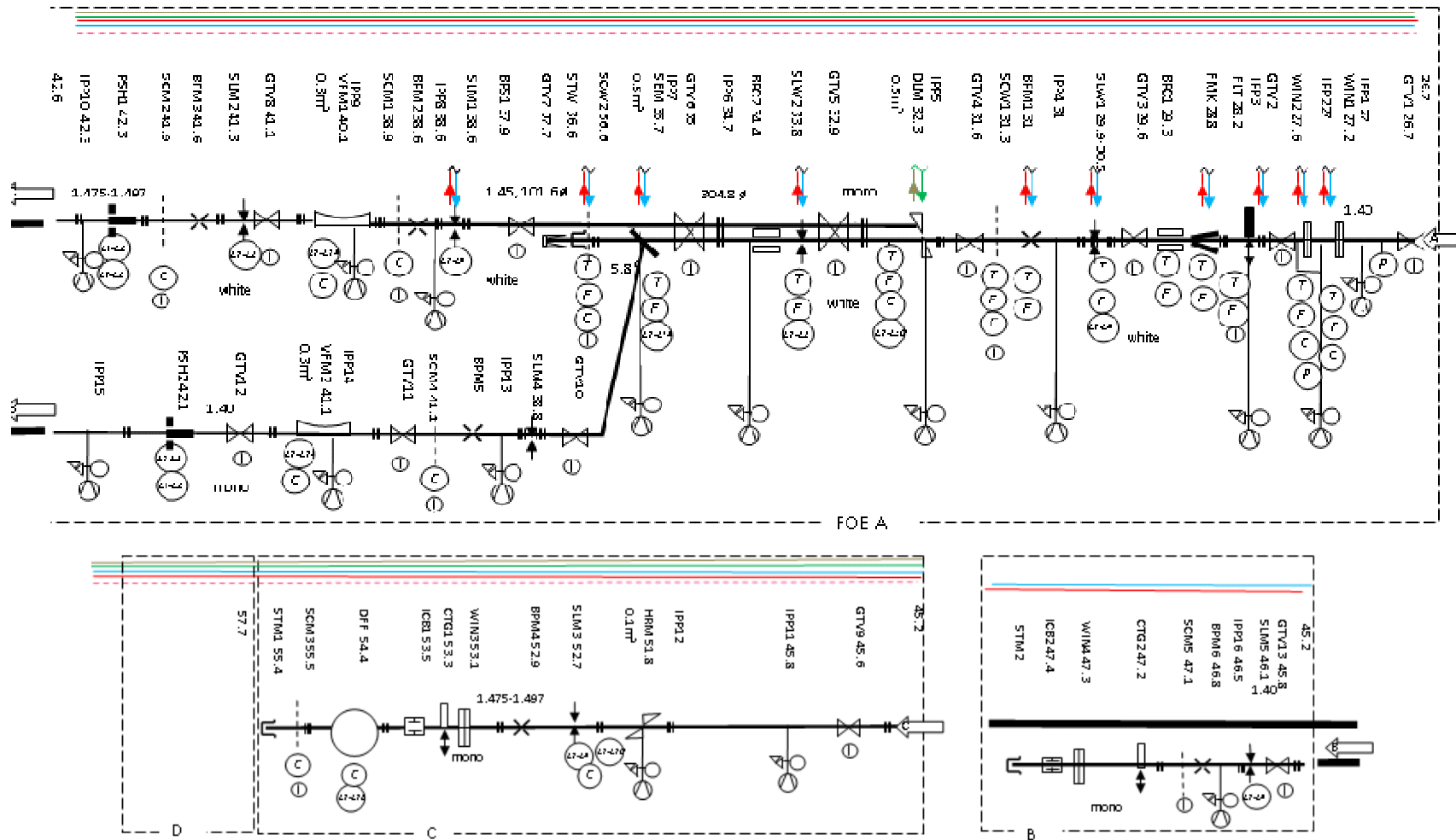


Fig. 13-16: Beamline Schematic. See legend on next page.

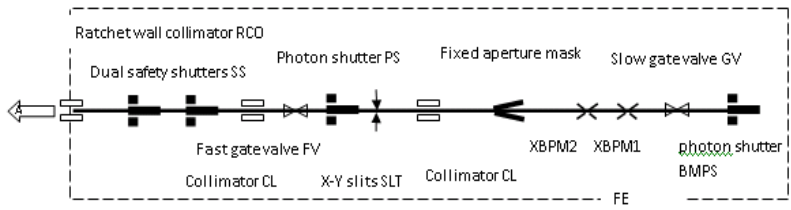


Fig. 13-17: FE Schematic.

Belows Gate valve GTV Ion pump IPP Pirani, CCT gage, bleed valve	Filter: ELT White beam slits SLW Mono beam slits SLM High resolution HRM	Mirror VFM Double Laue DLM Side Bounce SBM Ln2, supply, return DI water supply, return	White beam stop STW Mono beam stop STM White screen SCW Mono screen SCM Photon shutter SSH Xbpm BPM Pneumatic shielded pipe	Window WIN Beam collimator BRC Beam stop BRS Fixed mask FMK	Ion chamber ICB Diffractometer DFF Cartridge CTG
Limit On/off Camera	Flow Temperature Pressure				

Fig. 13-18: Symbol legend for process and instrumentation diagrams.

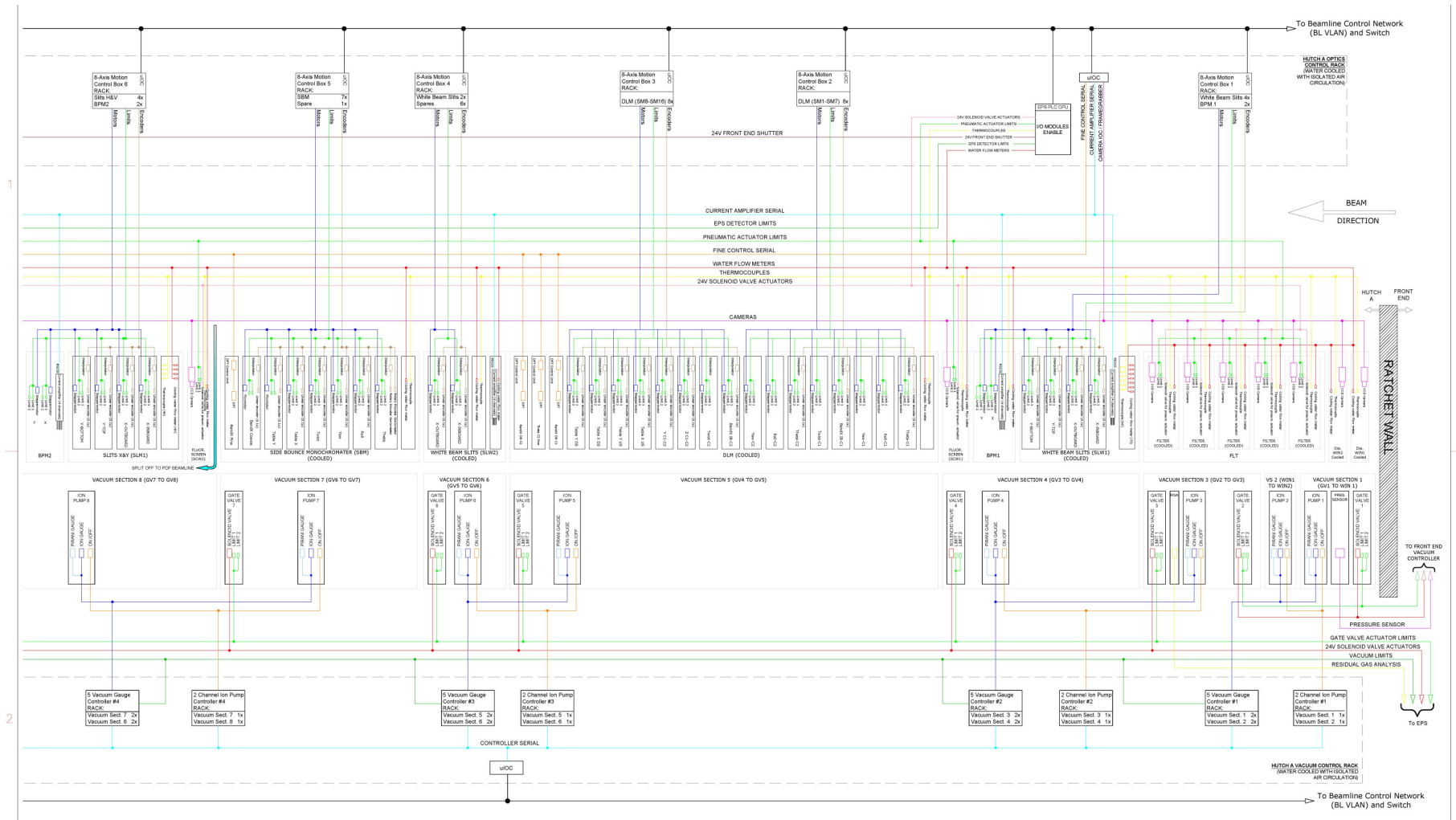


Fig. 13-19: Control block diagram, part 1 of 3.

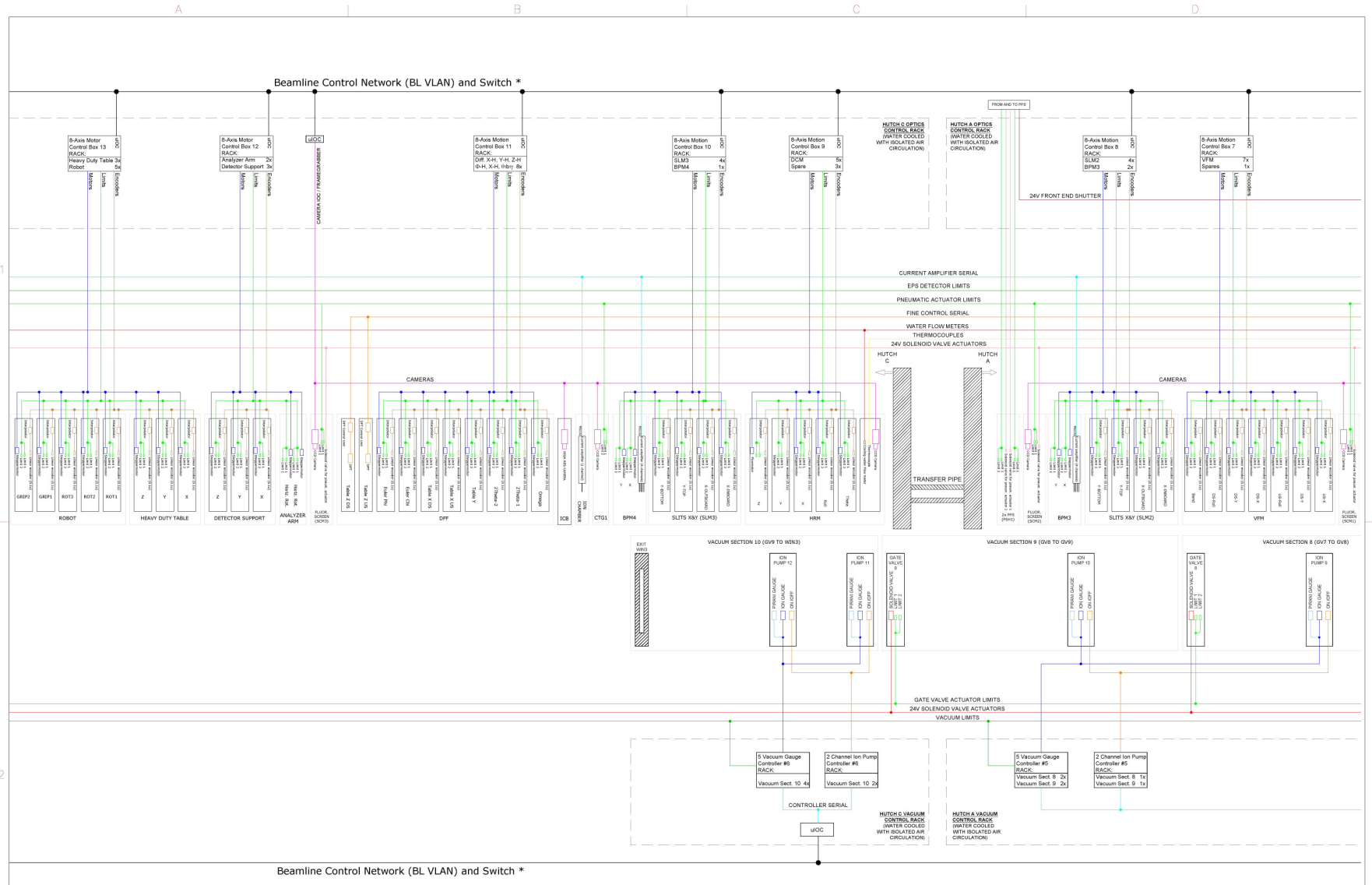


Fig. 13-20: Control block diagram, part 2 of 3.

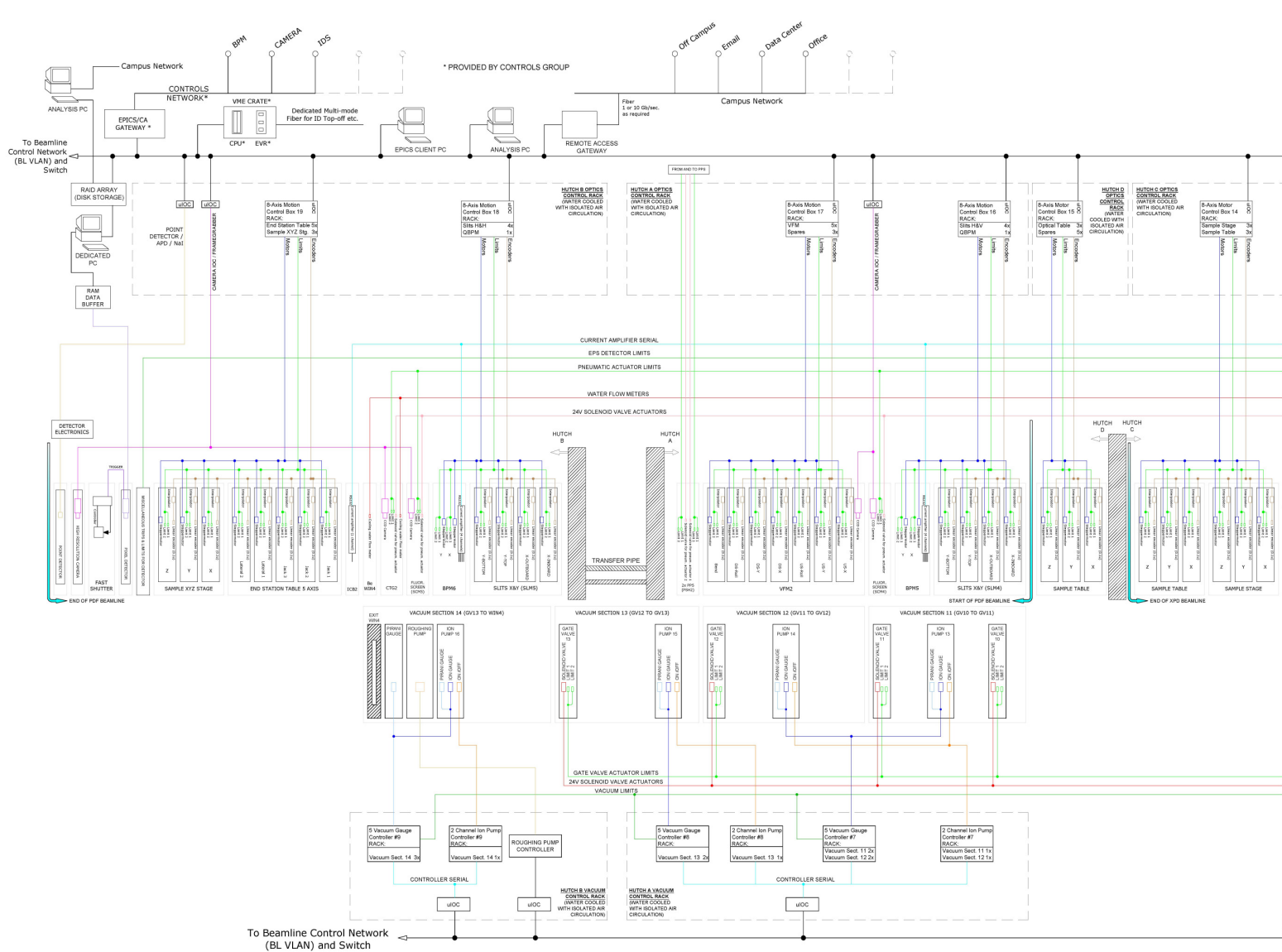


Fig. 13-21: Control block diagram, part 3 of 3.

## B.6 Personnel safety system schematic layout

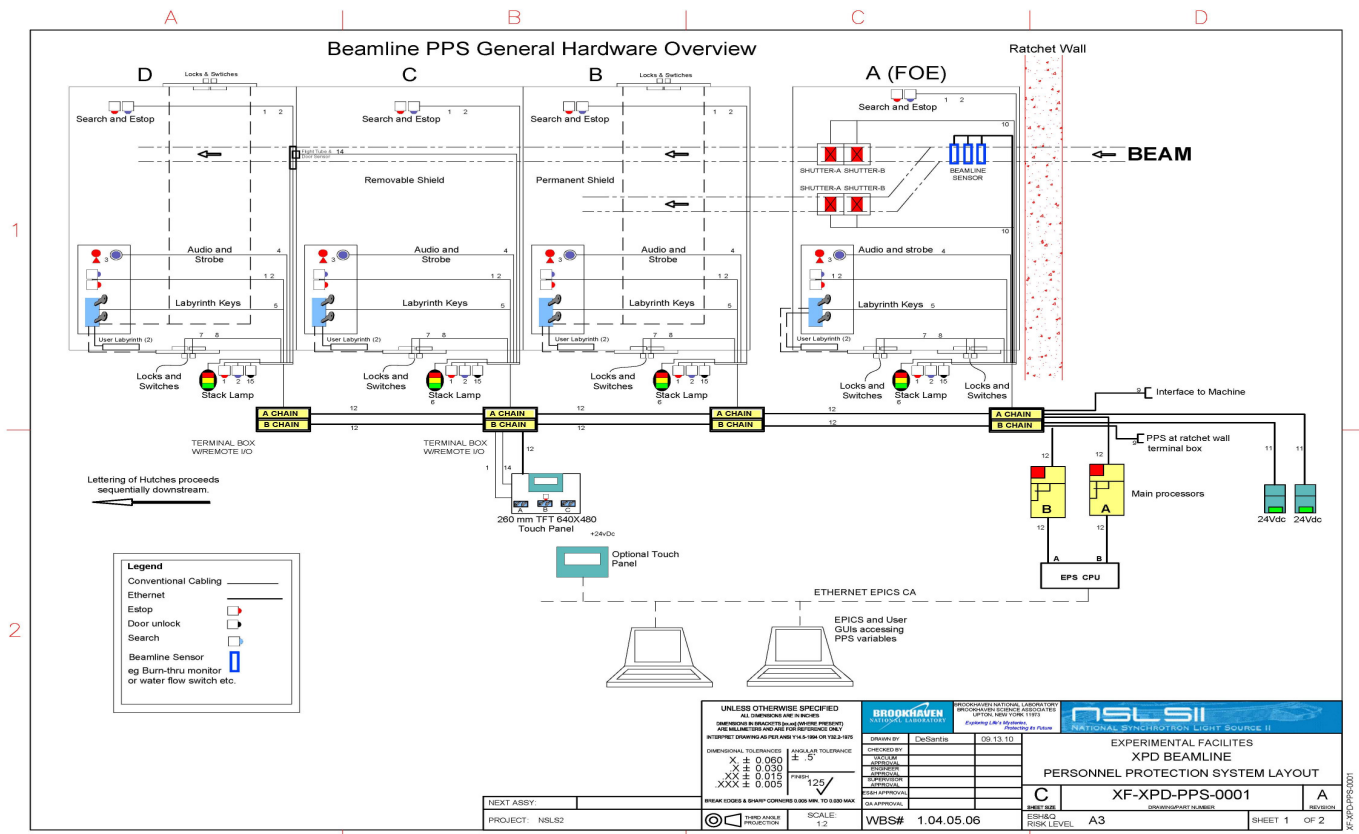


Fig. 13-22: Personnel safety system schematic.

## B.7 Vacuum system

See the Process & Instrumentation Diagram in Fig. 13-16.

The front end contains one or more all-metal isolation valves, a fast-closing valve, and a pneumatically actuated photon shutter (which is between the storage ring and the fast valve). Diamond windows isolating the beamline vacuum are the first components in the FOE past the valve. These windows and the first valve in the beamline are sufficient to isolate the beamline vacuum from that of the frontend and thus eliminate the need for a fast gate valve. Gate valves and fixed windows define vacuum sections. Each vacuum section will be equipped with at least one ion pump equipped with cold cathode gages and/or Pirani gages and bleed/relief valves. Each optical element with substantial volume also comes equipped with an ion pump. The base pressure in all vacuum components upstream of non-UHV equipment which is directly exposed to the storage ring vacuum must be less than  $1.5 \times 10^{-9}$  Torr ( $2 \times 10^{-9}$  mbar) at all times during the normal operation of the beamline. However, during the initial scrubbing of components with synchrotron radiation, an increase in pressure by at most an order of magnitude may be allowed. The maximum pressure downstream of the vacuum window may reach any sub-atmospheric value, as long as the above condition is always maintained, and providing this is commensurate with radiation safety requirements. The storage ring vacuum is protected by fast sensor interlocks in case of catastrophic failure, and by ion gauge pressure interlocks in the event of a relatively slow leak. This beamline has one fast sensor placed less than the recommended 10 m from the fast valve, to allow enough time for the fast valve to close before arrival of the gas wave front in the event of a vacuum break. The fast sensor is interlocked with the front-end valves and shutters.

The section of the beamline subjected to white beam will be baked to eliminate residual gases in order to achieve a vacuum pressure below  $10^{-9}$  mbar. The section of the beamline with monochromatic beam is designed to reach a pressure in the  $10^{-8}$  mbar range. In addition to the large flanges of the monochromator doors (Viton sealed) all flanges will be designed according to the Conflat standard.

## C SPECIFICATIONS FOR THE ENCLOSURES

	Enclosure designation	28-ID-A	28-ID-B	28-ID-C	28-ID-D
<b>Enclosure type</b>		<b>DW FOE</b>	<b>DW ES-B</b>	<b>DW ES-C</b>	<b>DW ES-D</b>
<b>Enclosure description</b>	PD Beamline Optics enclosure	Endstation A	Endstation B	Endstation C	Endstation D
<b>Shielding material</b>		Lead	Lead	Lead	Lead
<b>Dimensions (m)</b>	Height max Width max Length max	3.5 2.87 17.18	3.5 4.21 5.5	3.5 4.21 7	3.5 4.21 8
<b>Shielding</b>	Side (lateral) panels Roof panels Downstream wall panels Additional downstream wall panel Guillotine	18 mm lead 10 mm lead 50 mm lead 50 mm lead (1 × 1 m) Downstream wall	4 mm lead 3 mm lead 4 mm lead 4 mm lead (1 × 1 m) N/A	4 mm lead 3 mm lead 4 mm lead 4 mm lead (1 × 1 m) N/A	4 mm lead 3 mm lead 4 mm lead 4 mm lead (1 × 1 m) N/A
<b>Entry 1</b>	Position Size (m) Type Floor groove PSS Interfaces Mounting plates for magn. lock, dual pos. switches.	Outboard side 2.4 H × 2.0 W Sliding double Yes Yes	Outboard side 2.4 H × 2.0 W Sliding double Yes Yes	Outboard side 2.4 H × 2.0 W Sliding double Yes Yes	Outboard side 2.4 H × 2.0 W Sliding double Yes Yes
<b>Entry 2</b>	Position Size (m) Type Floor groove PSS Interfaces Mounting plates for magn. lock, dual pos. switches.	Outboard side upstream 2.4 H × 1.0 W Sliding double Yes Yes	Inboard side 2.4 H × 2.0 W Sliding double Yes Yes	N/A N/A N/A N/A N/A	N/A N/A N/A N/A N/A
<b>Hoist</b>	Manual 1000 kg (double sliding rail)	Yes	Yes	Yes	Yes
<b>Labyrinths</b>		Positions as specified on drawing, to be sealed with anti-tamper screws except where locks or interlocks are specified.			
	Fluids labyrinth (on roof)	2	0	1	1
	Electrical labyrinth (on roof)	3	1	1	1
	Air inlet labyrinth, with fan and filter (on roof)	2	1	1	1
	Air outlet labyrinth (at base of sidewall)	1	1	1	1
	User access labyrinth (on sidewall)	1, with interlock switches	2, with interlock switches	1, with interlock switches	1, with interlock switches
	Liquid nitrogen labyrinth (on sidewall)	1	2	1	1
<b>Bridges</b>	As required for non-adjacent hutches along the same beamline per Contract, minimum clearances	1.64m-long top of FOE to hutch B	1.64m-long top of ES-B to FOE	N/A	N/A
<b>Other</b>	Attachment points for adjacent enclosures	N/A	Yes (ES-C)	Yes (ES-D)	Yes (ES-C)

## D LAUE MONOCHROMATIZATION

### D.1 Horizontally deflecting side bounce monochromator

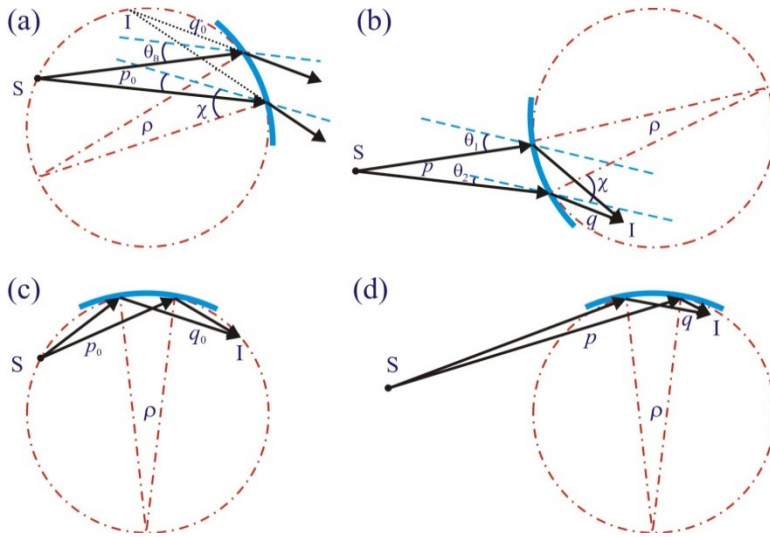


**Fig. 13-23:** The focusing geometries of the bent Laue/Bragg crystals (41).

Four cases of the focusing geometries of the cylindrically bent Laue/Bragg crystals are shown in Fig. 13-23: (a) Rowland Laue: the source and the virtual image are on the Rowland circle, (b) polychromatic focusing Laue: the source is on the convex side of the crystal and the image is real, (c) Rowland Bragg: monochromatic focusing, and (d) polychromatic focusing Bragg. The relation between the bending radius ( $\rho$ ), the source-to-crystal distance ( $p$ ) and the crystal-to-image distance ( $q$ ) is the following (41) (42) (43):

$$p_0 / p + q_0 / q = 2,$$

where  $p_0$  and  $q_0$  are those for the monochromatic focusing (Fig. 13-23(a) and (c)), given by

$$p_0 = \rho \cos(\chi \pm \theta_B),$$

$$q_0 = \rho \cos(\chi \mp \theta_B).$$

Here  $\theta_B$  is the Bragg angle and  $\chi$  is the asymmetry angle between the Bragg planes and the surface normal of the crystal. In the above equations,  $p$  is positive for a real source,  $q$  is of the same sign as  $p$  when the image and the source are on the same side of the crystal,  $\rho$  is positive if the source is on the concave side of the crystal. It is apparent that the bending radius of the Laue crystal depends on the choice of the asymmetry angle,  $\chi$ , for either the focusing or the Rowland case (Fig. 13-24).

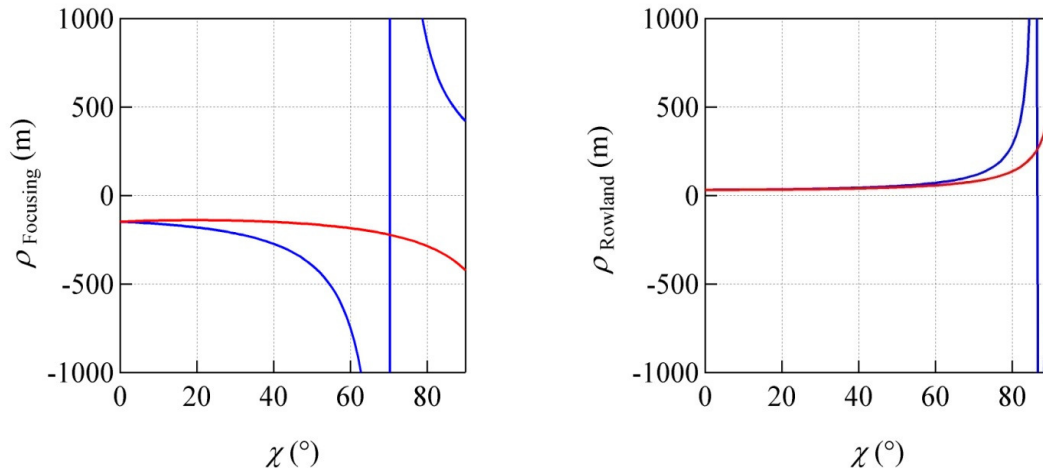


**Fig. 13-24:** The bending radius as a function of the asymmetry angle, with  $p = 36$  m,  $q = 12$  m for the focusing Laue case (left) and the Rowland Laue case (right). The red and the blue lines correspond to the upper and the lower signs in the geometric focusing equations.

The energy bandwidth  $\Delta E/E$  of the diffracted X-ray by a bent crystal is given by (7)

$$\Delta E/E = \cot \theta_B [\Delta\theta^2 + \omega_0^2 + (\sigma/p)^2]^{1/2}$$

where  $\Delta\theta$  is the variation of the incident angle due to the divergence  $\varphi$  of the beam,  $\omega_0$  is the intrinsic angular acceptance of the crystal, and  $\sigma/p$  is the angular aperture of the source size. Note that all the quantities above are referring to the horizontal direction (subscript  $h$ ) for the side bounce monochromator (SBM) and the vertical direction (subscript  $v$ ) for the double Laue monochromator (DLM). For the Damping Wiggler source at NSLS-II, the horizontal beam size is small ( $\sigma_h \approx 137\mu\text{m}$ ), which will introduce a  $\Delta E/E$  less than  $10^{-4}$ . For a flat perfect crystal,  $\omega_0$  is simply the Darwin width. For a bent crystal,  $\omega_0$  also accounts for the change in the Bragg angle across the crystal thickness (crystal distortion; see section 6.1). The integrated reflectivity of a Laue crystal with a bending radius of several tens of meters is 1-2 orders of magnitude larger than that of a perfect crystal. The divergence term,  $\varphi_h = h/p$ , where  $h$  is the horizontal beam size at the monochromator position, broadens the energy bandwidth by

$$\Delta\theta = h [1/p_0 - 1/p].$$

Following these equations, one can optimize (1) the energy bandwidth, (2) the beam spot size and (3) the reflectivity by selecting the reflection plane, the bending radius, the asymmetry angle and the thickness of the crystal.

Three possible geometries of the SBM of the XPD beamline are compared here: (a) the focusing Laue, (b) the Rowland Laue, and (c) the Rowland Bragg. Since the side bounce angle ( $2\theta_B \approx 5.8^\circ$ ) is preselected (section 4.2 for details), three possible optimized energies are calculated using different reflection planes. The ray tracing and calculation were performed using the SHADOW (44) VUI 1.08. The results are listed in Table 13-1. Note that the total flux is calculated analytically by

$$I = I_0 R_{int} / \tan(\theta_B) / 0.1\%$$

where  $I_0$  is the total flux (ph/s/0.1%BW) after the aperture,  $R_{int}$  is the integrated reflectivity (in radians) of the curved crystal.

All three designs give comparable output flux (photon/s) while each has its characteristic drawbacks. In the Laue case, the radius  $\rho$  is comparable to  $p$  (or  $q$ ). Therefore the Laue crystal is normally easier to handle because it has a smaller crystal size (large incidence angle), is easy and has stable bending (radius  $\approx$  tens of meters and increases with the asymmetry angle). The resulting bandwidth  $\Delta E$  depends on thickness and is much larger than that of the Bragg crystal. The focusing Laue case can provide small beam size but poor energy resolution due to the source divergence. On the other hand, the Rowland Laue case offers reasonable resolution and small beam divergence but

non-focused beam and lower flux. However, by carefully choosing the asymmetry angle  $\chi \approx 35^\circ$ , the bending radius  $\rho$  and the crystal thickness  $T_0$ , one can get almost the same flux as in the Bragg case as a result of the broadening of the rocking curve. The Bragg case can satisfy both the focusing geometry and the Rowland condition by choosing the correct asymmetry angle.  $\Delta E/E$  is small (no thickness effect – it is absorption limited) and the source size is demagnified. Since the radius of the Bragg crystal is  $\sim 10$  times larger than that of the Laue crystal, the sensitivity to thermal distortions is higher. In addition, the small Bragg angle at high energy (75 keV) implies a large crystal size (typically  $\geq 40$  mm). As a result, the alignment, focusing and stability become a concern. Moreover, the large divergence of the output beam reduces the instrumental resolution significantly:  $\Delta E/E = \Delta\theta / \tan\theta \approx 2\%$  if  $\Delta\theta \approx 1.1\text{mrad}$  (45).

**Table 13-1:** Comparison of the three cases for the PDF branchline with:

$E = 74.8$  keV,  $p = 35.7$  m,  $q = 11.7$  m,  $l_0 = 2.1 \times 10^{13}$  ph/s/0.1%BW, crystal thickness  $T_0 = 3$  mm. Crystal: 311 reflection,  $\theta_B = 2.9^\circ$ , Laue:  $\chi = 35^\circ$ , Bragg:  $\chi = 88.53^\circ$ .

Case	Focusing Laue		Rowland Laue		Bragg
$\rho$ (h) (m)	- 45.8	- 45.8	42.1	42.1	469
Slit:	No	Yes	No	Yes	No
$\Delta E/E$ ( $10^{-3}$ )	50	1.0	0.8	0.8	0.7
Horizontal beam size (mm)	0.8	0.5	50	1	0.5
Horizontal divergence (mrad)	2.5	0.13	1.1	0.021	1.1
Flux (ph/s)	$1.3 \times 10^{13}$	$2.9 \times 10^{11}$	$1.3 \times 10^{13}$	$2.5 \times 10^{11}$	$1.1 \times 10^{11}$
Flux (ph/s/eV)	$3.8 \times 10^9$	$3.8 \times 10^9$	$2.3 \times 10^{11}$	$4.5 \times 10^9$	$2.1 \times 10^9$
Flux (ph/s/mm)	$1.7 \times 10^{13}$	$5.8 \times 10^{11}$	$2.5 \times 10^{11}$	$2.5 \times 10^{11}$	$2.4 \times 10^{11}$

One possible design of the SBM of the XPD beamline is proposed here. The crystal is cut with at an angle of  $9.6^\circ$  to the (111) plane, and the bending axis is in the  $[0\bar{1}1]$  direction. The reflection planes for the three energies with the same Bragg angle ( $2.9^\circ$ ) are: (311) for 74.8 keV, (022) for 63.8 keV and (111) for 39.1 keV. The corresponding asymmetry angles are  $39.1^\circ$ ,  $25.7^\circ$ , and  $9.6^\circ$  respectively. With a large rotation stage, this single Laue crystal can cover all three energies and both the focusing and Rowland cases as need arises. The expected performances are listed in Table 13-2. The slit size regulates the energy resolution in the focusing Laue case and the beam size in the Rowland Laue case, while the total flux decreases accordingly.

**Table 13-2:** Expected performance of the SBM with:  $p = 35.7$  m,  $q = 11.7$  m, crystal thickness  $T_0 = 3$  mm.

Case	Focusing Laue			Rowland Laue		
$E$ (keV)	39.1	63.8	74.8	39.1	63.8	74.8
$l_0$ (ph/s/0.1%BW)	$3.7 \times 10^{14}$	$5.3 \times 10^{13}$	$2.1 \times 10^{13}$	$3.7 \times 10^{14}$	$5.3 \times 10^{13}$	$2.1 \times 10^{13}$
Transmission (filtering) <sup>1</sup>	22%	47%	52%	22%	47%	52%
$\rho$ (h) (m)	- 36.0	- 36.9	- 48.9	35.9	40.6	44.2
Slit	No	No	No	No	No	No
$\Delta E/E$ ( $10^{-3}$ )	46	50	47	0.9	0.8	0.8
Horizontal beam size (mm)	1	0.5	0.8	52	56	50
Flux (ph/s)	$3.3 \times 10^{13}$	$3.2 \times 10^{13}$	$1.3 \times 10^{13}$	$2.9 \times 10^{13}$	$2.9 \times 10^{13}$	$1.3 \times 10^{13}$
Flux (ph/s/eV)	$1.8 \times 10^{10}$	$1.0 \times 10^{10}$	$3.8 \times 10^9$	$6.2 \times 10^{11}$	$5.8 \times 10^{11}$	$2.3 \times 10^{11}$
Flux (ph/s/mm)	$3.3 \times 10^{13}$	$6.4 \times 10^{13}$	$1.7 \times 10^{13}$	$5.6 \times 10^{11}$	$5.1 \times 10^{11}$	$2.6 \times 10^{11}$

<sup>1</sup> The filtering follows the scheme presented in section 5.4.2. Full vertical acceptance of the 0.15 mrad beam is assumed.

## D.2 Sagittally focusing double-crystal Laue monochromator

After the sagittally bent Laue crystal monochromator was pioneered by Z. Zhong, et al. (6) (7) (8) (9), it has been tested and used on several beamlines at NSLS. The sagittal bending of the asymmetric Laue crystal provides focusing in the sagittal plane (typically used for the horizontal focusing of the large fan of a wiggler or bending magnet). The anticlastic bending in the meridional plane due to the anisotropic elasticity of the crystal (e.g., silicon) can be utilized in the inverse-Cauchois geometry to obtain better energy resolution in the vertical diffraction plane.

The sagittal focusing condition for the double Laue crystal monochromator is given by (7)

$$1/F_1 + 1/F_2 = 4 \sin \theta_B \sin \chi / R_s$$

where  $F_1$  and  $F_2$  are the source-to-crystal and the crystal-to-sample distances respectively,  $\theta_B$  is the Bragg angle,  $\chi$  is the asymmetry angle between the Bragg planes and the surface normal, and  $R_s$  is the sagittal bending radius. The anticlastic bending radius  $R_m$  is then given by  $R_m = R_s / C \nu$ , where  $\nu$  is the Poisson's ratio of the crystal for a given orientation and  $C$  is a correction term accounting for the crystal shape and the bending mechanism.

Fig. 13-25a presents the sagittal radius  $R_s$  needed for the horizontal focusing as a function of  $\chi$  obtained from the above equation.  $\chi$  should not be too small ( $< 20^\circ$ ), so as not to break the crystal. The Poisson's ratio  $\nu$  is highly dependent on the crystal orientation due to the anisotropy of silicon. Fig. 13-25b shows  $\nu$  as a function of  $\chi$  in the (011) plane. As a result,  $R_s/\nu$  (knowing that  $R_m$  is proportional to  $R_s/\nu$ ) achieves the maximum at  $\chi \approx 40^\circ$  (see the solid line in Fig. 13-25c). Considering that the required  $R_m$  for the Rowland condition (see the dotted line in Fig. 13-25c) is given by

$$R_{m,Rowland} = F_1 / \cos(\chi \pm \theta_B),$$

One finds that the value of  $\chi$  where  $R_s/\nu$  and  $R_{m,Rowland}$  are the closest is about  $35^\circ$ . This optimized  $\chi$  can be obtained by using the (100) crystal and the (111) reflection ( $\chi = 35.26^\circ$ ). Once the asymmetry angle is chosen, the real  $R_m$  is then a function of the constant  $C$ , which can be experimentally determined. This leads to the choice of the crystal dimensions (i.e., length, width and thickness) and the bender design (see appendix E for details).

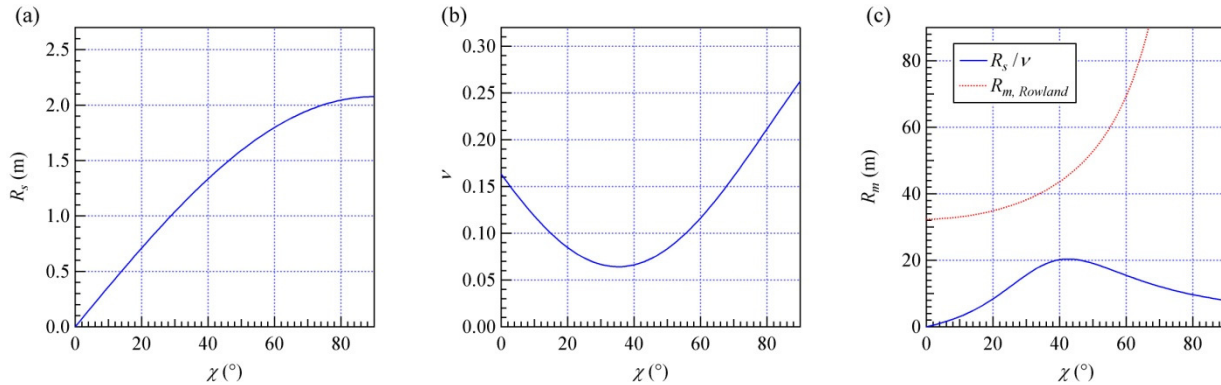


**Fig. 13-25:** (a)  $R_s$  as a function of  $\chi$ , (b) the Poisson's ratio  $\nu$  as a function of  $\chi$ , (c)  $R_s/\nu$  and  $R_m$  that satisfies the Rowland condition as a function of  $\chi$  at 50 keV, with  $F_1 = 32$  m and  $F_2 = 22$  m.

The rocking curve width,  $\omega_0$ , of the sagittally bent crystal is given by

$$\omega_0 \cong [\Delta\theta_D^2(T_0) + \omega_a^2]^{1/2}$$

where  $T_0$  is the thickness of the crystal and  $\omega_a$  is the Darwin width for a given material and Bragg reflection.  $\Delta\theta_D(T)$  is the total change of Bragg condition as a function of the crystal thickness,  $T$ , as a result of lattice distortion, given by (8)

$$\Delta\theta_D(T) = \frac{T}{R_s} \left\{ \begin{aligned} & \pm [(S'_{13} - CS'_{23}) \sin \chi \cos \chi - CS'_{23} \tan(\chi \mp \theta_B) + S'_{63} \cos^2 \chi] \\ & - \tan \theta_B [S'_{13} \sin^2 \chi + CS'_{23} \cos^2 \chi + S'_{63} \sin \chi \cos \chi] \end{aligned} \right\}$$

where  $S'_{ij} = S_{ij}/S_{33}$ , and  $S_{ij}$  are the elastic compliances of the crystal. Since the total distortion  $\Delta\theta_D(T_0)$  is proportional to the crystal thickness  $T_0$ , one has to increase the crystal thickness in order to achieve high flux at the detriment of energy resolution. Another limit for  $T_0$  is that stresses increase with thickness.

## E DESIGN OF THE DOUBLE LAUE MONOCHROMATOR

### E.1 Introduction

A large number of high energy beamlines use a Double Crystal Laue monochromator (DLM) to handle high energy beam, high heat load and large beam size. Different designs and bending concepts are adopted on those beamlines to address such challenges (Table 13-3). None of these designs attempts to control the bending of the DLM crystals in both the meridional and sagittal planes.

**Table 13-3:** Design characteristics of DLMs at other beamlines

	ID11-ESRF	ID1-APS	I12-DLS	X7B-NSLS	X17B1-NSLS
Energy range (keV)	23-140	50-130	50-150	35-50	40-120
Energy tunability	Yes	Yes	Yes	Yes	Yes
Beam size at sample (mm <sup>2</sup> )	0.5 × 0.2	1 × 0.01	50 × 15	0.3 × 1	2 × 1
Sagittal focusing	No	No	No	Yes	Yes
Meridional bending	Yes	Yes	Yes	No	No
Flux (ph/s)	10 <sup>10</sup> -10 <sup>12</sup>	10 <sup>10</sup> -10 <sup>12</sup>	10 <sup>10</sup> -10 <sup>12</sup>	10 <sup>8</sup> -10 <sup>9</sup>	10 <sup>9</sup> -10 <sup>11</sup>
Cooling	Water-InGa	LN	LN	none	Water

To the best of our knowledge, the closest double-bend mechanism is the one under test at the new X17A NSLS beamline for a single-crystal monochromator. The crystal is held on rotating hinges at its corners and bent along its four sides. The monochromator is designed to operate with a 3.5 mm horizontal beam footprint with no cooling. The major limitations of this design for our application are:

- a) the concept is not applicable for the ratio  $F_1/F_2$  of XPD
- b) since each crystal has eight degrees of freedom, matching the curvatures for the two crystals might prove challenging.
- c) the crystal is restrained at its corners and thus cannot expand under thermal load.
- d) achieving a uniform bending in both directions over a large beam footprint (35 mm (H) and 6 mm (V)) is difficult.
- e) implementing LN cooling in addition to the four point bending would increase the complexity of the current design.

A double-crystal sagittally focusing monochromator using a roller bender design with water cooling has been in use at the X17B1 beamline of NSLS (Fig. 13-26) for the past two decades, providing 67 keV x-rays. It focuses a horizontal divergence of 3 mrad to a brightness-limited horizontal dimension of 0.2 mm. The x-ray flux-density at the focus is a few hundred times larger than that of unfocused x-rays.

A leaf bender designed for sagittally focusing monochromator, with no cooling, has been implemented at X7B of NSLS (Fig. 13-27). Our recent tests at X7B show the horizontally focused beam at the energy of 39 keV, a demagnification factor of ~30 is achieved.

The rotation axes of the crystals at X7B and X17B1 are horizontal (vertically deflecting geometry).

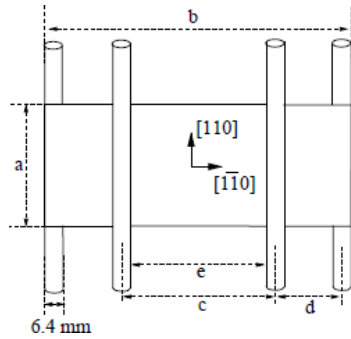


**Fig. 13-26:** (left) Roller bender design DLM with water conduction cooling at X17B1 NSLS. (center) Roller bender schematic.

**Fig. 13-27:** (right) Leaf bender design DLM without cooling at X7B NSLS.

The proposed conceptual design for the XPD beamline follows Z. Zhong's DLM designs (6), incorporating different options for bending and cooling. Three crystals of different dimensions have been mounted on the in-house holder of Fig. 13-28 and bent to  $R_s < 1$  m and  $R_m = 25 - 50$  m (section E-2). FEA (section E-3) is performed to optimize the crystal dimension, design and cooling in a number of variants which are described below: sections E-4 to E-8.

## E.2 Measurement of the bending radii of the leaf bender

Using the bender of Fig. 13-28, the sagittal bending radius is adjusted by pushing one of the two stainless steel supporting flexible legs and the other one is fixed. The clamping is achieved by wedging the crystal directly with an aluminum spacer tightened by two screws in a groove on each side.

The Zygo Verifire MST interferometer (NSLS-II) is used to measure the bending radii  $R_s$  and  $R_m$  of the crystal samples. Fig. 13-29 shows test results for three crystals of different sizes clamped at their edges: only the narrowest crystal shows a linear behaviour. As the crystal becomes wider, the anticlastic effect is reduced, and therefore, the meridional bending radius,  $R_m$ , approaches a plateau with increasing sagittal bending.  $R_m$  remains within the 25 m – 30 m range for  $R_s$  values ranging between 1 m and 2 m. These tests illustrate the dependence of the ratio of bending radii on the crystal's aspect ratio. Moreover, it will be shown in section E-4 that the non-linear behavior is predicted by the large deformation theory.

Another observation is that none of the curves extrapolates to zero and the offsets of the curves vary, i.e., the crystal is rarely flat even if the bending is released. This may be caused by the residual strain with different clamping conditions (e.g., tightness and unevenness). Table 13-4 presents the results of  $R_m$  values for the working  $R_s$  range.

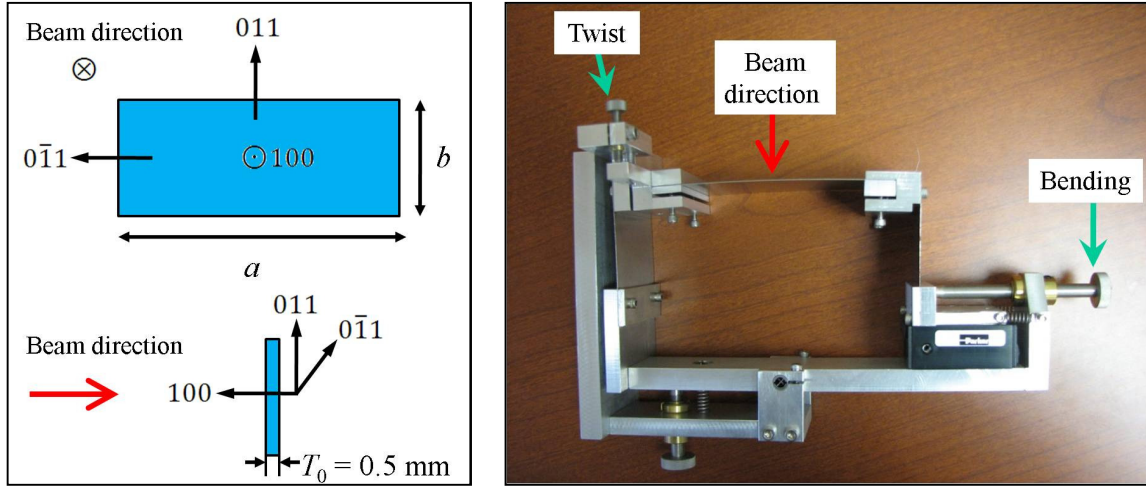


**Fig. 13-28:** The crystal geometry showing crystal planes. (right) The test bender used for the measurements of bending radii.

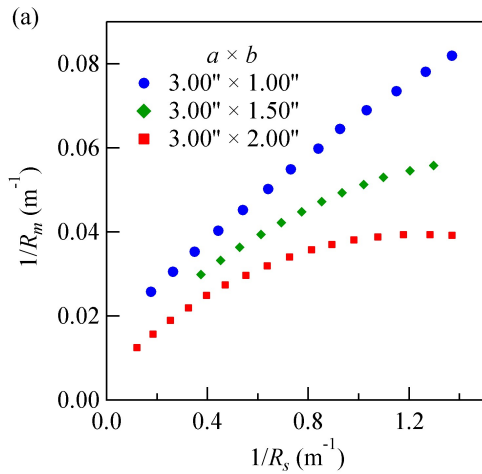


**Fig. 13-29:** The inverse of the meridional bending radius  $1/R_m$  as a function of the inverse of the sagittal bending radius  $1/R_s$  for different crystal dimensions (experimental results).

**Table 13-4:**  $R_m$  for different crystal dimensions at various bending radii  $R_s$ .

$R_s$ (m)	2.0	1.5	1.2	1.0	0.8
a/b	$R_m$ (m)				
3.0	23.1	19.3	16.7	14.8	12.9
2.4	29.9	24.8	21.4	18.9	16.6
2.0	28.5	24.2	21.5	19.7	18.1
1.7	28.7	25.3	23.4	22.2	21.7
1.5	31.9	27.9	25.5	24.2	23.6

### E.3 Numerical simulations

The main requirements for the DLM design are:

- the crystals should be bent to  $R_s$  values ( $\sim 1\text{ m} - 2\text{ m}$ ) while  $R_m$  remains within its prescribed range ( $\sim 25\text{ m} - 50\text{ m}$ ) over the beam nominal footprint.
- cooling should minimize the thermal bump, a support system that allows unconstrained thermal expansion is desirable.
- vibration due to cooling or other sources should be minimal.

The input parameters are as follows:

- crystal dimension is  $84 \times 38 \times 0.5\text{ mm}^3$  and beam dimension is  $35 \times 5 \times 0.5\text{ mm}^3$ .
- the Si crystal surface normal is (100) and the other two perpendicular directions are (011) and (0-11) (Fig. 13-30).
- the thermal heat load on the DLM is  $0.5\text{ W/mm}^3$  in a volume of  $35 \times 5 \times 0.5 / \sin(35.26 + \theta_B)\text{ mm}^3$ .
- anisotropic Si crystal properties and temperature dependent material properties (thermal conductivity and coefficient of thermal expansion) are taken into account in the calculations.
- the large deflection theory is applied since the deformation and the thickness of the crystal are of the same order of magnitude (Kirchoff-Love classic thin plate theory). This implies that only a numerical solution is available, but the closed form expression provides design insight.

According to the linear elasticity theory for isotropic material,  $R_s/R_m$  is proportional to the Poisson's ratio  $\nu$ . The expression for the ratio of curvatures is generalized for the case of an anisotropic material in (46). This reference identifies four factors defining the ratio  $R_s/R_m$ :

- a) anisotropic material properties defined by the stiffness matrix and crystal orientation
- b) crystal aspect ratio  $a/b$  (quadratic dependence)
- c) stiffening ribs in one direction only change the moment of inertia and introduce orthotropy
- d) boundary conditions (clamped or simply supported edge): influence on the anticlastic bending depends on  $a/b$

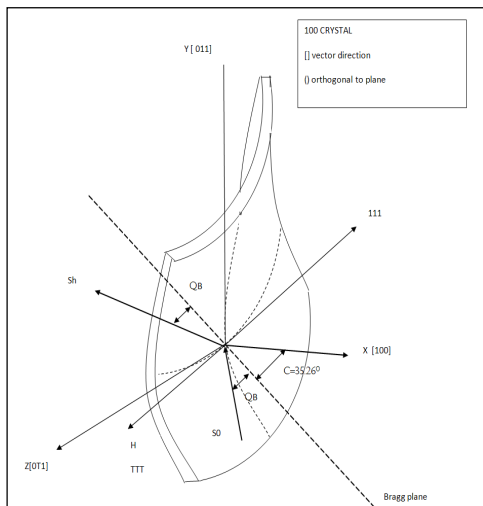


**Fig. 13-30:** Si (100) crystal orientation used in the ANSYS calculation.

### E.4 Analysis of the leaf bender

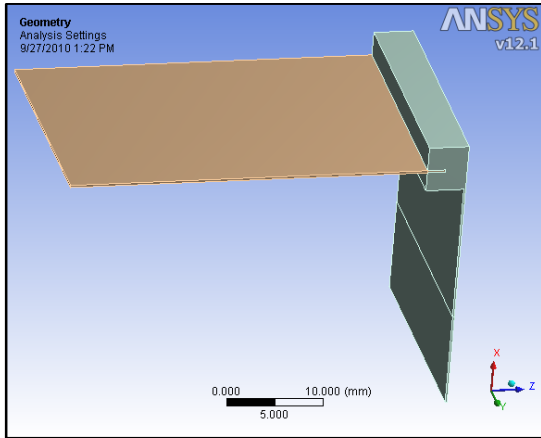


Fig. 13-31: Leaf bender (quarter model).

The leaf bender design consists of a crystal clamped at its edges and bent by pushing on the sides of supporting flexible legs. Tests were performed without heat load. Should there be some heat load, cooling by conduction would have to occur at the clamped edge. Cooling the bottom of the leg is not effective due to the long and narrow conduction path provided by the leaf. The cooling is expected to induce undesirable vibrations.

### E.5 Analysis of the leaf bender with rib

Another method of altering the natural anticlastic curvature is to introduce ribs along the width of the crystal. The rib dimensions (width, height and location) are chosen to obtain the desired anticlastic bending for a given sagittal bending. ANSYS calculations confirm that there is always a possible solution. Theoretically, the ratio of bending radii depends on the cube of the rib height and linearly on the width and location.

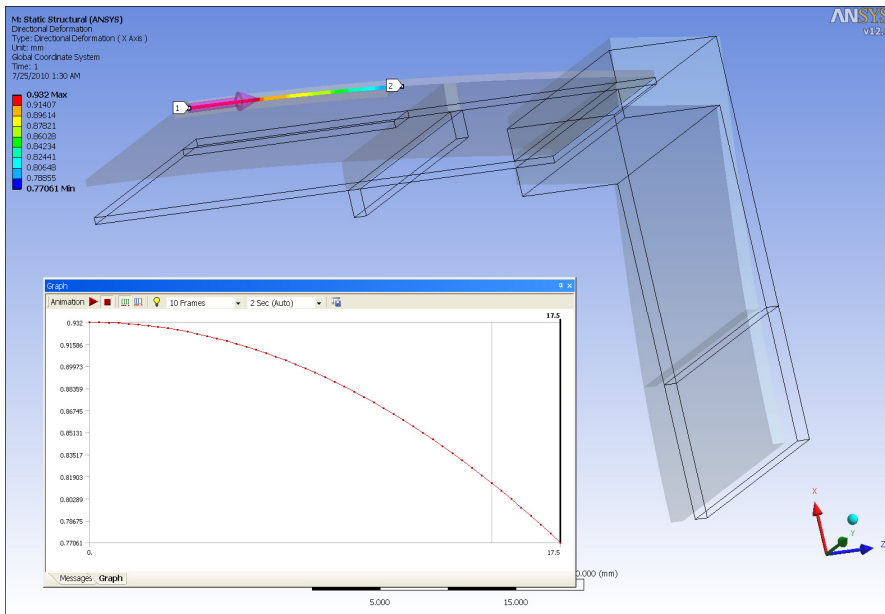


Fig. 13-32: ANSYS results showing the bending of the leaf bender with rib (quarter symmetric model).

With the introduction of a rib (size =  $2 \times 1 \text{ mm}^2$ ), the bending radius  $R_m$  is about 40 m while  $R_s$  is 1 m. When applying the heat load, meridional bending is reduced but there is no change in the sagittal bending. The bending radius  $R_m$  remains about 60 m for  $R_s$  of 1 m.

Although the leaf bender design with a rib seems a promising solution for achieving the required bending in both the sagittal and meridional directions, this design has the following disadvantages:

- a uniform  $R_m$  range (25 m – 50 m) is difficult to achieve within the beam footprint. Variations in  $R_m$  could be reduced by varying the crystal width: an increase at the centre could locally reduce the value.
- the clamped edges do not allow the crystal to expand freely under thermal load, thus introducing additional deformations.
- most importantly vibrations are not reduced.
- it is not realistic to exchange crystals with different ribs inside the DLM to vary the anticlastic bending when working at different energies.

## E.6 Analysis of the roller bender with integrated cooling

In order to circumvent the limits of the design in E-5, the response of the crystal to a roller bending mechanism is analyzed. The required bending moment is applied by controlling the horizontal and vertical spacings between the rollers. The crystal edges are conduction-cooled with LN flowing through the channels. The cooling channels can run through a monolithic piece of silicon, or through Cu pieces bonded to Si. This roller bender design has advantages over a clamped system:

- The rollers make two lines of contact and hence let the crystal expand freely, without exceedingly high stresses. The thermal stresses are minimized in this unconstrained crystal configuration.
- by changing the spacing between the rollers, the effective crystal aspect ratio changes.
- the position of the rollers can be dynamically changed

Therefore the ratio of anticlastic to sagittal bendings is adjustable and changes with the square of the aspect ratio.

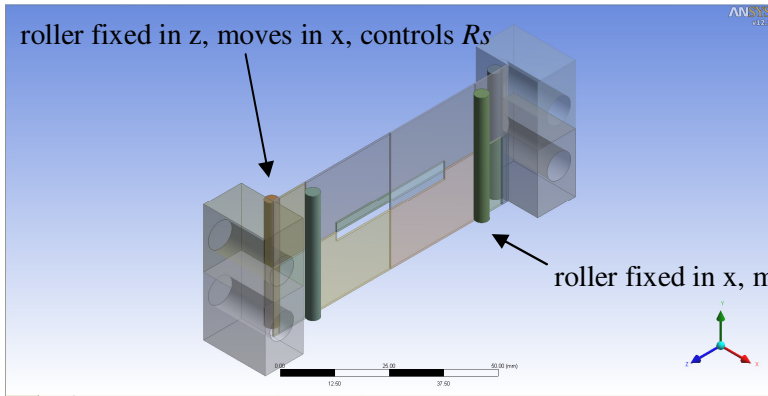


**Fig. 13-33:** ANSYS model showing the bending of the roller bender.

The displacement of outer rollers normal to the crystal drives the sagittal bending radius. By changing the position of the inner rollers, the meridional bending radius  $R_m$  can be controlled dynamically for a given  $R_s$ . Different cooling schemes are compared in Table 13-5. Radiative cooling is always present and treated as an additional effect but not solely relied on. The main drawback of this design is the risk of coolant flow induced vibrations.

**Table 13-5:** Evaluation of different cooling schemes.

Schemes	Pros	Cons	Notes
Water cooling	Simple to handle low vibration effects steady temperature.	Limited heat dissipation capacity	Insufficient for the high heat load at XPD.
InGa bath cooling	Relatively simple to handle very low vibration effects.	The heat dissipation in the meridional direction is asymmetric. Therefore $R_m$ is non-uniform.	High constraints on the design (see for example (12)).
LN cooling	Very good heat dissipater, very low slope error.	Direct cooling would introduce undesirable vibrations	Non linear material properties extremely well matched to nitrogen temperature: zero thermal expansion, thermal conductivity higher by one order magnitude at nitrogen temperature
Gaseous Nitrogen	Cooling without introducing mechanical complications	Possible gas induced vibrations Introduction of nitrogen in beamline vacuum low film coefficient	Could be used as a supplement to edge cooling, if edge insufficient

## E.7 Analysis of the roller bender with cooling through braids

Cooling is provided by braids attached to the edges to eliminate vibrations that may arise from the LN flow. As with the previous design a variable  $R_s/R_m$  ratio is achieved by changing the location of the outer rollers and by varying the position of the inner rollers (Fig. 13-34).

Design assumptions:

- Liquid nitrogen flows through a copper block, the wall of the channels is kept at  $-196^\circ\text{C}$
- The heat of 70 W is uniformly applied in the volume, although the validity of this assumption needs to be assessed. The uniform heat distribution over the beam footprint is not a conservative assumption and

temperatures are underestimated. The actual heat has the shape of a Gaussian and is not uniformly deposited throughout the thickness of the crystal

In order to eliminate vibrations, copper braids are used to connect the crystal to a LN cooling channel (47). The heat exchange area is further reduced by a factor of two to account for imperfect thermal contact.

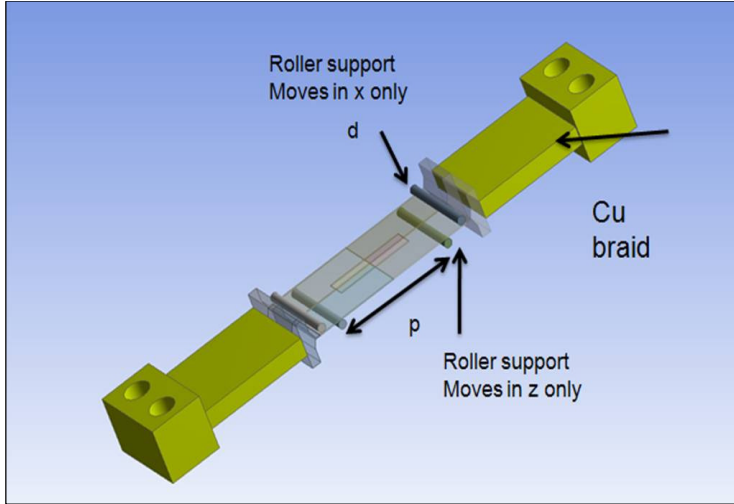


**Fig. 13-34:** Roller bender design with indirect LN cooling through Cu braids.

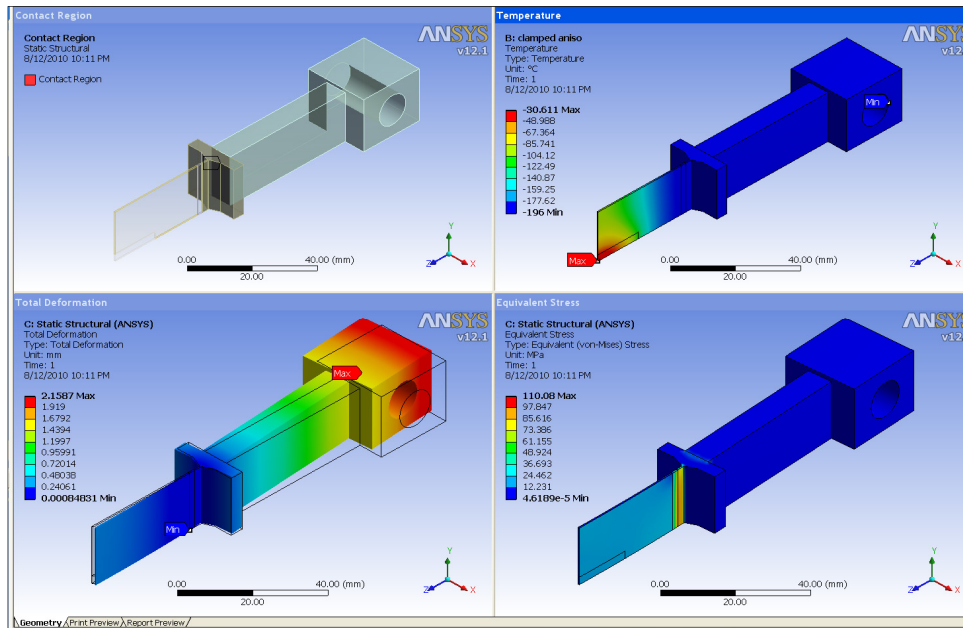


**Fig. 13-35:** FEA analysis of the Roller bender design. Maximum temperature  $-31^{\circ}\text{C}$ , maximum stress 110 MPa, deformation at center about 1 mm. one quarter model).

The results are:

- The maximum temperature is  $-34^{\circ}\text{C}$ , and stress in the crystal well below 120 MPa, except under the rollers where one expects high localized stresses. For comparison, water cooling would result in maximum temperature of  $722^{\circ}\text{C}$  and stresses of 210 MPa in the centre of the crystal; **water is thus not an option**. Error slopes are small, of the order of  $1\ \mu\text{rad}$  along z, and  $0.1\ \mu\text{rad}$  along x.

- The displacement of the inner rolls on the internal surface of the crystal has been varied to obtain the desired  $R_s$  at various energies. The corresponding  $R_m$  at  $z = 0$  and  $z = 17.5$  mm have been tabulated for comparison with the permissible value. A prime (') denotes a calculated value. Fig. 13-36 and Table 13-6 show that  $R'_m$  stays within the prescribed boundaries for the energy range 30 to 70 keV.
- The Cu braids reduce the vibration generated at the Cu cooling channel. This design of the braid has been tested for a DCM design.

**Table 13-6:** FEA results: Variable  $R'_m$  for variable energies for the roller bender.

Energy (keV)	$d$ (mm)	$R'_s$ (m)	$R'_{m\_min}$ (m)	$R'_{m\_max}$ (m)
30	-0.037	2.07	52.03	73.21
40	-0.050	1.52	35.97	58.21
50	-0.062	1.22	27.03	40.65
60	-0.075	1.00	23.70	37.31
70	-0.088	0.86	20.83	31.06

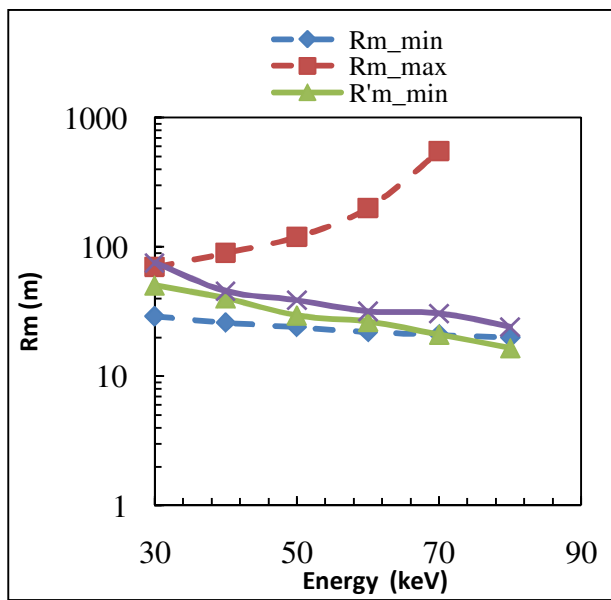


**Fig. 13-36:** FEA results: Calculated  $R'_m$  at variable energies for the roller bender

Fig. 13-36 shows the  $R_m$  values for variable energies. The dotted lines represent the allowed bounds; the solid lines are calculated values at the center ( $R'_{m\_min}$ ) and at the edge of the beam footprint ( $R'_{m\_max}$ ). Variability within the footprint could be reduced by increasing the width of the crystal at the center, resulting in a lozenge shape. This is a third order effect and it has not been investigated yet.

As a conclusion, the numerical analysis guided by theory has helped in defining a possible design. The engineering challenges reside in the execution of the roller mechanism with variable positioning and in keeping the roller aligned and parallel. The edge cooling with braids may not be sufficient in which case additional cooling must be considered (side or convective) or the incident heat reduced. Thermal expansion forces are typically orders of magnitude greater than friction forces, but there may be locked-in stresses due to crystal imperfections. Further engineering and testing are necessary to explore the validity of this design.

## F REFRACTIVE OPTICS

The compound refractive lens (CRL) can be used as the vertical focusing optics for both branches of the XPD beamline. For a CRL with  $N$  cylindrical holes, the focal length  $F$  is given by:  $F = R/(2N\delta)$ , where  $R$  is the radius of the lens,  $\delta$  is the real part of the refractive index decrement. The required focal lengths are 5.5 m for branchline 2 and 10.5 m for branchline 1. The effective aperture  $A_a$  due to absorption, one of the most essential features of CRLs, is given by (48)

$$A_a = (4\pi F\delta/\mu)^{1/2}$$

where  $\mu$  is the linear attenuation coefficient. At energies above 30 keV, the effective aperture is always less than 1 mm (Fig. 13-37).

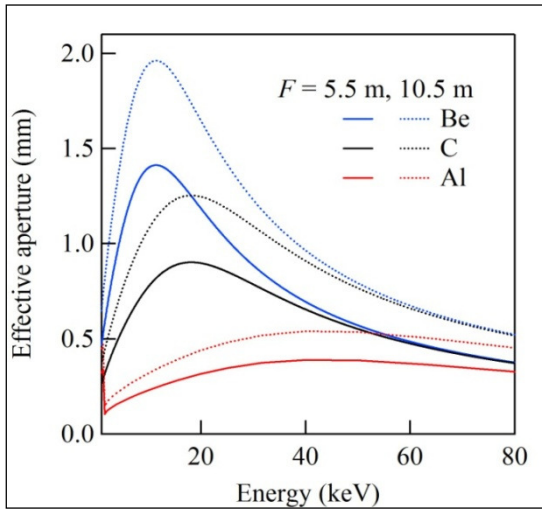


**Fig. 13-37:** Effective aperture as a function of photon energy for the focal length  $F = 5.5$  m (solid line) and  $F = 10.5$  m (dotted line).

CRLs with circular holes also suffer from the spherical aberration. The geometric aperture  $A_g$  due to the deviation from the ideal parabolic shape ( $\pi$  phase shift) is then (49)

$$A_g = 2(4\lambda FR^2)^{1/4}$$

where  $\lambda$  is the wavelength. In practice, the effective aperture  $A$  is chosen as the smallest of the two above values. At high energies ( $> 30$  keV),  $A_g$  is always the limiting factor of circular CRLs. The length of the circular CRL is given by  $L = N(2R + d)$ , with  $d$  is the spacing between holes. While using wiggler sources, one wants to increase  $A_g$  by increasing  $R$  (by the  $1/2$  order), which will, however, increase the total length (by the  $2^{\text{nd}}$  order of  $R$ ) of the CRL. Therefore, circular CRLs are not suitable for high energy beamlines with large divergence.

For the parabolic CRLs, the effective aperture  $A$  is always equal to  $A_a$  due to the absence of the spherical aberration. One would then choose the aperture (parabolic width) as  $A_a$ . The radius,  $R$ , at the apex of the parabola still determines the number of holes,  $N$ , through  $N = R/2F\delta$ . The longitudinal size of each hole is given by  $L_1 = A_a^2/4R + d$  and the total length of the CRL is  $L \approx A_a^2/8 F\delta + Rd/2F\delta$ . Since  $d$  is small in comparison with  $A_a^2/4R$ , the total length is invariant with  $R$ . When  $R = 2F\delta$  (for  $F = 5.5$  m and  $\delta = 6.1 \times 10^{-8}$ ,  $R$  is  $0.67 \mu\text{m}$ ), the case of a single parabolic concave lens is restored. However, the lens with such a small  $R$  and large  $L_1$  is extremely difficult to manufacture. Therefore, choosing  $R$  to be comparable with  $L_1$  will be the optimized condition.

### Table 13-7 and

Table 13-8 show some Be CRL parameters comparing the circular and the parabolic shapes. Note that the gain of a focusing device is the ratio of the flux density in the focal spot to the flux density in the same area, without lens. The gain of CRL is calculated as (49):

$$g = \frac{A}{\sigma_s} \left( \frac{F_1}{F_2} + 1 \right) \exp(-\mu N d),$$

where  $\sigma_s$  is the source size. A parabolic shape CRL is needed in order to achieve the maximum effective aperture and gain while keeping a reasonable total length. When designing parabolic CRL arrays for working at different energies, one should choose the largest aperture  $A_a$  at the lowest energy along with a reasonable  $R$  to accommodate all energies.

Table 13-9 presents the optimized characteristics of parabolic CRLs for both branches of the XPD beamline. The effective aperture of a CRL is about half of the acceptance of a 1 m Pt-coated mirror for all energies. In addition, the horizontal acceptance of the CRL is limited to several millimeters, which does not match the large horizontal fan of the Wiggler source.

**Table 13-7:** Calculated Be CRL parameters at 74.8 keV with:  $d = 10 \mu\text{m}$ ,  $F = 5.5 \text{ m}$ .

Lens Radius $R$ (mm)	Number of Lenses $N$	Effective Aperture $A$ (mm)	Real Gain $g$	Length $L$ (cm)
<b>Circular</b>				
0.25	376	0.138	192	19
0.5	751	0.195	246	76
1	1502	0.276	285	302
<b>Parabolic</b>				
0.2	300	0.399	566	6.3

**Table 13-8:** Calculated Be CRL parameters at 50 keV with:  $d = 10 \mu\text{m}$ ,  $F = 10.5 \text{ m}$ .

Lens Radius $R$ (mm)	Number of Holes $N$	Effective aperture $A$ (mm)	Real Gain $g$	Length $L$ (cm)
<b>Circular</b>				
0.25	87	0.180	136	4
0.5	174	0.254	188	18
1	348	0.360	253	70
1.5	1007	0.374	430	303
<b>Parabolic</b>				
0.4	139	0.793	591	5.6

**Table 13-9:** Optimized parabolic CRL parameters for the XPD beamline.

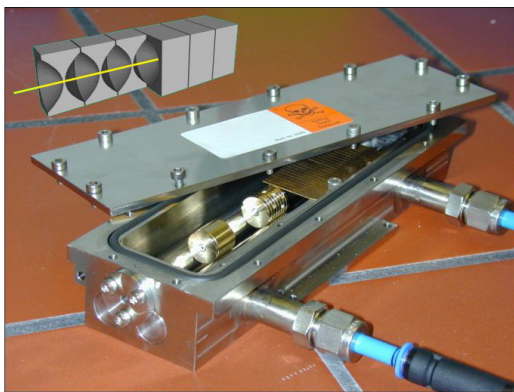
Energy (keV)	Apex Radius (mm)	Effective aperture (mm)	No. of lenses	Transm. of full vert. beam*	Horizontal acceptance*
<b>Branch 2 (endstation B), <math>F = 5.5</math> m</b>					
39.1	0.2	0.71	82	9.5%	17%
63.8	0.2	0.46	219	6.0%	17%
74.8	0.2	0.40	300	5.1%	17%
<b>Branch 1 (endstation C), <math>F = 10.5</math> m</b>					
30	0.4	1.23	50	17%	15%
40	0.4	0.96	89	13%	15%
50	0.4	0.79	139	11%	15%
60	0.4	0.67	200	8.9%	15%
70	0.4	0.59	273	7.7%	15%

\* Assuming the horizontal acceptance of the CRL is 3.5 mm and both branches have horizontal focusing optics (DLM for first branch and SBM for the PDF branch) before the CRLs. The vertical transmission is calculated for the full horizontal beam, and the horizontal acceptance is obtained for the full vertical beam.

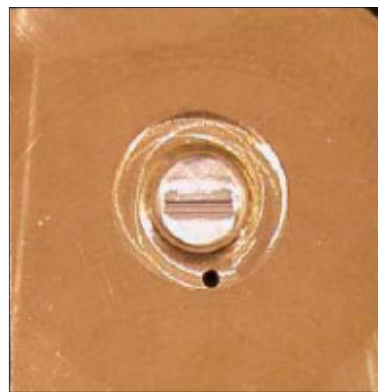
CRL are increasingly used at high-energy x-ray beamlines, e.g., at the ESRF or at the APS (11) (10). High energy x-ray operation overcomes the main weakness of the CRL, i.e., the attenuation of the beam through the CRL is not as critical. The applicability of low-Z lenses (e.g., Be, B, C) at high energies is limited because the refractivity decreases. Hence the number of individual lenses required to produce the required focal distance grows quickly with energy. The refraction power of denser lens materials (e.g., Al, Si, Ge or even Ni) is higher and thus the number of lenses can be reduced, while the absorption remains tolerable. A detailed study of the CRL parameters for optimized focusing capability and flux is performed and shown in Table 13-7 to

Table 13-9.

Commercial CRL of high quality are available. Parabolic Al lenses of 3.5 mm H  $\times$  1 mm V have now become available<sup>27</sup>. Such lenses are shown below.



**Fig. 13-38:** Photo of commercially available CRL<sup>27</sup>.



**Fig. 13-39:** Linear Al lens: opening = 1  $\times$  3.5 mm<sup>2</sup> and  $R = 200$   $\mu$ m. (Lengeler, Snigirev)

In the transfocator, CRL are focusing optics whose aperture and lens can be varied. Prism-shaped CRL are also used as condensers for providing larger aperture and transparency. Details about the transfocator and the condenser are described below.

<sup>27</sup> Technical University of Aachen, Prof. Dr. Lengeler

**Transfocator:** a tunable x-ray focusing apparatus based on CRL has been recently designed and tested at the ESRF (11). The transfocator is a lens assembly whose focal length can be continuously adjusted by the mechanical movement of one or more groups of individual parabolic lenses. By varying the number of lenses in the beam, the energy focused and the focal length can be varied continuously throughout a large range of energies and distances, e.g., focusing 50keV x-ray beam and partially collimating the 80keV photons. The transfocator can be used either as a stand-alone instrument in both white and monochromatic beams to vertically focus the beam, or in conjunction with another optical element downstream (CRL or multilayer mirror). Substantial gains in flux ( $\geq 10^4$ ) are observed. In addition, the transfocator can deliver a vertically-collimated beam, instead of a naturally diverging beam, which better matches the acceptance of a secondary optics downstream, e.g., a high-resolution monochromator or a secondary focusing device.

**Condenser:** as mentioned above, existing refractive x-ray lenses are characterized by either small apertures or high absorption in the border areas. Increasing transparency and aperture is shown to be possible e.g., using an array of prism-shaped structures (X-ray prism lenses) (50). The concept of a 3-4 mm aperture condenser made by deep lithography and LIGA techniques could be a better source for wiggler beamlines.

## G MULTILAYERED MIRRORS

See discussion in b) of section 5.6.1.

**Table 13-10:** Calculated multi-layered mirror characteristics with different materials.

	Pt/B <sub>4</sub> C	W/B <sub>4</sub> C	Ru/B <sub>4</sub> C	Ni/B <sub>4</sub> C	Mo/B <sub>4</sub> C
<b>75 keV, 2nm bilayer</b>					
Grazing angle (mrad)	4.23	4.21	4.2	4.19	4.19
reflectivity	96.0%	83.4%	95.4%	98.7%	95.6%
FWHM (μrad)	67.8	56	39.9	32.2	28.7
ΔE/E: (10 <sup>-3</sup> )	16.1	13.3	9.5	7.7	6.8
<b>64 keV, 2.36nm bilayer</b>					
Grazing angle (mrad)	4.23	4.22	4.19	4.18	4.18
reflectivity	95.3%	96.0%	94.5%	98.5%	94.5%
FWHM (μrad)	95.9	86.8	56	46.9	45.5
ΔE/E: (10 <sup>-3</sup> )	22.8	20.6	13.4	11.2	10.9
<b>39 keV, 4nm bilayer</b>					
Grazing angle (mrad)	4.26	4.24	4.17	4.14	4.14
reflectivity	91.5%	92.6%	89.7%	96.8%	90.3%
FWHM (μrad)	281	255	167	129	135
ΔE/E: (10 <sup>-3</sup> )	66.9	60.7	39.8	30.7	32.1

**Table 13-11:** Calculated Pt / B<sub>4</sub>C multi-layered mirror (2nm bilayers) characteristics with different gamma ratios at 75 keV.

Gamma	0.2	0.3	0.4	0.5	0.6	0.7	0.8
Grazing angle (mrad)	4.19	4.2	4.21	4.23	4.24	4.25	4.26
reflectivity	97.7%	97.3%	96.8%	96.0%	94.7%	92.5%	88.2%
FWHM (μrad)	43.1	58.1	66	67.8	60.7	51	36.1
ΔE/E: (10 <sup>-3</sup> )	10.3	13.8	15.7	16.1	14.5	12.1	8.6

**Table 13-12:** Calculated multi-layered mirror characteristics with different numbers of bilayers.

No. of bilayers	50	100	200	300	400	500
<b>75 keV, 2 nm bilayer</b>						
Pt/B4C	63.4%	91.6%	95.9%		96.0%	
W/B4C	50.3%	77.4%	83.2%		83.4%	
Ni/B4C	20.4%	55.7%	90.9%	97.5%	98.5%	98.7%
<b>64 keV, 2.36 nm bilayer</b>						
Pt/B4C	83.9%	94.7%			95.3%	
W/B4C	79.9%	94.9%			96.0%	
Ni/B4C	39.4%	80.1%	97.3%	98.4%		98.5%
<b>39 keV, 4 nm bilayer</b>						
Pt/B4C				91.5%		
W/B4C				92.6%		
Ni/B4C	93.7%	96.7%			96.8%	

## H DETECTOR DEVELOPMENT

### H.1 1D strip detectors

Ongoing R&D seeks to develop PSD systems which combine high resolution with faster data acquisition rates and simple calibration without compromising the signal-to-noise (S/N) ratio. The current challenge is to fabricate the Ge analog of Si x-ray detectors including PSDs, fully depleted CCDs or pixelated structures. The Ge technology is impeded but such issues as GeO oxide stability, high temperature annealing, absence of wet lithography, dangling states and cooling. CdTe (notwithstanding the polarization problems) and CdZnTe are alternative sensor materials (51).

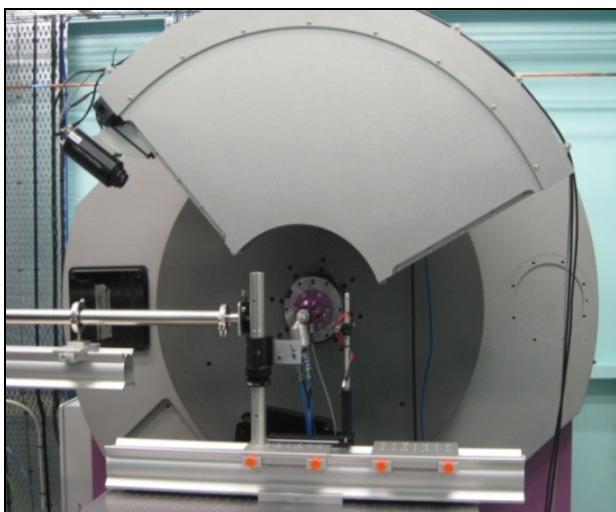


**Fig. 13-40:** Mythen detector at the PD beamline at the Australian Source, courtesy of Kia Wallwork and Justin Kimpton.

### H.2 2D pixel detectors

The rear face of the sensor is pixellated and each pixel is connected to a complete independent photon-counting readout electronic (in-pixel processing). Therefore, a pixelated array detector offers a spectrum-per-pixel response, with adequate energy and spatial resolution, and hence allows simultaneous spectroscopy/diffraction experiments. Its high frame rate, noiseless and stable operation, energy discrimination capability (elimination of inelastic scattering e.g., Compton), electronic shuttering and very large dynamic range stretch the capabilities of PD experiments. Pangaud et al. (51) shows an experiment where the parallel architecture of the XPAD detector design collects 423 images with less than 10ms exposure (16 bits) or 233 images exposed for more than 10ms (dynamic range=32 bits). In both cases the dead time between two consecutive images is no more than 2 ms; it will be further reduced to below 1 msec with buffered output logics in next generation detectors. The full diffraction “movie” is transferred afterwards to the acquisition station after the measurement via a 100MB ethernet link. More applications of the hybrid photon-counting pixel detector in PD is given in reference (52). New sensor materials (Ge, Cd(Zn)Te, GaAs) have recently become available in sufficiently high quality to envisage the next generation of Hybrid Pixel Array Detectors (53) (54) (55) (56). Besides the recent improvements in the material quality and the processing technology of CdTe, 1 mm thick CdTe offers an absorption probability, which is high up to photon energies of 100 keV.

The main existing developments are :

- PILATUS (57) (58)
- MEDIPIX2 (59) (60)
- XPAD (61) (62) (63)

- XAMPS (X-ray Active Matrix Pixel Sensors, developed at NSLS and initially developed for the X-ray Pump Probe (XPP) instrument at the Linac Coherent Light Source (LCLS) in Stanford (CA).

Another significant breakthrough of this technology is that the pulse counting can be performed on a chip by a 12-bit counter with an overflow bit whose state can be scanned at high frequency without interrupting the counting process. This continuous reading and treatment of this overflow bit allows the image dynamic range to increase virtually to infinity (27-bit for XPAD3 in (64)). This supersedes the effective dynamic range of integrating devices such as CCDs.

One downside of these detectors is the relatively small active area per module. When budget permits, the single chips can be tiled together to form larger sensitive arrays.

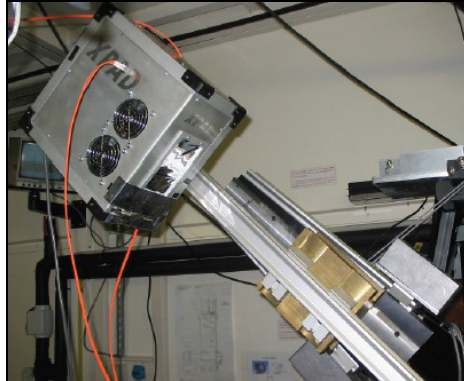


**Fig. 13-41:** View of the XPAD detector at the BM02 beamline at the ESRF.

### H.3 Large-area image plates

Image plates (IP) are still useful in those PD applications which do not require second or sub-second time resolution but where a large angle coverage at low cost with adequate resolution, low noise, and large dynamics are needed (e.g., see (65)). Image remanence and ghosting effects can be a concern, depending on the incident flux and radiation dose rate.

The MAR345 image plate scanner (circular active area of diameter 345 mm with a pixel size of 150  $\mu\text{m}$  or 100  $\mu\text{m}$  depending on the readout mode) is also a widespread high-energy detector, but the Point Spread Function deteriorates the pixel size by  $\sim 3$  and the efficiency at 90 keV is as low as 10%. Yet the readout of this image (including erase cycle and control macro completion) requires approximately 90 seconds. Since time-dependent measurements are part of the scientific core of XPD (section 1.1), IP is not an option over the long term.

### H.4 High-resolution CCD cameras

The CCD ship fiber-tapered to a phosphor screen advantageously replaces the IP, but in comparison, it still shows some limitations regarding the noise integration and the relatively low counting dynamics. In addition, the optical demagnification using phosphor screens might corrupt the transfer function (variable image distortions) and the statistical properties of the counting can be lost. Another issue is radiation damage: Compton scattering obscures the camera lens optics (color-centers in lenses and fibers). The readout-time can be improved by the on-ship pixel binning but the noise deteriorates with fast read-out. Nowadays, the frame transfer mode, the pipeline readout mode or more recently the split frame transfer mode use the principle of ship-masking and in-ship storage and yield frame rates as high as 100 frames per second (fps). Customized aspect ratios and scintillators with a notch (which lets the direct beam passing through) have become commercially available.

### H.5 High-speed flat panel detectors

The CMOS-based digital flat-panel detector technology makes the indirect conversion mode (phosphors and fiber optic tapers) less attractive. Initially designed for medical imaging, the digital flat-panel detectors can combine an

amorphous Si panel with a CsI:Tl scintillator and thus show a superior efficiency at high x-ray energies. The detector exhibits a narrow (one-pixel) point-spread function and a distortion-free image, most appropriate for the acquisition of high-quality diffraction data. High frame rates and shutterless operation extend the experimental possibilities for PD. Long series of 2D diffraction images at several thousands of frames per second ( $1000 \times 1000$  pixels, minimum dynamic range  $\geq 10$  bits) can be acquired with the CMOS-based detectors. A good scattering sample requires a detector image plate, such as the MAR555 ( $140 \mu\text{m} \times 140 \mu\text{m}$  pixel size,  $430 \times 350 \text{mm}^2$ ,  $\sim 1 \text{Hz}$ , 18 bit contrast resolution), be exposed only for a few hundred microseconds.



**Fig. 13-42:** Perkin-Elmer flat panel detector.

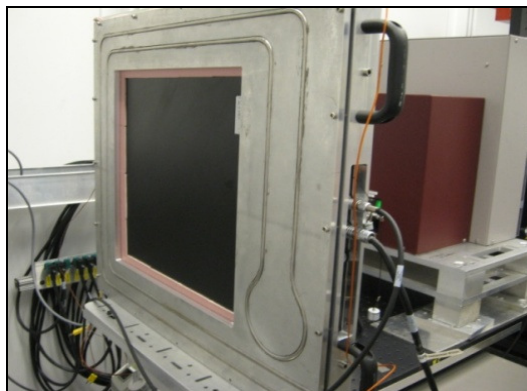


**Fig. 13-43:** Flat panel detector at 11-ID, courtesy of P. Chupas.

**Table 13-13:** CCD and pixel detectors.

	<b>XPAD3 (64)</b>	<b>Pilatus (66)</b>	<b>MARCCD</b>	<b>Frelon-2K (67)</b>	<b>SX 165</b>	<b>MX 325</b>
Sensor	700mm-thick, high resistivity p-type CdTe	320 $\mu$ m hybrid CMOS	45 $\mu$ m Gd <sub>2</sub> O <sub>2</sub> S:Tb	CCD	CCD	CCD
No. of pixels	9600 x 9600	2463 x 2527	4096 x 4096	2048 x 2048	2048 x 2048	16 x (2048 x 2048)
Pixel size ( $\mu$ m)	130	172	80 or 160	14	40	15
Active area (cm) of 1 module	7.5 x 3	42.4 x 43.5	165mm diameter		16.5cm dia.	32.5 x 32.5
Max. count rate (Mcps)	$\leq 1$	2			50,000 ph/pixel	72,000 ph/pixel
Dead time loss	$\leq 10\%$					
read out time	2msec/frame	2.3 msec	2 s	0.25 s	2.5 sec	1 sec
Frame rate	500 Hz	12 Hz		4 Hz		
Energy resolution	8% at 35 keV	500eV				
Dynamic range (bits)	32	20	16	16	16	16
Spread Function	x 1	x 1	x 1.3		100 $\mu$ m	100 $\mu$ m
Energy range (keV)	40-60	3-30				
Read-out Noise		No			2 ph/pixel	2 ph/pixel
Quantum efficiency		55% @ 15 keV			80% @ 12keV	80% @ 12keV
Working temperature	ambient	water cooling	-80°C	-20°C	-70°C	-80°C
Weight (kg)		95	20			125
Proprietary	ImXPad	Dectris	Mar Research	ESRF	RayoniX	RayoniX

**Table 13-14:** Image plate and flat panel CMOS detectors.

	<b>MAR345</b>	<b>MAR353</b>	<b>MAR555*</b>	<b>GE Medical</b>	<b>PE XRD 1621 (68)</b>	<b>Pixium 4700 (69)</b>
Sensor	207 $\mu$ m BaFBr:Eu	Se-coated TFT	Se-coated TFT	a-Si + 0.5 mm CsI	a-Si + 0.5 mm CsI	a-Si + 0.5 mm CsI
No. of pixels	3096 x 3096	2048 x 2048	3072 x 2560	2048 x 2048	2048 x 2048	1910 x 2480 2840 x 2874
Pixel size ( $\mu$ m)	100 or 150	122	139	200	200	154 43
Active area (cm) of 1 module	34.5 diameter	35.3 diameter	43 x 35	41 x 41	41 x 41	29.4 x 37.9 43 x 43
Max. count rate (MHz)						
Dead time loss						
read out time	108 or 80s (incl. read/erase time)	0.1 s	1.2 s			
Frame rate		10 Hz	~1Hz	15-30 Hz	15-30 Hz	7.5-60 Hz
Energy resolution						
Dynamic range (bits)	17	18	18	16	16	14
Spread Function	x 2.8			x 1.1	x 1.1	x 1.5
Energy range (keV)	4-100	6-100	10-100			
Dark current			none			
Noise			5 photons@12keV			
Efficiency						
Working temperature	Ambient		ambient	ambient	ambient	ambient
Weight (kg)	53		30	25	25	20
Proprietary	Mar Research	Mar Research	MarResearch	GE	Perkin Elmer	

\* No longer supported

**Table 13-15:** 1D pixel detectors.

	<b>Ge XSTRIP (70)</b>	<b>Si Strip</b>
Sensor	1mm-thick a-Ge	0.35 mm-thick Si
Nb of pixels	1024	1280
Pixel size ( $\mu\text{m}$ )	50	50
Active area (cm) /module	0.5	0.8 x 0.64
Max. count rate (MHz)		0.2/pixel @8 keV
Read out time	10 $\mu$ s	0.3 ms
Frame rate	100kHz	25Hz (24bit) 500Hz (4bit)
Energy resolution		350eV @ 5.9keV
Dynamic range (bits)		24
Spread Function	x 3 (150 $\mu\text{m}$ )	
Energy range (keV)	5-40	5-30
Dark current	10% of full dynamic range	
Noise		
Quantum Efficiency	$\geq 90\%$ @30keV	8% @ 30 keV
Working temperature	230 K	Air
Weight (kg)		0.3
Proprietary	Daresbury Lab. Laur. Berkeley Nat. Lab.	Dectris

